Carbon-based nanomaterials for energy applications
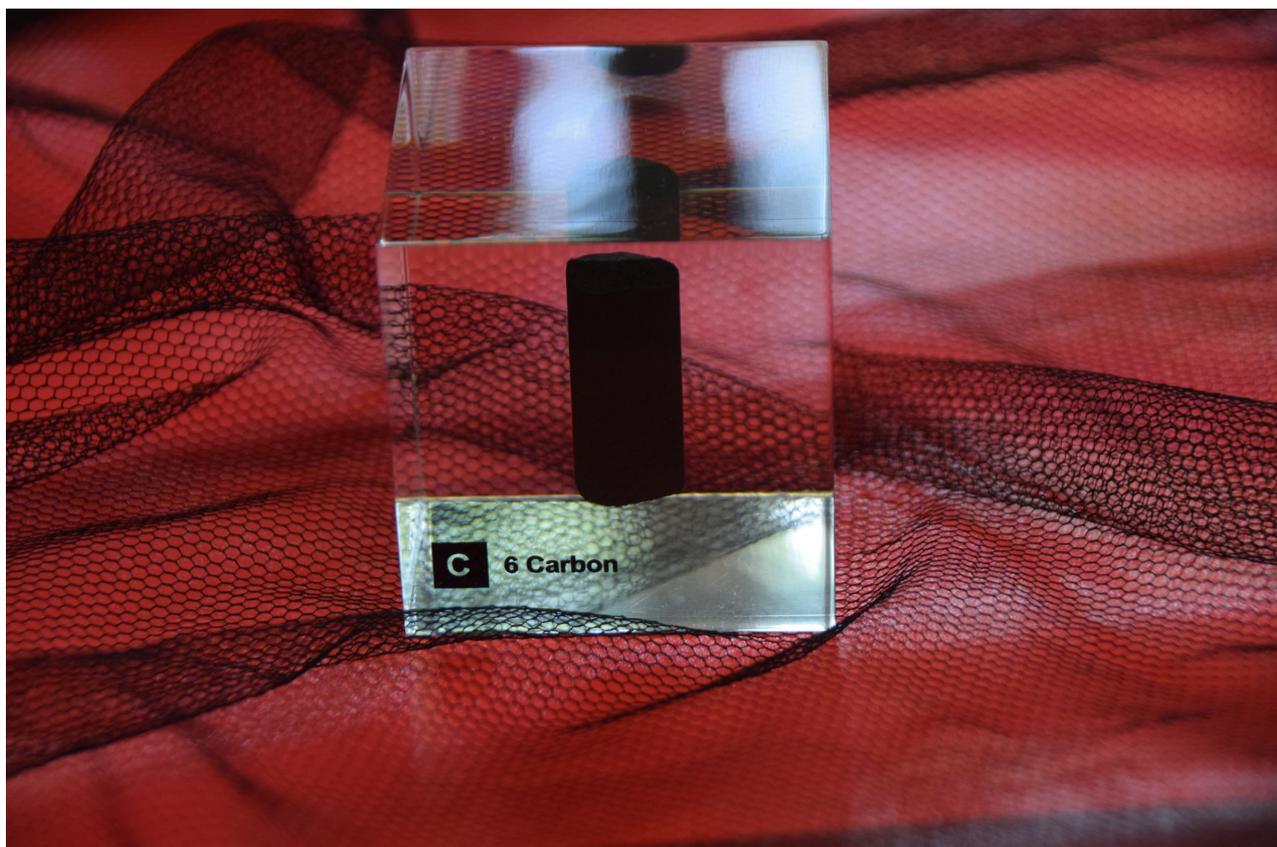
Edited by Jörg J. Schneider and Bastian J. M. Etzold

Imprint

Improving control of carbide-derived carbon microstructure by immobilization of a transition-metal catalyst within the shell of carbide/carbon core–shell structures

Teguh Ariyanto[*1,2], Jan Glaesel[2,3], Andreas Kern[2], Gui-Rong Zhang[2,3] and Bastian J. M. Etzold[*2,3]

Full Research Paper

Address:
[1]Department of Chemical Engineering, Faculty of Engineering, Universitas Gadjah Mada, 55281 Yogyakarta, Indonesia, [2]Lehrstuhl für Chemische Reaktionstechnik, Friedrich-Alexander-Universität Erlangen-Nürnberg, Egerlandstrasse 3, 91058 Erlangen, Germany and [3]Ernst-Berl-Institut für Technische und Makromolekulare Chemie, Technische Universität Darmstadt, Alarich-Weiss-Strasse 8, 64287 Darmstadt, Germany

Email:
Teguh Ariyanto[*] - teguh.ariyanto@ugm.ac.id; Bastian J. M. Etzold[*] - etzold@tc1.tu-darmstadt.de

* Corresponding author

Keywords:
carbon shell; catalytic graphitization; graphitic carbon; pore structure; transition metal

Abstract

Carbon materials for electrical energy devices, such as battery electrodes or fuel-cell catalysts, require the combination of the contradicting properties of graphitic microstructure and porosity. The usage of graphitization catalysts during the synthesis of carbide-derived carbon materials results in materials that combine the required properties, but controlling the microstructure during synthesis remains a challenge. In this work, the controllability of the synthesis route is enhanced by immobilizing the transition-metal graphitization catalyst on a porous carbon shell covering the carbide precursor prior to conversion of the carbide core to carbon. The catalyst loading was varied and the influence on the final material properties was characterized by using physisorption analysis with nitrogen as well as carbon dioxide, X-ray diffraction, temperature-programmed oxidation (TPO), Raman spectroscopy, SEM and TEM. The results showed that this improved route allows one to greatly vary the crystallinity and pore structure of the resulting carbide-derived carbon materials. In this sense, the content of graphitic carbon could be varied from 10–90 wt % as estimated from TPO measurements and resulting in a specific surface area ranging from 1500 to 300 $m^2 \cdot g^{-1}$.

Introduction

Carbon is a versatile material that has been widely utilized in many applications such as adsorption [1-3], catalysis [4,5], catalyst support [6-8], molecular sieves [9,10] and energy storage [11-13], owing to its large specific surface area and distinct pore character. For applications in which electrical conductivity plays an important role, e.g., battery electrodes, fuel-cell catalysts or supercapacitors [14-16], it is necessary for carbon to not only show porosity but also to feature a graphitic structure. The reason is that graphitic carbon consists of crystalline sp^2-hybridized fractions that induce high electron conductivity. Moreover, an enhanced crystallinity is favorable in terms of chemical stability, which is required especially when working under harsh conditions.

Many synthetic approaches were employed to produce carbon combining porosity and graphitic structure [17-19]. Among them, the carbide-derived carbon (CDC) is a promising route. CDC can be synthesized through the selective extraction of metals or metalloid atoms from metal carbides (Me_xC, e.g., TiC, SiC, VC, and Mo_2C) by using halogen gases at elevated temperatures. Depending on the carbide and parameters employed during the synthesis, CDC can be varied from extremely amorphous to highly crystalline microstructures and from ultra-micro- to mesoporous pore structures. Therefore, CDC is known as material with tunable microstructure and pore structures [20].

To produce CDC with a high content of graphitic structure, there are two possibilities that can be applied (neglecting a post-synthesis treatment after CDC synthesis). The first is very high synthesis temperatures (ca. 1500 °C) [4], which is, however, associated with a pronounced energy consumption for the reactor heating as well as with challenges to handle chlorine at such high temperatures. The second approach is using catalytic graphitization during the material synthesis. It typically requires only moderate temperatures (typically starting from 800 °C, depending on types of carbides [19]). Commonly used graphitization catalysts are transitions metals such as Fe, Ni, and Co [18,21,22]. The conventional method for catalytic graphitization is to mix the non-porous carbide and metal catalyst precursor prior to the selective etching at high temperature. Indeed,

the graphitic content is present, but the overall material is rather inhomogeneous [18,23]. Most likely the physical powder mixture or the simple dip coating of the powder carbide precursor with the transition-metal catalyst lead to a very inhomogeneous starting mixture, which is responsible for the final heterogeneous combination. Immobilizing the transition metal-catalyst at each particle would ensure a homogeneous catalytic graphitization of the whole powder samples.

We recently introduced the possibility to obtain core–shell particles in which a nanoporous carbon shell is covering a carbide core [14,15,24,25]. The porosity of this shell could suit for the immobilization of the transition-metal catalyst, as capillary forces would suck the impregnation solution within the shell and only excess solution would go into the voids between the particles. Subsequent chlorination of the carbide core to obtain carbide-derived carbon would be influenced by the transition-metal catalyst in the shell of each particle. This work studies the use of core–shell carbon/carbide hybrids to immobilize different amounts of graphitization catalyst as illustrated in Figure 1. The resulting microstructure and pore structure of the carbon material is characterized by X-ray diffraction (XRD), temperature-programmed oxidation (TPO) and physisorption analysis.

Results and Discussion
Properties of CDC-shell/carbide core starting material

First of all, the properties of the hybrid starting material (Figure 1, left) were studied. A partial conversion to obtain 30% shell and 70% core was set and confirmed by the mass loss recorded. Figure 2a shows a TEM image where clearly a porous carbon shell covering a carbide core is seen, which originates from the shrinking core like conversion mechanism in combination with the partial conversion [15,26].

Figure 2b shows the pore structure of the partially converted carbide at 800 °C characterized by N_2 sorption analysis. The adsorption–desorption curve shows a similar shape compared to a typical fully CDC material synthesized at 800 °C but features a lower uptake due to the mass of the non-porous carbide core [15]. According to the IUPAC classification, the isotherm can
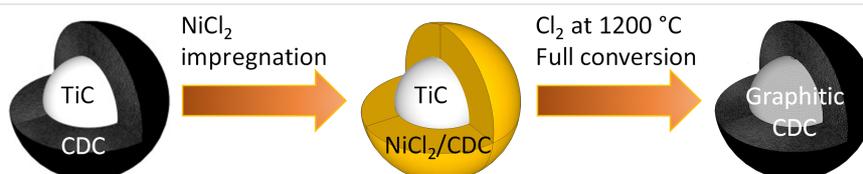

Figure 1: The schematic of graphitic CDC production via immobilization of transition-metal graphitization catalyst on CDC/carbide core–shell precursors.
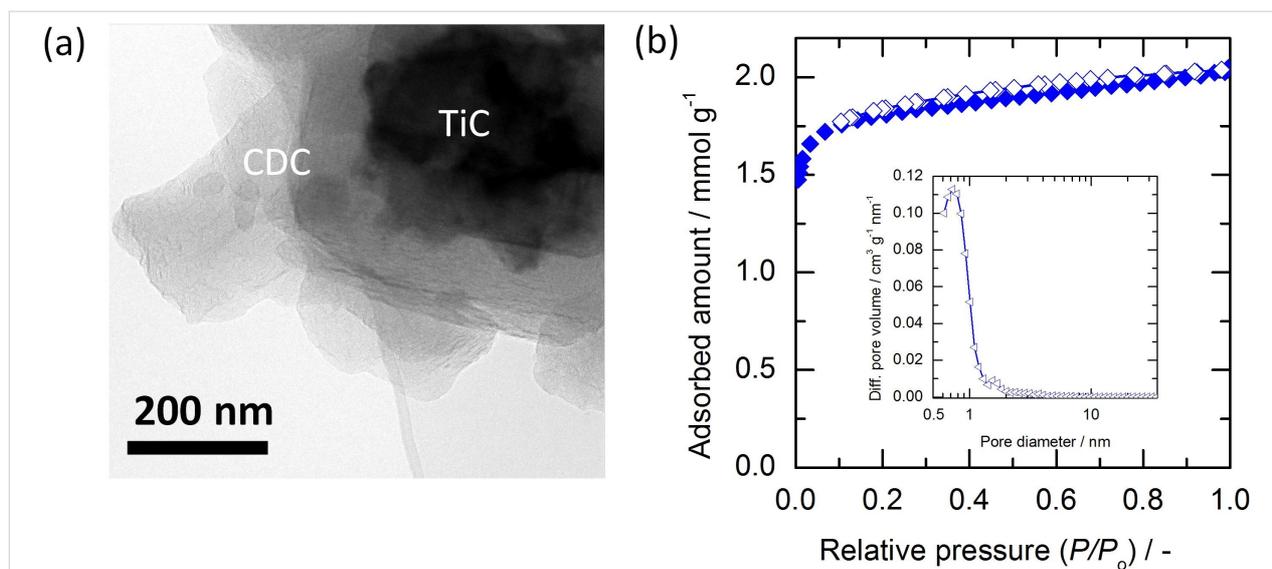
Figure 2: (a) TEM analysis of partially chlorinated carbide (CDC-shell) showing transparent CDC covering the carbide core; (b) N$_2$-sorption isotherm of the CDC-shell and inset of its QSDFT pore size distribution.

be classified as type Ia suggesting a highly (ultra-)microporous material [27]. The pore size distribution (PSD) of the material was evaluated by using the quenched solid density functional theory (QSDFT) method (result displayed as inset in Figure 2b). CDC-shell contains mainly micropores (95 vol %) with a high peak of differential pore volume centered at ca. 0.8 nm. The surface area of CDC-shell is 160 m$^2 \cdot$g^{-1} per total mass of material (shell and core). It can be concluded from the pore analysis that the porous CDC was obtained by the partial chlorination of carbide. For more details, the pore textural parameters are summarized below in Table 1.

To study whether the shell of partially converted carbide influences the distribution of the nickel precursor after the impregnation step, the impregnation of untreated titanium carbide was compared with the same loading (30 mg of nickel per gram of equivalent carbide). EDX mapping (see Figure S1 in Supporting Information File 1) of the impregnated core–shell material shows clearly the remaining core in the Ti K edge signal, while the Ni K and Cl K edges show that nickel chloride is homogeneously immobilized within the shell. A clustering on top of the particle seems not to take place. In contrast, the SEM image of the untreated titanium carbide shows nickel chloride crystals covering the particles. This is further corroborated through the EDS mapping (Figure S2 in Supporting Information File 1).

Influence of nickel loading on the microstructure of the final carbon material

The porous-carbon-on-carbide-core material (CDC-shell) was impregnated with different amounts of nickel chloride hexahy-

drate (Figure 1, middle) and further chlorinated at 1200 °C to obtain the final material (Figure 1, right). The amount of nickel added was varied from 5 up to 60 mg of nickel per gram of equivalent carbide. The effect of nickel catalyst on the microstructure of final carbon was investigated using XRD, temperature-programmed oxidation (TPO), HRTEM and Raman spectroscopy.

The XRD patterns for the different catalyst loadings are given in Figure 3a. The CDC-Ni0 reference material shows no reflexes indicating an amorphous character, which is in agreement with the literature [15]. Once adding graphitization catalyst (CDC-Ni5 to CDC-Ni60) clearly graphitic reflexes of C(002) and C(100/101) at 2θ ≈ 26° and 2θ ≈ 43° and even of C(004) and C(110) are observable. Figure 3a also depicts that the diffraction peak intensity increases with higher nickel loading, indicating a larger portion of crystalline carbon with rising nickel content. To investigate further the effect of nickel loading to the crystallite dimension, the parallel and in-plane symmetry crystallite sizes corresponding to C(002) (2θ ≈ 26°) and C(100) (2θ ≈ 43°) were evaluated using the Scherrer equation (peak deconvolution, see Experimental section). It is noted that the Scherrer equation provides an only rough estimation of crystal dimensions but can serve as basis for the discussion of microstructural trends. The evaluation reveals that the crystallite dimensions, i.e., width (L_a) and height (L_c) for final CDC are largely independent of the amount of employed nickel catalyst (see Figure 3b). Despite the relative constant crystal sizes, the increasing intensity of the XRD reflexes indicates that the amount of crystalline carbon compared to amorphous phase is increasing with higher nickel loading.
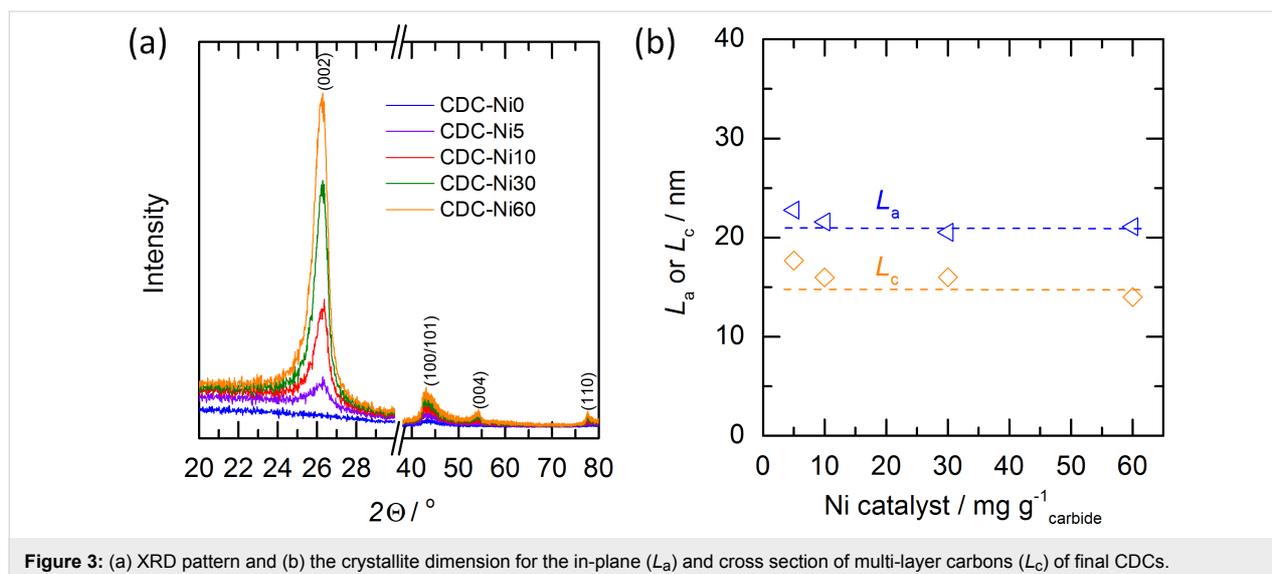
Figure 3: (a) XRD pattern and (b) the crystallite dimension for the in-plane (L_a) and cross section of multi-layer carbons (L_c) of final CDCs.

TPO was employed to probe the ratio between of amorphous and crystalline carbon, based on the different oxidation stability [4,28]. Differential mass-loss curves from the TPO analysis of materials with varying nickel loading are displayed in Figure 4a. It can be seen that CDC-Ni0 shows only a single oxidation peak with a maximum at approx. 596 °C. The CDC-Ni5 reference with the smallest amount of graphitization catalyst added, exhibits also a large signal with an oxidation peak of 595 °C and shows a second peak rising at approx. 700 °C. With even higher nickel contents (CDC-Ni10 and higher) clearly two oxidation peaks can be distinguished, where the first peak corresponds to the more amorphous carbon obtained without adding catalyst (CDC-Ni0). It can therefore be speculated that the second peak at higher oxidation temperatures belongs to the graphitic domains generated with the nickel catalyst.

As there is a distinct separation of both peaks at 610 °C, the TPO signal is divided into two areas, i.e., "Area I" in the region below 610 °C and "Area II" in the region above 610 °C. From integrating both regions the ratio between amorphous and graphitic carbon can be roughly estimated. Figure 4b plots this ratio as a function of the Ni catalyst loading. It can be clearly seen that the portion of crystalline carbon increases to 67% when adding 5 and 10 mg of nickel per g of carbide. Adding more nickel (30 mg·g⁻¹) increases the ratio up to approx. 90% while a further increase to 60 mg·g⁻¹ shows no additional improvement.

TEM images of crushed particles of CDC-Ni0 and CDC-Ni60 are given in Figure 5 and support the findings. Clearly CDC-Ni0 exhibits an amorphous character. The CDC-Ni60 exhibits
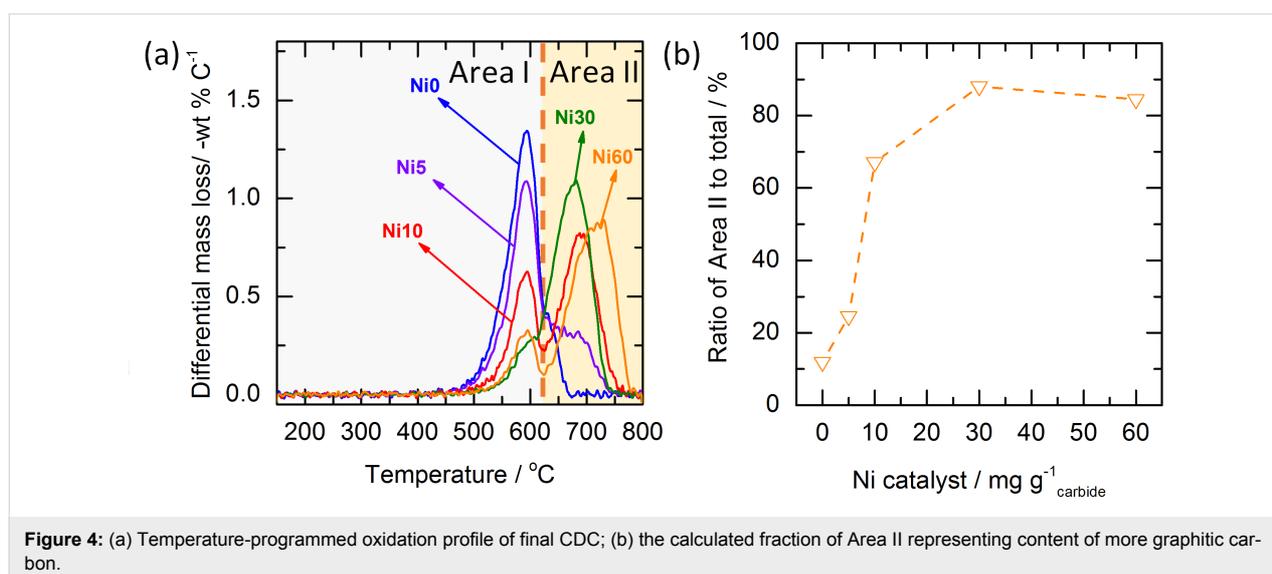

Figure 4: (a) Temperature-programmed oxidation profile of final CDC; (b) the calculated fraction of Area II representing content of more graphitic carbon.
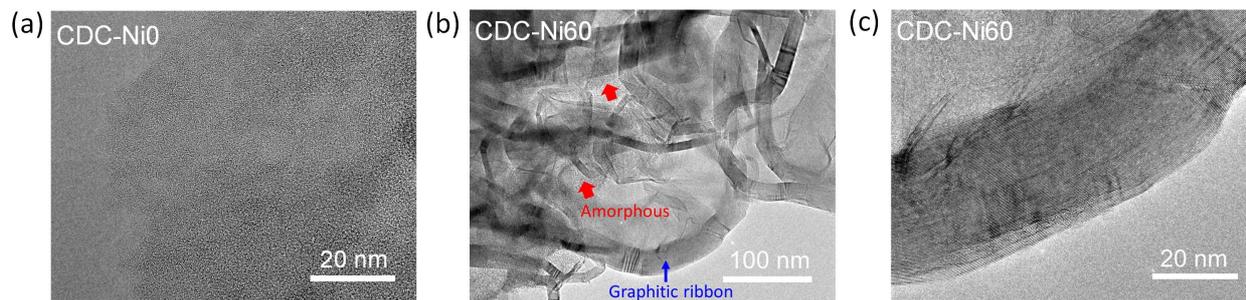
Figure 5: TEM images of CDC-Ni0 (a) and CDC-Ni60 (b,c).

graphitic character indicated by the formation of graphitic ribbons (Figure 5b). The stacking height corroborates the XRD diffractogram evaluation. Parallel fringes are seen in the magnification of the graphitic ribbons (Figure 5c). From the TEM study it seems that also for CDC-Ni60 some amorphous carbon is homogeneously distributed among the graphitic domains (Figure 5b). Raman spectra were recorded for CDC-Ni0, CDC-Ni10 and CDC-Ni60 and are given in Supporting Information File 1 (Figure S3). Surprisingly, in contrast to TPO, XRD and TEM, no strong differences in crystallinity of the samples can be observed by using Raman spectroscopy. All spectra are characterized by the presence of two more or less overlapping D- and G-bands centered at ca. 1325 and 1583 cm^{-1}. CDC-Ni0 shows a slightly higher level of disorder, while the spectra of CDC-Ni10 and CDC-Ni60 are similar. The reason for the deviation from the other characterization results could be the penetration depth of the Raman laser, which probably is probing especially the shell of the core–shell material. As the initial shell is produced without graphitization catalyst here, more amorphous carbon is expected. The Raman results indicate, that the initial

amorphous shell is not strongly recrystallizing during the second chlorination step. This could be also the reason for the amorphous carbon detected in the TPO characterization even for high nickel loadings.

The results show that the loading of graphitization catalyst allows one to tune the content of crystalline carbon. Furthermore, if sufficient catalyst is immobilized within the porous shell, the whole particles seem to benefit from the graphitization catalyst. It also needs to be noted that in the final material no remaining nickel was found by XRD (Figure 3a), in the ash of the TPO measurements (see Figure S4 in Supporting Information File 1) or in the TEM images. The absence of nickel residues can be explained by the formation of volatile $NiCl_2$ during the chlorination of the core at 1200 °C [29].

Influence of nickel loading on the pore structure of the final carbon material

Figure 6a shows the resulting nitrogen-sorption isotherms for varying amounts of nickel loading. The material without graphi-
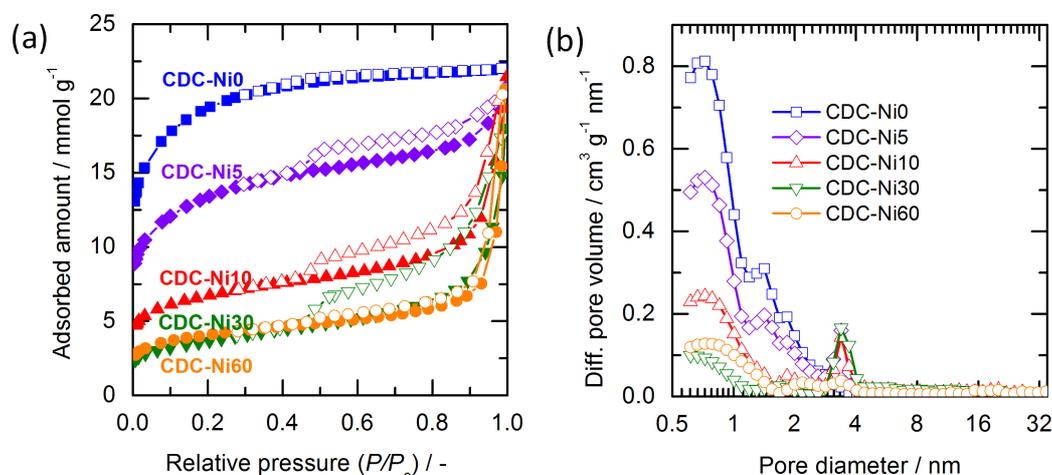

Figure 6: (a) N$_2$-sorption isotherm of final CDC material (closed and open symbols show the adsorption and desorption branches, respectively); (b) Pore size distribution of final CDC evaluated by QSDFT method.

tization catalyst (CDC-Ni0) shows an isotherm with a wider knee in the low-pressure range (type Ib) isotherm, indicating a broad range of micropores. This is in accordance with pore size distributions obtained for TiC-CDC at 1200 °C [4,30]. The addition of 5 mg of nickel per gram of carbide (CDC-Ni5) already shows a pronounced influence on the resulting isotherm, which is a combination of type I and type II with a pronounced H3 hysteresis loop. It suggests that a larger pore exists in CDC-Ni5, which is likely induced by the graphitizing effect of the nickel catalyst, as described in [18,31]. Increasing the nickel loading from 5 to 30 mg·g^{-1} carbide, leads to similar isotherm shapes but a decrease in the adsorbed volume of N$_2$ in the low-pressure range. The pore size distributions evaluated by the QSDFT model are displayed in Figure 6b. CDC-Ni0 displays mainly pores in the micropore regime (<2 nm). On the other hand, the CDCs produced with the aid of the nickel catalyst show pores in the range of 3–4 nm, which are not present in the CDC-Ni0 sample.

The structural properties (specific surface area (SSA), total pore volume (V_T) and mean pore size (d_m)) are summarized in Table 1. There are two types of SSA, SSA$_{N2}$ and SSA$_{CO2}$, obtained from nitrogen and carbon dioxide sorption analysis. Due to the low pressure of the CO$_2$ analysis ($P/P_0 = 2.9 \times 10^{-2}$), only pores in the micropore regime up to 1.5 nm can be probed [32]. Therefore, the mesopore/macropore structures can be roughly estimated by subtracting the contribution of micropore structures (CO$_2$ sorption) from the total pore structures (N$_2$ sorption). The reference of CDC-Ni0 features SSA$_{N2}$ of ca. 1500 m^2·g^{-1} and a mean pore size of 0.94 nm. CDC-Ni5 displays a lower surface area of ca. 1000 m^2·g^{-1}, which is caused by the presence of larger pores as a consequence of the nickel catalyst. The mean pore size of CDC-Ni5 increases by 32% compared to the CDC-Ni0. The specific surface area follows a reverse trend with respect to the nickel content (up to 30 mg·g^{-1} carbide), but the average pore size increases, e.g., it is 3.53 nm for CDC-Ni30 and therefore more than three times as large as that of pristine CDC-Ni0. The results of CO$_2$ sorp-

tion analysis corroborate the finding that the micropore portion decreases from 86 to 13 vol % when employing nickel loadings of 0–30 mg·g^{-1} carbide. Interestingly, increasing the nickel loading from 30 to 60 mg·g^{-1} does not lead to strong changes in the pore structure. In accordance with the TPO results, where the ratio of amorphous to graphitic carbon also did not change further, it can be speculated that 30 mg·g^{-1} of nickel are the maximum amount of catalyst needed for full graphitization.

Conclusion

A new synthesis strategy to obtain graphitic CDC was introduced in which nickel as graphitization catalyst is immobilized on a porous shell covering each particle. This approach allows one to vary the ratio of graphitic to amorphous carbon in the final material through the amount of immobilized nickel. Increasing the loading up to 30 mg$_{Ni}$·g^{-1}$_{carbide}$ increased the graphitic content from 10 to 90% as estimated from TPO measurements, while the crystalline character (stacking height and width) is independent of the graphitic portion. This has a direct influence on the resulting pore structure showing a decreasing amount of micropores and increasing amount of meso- and macropores. Increasing the nickel loading above 30 mg$_{Ni}$·g^{-1}$_{carbide}$ did not change the material properties further and probably additional nickel can be seen to some extent as inert material not participating in the conversion. The new synthesis route seems to result in more homogeneous materials and allows for a better control of the final material properties.

Experimental
Materials
Commercial TiC (d_{ave} of 90 μm, 99.8%, Goodfellow) was employed as carbon precursor. Chlorine (purity 2.8, Linde AG) and hydrogen (purity 5.0, Linde AG) diluted by helium (purity 4.6, Linde AG) were used to perform reactive extraction of carbide (chlorination) and subsequent carbon surface annealing. Nickel chloride hexahydrate (99.95% purity, Alfa Aesar) was used as precursor of the Ni catalyst.

Table 1: Structural parameters of CDC material characterized by N$_2$- and CO$_2$-sorption.

sample	SSA$_{N2}$[a] [m^2/g]	V_T [cm^3/g]	d_m[b] [nm]	SSA$_{CO2}$[c] [m^2/g]	V_{CO2}[d] [cm^3/g]	V_{CO2}/V_T [%]
CDC-shell	160	0.07	0.81	157	0.06	86
CDC-Ni0	1494	0.71	0.94	1278	0.47	66
CDC-Ni5	1030	0.64	1.24	785	0.29	45
CDC-Ni10	533	0.60	2.24	423	0.16	27
CDC-Ni30	297	0.52	3.53	176	0.07	13
CDC-Ni60	309	0.45	2.92	258	0.10	22

[a]Specific surface area obtained by N$_2$-sorption analysis, [b]mean slit-pore size, (d_m) = 2V_T/SSA$_{N2}$, [c]specific surface area obtained by CO$_2$ sorption analysis, [d]pore volume taken from CO$_2$ sorption analysis.

Synthesis of carbon shell/carbide core starting material

The synthesis of hybrid particles where carbide cores are covered with a porous carbon shell, was reported previously in detail [15]. Briefly, a vertical quartz tube reactor (d_i = 0.034 m, l = 1 m) was employed to perform partial chlorination of carbide to carbon. About 1 g of TiC powder was loaded on the top of a quartz frit of a quartz tube. The reactor was then placed in an isothermal zone of the vertical furnace (Gero Company, Germany). After the tightness of reactor was verified, the reactor was heated to 800 °C under helium flow (superficial velocity, v = 0.015 m·s^{-1}) with a heating rate of 10 °C·min^{-1}. The chlorination reaction was then carried out at 800 °C by dosing chlorine (0.5 mol·m^{-3} Cl$_2$ diluted in helium, v = 0.015 m·s^{-1}) for 30 min reaction time. The chlorine flow was then stopped, and the reactor was flushed with helium. To remove residual chlorine in the pores, the sample was subsequently treated with 0.5 mol·m^{-3} hydrogen. Eventually, the reactor was cooled down to ambient temperature under helium purge. The carbon shell/carbide core intermediate produced is denominated as CDC-shell.

Impregnation of nickel in carbon shell/carbide core starting material

The nickel precursor was loaded to CDC-shell through wet impregnation, i.e., about 1 g of CDC-shell was mixed with a defined amount of nickel chloride hexahydrate dissolved in 3 mL ethanol. The solution was homogenized by ultrasonication for 30 min. The solvent was evaporated, and the nickel chloride-loaded CDC-shell was dried in an oven at 60 °C overnight. The loading of nickel on CDC-shell (wt Ni/wt equivalent carbide) was set to 5, 10, 30, and 60 mg·g^{-1}$_{carbide}$. The equivalent mass of carbide (m_{TiC}) is determined using Equation 1.

$$m_{TiC} = \frac{m_{CDC\text{-}shell}}{\left(1 - X \dfrac{M_{Ti}}{M_{TiC}}\right)},$$ (1)

where $m_{CDC\text{-}shell}$ is the mass of carbon shell/carbide core starting material, X is the conversion rate, and M_{Ti} and M_{TiC} are the molar weight of Ti and TiC, respectively.

Synthesis of final carbide-derived carbon

The Ni/CDC-shell was further chlorinated at 1200 °C to complete the conversion of the carbide to the carbon. This reactive extraction was carried out using a horizontal chlorination setup as described in [4]. The reaction conditions were set to 3 cm·s^{-1} superficial velocity, 1 mol·m^{-3} chlorine and 3 h reaction time. To remove residual chlorine, an annealing treatment using

hydrogen (0.5 mol·m^{-3}) again was carried out after the extractive reaction. The nomenclature of the final carbon material obtained is "CDC" followed by "Ni" and catalyst loading. For instance, CDC-Ni30 refers to the CDC material prepared by i) impregnation of CDC-shell with NiCl$_2$·6H$_2$O with 30 mg Ni·g^{-1}$_{CDC\text{-}shell}$ and ii) chlorination until full conversion of Ni/CDC-shell at 1200 °C.

Characterization methods

The pore structure of CDC-shell and final CDC materials was characterized by N$_2$ sorption at −196 °C using liquid nitrogen as coolant (Quantachrome Quadrasorb Si-MP) and CO$_2$ sorption measurements at 0 °C using a cryostat (Quantachrome Nova 4200e). Before the measurement, the sample was degassed at 250 °C for 4 h (N$_2$ sorption) or 100 °C for 24 h (CO$_2$ sorption). The pore size distributions were evaluated from the sorption-isotherm data by using quenched solid density functional theory (QSDFT) equilibrium models for carbon with slit-shaped pores [33] provided by the QuadraWin 5.04 software (Quantachrome Instruments, USA). Temperature-programmed oxidation measurements (TPO) of the carbon materials were recorded in a Netzsch STA 409 PC Luxx (Germany) under air flow. The method consisted of isothermal drying at 150 °C for 1 h followed by heating from 150 to 800 °C at a constant ramp rate of 2.5 °C·min^{-1}. Peak deconvolution of the TPO curves was carried out with two bi-Gaussian functions. Raman spectra were taken using Jobin Yvon HR 800 with a HeNe laser (633 nm and 20 mW power). Peak deconvolution of Raman spectra was carried by peak fitting with four Lorentzian/Gaussian functions as described in [15]. Energy-dispersive spectroscopy (EDS) measurements were performed on a scanning electron microscope (Philips XL30 FEG, 30 kV) equipped with an EDAX X-ray detector. Transmission electron microscopy (TEM) images were captured using a JEOL JEM-2100F microscope operated at 200 kV. The TEM samples were prepared by placing a drop of catalyst powder dispersion in deionized water onto a carbon-coated Au grid (G200F1, Quantifoil), followed by drying under ambient conditions. XRD patterns were recorded using a Philips X'pert Pro by PANalytical, Netherlands (40 kV and 40 mA using Cu Ka radiation). The XRD diffractograms were recorded in the 2θ range of 2–80° in steps of 0.03° with an acquisition time of 5 s per step. The XRD diffractograms were deconvoluted to evaluate the properties of graphitic reflexes (see exemplary deconvolution in Figure 7).

The graphite dimension (L_a of the in-plane and L_c of the cross section size) was evaluated by the Scherrer equation shown in Equation 2 [34].

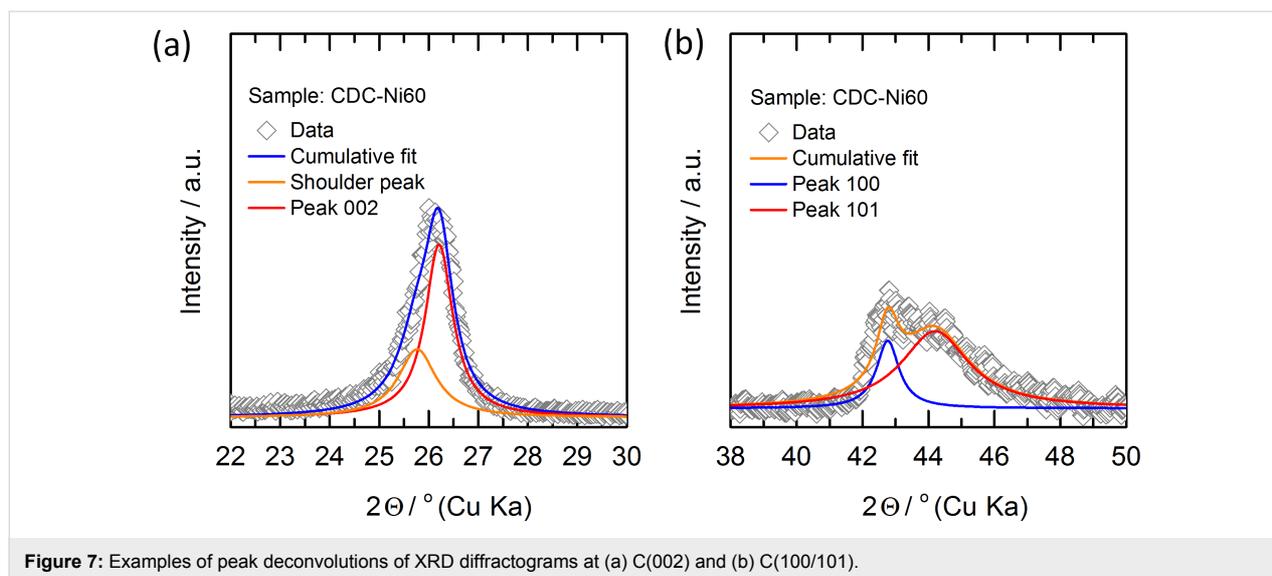$$L_{a/c} = \frac{K\lambda}{\beta \cos\theta},$$ (2)

Figure 7: Examples of peak deconvolutions of XRD diffractograms at (a) C(002) and (b) C(100/101).

where λ is the X-ray wavelength (0.154 nm), θ is the diffraction angle, β is the full width at half maximum (FWHM) of the deconvoluted peak in radian units and K is a constant ($K = 1.84$ for L_a at C(100/101) and $K = 0.89$ for L_c at C(002)).

Supporting Information

Supporting Information File 1

Additional data on SEM-EDX, Raman spectroscopy and temperature-programmed oxidation.
[https://www.beilstein-journals.org/bjnano/content/supplementary/2190-4286-10-41-S1.pdf]

Acknowledgements

ORCID® iDs

Teguh Ariyanto - https://orcid.org/0000-0002-9454-9541
Jan Glaesel - https://orcid.org/0000-0002-9301-8685
Bastian J. M. Etzold - https://orcid.org/0000-0001-6530-4978

References

1. Kameda, T.; Ito, S.; Yoshioka, T. *J. Dispersion Sci. Technol.* **2017,** *38,* 1063–1066. doi:10.1080/01932691.2016.1219953
2. Altenor, S.; Carene, B.; Emmanuel, E.; Lambert, J.; Ehrhardt, J.-J.; Gaspard, S. *J. Hazard. Mater.* **2009,** *165,* 1029–1039. doi:10.1016/j.jhazmat.2008.10.133
3. Yi, H.; Li, F.; Ning, P.; Tang, X.; Peng, J.; Li, Y.; Deng, H. *Chem. Eng. J.* **2013,** *215–216,* 635–642. doi:10.1016/j.cej.2012.11.050
4. Gläsel, J.; Diao, J.; Feng, Z.; Hilgart, M.; Wolker, T.; Su, D. S.; Etzold, B. J. M. *Chem. Mater.* **2015,** *27,* 5719–5725. doi:10.1021/acs.chemmater.5b02262
5. Wang, L.; Yao, Y.; Zhang, Z.; Sun, L.; Lu, W.; Chen, W.; Chen, H. *Chem. Eng. J.* **2014,** *251,* 348–354. doi:10.1016/j.cej.2014.04.088
6. Faria, P. C. C.; Órfão, J. J. M.; Pereira, M. F. R. *Appl. Catal., B* **2009,** *88,* 341–350. doi:10.1016/j.apcatb.2008.11.002
7. Kirilin, A. V.; Hasse, B.; Tokarev, A. V.; Kustov, L. M.; Baeva, G. N.; Bragina, G. O.; Stakheev, A. Y.; Rautio, A.-R.; Salmi, T.; Etzold, B. J. M.; Mikkola, J.-P.; Murzin, D. Y. *Catal. Sci. Technol.* **2014,** *4,* 387–401. doi:10.1039/c3cy00636k
8. Munoz, M.; Zhang, G.-R.; Etzold, B. J. M. *Appl. Catal., B* **2017,** *203,* 591–598. doi:10.1016/j.apcatb.2016.10.062
9. Prasetyo, I.; Rochmadi, R.; Wahyono, E.; Ariyanto, T. *Eng. J.* **2017,** *21,* 83–94. doi:10.4186/ej.2017.21.4.83
10. Silvestre-Albero, A.; Rico-Francés, S.; Rodríguez-Reinoso, F.; Kern, A. M.; Klumpp, M.; Etzold, B. J. M.; Silvestre-Albero, J. *Carbon* **2013,** *59,* 221–228. doi:10.1016/j.carbon.2013.03.012
11. Sevilla, M.; Foulston, R.; Mokaya, R. *Energy Environ. Sci.* **2010,** *3,* 223–227. doi:10.1039/b916197j
12. Prasetyo, I.; Rochmadi, R.; Ariyanto, T.; Yunanto, R. *Indones. J. Chem.* **2013,** *13,* 95–100. doi:10.22146/ijc.21290
13. Gütlein, S.; Burkard, C.; Zeilinger, J.; Niedermaier, M.; Klumpp, M.; Kolb, V.; Jess, A.; Etzold, B. J. M. *Environ. Sci. Technol.* **2015,** *49,* 672–678. doi:10.1021/es504141t
14. Zeiger, M.; Ariyanto, T.; Krüner, B.; Peter, N. J.; Fleischmann, S.; Etzold, B. J. M.; Presser, V. *J. Mater. Chem. A* **2016,** *4,* 18899–18909. doi:10.1039/c6ta08900c
15. Ariyanto, T.; Dyatkin, B.; Zhang, G.-R.; Kern, A.; Gogotsi, Y.; Etzold, B. J. M. *Microporous Mesoporous Mater.* **2015,** *218,* 130–136. doi:10.1016/j.micromeso.2015.07.007
16. Schlange, A.; dos Santos, A. R.; Hasse, B.; Etzold, B. J. M.; Kunz, U.; Turek, T. *J. Power Sources* **2012,** *199,* 22–28. doi:10.1016/j.jpowsour.2011.09.107
17. Jin, H.; Li, J.; Gao, L.; Chen, F.; Zhang, H.; Liu, Q. *Int. J. Hydrogen Energy* **2016,** *41,* 9204–9210. doi:10.1016/j.ijhydene.2016.04.081
18. Kormann, M.; Gerhard, H.; Zollfrank, C.; Scheel, H.; Popovska, N. *Carbon* **2009,** *47,* 2344–2351. doi:10.1016/j.carbon.2009.04.018

19. Sevilla, M.; Fuertes, A. B. *Carbon* **2006,** *44,* 468–474.
doi:10.1016/j.carbon.2005.08.019

20. Gogotsi, Y.; Nikitin, A.; Ye, H.; Zhou, W.; Fischer, J. E.; Yi, B.;
Foley, H. C.; Barsoum, M. W. *Nat. Mater.* **2003,** *2,* 591–594.
doi:10.1038/nmat957

21. Jeong, J.-H.; Bae, H.-T.; Lim, D.-S. *Carbon* **2010,** *48,* 3628–3634.
doi:10.1016/j.carbon.2010.06.017

22. Borchardt, L.; Hasché, F.; Lohe, M. R.; Oschatz, M.; Schmidt, F.;
Kockrick, E.; Ziegler, C.; Lescouet, T.; Bachmatiuk, A.; Büchner, B.;
Farrusseng, D.; Strasser, P.; Kaskel, S. *Carbon* **2012,** *50,* 1861–1870.
doi:10.1016/j.carbon.2011.12.036

23. Xu, J.; Zhang, R.; Ge, S.; Wang, J.; Liu, Y.; Chen, P.
Mater. Chem. Phys. **2013,** *141,* 540–548.
doi:10.1016/j.matchemphys.2013.05.059

24. Ariyanto, T.; Kern, A. M.; Etzold, B. J. M.; Zhang, G.-R.
Electrochem. Commun. **2017,** *82,* 12–15.
doi:10.1016/j.elecom.2017.07.010

25. Ariyanto, T.; Zhang, G.-R.; Riyahi, F.; Gläsel, J.; Etzold, B. J. M.
Carbon **2017,** *115,* 422–429. doi:10.1016/j.carbon.2017.01.032

26. Knorr, T.; Kaiser, M.; Glenk, F.; Etzold, B. J. M. *Chem. Eng. Sci.* **2012,**
69, 492–502. doi:10.1016/j.ces.2011.11.002

27. Thommes, M.; Kaneko, K.; Neimark, A. V.; Olivier, J. P.;
Rodriguez-Reinoso, F.; Rouquerol, J.; Sing, K. S. W. *Pure Appl. Chem.*
2015, *87,* 1051–1069. doi:10.1515/pac-2014-1117

28. Pérez, C. R.; Yeon, S.-H.; Ségalini, J.; Presser, V.; Taberna, P.-L.;
Simon, P.; Gogotsi, Y. *Adv. Funct. Mater.* **2013,** *23,* 1081–1089.
doi:10.1002/adfm.201200695

29. Galetz, M. C.; Rammer, B.; Schütze, M. *Mater. Corros.* **2015,** *66,*
1206–1214. doi:10.1002/maco.201408130

30. Presser, V.; Heon, M.; Gogotsi, Y. *Adv. Funct. Mater.* **2011,** *21,*
810–833. doi:10.1002/adfm.201002094

31. Leis, J.; Perkson, A.; Arulepp, M.; Nigu, P.; Svensson, G. *Carbon* **2002,**
40, 1559–1564. doi:10.1016/s0008-6223(02)00019-2

32. Schmirler, M.; Glenk, F.; Etzold, B. J. M. *Carbon* **2011,** *49,* 3679–3686.
doi:10.1016/j.carbon.2011.05.003

33. Gor, G. Y.; Thommes, M.; Cychosz, K. A.; Neimark, A. V. *Carbon* **2012,**
50, 1583–1590. doi:10.1016/j.carbon.2011.11.037

34. Dinnebier, R. E.; Billinge, S. J. L., Eds. *Powder Diffraction;* Royal
Society of Chemistry: Cambridge, United Kingdom, 2008.
doi:10.1039/9781847558237

Concurrent nanoscale surface etching and SnO$_2$ loading of carbon fibers for vanadium ion redox enhancement

Jun Maruyama[*1], Shohei Maruyama[1], Tomoko Fukuhara[1], Toru Nagaoka[2] and Kei Hanafusa[3]

Full Research Paper

Address:
[1]Research Division of Environmental Technology, Osaka Research Institute of Industrial Science and Technology, 1-6-50, Morinomiya, Joto-ku, Osaka 536-8553, Japan, [2]Research Division of Materials Science and Engineering, Osaka Research Institute of Industrial Science and Technology, 1-6-50, Morinomiya, Joto-ku, Osaka 536-8553, Japan and [3]Power Systems R&D Center, Sumitomo Electric Industries, 1-1-3, Shimaya, Konohana-ku, Osaka 554-0024, Japan

Email:
Jun Maruyama[*] - maruyama@omtri.or.jp

* Corresponding author

Abstract

Facile and efficient methods to prepare active electrodes for redox reactions of electrolyte ions are required to produce efficient and low-cost redox flow batteries (RFBs). Carbon-fiber electrodes are widely used in various types of RFBs and surface oxidation is commonly performed to enhance the redox reactions, although it is not necessarily efficient. Quite recently, a technique for nanoscale and uniform surface etching of the carbon fiber surface was developed and a significant enhancement of the negative electrode reaction of vanadium redox flow batteries was attained, although the enhancement was limited to the positive electrode reaction. In this study, we attempted to obtain an additional enhancement effect of metal-oxide nanoparticles without the need for further processing steps. A coating with carbonaceous thin films was obtained coating by sublimation, deposition, and pyrolysis of tin(II) phthalocyanine (SnPc) on a carbon fiber surface in a single heat-treatment step. The subsequent thermal oxidation concurrently achieved nanoscale surface etching and loading with SnO$_2$ nanoparticles. The nanoscale-etched and SnO$_2$-loaded surface was characterized by field-emission scanning electron microscopy (FESEM), Raman spectroscopy, and X-ray photoelectron spectroscopy (XPS). The activity for the vanadium ion redox reactions was evaluated by cyclic voltammetry (CV) to demonstrate the enhancement of both the positive and negative electrode reactions. A full cell test of the vanadium redox flow battery (VRFB) showed a significant decrease of the overpotential and a stable cycling performance. A facile and efficient technique based on the nanoscale processing of the carbon fiber surface was presented to substantially enhance the activity for the redox reactions in redox flow batteries.

Introduction

Redox flow batteries (RFBs) are energy conversion and storage devices that involve the reduction and oxidation of electroactive species in electrolyte solutions and have attracted much attention due to their scalability and safety. Various types of RFBs have been developed using aqueous and nonaqueous electrolytes with inorganic and organic electroactive species [1-4]. There is an increasing demand for electrodes that are active in the redox reactions of every type of RFBs to enhance the reaction rate, improve the energy efficiency [5,6], and to allow for a compact cell design. Feasible production methods are also required to provide low production cost.

Carbon-fiber electrodes are conventionally used in RFBs and surface oxidation is often performed to enhance the redox reactions [7-14], although a sufficient activity has not yet been obtained. Recently, we found a method to efficiently expose the edge planes of the carbon fiber surface by nanoscale etching, which had a significant enhancement effect on the redox reactions of vanadium ions [15]. The reactions shown below are involved in the vanadium redox flow batteries (VRFBs), which are in the most advanced stage of research and development:

$$VO_2^+ + 2H^+ + e^- \rightleftharpoons VO^{2+} + H_2O \ \left(\text{positive electrode}\right),$$

$$V^{2+} \rightleftharpoons V^{3+} + e^- \qquad\qquad \left(\text{negative electrode}\right).$$
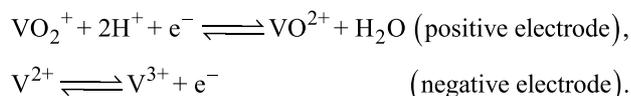
Nanoscale surface etching was attained by coating the surface with a carbonaceous thin film derived from cobalt(II) phthalocyanine (CoPc) and subsequent thermal oxidation followed by acid washing. The carbonaceous thin film was formed by sublimation, deposition, and pyrolysis of CoPc on the carbon fiber surface during a single heat-treatment step using a conventional crucible. The treatment substantially enriched edge planes and produced an enhanced activity for the positive and negative electrode reactions, although the enhancement of the former was limited.

It has been recognized that the modification of the carbon fiber surface by metal oxide nanoparticles also enhances the redox reactions [16-18]. In this study, we attempted the combination of the effects of edge-plane exposure and loading with metal-oxide nanoparticles to further enhance the activity and found that through the thermal oxidation of the carbonaceous thin film derived from SnPc both types of enhancement can be concurrently achieved. The formed metal oxide, SnO_2, is one of the candidates for a durable catalyst support used in an acidic electrolyte [19]; thus, is assumed to also be stable in the RFB environment. The activity for both the positive and negative elec-

trode reactions of a VRFB were clearly enhanced at the finely etched and SnO_2-loaded carbon-fiber electrode and a stable performance was demonstrated by full cell cycle tests.

Results and Discussion

Concurrent surface etching and SnO_2 loading

Graphitic carbon paper (TGP-H-090, Toray, abbreviated as TGP) was used as the substrate. The SnPc-derived carbonaceous thin film (CSnPc; obtained thorugh sublimation, deposition, and pyrolysis of SnPc in a single-step heat treatment in an Ar atmosphere at 700 °C) was coated on the carbon fiber surface following the method reported in [15,20]. The obtained sample was labeled TGP-CSnPc. Then, a heat treatment in air at $T = 500, 550, 600,$ and 650 °C was performed to obtain TGP-CSnPc-TAir. The thermal oxidation at 550 °C was also performed without CSnPc for comparison. The treatment conditions and the obtained samples are summarized in Table 1.

Table 1: Conditions for TGP surface treatments and obtained samples.

	SnPc-derived carbonaceous thin film	thermal oxidation temperature [°C]
TGP	—	—
TGP-550Air	—	550
TGP-CSnPc	coated	—
TGP-CSnPc-500Air	coated	500
TGP-CSnPc-550Air	coated	550
TGP-CSnPc-600Air	coated	600
TGP-CSnPc-650Air	coated	650

Surface morphology

The FESEM images of TGP, TGP-CSnPc, and TGP-CSnPc-550Air are shown in Figure 1 and Figure S1 (Supporting Information File 1). The surface morphology of the carbon fiber coated with CSnPc is similar to that without the coating. After the thermal oxidation of TGP-CSnPc at 550 °C, tin-oxide nanoparticles were generated on the surface. In addition, there are many shallow elongated dents along the fiber axis, which were generated by the fine surface etching. Although a clear demonstration of this surface-structure change is difficult through FESEM observation only, Raman spectroscopy and electrochemical measurements can show clear differences as described below.

The degree of the surface etching depends on the temperature of the thermal oxidation (Figure 1e and Figure S2, Supporting
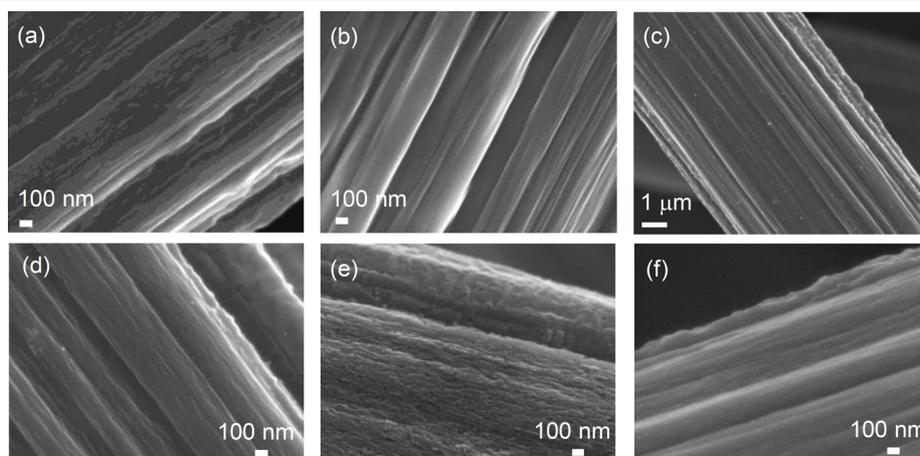
Figure 1: FESEM images of (a) TGP, (b) TGP-CSnPc, (c) TGP-CSnPc-550Air, (d) magnified view of (c), and (e) TGP-CSnPc-650Air. FESEM image of TGP-550Air (f) is also shown for comparison. FESEM images of TGP-CSnPc-*T*Air (*T* = 500, 550, 600 and 650 °C) are shown in Figure S2 (Supporting Information File 1).

Information File 1). The surface was roughened with an increase in the temperature. It should be noted that the roughening was uniformly attained over the entire surface at every treatment temperature.

Edge plane exposure

The further evaluation of the etched surface was carried out by Raman spectroscopy. Figure 2 shows the Raman spectra of TGP and the treated samples. After the coating of TGP with CSnPc,

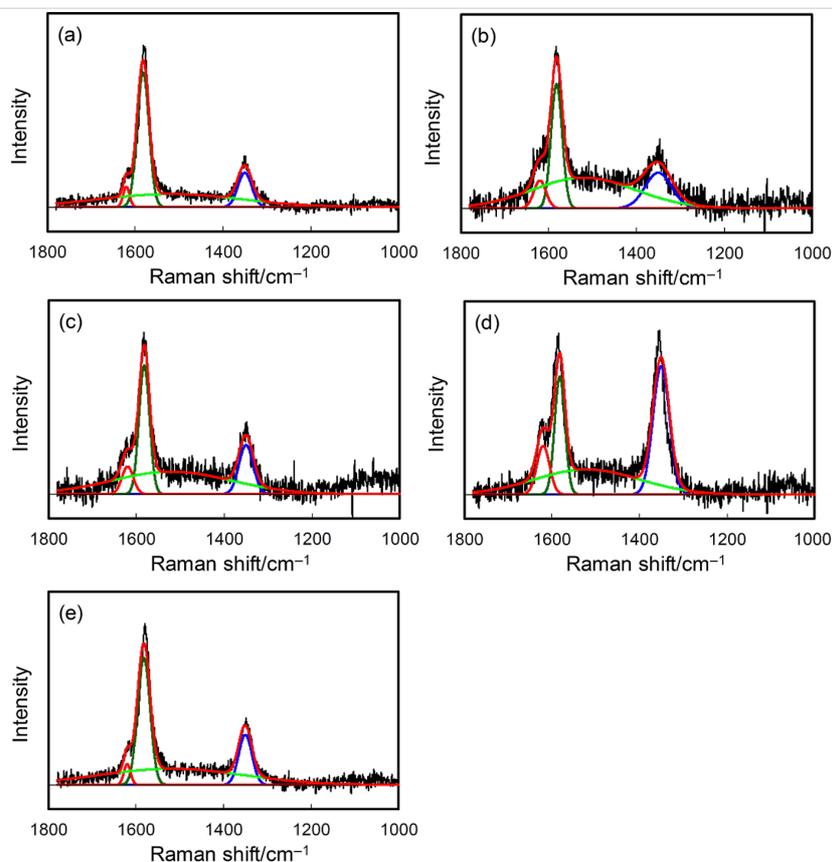**Figure 2:** Raman spectra of (a) TGP, (b) TGP-CSnPc, (c) TGP-CSnPc-550Air, (d) TGP-CSnPc-650Air, and (e) TGP-550Air. The deconvoluted components, D2, G, Am, D, and the fitting result are shown in orange, green, light green, blue, and red lines, respectively. The spectra of TGP-CSnPc-*T*Air (*T* = 500, 550, 600 and 650 °C) are given in Figure S3 (Supporting Information File 1).

the Am and D2 peaks appeared in addition to the G and D peaks. The peaks are ascribed to amorphous carbon, the surface graphene layers as a disordered graphitic lattice, the ideal graphitic lattice, and the graphene layer edges also as the disordered graphitic lattice, respectively [21,22]. The presence of the Am peak indicates that CSnPc is amorphous. The Am peak is decreased (Table 2) and the D peak is increased in the spectrum for TGP-CSnPc-550Air. The ratios between the intensities of the D peak and the G peak (I_D/I_G) increased from 0.255 (TGP) to 0.382 (TGP-CSnPc-550Air), suggesting the exposure of the edge planes on the carbon fiber surface and also a slight retention of the amorphous carbon [23]. This assumption is based on the general recognition that the ratio is related to the concentration of the defects and the extent of the structural disorder [21]. The I_D/I_G value is similar to that of TGP-550Air. The I_D/I_G value depends on the thermal oxidation temperature and a highly developed D peak and a slight increase in the Am peak intensity were observed in the spectrum for TGP-CSnPc-650Air, which is in agreement with the FESEM image.

Table 2: Ratio between the intensity of the D, Am, and D2 peaks and that of the G peak.

	I_D/I_G	I_{Am}/I_G	I_{D2}/I_G
TGP	0.255	0.097	0.150
TGP-550Air	0.395	0.127	0.163
TGP-CSnPc	0.285	0.246	0.222
TGP-CSnPc-500Air	0.315	0.185	0.216
TGP-CSnPc-550Air	0.382	0.175	0.214
TGP-CSnPc-600Air	0.556	0.167	0.223
TGP-CSnPc-650Air	1.087	0.212	0.413

Surface species

The presence of tin oxide on the thermally oxidized surface of the CSnPc-coated carbon fibers was confirmed by XPS. It should be noted here that the Sn content was below the detection limit for the elemental mapping by energy-dispersive X-ray spectrometry because the SnO_2 particles were of the order of nanometers and present only on the surface of the larger-scale carbon-fiber material. The XPS analysis area was 0.3×0.7 mm, yielding average values of the sample. Figure 3 shows the Sn 3d and O 1s XPS spectra of TGP, TGP-CSnPc-550Air, and TGP-550Air. The Sn 3d spectra indicated the presence of Sn in the form of SnO_2 [24-26]. Although the C 1s spectra show little appreciable difference among these samples (Figure S4, Supporting Information File 1), the O 1s spectra for TGP-CSnPc-550Air clearly showed the presence of oxygen attributed to the metal oxide and oxygen-containing surface functional groups (Figure S5, Supporting Information File 1). The amount of the latter was comparable to that in TGP-550Air. Table 3 shows the surface compositions of these samples. The CSnPc coating and

its conversion through thermal oxidation were reflected by the change in nitrogen surface concentration from TGP-CSnPc to TGP-CSnPc-550Air. The high oxygen surface concentration in TGP-CSnPc was attributed to its rough surface due to the structural disorder of the amorphous carbon, which was susceptible to oxidation upon exposure to air after the CSnPc deposition. The graphitic surface is much less susceptible to the oxidation [27]. Thus, the oxygen surface concentration decreases from TGP-CSnPc to TGP-CSnPc-550Air also suggested the removal of the CSnPc coating.
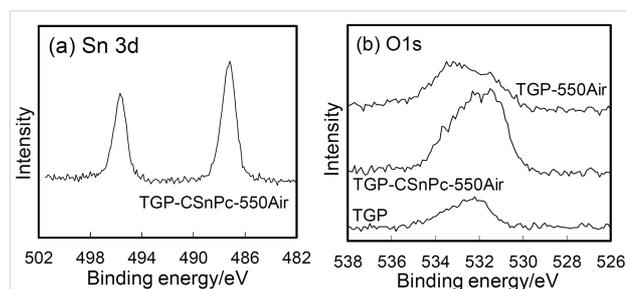
Figure 3: XPS spectra of (a) Sn 3d and (b) O 1s in TGP, TGP-CSnPc-550Air, and TGP-550Air.

Table 3: Surface concentrations of C, O, and Sn [atom %].

	C 1s	O 1s	N 1s	Sn 3d
TGP	99.54	0.46	—	—
TGP-550Air	99.12	0.88	—	—
TGP-CSnPc	90.45	5.59	3.16	0.8
TGP-CSnPc-550Air	98.26	1.42	0.05	0.27

Electrochemical behavior without vanadium ions

The cyclic voltammograms (CVs) obtained in an acidic electrolyte without vanadium ions are shown in Figure 4. The current in the voltammogram is composed from three components, i.e., the electrochemical double-layer charging current at the carbon–electrolyte interface, and the faradaic currents due to the redox reactions of the surface functional groups and the carbon surface oxidation. The electrochemical double-layer charging yields a constant current and a rectangular CV shape. The current depends on the extent of the exposure of the basal and edge planes, the specific capacitances of which are 16 and 50–70 μF·cm^{-2} (microscopic actual surface area), respectively, according to the report by Yeager and co-workers [28]. The broad redox peaks around 0.5 V and the oxidation current above 0.8 V were attributed to the redox reactions of the quinone/hydroquinone-like surface functional groups and the carbon surface oxidation, respectively. These currents increased after the thermal oxidation and also increase with increasing tempera-

ture during thermal oxidation of TGP-CSnPc. The increase in the electrochemical double-layer current was attributed to the exposure of the edge planes, which is in agreement with the Raman spectra. The large carbon surface oxidation current observed for TGP-CSnPc-650Air implied the development of high surface roughness.

Figure 4: Cyclic voltammograms in Ar-saturated 2 M H_2SO_4 at 25 °C for TGP, TGP-550Air, and TGP-CSnPc-TAir (T = 500, 550, 600 and 650 °C). The reference electrode was Ag/AgCl/NaCl (3 M). The counter electrode was carbon cloth. Scan rate: 50 mV·s^{-1}.
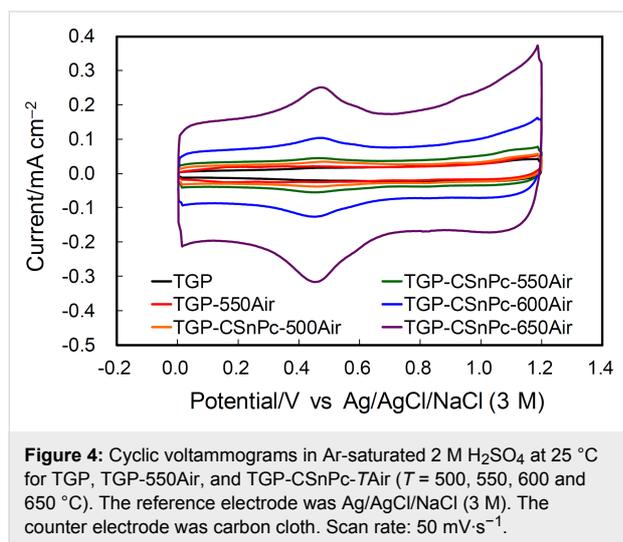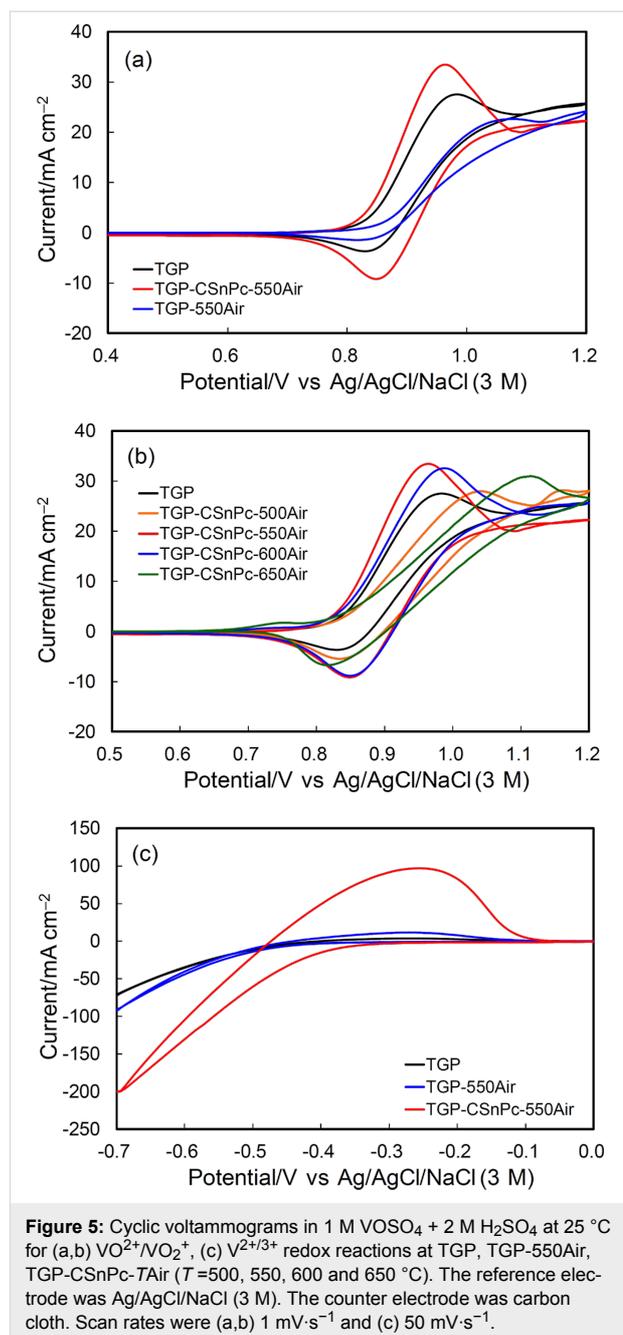
Redox reactions of vanadium ions

The CVs in the potential ranges corresponding to the positive and negative electrode reactions in an acidic electrolyte containing vanadium ions are shown in Figure 5 for TGP and TGP-CSnPc-TAir. The CVs for TGP-550Air are also shown for comparison. The enhancement of the VO^{2+}/VO_2^+ redox reactions at the TGP-CSnPc-550Air electrode is clearly demonstrated by the negative and positive peak shifts for the oxidation and reduction peaks, respectively, as well as the increased peak currents. This enhancement was attributed to the loading with SnO_2 nanoparticles, considering the limited increase in the activity by the exposure of the edge plane obtained in a previous study [15] without SnO_2, and the lower activity for the only thermally oxidized surface (TGP-550Air), which suffered from inhibition by the adsorption of VO_2 [23,29]. The excessive exposure of the edge plane led to an activity decrease at TGP-CSnPc-600Air and TGP-CSnPc-650Air due to this inhibition and the optimized activity was attained with TGP-CSnPc-550Air in this study. The drastic change in the surface structure was attributed to a temperature-dependent catalytic effect of the tin-oxide nanoparticles on the carbon surface oxidation leading to fine etching.

A significant enhancement of the activity for the $V^{2+/3+}$ redox reactions was also observed at TGP-CSnPc-550Air. The activity was equivalent to that obtained for the finely etched surface obtained in the previous study [15] without SnO_2 nanoparticles.

Figure 5: Cyclic voltammograms in 1 M $VOSO_4$ + 2 M H_2SO_4 at 25 °C for (a,b) VO^{2+}/VO_2^+, (c) $V^{2+/3+}$ redox reactions at TGP, TGP-550Air, TGP-CSnPc-TAir (T =500, 550, 600 and 650 °C). The reference electrode was Ag/AgCl/NaCl (3 M). The counter electrode was carbon cloth. Scan rates were (a,b) 1 mV·s^{-1} and (c) 50 mV·s^{-1}.

Because the V^{2+} ions generated by the negative scan could be easily oxidized by VO^{2+} to generate V^{3+}, a scan rate of 50 mV·s^{-1} was chosen in order to observe the V^{2+} oxidation current before its loss. Clear $V^{2+/3+}$ redox peaks were absent due to the distortion of the voltammograms. Nevertheless, the information about the order of the activity of the electrodes (TGP < TGP-550Air << TGP-CSnPc-550Air) was satisfactory.

Flow cell tests

The flow cell was assembled using TGP or TGP-CSnPc-550Air in both the positive and negative electrodes to verify the en-

hancement effect observed by using cyclic voltammetry. Figure 6 shows the charge–discharge curves and cycling performances for the two full cells. Significant decreases in the overpotential for both charge and discharge processes were attained in the full cell with the TGP-CSnPc-550Air electrodes compared to that with the TGP electrodes. A stable coulomb efficiency is demonstrated by the cycling performance, indicating no influence of a potential Sn^{2+} contamination on the cycling performance. The finely etched surface and the slightly retained amorphous carbon might prevent potential dislocation and dissolution of the SnO_2 particles.
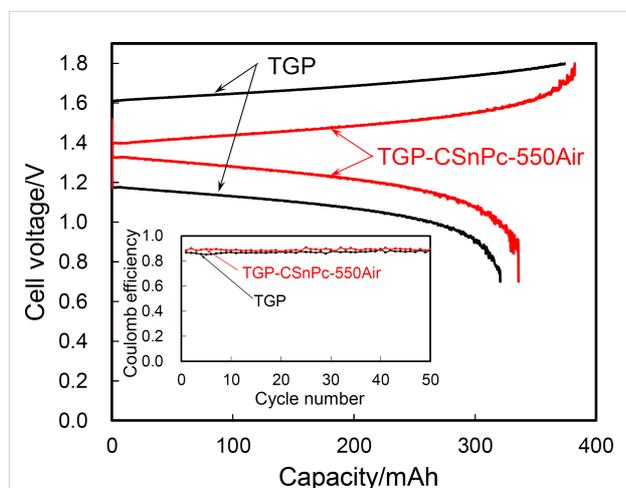

Figure 6: Charge–discharge curves and cycling performance for flow cells using three layers of TGP and TGP-CSnPc-550Air as electrodes. The electrode area was 3 cm^2. The current density was 50 mA·cm^{-2}. The flow rate was 3 cm^3·min^{-1}. The concentrations of the vanadium species and sulfate ion in the anolyte (20 cm^3) and catholyte (20 cm^3) were 1 and 3 M, respectively.

Conclusion

The thermal oxidation of Sn-containing carbonaceous thin films on a carbon fiber surface, which was formed by sublimation, deposition, and pyrolysis of SnPc during a single-step heat treatment in Ar atmosphere at 700 °C, achieved concurrent nanoscale surface etching and SnO_2 loading on the carbon fibers. Both the positive and the negative electrode reactions of VRFB were enhanced and the full cell tests showed the significant decreases in the overpotential for both the charge and the discharge processes, as well as a stable cycling performance. A facile and efficient technique based on the nanoscale processing of the carbon fiber surface was presented to substantially improve the VRFB performance.

Experimental
Materials
Graphitic carbon paper (TGP-H-090, Toray, abbreviated as TGP), tin phthalocyanine (SnPc, Sigma-Aldrich), and ethanol

(99.5%, Nacalai Tesque) were used as received. High-purity water was obtained by circulating ion-exchanged water through an Easypure water-purification system (Barnstead, D7403). Sulfuric acid (6 M, Kishida Chemical Co., Ltd.) was diluted with the high-purity water to prepare a 2 M H_2SO_4 solution. Oxovanadium sulfate hydrate, $VOSO_4 \cdot n H_2O$, was purchased from Sigma-Aldrich (purity > 99.99%) and Nacalai Tesque, which was dissolved in 2 M H_2SO_4 to prepare $VOSO_4$ (1 M)/H_2SO_4 (2 M). The number of water of hydration, *n*, was provided by the manufacturer or determined in advance by thermogravimetry and a differential thermal analysis using an SSC/5200 thermal analyzer (Seiko Instruments).

Concurrent surface etching and SnO_2 loading
For depositing the Sn-containing carbonaceous thin films (CSnPc), eight pieces of TGP (1 cm^2) and 10 mg of SnPc were placed in a crucible (15 cm^3) with a cap and heat-treated at 700 °C for 1 h after raising the temperature at 5 °C·min^{-1} in an Ar atmosphere. The sample was labeled TGP-CSnPc. The heat treatment in air was performed for TGP-CSnPc at *T* = 500, 550, 600 and 650 °C for 1 h. The obtained samples were labeled TGP-CSnPc-*T*Air. For comparison, the heat treatment of TGP without CSnPc was also performed in air at 550 °C for 1 h (TGP-550Air).

Characterization of carbon fiber surface
A field-emission scanning electron microscope (FESEM, JSM-6700F, JEOL) was used to observe the surface structure. The Raman spectra were obtained in backscattering mode by an NRS-3100 spectrometer (JASCO) using an Ar$^+$-ion laser (532.05 nm, 0.3 mW) as the excitation source. The laser beam was focused on the surface of the carbon thin film, producing a spot (analysis area) of approximately 4 mm in diameter. A custom-written software using Microsoft Excel based on Gaussian functions was used for the Raman peak deconvolution and fitting. Energy-dispersive X-ray spectrometry was performed using a FESEM (JSM-7800F, JEOL) and EDX (Octane Elect Super, EDAX). X-ray photoelectron spectroscopy (XPS) was carried out using an AXIS ULTRA DLD system (Kratos Analytical) with Al Ka radiation (1486.6 eV) and the accompanying Vision processing software. The XPS analysis area was 0.3 × 0.7 mm.

Electrochemical measurements
As described in [15], cyclic voltammetry was carried out using a three-electrode glass cell and an electrochemical analyzer, 100B/W (BAS). An Au wire as a lead was connected to the upper side of the 1 cm^2 sample to form the working electrode. The electrode was immersed in ethanol and then rinsed with high-purity water to fully wet the electrode and to minimize the

influence of wetting [7,30]. The counter electrode was carbon cloth (ElectroChem). The reference electrode was Ag/AgCl/NaCl (3 M) (0.212 V vs standard hydrogen electrode). The electrolytes were H_2SO_4 (2 M) and $VOSO_4$ (1 M)/H_2SO_4 (2 M). The measurements were carried out under Ar atmosphere at 25 °C. A flow cell test was performed using three layers of 3 cm^2 of TGP-CSnPc-550Air as the negative and positive electrodes, and Nafion 212 as the separator, incorporated into a flow cell similar to that used in a previous study [31]. The number of the layers was also chosen according to the results of this study. TGP-CSnPc-550Air was immersed in ethanol and rinsed with high-purity water before the incorporation. The anolyte (40 cm^3) and catholyte (20 cm^3) were prepared by electrolysis (charging) of 1 M $VOSO_4$ + 2 M H_2SO_4 until the full conversion of VO^{2+} to VO_2^+ and V^{2+}. After the electrolysis, half of the anolyte was removed and the pre-discharge was carried out at 50 mA·cm^{-2}, followed by measurement of the charge–discharge curve. The flow rate was 3 cm^3·min^{-1}. The current density was 50 mA·cm^{-2}. A flow cell using TGP was similarly tested for comparison.

Supporting Information

Supporting Information File 1

Enlarged views of FESEM images, Raman spectra, C 1s XPS spectra, deconvoluted O 1s XPS spectra, and the content of surface oxygen species.

[https://www.beilstein-journals.org/bjnano/content/supplementary/2190-4286-10-99-S1.pdf]

Acknowledgements

ORCID® iDs

Jun Maruyama - https://orcid.org/0000-0001-8898-7062
Shohei Maruyama - https://orcid.org/0000-0002-7085-3207

References

1. Friedl, J.; Lebedeva, M. A.; Porfyrakis, K.; Stimming, U.; Chamberlain, T. W. *J. Am. Chem. Soc.* **2018,** *140,* 401–405. doi:10.1021/jacs.7b11041
2. Winsberg, J.; Hagemann, T.; Janoschka, T.; Hager, M. D.; Schubert, U. S. *Angew. Chem., Int. Ed.* **2017,** *56,* 686–711. doi:10.1002/anie.201604925
3. Leung, P.; Shah, A. A.; Sanz, L.; Flox, C.; Morante, J. R.; Xu, Q.; Mohamed, M. R.; Ponce de León, C.; Walsh, F. C. *J. Power Sources* **2017,** *360,* 243–283. doi:10.1016/j.jpowsour.2017.05.057
4. Noack, J.; Roznyatovskaya, N.; Herr, T.; Fischer, P. *Angew. Chem., Int. Ed.* **2015,** *54,* 9776–9809. doi:10.1002/anie.201410823
5. Gattrell, M.; Park, J.; MacDougall, B.; Apte, J.; McCarthy, S.; Wu, C. W. *J. Electrochem. Soc.* **2004,** *151,* A123–A130. doi:10.1149/1.1630594
6. Sun, C.-N.; Delnick, F. M.; Aaron, D. S.; Papandrew, A. B.; Mench, M. M.; Zawodzinski, T. A. *ECS Electrochem. Lett.* **2013,** *2,* A43–A45. doi:10.1149/2.001305eel
7. Pezeshki, A. M.; Clement, J. T.; Veith, G. M.; Zawodzinski, T. A.; Mench, M. M. *J. Power Sources* **2015,** *294,* 333–338. doi:10.1016/j.jpowsour.2015.05.118
8. Sun, B.; Skyllas-Kazacos, M. *Electrochim. Acta* **1992,** *37,* 1253–1260. doi:10.1016/0013-4686(92)85064-r
9. Agar, E.; Dennison, C. R.; Knehr, K. W.; Kumbur, E. C. *J. Power Sources* **2013,** *225,* 89–94. doi:10.1016/j.jpowsour.2012.10.016
10. Kim, K. J.; Lee, S.-W.; Yim, T.; Kim, J.-G.; Choi, J. W.; Kim, J. H.; Park, M.-S.; Kim, Y.-J. *Sci. Rep.* **2014,** *4,* 6906. doi:10.1038/srep06906
11. Sun, B.; Skyllas-Kazacos, M. *Electrochim. Acta* **1992,** *37,* 2459–2465. doi:10.1016/0013-4686(92)87084-d
12. Yue, L.; Li, W.; Sun, F.; Zhao, L.; Xing, L. *Carbon* **2010,** *48,* 3079–3090. doi:10.1016/j.carbon.2010.04.044
13. Maruyama, J.; Hasegawa, T.; Iwasaki, S.; Fukuhara, T.; Nogami, M. *J. Electrochem. Soc.* **2013,** *160,* A1293–A1298. doi:10.1149/2.108308jes
14. Zhang, W.; Xi, J.; Li, Z.; Zhou, H.; Liu, L.; Wu, Z.; Qiu, X. *Electrochim. Acta* **2013,** *89,* 429–435. doi:10.1016/j.electacta.2012.11.072
15. Maruyama, J.; Maruyama, S.; Fukuhara, T.; Hanafusa, K. *J. Phys. Chem. C* **2017,** *121,* 24425–24433. doi:10.1021/acs.jpcc.7b07961
16. Bayeh, A. W.; Kabtamu, D. M.; Chang, Y.-C.; Chen, G.-C.; Chen, H.-Y.; Lin, G.-Y.; Liu, T.-R.; Wondimu, T. H.; Wang, K.-C.; Wang, C.-H. *ACS Sustainable Chem. Eng.* **2018,** *6,* 3019–3028. doi:10.1021/acssuschemeng.7b02752
17. Zhou, H.; Shen, Y.; Xi, J.; Qiu, X.; Chen, L. *ACS Appl. Mater. Interfaces* **2016,** *8,* 15369–15378. doi:10.1021/acsami.6b03761
18. Li, B.; Gu, M.; Nie, Z.; Wei, X.; Wang, C.; Sprenkle, V.; Wang, W. *Nano Lett.* **2014,** *14,* 158–165. doi:10.1021/nl403674a
19. Takasaki, F.; Matsuie, S.; Takabatake, Y.; Noda, Z.; Hayashi, A.; Shiratori, Y.; Ito, K.; Sasaki, K. *J. Electrochem. Soc.* **2011,** *158,* B1270–B1275. doi:10.1149/1.3625918
20. Maruyama, J.; Shinagawa, T.; Siroma, Z.; Mineshige, A. *Electrochem. Commun.* **2011,** *13,* 1451–1454. doi:10.1016/j.elecom.2011.09.026
21. Sadezky, A.; Muckenhuber, H.; Grothe, H.; Niessner, R.; Pöschl, U. *Carbon* **2005,** *43,* 1731–1742. doi:10.1016/j.carbon.2005.02.018
22. Jaouen, F.; Charreteur, F.; Dodelet, J. P. *J. Electrochem. Soc.* **2006,** *153,* A689–A698. doi:10.1149/1.2168418
23. Maruyama, J.; Shinagawa, T.; Hayashida, A.; Matsuo, Y.; Nishihara, H.; Kyotani, T. *ChemElectroChem* **2016,** *3,* 650–657. doi:10.1002/celc.201500543
24. Zhang, C.; Li, L.; Ju, J.; Chen, W. *Electrochim. Acta* **2016,** *210,* 181–189. doi:10.1016/j.electacta.2016.05.151
25. Song, H.; Zhang, L.; He, C.; Qu, Y.; Tian, Y.; Lv, Y. *J. Mater. Chem.* **2011,** *21,* 5972–5977. doi:10.1039/c0jm04331a
26. Wang, Y.; Djerdj, I.; Smarsly, B.; Antonietti, M. *Chem. Mater.* **2009,** *21,* 3202–3209. doi:10.1021/cm9007014
27. Shemet, V. Z.; Pomytkin, A. P.; Neshpor, V. S. *Carbon* **1993,** *31,* 1–6. doi:10.1016/0008-6223(93)90148-4

28. Randin, J.-P.; Yeager, E. *J. Electrochem. Soc.* **1971,** *118,* 711–714. doi:10.1149/1.2408151

29. Fink, H.; Friedl, J.; Stimming, U. *J. Phys. Chem. C* **2016,** *120,* 15893–15901. doi:10.1021/acs.jpcc.5b12098

30. Goulet, M.-A.; Skyllas-Kazacos, M.; Kjeang, E. *Carbon* **2016,** *101,* 390–398. doi:10.1016/j.carbon.2016.02.011

31. Liu, Q. H.; Grim, G. M.; Papandrew, A. B.; Turhan, A.; Zawodzinski, T. A.; Mench, M. M. *J. Electrochem. Soc.* **2012,** *159,* A1246–A1252. doi:10.1149/2.051208jes

Glucose-derived carbon materials with tailored properties as electrocatalysts for the oxygen reduction reaction

Rafael Gomes Morais, Natalia Rey-Raap[*], José Luís Figueiredo
and Manuel Fernando Ribeiro Pereira[*]

Abstract

Nitrogen-doped biomass-derived carbon materials were prepared by hydrothermal carbonization of glucose, and their textural and chemical properties were subsequently tailored to achieve materials with enhanced electrochemical performance towards the oxygen reduction reaction. Carbonization and physical activation were applied to modify the textural properties, while nitrogen functionalities were incorporated via different N-doping methodologies (ball milling and conventional methods) using melamine. A direct relationship between the microporosity of the activated carbons and the limiting current density was found, with the increase of microporosity leading to interesting improvements of the limiting current density. Regardless of the doping method used, similar amounts of nitrogen were incorporated into the carbon structures. However, significant differences were observed in the nitrogen functionalities according to the doping method applied: ball milling appeared to originate preferentially quaternary and oxidized nitrogen groups, while the formation of pyridinic and pyrrolic groups was favoured by conventional doping. The onset potential was improved and the two-electron mechanism of the original activated sample was shifted closer to a four-electron pathway due to the presence of nitrogen. Interestingly, the high pyridinic content related to a high ratio of pyridinic/quaternary nitrogen results in an increase of the onset potential, while a decrease in the quaternary/pyrrolic nitrogen ratio favors an increase in the number of electrons. Accordingly, the electrocatalyst with the highest performance was obtained from the activated sample doped with nitrogen by the conventional method, which combined the most appropriate textural and chemical properties: high microporosity and adequate proportion of the nitrogen functionalities.

Introduction

Due to the recent increase in interest for more sustainable, renewable and cheaper energy, multiple conversion devices are being developed using new and innovative materials. Fuel cells are outstanding conversion devices, as they convert chemical energy directly into electrical energy with high efficiency and low emission of pollutants (the by products are water and heat) [1,2]. Fuel cells offer the best advantages for use with engines, as they are able to function as long as there is fuel, and for batteries, as they have similar characteristics under load conditions [1]. The performance of a fuel cell is mainly controlled by the oxygen reduction reaction (ORR) that takes place at the cathode [2], specifically by the electrocatalyst used for the reaction. The most commonly used electrocatalyst to supply faster kinetics and a four-electron pathway are platinum-based materials [3,4], which are costly and may assume up to 50% of the total cost of a fuel cell [5].

Transition metals [6,7], metal oxides [8,9] and carbon materials [3,4] have been widely studied as electrocatalysts in ORR due to their attractive physical and electrochemical properties. Among these materials, metal-free carbon materials have received tremendous attention due to their versatility and lower price in comparison with metal-based materials [2]. The main advantage of carbon materials is the possibility of modifying their physical and chemical properties resulting in a more electroactive material [2,3,10], which is an especially important feature for the ORR. The incorporation of heteroatoms like nitrogen [11,12], oxygen [13], sulfur [14,15], phosphorous [16,17] and boron [18,19] has been proven to enhance the electroactivity of carbon materials. Nitrogen has been the most studied heteroatom in the context of the reaction mechanism, since nitrogen-doped materials can achieve a four-electron pathway towards ORR [20-22]. However, there is some controversy related to the effect of the different nitrogen functionalities in the process. Some investigations suggest that the reduction of oxygen is promoted by pyridinic groups [23], while other researchers reported that quaternary nitrogen groups are the most active sites [24,25], and some studies assume that both functionalities contribute to enhancing the performance of the materials towards ORR [20]. In addition, a recent study with carbon nanotubes (CNTs) reported that an increase of the pyridinic-N/quaternary-N and pyridinic-N/pyrrolic-N ratios increases the electroactivity and that decreasing the quaternary-N/pyrrolic-N ratio increases the number of electrons involved in the ORR [12]. The electron density movement due to the presence of quaternary nitrogen favors the O_2 dissociation, while the pyridinic nitrogen favors the bonding of oxygen to the neighboring carbon. Accordingly, the appropriate ratio between both nitrogen functionalities seems to be essential to improve the electroactivity of carbon materials. The differences reported

on the influence of the nitrogen functionalities may be related to the nature and type of the carbon material employed, which in turn, depends on the precursors used and the method of synthesis applied.

Nitrogen-doped carbon materials have been synthesized by applying different doping methods to different types of materials, such as CNTs [12,23,26], graphene [20,25,27], carbon aerogels [15,28], carbon nanofibers [29], carbon nitrides [30], activated carbons [31] or mesoporous carbons [32,33]. Some of these materials are obtained from chemical compounds, fossil fuels or by complex and expensive synthesis procedures. In order to keep fuel cells as ecologically friendly as possible, the use of biomass as a carbon source appears to be an attractive alternative. In this context, hydrothermal carbonization (HTC) has appeared in recent years as an interesting strategy to obtain biomass-derived carbons due to its low cost and mild synthesis conditions, making the process environmentally friendly [34]. However, the main drawback of HTC is that the as-prepared hydrothermal carbon materials usually exhibit limited porosity and inadequate chemical properties for the ORR. To solve this problem, different strategies can be addressed: i) carbonization and activation methods to tailor the porosity and ii) the incorporation of heteroatoms to modify the surface chemistry, specifically by adding nitrogen functionalities. Biomass-derived carbons have been functionalized by applying thermal treatments in the presence of a gaseous or solid nitrogen precursor [35,36] or without any precursor in the case where the biomass already contains nitrogen in its constitution [11,37], and by in situ methods in which nitrogen precursors are introduced during the hydrothermal carbonization [38]. An additional strategy that can be applied to biomass processing is ball milling, which has been proposed as a green, cheap and easy method to incorporate nitrogen atoms and to modify the surface chemistry of carbon materials [39,40]. Some of these doping techniques have shown to provide materials with similar ORR performance as commercially available Pt/C electrocatalysts [39]. However, most of these studies have been focused only on the effect of nitrogen functionalities on the ORR, leaving aside the effect of porosity. In fact, although some studies suggest the importance of microporosity on the ORR [41], there is a lack of knowledge about its real effect on the ORR performance of nitrogen-doped porous carbon materials, and more specifically, of biomass-derived carbons.

Therefore, this study aims to prepare glucose-derived carbon materials with different textural and chemical properties and to correlate these properties with the performance towards ORR. Activated carbons with different microporosity were prepared by activating the samples at different times to determine the

relationship between the textural properties and the ORR performance. Moreover, different doping strategies were applied to assess the effect of such methods on the incorporation of nitrogen functionalities and to evaluate the influence of the different functional groups on the response of the electrocatalyst towards the oxygen reduction reaction.

Results and Discussion
Effect of microporosity

The nitrogen adsorption–desorption isotherms and the pore size distributions obtained by applying the quenched solid density functional theory (QSDFT) are presented in Figure 1a and 1b, respectively.

Activated carbons display isotherms of type I according to the International Union of Pure and Applied Chemistry (IUPAC) classification, attributed to microporous materials. As expected, the volume of nitrogen adsorbed at low relative pressure increases with the time of activation, resulting in materials with a larger volume of micropores (Supporting Information File 1, Table S1). This effect is due to the reverse Boudouard reaction, which extracts carbon atoms from the carbon structure, developing the porosity of the material [42]. Accordingly, a prolonged contact time between the carbon material and the activating agent results in materials with a more developed microporosity. In addition, the pore size of the samples is also broadened by increasing the contact time (Figure 1b). The reaction occurring during the physical activation of the samples removes carbon atoms, giving rise to larger voids inside the particles, and hence, to larger pore sizes.

Regarding the chemical composition, the activated samples are mainly composed of carbon, with a smaller percentage of

oxygen in the range of 2–4 wt % (Supporting Information File 1, Table S2). Although these values are not too high, oxygen functionalities can modify the electroactivity of carbon materials [13], therefore the nature of these functional group has been analyzed by temperature programmed desorption (TPD) experiments to evaluate possible differences in the oxygen functionalities. The total amount of CO (anhydrides, phenols, carbonyls) and CO_2 (carboxylic acids, anhydrides, lactones) released was calculated from the corresponding TPD profiles, and the values obtained are compiled in Supporting Information File 1, Table S3. The CO_2 and CO desorption profiles, obtained for samples AG_{1h} and AG_{6h} are also shown in Supporting Information File 1, Figure S1. The TPD profiles show that the sample with the highest degree of activation (AG_{6h}) has a lower amount of phenols due to the longer time used for the activation. However, in general terms, the released CO and CO_2 and their ratio are quite similar, so it can be assumed that there are no significant differences between the chemical composition of the samples, and therefore, any difference in the ORR performance can be exclusively related to the microporosity and/or the degree of activation.

Linear sweep voltammograms (LSVs) recorded in an O_2-saturated basic electrolyte at 1600 rpm and the Nyquist plot obtained from electrochemical impedance spectroscopy measurements are shown in Figure 2a and 2b, respectively.

To evaluate the performance of the prepared electrocatalysts, cyclic voltammetry (CV) and linear sweep voltammetry (LSV) were performed. LSV curves of the activated samples show two main differences: i) the onset potential shifts to more positive values by increasing the time of activation, which can be related to the more graphitic structure that is generated during activa-
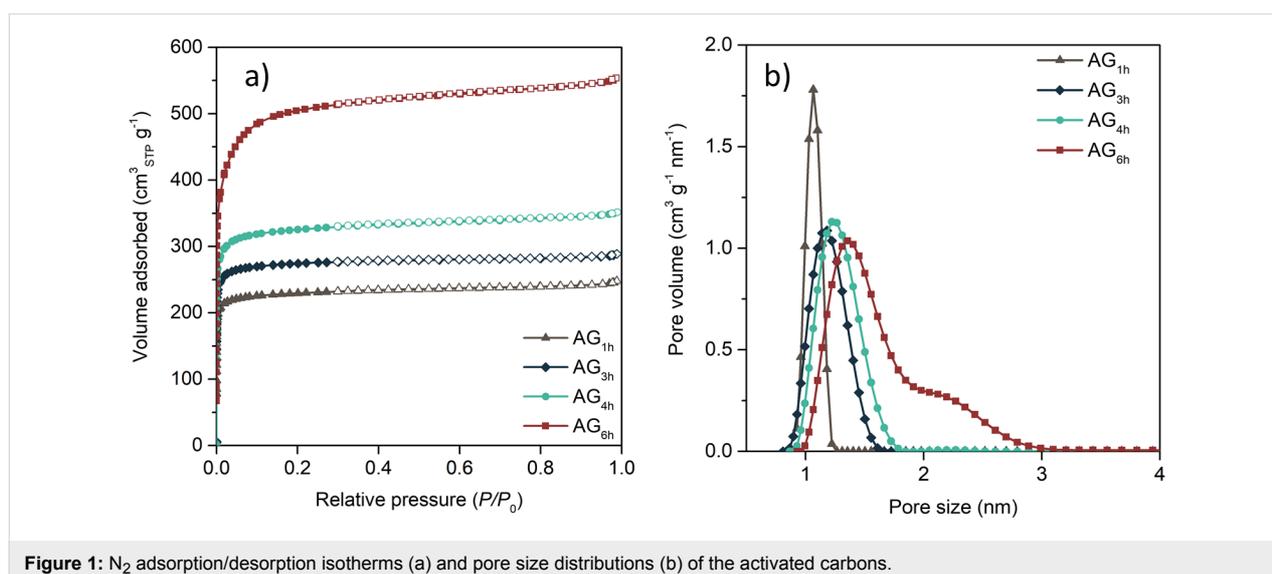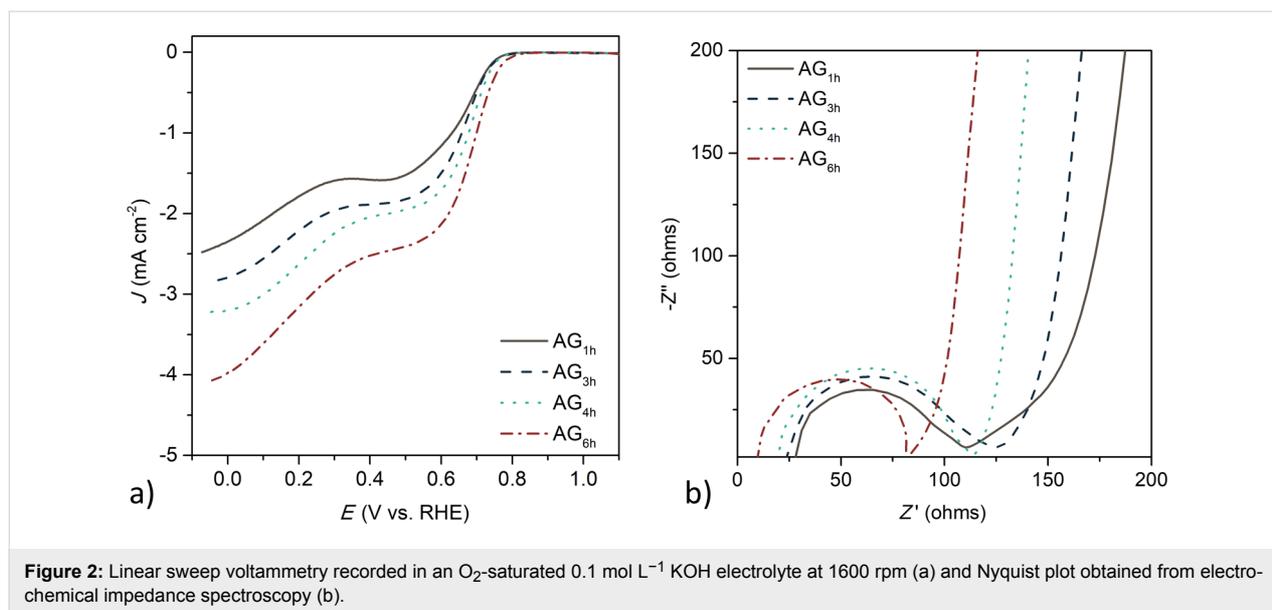

Figure 1: N_2 adsorption/desorption isotherms (a) and pore size distributions (b) of the activated carbons.

Figure 2: Linear sweep voltammetry recorded in an O_2-saturated 0.1 mol L^{-1} KOH electrolyte at 1600 rpm (a) and Nyquist plot obtained from electrochemical impedance spectroscopy (b).

tion; and ii) the value of the limiting current density increases with microporosity, which can be related to the more developed porous structure. These two effects can be confirmed by the electrochemical impedance spectroscopy measurements (Figure 2b). The Nyquist plot shows that a higher degree of activation results in a lower cell resistance and a smaller semicircle at high frequencies, indicating a lower charge transfer resistance, which allows the kinetics of the ORR to increase, and consequently, a higher onset potential is observed for sample AG_{6h} (the values of the onset potential are shown in Supporting Information File 1, Table S4). In addition, these results also suggest that a more developed microporous structure favors the electrolyte diffusion to the most electrochemically active pores, which also contributed to the ORR kinetics. Moreover, clear differences regarding ionic transportation are also observed at medium frequencies. Sample AG_{1h} shows a more defined Warburg impedance, indicating a higher resistance of the electrolyte ion diffusion into the porous structure, and hence, a lower value of limiting current density. These diffusion limitations are less evident for those samples with wider pore size, as pores act as diffusion channels favoring the kinetics of the ORR. In fact, a direct relationship was observed for microporosity and limiting current density for these carbon materials (Figure 3).

However, regardless of the time used for the activation, all samples show a LSV curve with a similar shape. The reduction reaction occurs at two different potentials (0.75–0.78 V and 0.30–0.33 V), indicating that the ORR mechanism proceeds via the two-electron pathway. These results are corroborated by the experiments performed with a rotating ring disk electrode, from which the production of hydrogen peroxide was evaluated.

Figure 3: Relationship between BET surface area and the limiting current density of the activated samples.
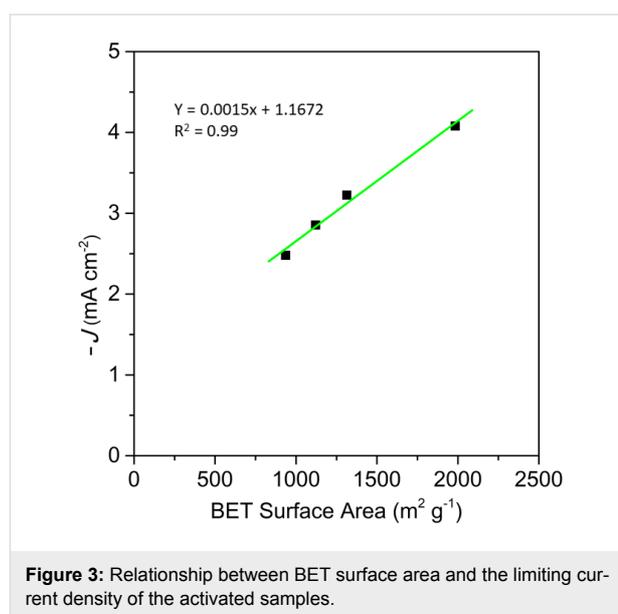
More than 18% of hydrogen peroxide was produced with AG_{6h} (Supporting Information File 1, Figure S2), which is not desirable for the ORR. These results indicate that further modifications of this sample are needed to enhance the performance of the biomass-derived carbons towards ORR.

Effect of the surface chemistry

In order to improve the performance of glucose-derived activated carbons, the surface chemistry of the sample AG_{6h} (from now on simply named AG) was modified by applying different doping methods: ball milling and conventional mixing. In addition, such methods were also applied to a carbonized sample to evaluate the effect of the doping method according to the micro-

porosity generated from the initial thermal treatment. Both activated and carbonized samples also underwent the ball milling method without nitrogen precursor to discriminate among the modifications resulting from ball milling and those due to the conjugation of ball milling and the nitrogen precursor. The results obtained from the elemental analysis are presented in Table 1.

Table 1: Chemical composition determined by elemental analysis.

Sample	Carbon (wt %)	Nitrogen (wt %)	Oxygen (wt %)	Hydrogen (wt %)
AG	97.3	–	2.4	0.3
AG_{BM}	89.4	–	9.5	1.1
$N-AG_{BM}$	87.3	4.3	7.0	1.4
$N-AG_C$	90.1	4.1	4.9	0.9
CG	93.6	–	4.7	1.6
CG_M	85.5	–	12.3	2.2
$N-CG_{BM}$	82.9	6.9	8.8	1.4
$N-CG_C$	83.1	6.2	9.2	1.5

As expected, all samples are mainly composed of carbon, where the percentage is slightly higher for activated samples than for carbonized materials, due to the higher temperature used for activation (900 °C). The application of ball milling in both activated and carbonized samples results in a noticeable increase in the oxygen content. This phenomenon may be due to the defects created in the carbon structure during the milling process that react with air and incorporate oxygen. This effect is also observed for N-doped samples by ball milling. However, doped samples undergo a second thermal treatment that partially removes the oxygen incorporated during the ball milling process, resulting in lower oxygen content. Nevertheless, although the amount of oxygen in samples doped by ball milling is lower than in undoped samples, the percentage detected is still significant. As for conventionally doped samples, the oxygen content is twice the oxygen found in the original samples. Regardless of the degree of activation of the samples, the amount of nitrogen incorporated by the ball milling method is similar to that obtained by the conventional method. However, the incorporation of oxygen and nitrogen in the activated structures is lower than in carbonized samples. Activation at high temperature results in a structure with higher chemical stability and lower amount of defects in which heteroatoms can be incorporated, and so materials with a lower degree of functionalization are obtained.

Further understanding of the functionalities of the carbon materials was achieved by analyzing their surface composition by X-ray photoelectron spectroscopy (XPS). The XPS spectra in the C 1s, O 1s and N 1s regions were deconvoluted to identify the types of functionalities present in the surface of the carbon materials. The deconvolution of the C 1s spectra for undoped samples presents five main peaks (Supporting Information File 1, Figure S3), representing the following by increasing binding energy: i) carbon sp^2 (C=C, peak I) at 284.6 ± 0.1 eV; ii) carbon in phenol, alcohol, ether bonds (C–O, peak II) at 285.8 ± 0.2 eV; iii) carbonyl or quinone groups (C=O, peak III) at 287.2 ± 0.2 eV; iv) carboxyl groups (COOH, peak IV) at 288.9 eV ± 0.3; and v) the shake-up satellite due to π–π* transitions in aromatic rings (peak V) at 290.6 ± 0.5 eV [43]. Carbon sp^2 (peak I) is an asymmetric peak consisting of a tail towards higher binding energies that represents ≈80% of surface carbon, which does not show significant differences for activated and carbonized samples. However, noticeable differences in the peaks attributed to carbon–oxygen bonds are observed due to the ball milling process and the doping methods applied. The peak attributed to carboxylic acids (peak IV) is significantly more pronounced for ball-milled samples (AG_{BM} and CG_{BM}), suggesting that the increase of oxygen detected by elemental analysis (Table 1) was due to the formation of a large number of carboxylic acids, which further reinforces the possible reaction between the defects generated on the sample during the ball milling process and air moisture. The XPS spectra for the C 1s region of the doped samples exhibit the same five peaks as those observed for the undoped samples. However, peak II and peak III also have contributions of C–N and C=N interactions, respectively [15]. These phenomena result in a significantly higher contribution of these two peaks than those observed for the undoped samples. Additionally, peak IV in conventionally doped materials ($N-AG_C$ and $N-CG_C$) is more pronounced than that of their doped ball-milled counterparts. This peak can be assigned to sp^2-hybridized carbons in a triazine aromatic ring (N–C=N) [30], which may result from the polymerization of melamine during the subsequent thermal treatment. This effect is less obvious in the spectra of the activated sample, as its higher chemical stability results in a lower degree of functionalization and, therefore, a lower formation of the triazine aromatic ring.

The high-resolution N 1s spectra of doped samples was deconvoluted into three different peaks (Figure 4) representing the three major nitrogen groups, which are, by increasing binding energy: pyridinic at 398.4 ± 0.1 eV (N-6), pyrrolic at 400.0 ± 0.1 eV (N-5) and quaternary nitrogen at 401.4 ± 0.3 eV (N-Q) [12,26]. Additionally, another peak was observed at 403.2 ± 0.1 eV in samples $N-AG_{BM}$ and $N-CG_{BM}$, attributed to oxidized nitrogen groups (N-X) [26], suggesting that the ball milling process is related to the appearance of oxidized groups, as this peak is not observed for conventionally doped samples (sample $N-AG_C$ and $N-CG_C$). The ball milling method seems to
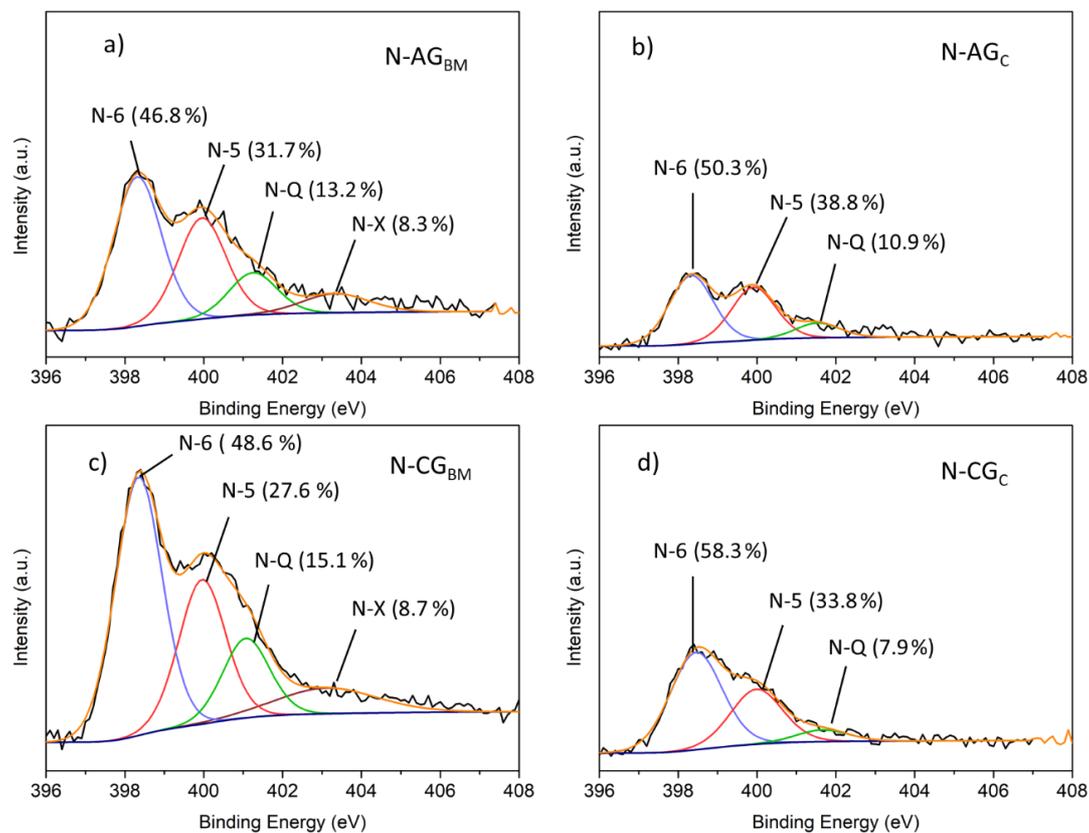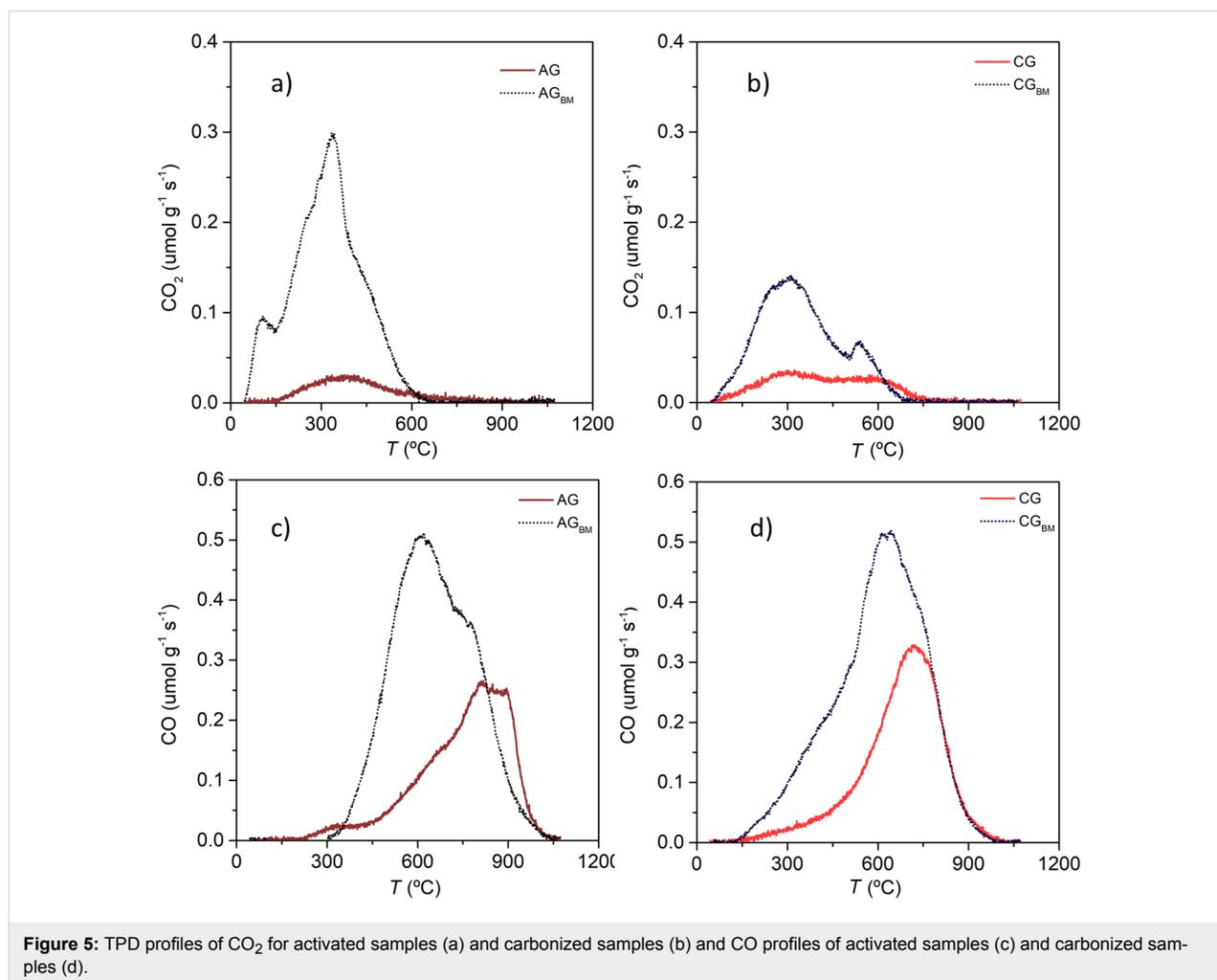
Figure 4: Deconvolution of the XPS N 1s spectra for N-AG$_{BM}$ (a) N-AG$_C$ (b), N-CG$_{BM}$ (c) and N-CG$_C$ (d).

modify the carbon structure promoting the contact between oxygen and nitrogen-containing species, which will react during the subsequent thermal treatment, oxidizing the nitrogen groups. In addition, differences in the contribution of each nitrogen group due to the doping method were also observed.

Samples doped via ball milling (Figure 4a and 4c) exhibit slightly lower percentages of pyridinic and pyrrolic groups than their conventionally doped counterparts (Figure 4b and 4d). Regarding quaternary nitrogen, significant differences were observed for both the doping method and the structure of the carbon. Activated samples exhibit similar contributions (13% and 11% for samples N-AG$_{BM}$ and N-AG$_C$, respectively), although ball milling seems to favor the incorporation of a slightly larger amount of N-Q. This effect is much more pronounced in carbonized samples that present larger differences as a function of the doping method: N-CG$_{BM}$ incorporated almost twice N-Q groups as N-CG$_C$. These results suggest that the ball milling process is more prone to incorporate quaternary groups as it creates defects in the activated and carbonized glucose structure, creating more sites to form quaternary structures inside the carbon matrix.

The XPS spectra in the O 1s region are shown in Supporting Information File 1, Figure S4. Three main oxygen peaks were identified, attributed to C=O bonds at 530.7 ± 0.3 eV (peak I), C–O groups at 532.0 ± 0.2 eV (peak II) and carboxylic acids at 533.3 ± 0.2 eV (peak III) [27]. Interesting differences are detected for N-doped carbons prepared by the ball milling method, as an additional peak is detected at higher binding energies corresponding to N–O–C bonds (peak IV), which is in agreement with the oxidized nitrogen peak also shown in the N 1s spectra. In addition, different contributions of the oxygen functionalities related to carbon bonds are presented, which is in agreement with those results obtained by the deconvolution of the C 1s spectra, especially for undoped ball-milled samples that exhibited a pronounced peak attributed to carboxylic acids. The O 1s spectra deconvolution does not clearly distinguish the contribution of the various surface groups due to overlaps in their binding energies. Therefore, the contribution of oxygen-containing surface groups in undoped samples was further analysed by TPD. The CO and CO$_2$ measurements obtained for undoped activated and carbonized samples are presented in Figure 5, while the deconvolution of the profiles is shown in Figures S5, S6, S7 and S8 in Supporting Information File 1.

Figure 5: TPD profiles of CO_2 for activated samples (a) and carbonized samples (b) and CO profiles of activated samples (c) and carbonized samples (d).

The amount of CO_2 and CO released from ball-milled samples is significantly higher than that of their original counterparts. Analyzing the CO_2 profiles of activated samples three peaks can be observed (Supporting Information File 1, Figures S5a and S6a), which could be attributed to carboxylic acids, anhydride and lactone groups, respectively [26,44]. The peaks presented for the ball-milled activated sample are much more intense, especially the carboxylic acid peak, which is in agreement with the results obtained from XPS. The deconvolution of the CO profiles (Supporting Information File 1, Figures S5b, S6b, S7b and S8b) of all samples showed the presence of three main peaks corresponding to anhydrides, phenols and carbonyl/quinone groups [26,44]. Ball-milled samples present a much more significant contribution of phenols, corroborating the hypothesis that ball milling generates oxygen functional groups with weaker bonds due to reaction with air moisture. It should also be noted that the temperature at which oxygen groups are released as CO_2 and CO is higher for sample AG than for sample CG, confirming that the activated sample is more chemically stable.

The doping methods employed may also have an effect on the textural properties, which, as explained above, may modify the electroactive character of the biomass-derived carbons. Therefore, to evaluate the modifications caused to the textural properties due to the surface chemistry changes, nitrogen adsorption–desorption isotherms were obtained (Figure 6). The pore size distributions determined by applying the QSDFT are shown in Supporting Information File 1, Figure S9.

Like activated samples shown in Figure 1, modified activated and carbonized carbon materials display type I isotherms, characteristic of microporous materials. The application of ball milling and the different doping methods to both activated and carbonized samples led to a decrease in the volume of nitrogen adsorbed at low relative pressure, resulting in materials with a smaller volume of micropores (Supporting Information File 1, Table S5) and lower surface area (a decrease of ≈500 and 100 m^2 g^{-1} is observed after ball milling in the activated and carbonized samples, respectively). This decrease in microporosity suggests that the carbon material suffered changes in its
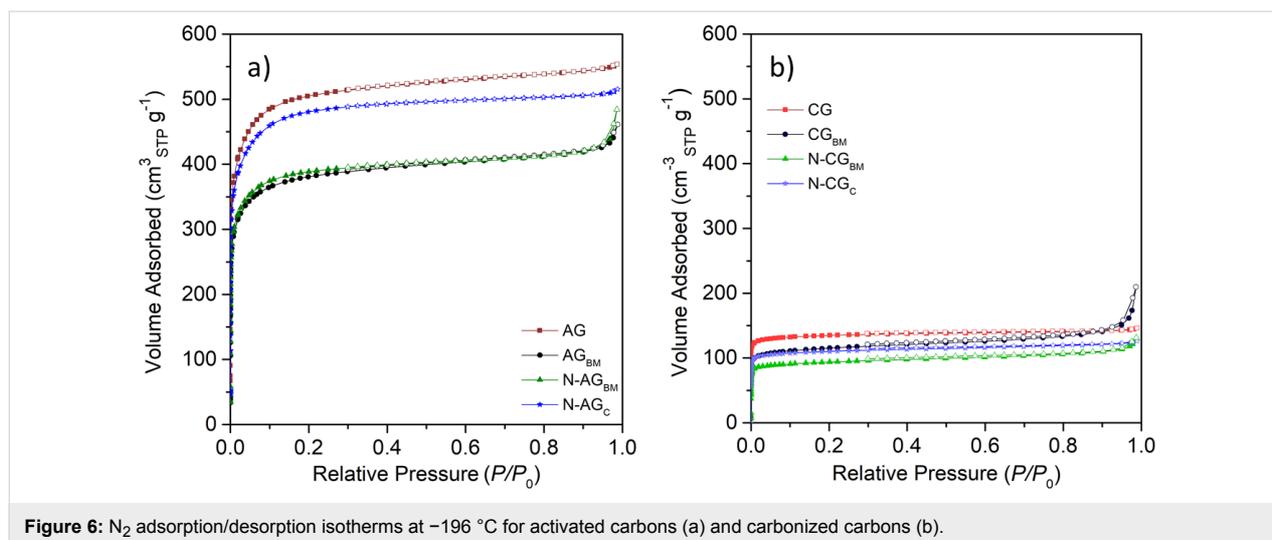
Figure 6: N_2 adsorption/desorption isotherms at −196 °C for activated carbons (a) and carbonized carbons (b).
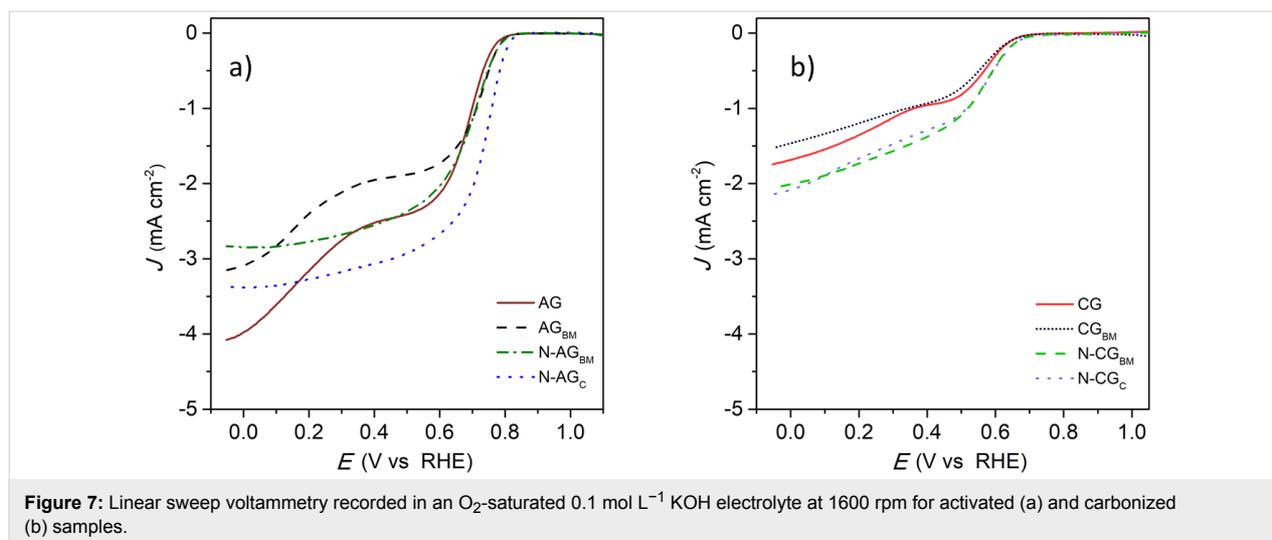
structure due to the ball milling process, especially for the activated sample (Supporting Information File 1, Figure S10). This effect may be due to the loss of mass during the activation that results in materials with lower mechanical resistance than that of carbonized samples [45,46]. Moreover, ball-milled samples exhibit an increase of nitrogen adsorbed at high relative pressure ($P/P_0 > 0.9$), suggesting the formation of macropores. The addition of nitrogen by conventional mixing the carbon materials with melamine also results in a decrease in the surface area. In this case, the decrease is analogous for both activated and carbonized sample, suggesting that the N-groups introduced into the structure are blocking some pores, preventing the access of N_2 to the innermost pores of the carbon material during the isotherm measurements. The incorporation of nitrogen functionalities by using the ball milling process also modified the microporosity of the samples. However, differences are observed for the activated and carbonized sample. In the case of the activated sample, the incorporation of nitrogen does not seem to produce a noticeable blockage of the pores as previously observed for sample N-AG$_C$, resulting in a material with a BET surface area similar to that obtained for sample AG$_{BM}$, with ball milling being the predominant effect. In the case of sample N-CG$_{BM}$, the ball milling process and the incorporation of nitrogen seem to have a synergistic effect, resulting in a decrease of the S$_{BET}$ almost equivalent to the sum of that observed for sample CG$_{BM}$ and N-CG$_C$.

Electrochemical measurements

Cyclic voltammograms recorded for activated samples and carbonized samples in a N_2- and O_2-saturated basic electrolyte at 5 mV s^{-1} are shown in Supporting Information File 1, Figure S11, while the LSV of activated and carbonized samples recorded in an O_2-saturated basic electrolyte at 1600 rpm are shown in Figure 7a and 7b, respectively.

Cyclic voltammograms measured in O_2-saturated electrolyte (Supporting Information File 1, Figure S11a) and LSV of activated samples show a reduction reaction peak starting at 0.78–0.82 V. This peak does not appear for N_2-saturated cyclic voltammograms (Supporting Information File 1, Figure S11c), thus confirming that the catalytic activity of the prepared electrocatalysts exists at the mentioned potentials. Table 2 summarizes the electrochemical results of the samples.

The onset potential of sample AG slightly shifts to more positive values from 0.78 V to 0.79 V by ball milling the sample (AG$_{BM}$) as shown in Figure 7a and Table 2. This increase may be due to the smaller particle size of the carbon powder obtained after ball milling, which could result in a material with higher electrical conductance, or due to the higher amount of oxygen [13]. The LSV of carbonized samples reveals that although sample CG$_{BM}$ presents a much higher oxygen content, CG and CG$_{BM}$ samples display the same onset potential (0.64 V), which suggests that the more positive onset potential of sample AG$_{BM}$ is due to its higher conductance. Moreover, samples AG and AG$_{BM}$ exhibit a second shoulder at more negative potentials, indicating that the ORR mechanism proceeds via the two-electron pathway producing hydrogen peroxide. This second reduction shoulder does not appear for the doped activated samples, suggesting that the mechanism of the reaction has shifted to the four-electron pathway. However, the incorporation of nitrogen atoms by ball milling the activated sample (N-AG$_{BM}$) does not modify the onset potential when compared to the undoped counterpart (AG$_{BM}$). This indicates that the simple incorporation of nitrogen atoms is not enough to increase the onset potential to more positive values for this type of carbon material. Contrary to activated samples, the incorporation of nitrogen atoms using the ball milling method in the carbonized sample (N-CG$_{BM}$) slightly

Figure 7: Linear sweep voltammetry recorded in an O$_2$-saturated 0.1 mol L^{-1} KOH electrolyte at 1600 rpm for activated (a) and carbonized (b) samples.

increases the onset potential regarding the undoped sample (CG$_{BM}$) from 0.64 V to 0.67 V. Like in activated samples, this is probably due to the smaller particle size obtained after ball milling, which could result in a material with higher electrical conductance.

The onset potential of sample N-AG$_C$ is shifted to more positive values in relation to AG (from 0.78 V to 0.82 V). AG and N-AG$_C$ do not present significant differences in the nature and amount of oxygen groups at their surface (Supporting Information File 1, Figure S4), which suggests that the increase in the onset potential is due to the incorporation of nitrogen. However, sample N-AG$_{BM}$ and N-AG$_C$ present similar nitrogen content (Table 1), but different values of onset potential are obtained, suggesting that the percentage of incorporated nitrogen is not the key factor, but the type of nitrogen functionality. Likewise, the addition of nitrogen using the conventional method (N-CG$_C$) also results in the same slight shift of the onset potential to more positive values in relation to CG and CG$_{BM}$.

In order to further understand the effect of nitrogen functionalities in the ORR, doped samples must be thoroughly compared. A difference in the content of pyridinic nitrogen is observed for doped activated samples (39% vs 32% for N-AG$_C$ and N-AG$_{BM}$, respectively, Figure 4). Accordingly, the increase of the onset potential may be due to the presence of pyridinic nitrogen groups in the N-AG$_C$ sample, which is in agreement with some studies in the literature [23]. The sample N-AG$_C$ showed a higher value of the pyridinic-N/quaternary-N ratio than the sample N-AG$_{BM}$ (3.6 vs 2.4, respectively) and a slightly higher value of the pyridinic-N/pyrrolic-N ratio (0.8 vs 0.7, respectively) which corroborates the theory that the increase of these two ratios is beneficial for the electrochemical activity of the prepared electrocatalysts [12]. This is not observed for carbonized samples as they do not present superior textural properties, compromising some of the effects that nitrogen could have on the carbon as a catalyst.

Information about the limiting current density can also be obtained from the LSV curves. As previously observed for acti-

Table 2: Electrochemical results of the synthesized samples.

Sample	Onset potential (V vs RHE)	Limiting current density (mA cm^{-2})	Electrons exchanged at 0.4 V vs RHE	H$_2$O$_2$ production (%)
AG	0.78	4.08	2.3	18
AG$_{BM}$	0.79	3.15	2.0	21
N-AG$_{BM}$	0.79	3.37	2.9	9
N-AG$_C$	0.82	2.83	3.2	7
CG	0.64	1.74	1.8	–
CG$_{BM}$	0.64	1.53	2.3	–
N-CG$_{BM}$	0.67	2.15	2.1	–
N-CG$_C$	0.67	2.05	2.1	–

vated samples at different times, there is a direct relationship between microporosity and the limiting current density (Figure 3). This trend is also observed for sample group AG, AG$_{BM}$, CG and CG$_{BM}$ and for samples N-AG$_C$, N-AG$_{BM}$, CG$_C$ and N-CG$_{BM}$ (Figure 8).
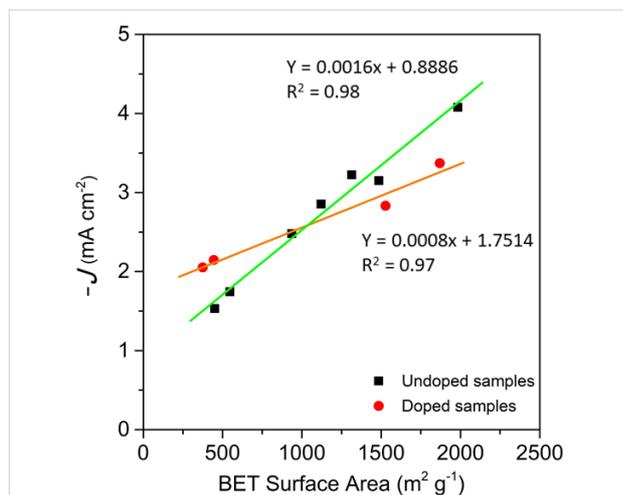

Figure 8: Relationship between BET surface area and limiting current density of undoped and doped samples.

These results indicate that the effect of microporosity cannot be compared between doped and undoped samples, suggesting that the limiting current density does not only depend on microporosity, but also on the surface chemistry of the samples.

Significant differences in the shape of the LSVs shown in Figure 7 are also observed due to the incorporation of nitrogen, which is related to the reaction mechanism. At lower potential, all activated samples present more than three electrons exchanged during the reduction reaction (Supporting Information File 1, Figure S12a). Regarding carbonized samples (Supporting Information File 1, Figure S12b), the number of electrons of CG and CG$_{BM}$ represents a two-pathway mechanism at all potentials applied, unlike for the AG electrocatalysts. The electron exchange in the AG sample is reduced to two as the potential increases. The same effect was registered for the AG$_{BM}$ sample that, even with a slightly inferior number of electrons exchanged at the lowest potential, the number of electrons also decreases to two as the potential applied increases. The incorporation of nitrogen atoms with the ball milling method (N-AG$_{BM}$) mitigated this effect, as the number of electrons exchanged during the oxygen reduction reaction stays at approximately three electrons, demonstrating that nitrogen incorporation helps to stabilize the number of electrons for a larger potential range. The conventionally doped sample (N-AG$_C$) shows the same pattern as the ball-milled doped sample, but its electron exchange stabilized slightly closer to the

four-electron mechanism, probably due to the higher catalytic performance of pyridinic nitrogen groups, which maintains the reaction mechanism closer to a four-electron pathway. On the other hand, the decrease of the quaternary-N/pyrrolic-N ratio (from 0.28 to 0.22 for N-AG$_{BM}$ and N-AG$_C$, respectively) resulted in an increase of the number of electrons involved, which is in agreement with recent studies [12]. Unlike in activated samples, the addition of nitrogen atoms through ball milling (N-CG$_{BM}$) does not result in an increase of electrons exchanged or in the stabilization of that number throughout the different applied potentials. This sample has a high quaternary-N/pyrrolic-N ratio (0.31), which does not favor the four-electron pathway.

Carbonized samples present a mechanism close to two-electrons throughout all potentials. Without a considerable number of electrons exchanged during the ORR, the nitrogen atoms do not seem to improve their stability to stay closer to a four-electron pathway. However, the conventionally doped sample (N-CG$_C$) displays a slight increase of electron exchange at low potentials, but still shifts to a two-electron pathway with increasing applied potential. The slight increase of the electrons may be related to the very low quaternary-N/pyrrolic-N ratio (0.13), which is reported to influence the number of electrons. The fact that the addition of nitrogen functionalities on carbonized samples does not seem to enhance the electroactivity as for activated samples indicates that it is fundamental to design both the surface chemistry and the textural proprieties of the carbon materials, as the modification of a single parameter is not enough to obtain acceptable electrocatalysts for ORR.

The approximation to a four-electron pathway with the modification of the surface chemistry is important to reduce the amount of hydrogen peroxide produced. The production of H$_2$O$_2$ was only determined for activated samples, since they have a mechanism closer to four-electron, whereas carbonized samples have a two-electron mechanism that would result in high amounts of this intermediate product. The improvement of the reaction mechanism of the modified activated carbon materials led to a decrease in the production of H$_2$O$_2$ from 18% with sample AG to 7% with N-AG$_C$ (Supporting Information File 1, Figure S13). These results show that the proper combination of high microporosity associated with high pyridinic-N/quaternary-N ratio and low quaternary-N/pyrrolic-N ratio is essential to enhance the electrochemical performance of the developed electrocatalysts.

Conclusion

In this study, the effect of microporosity of glucose-derived carbon materials on the catalytic activity towards ORR was demonstrated. The increase of microporosity led to an increase

of the limiting current density and a slight increase of the onset potential, thus playing a key role in the ORR. The incorporation of nitrogen functionalities by employing different doping methods was also investigated. The amount of nitrogen incorporated was similar for all methods. The ball milling doping method led to a higher content of quaternary nitrogen and to the formation of oxidized nitrogen, while conventional doping favored the incorporation of pyridinic and pyrrolic functionalities. The results obtained reveal that the content of nitrogen is not as important as the type of functional groups incorporated for improving the performance of carbon materials towards ORR. In fact, a relationship between the nitrogen functionalities and the electroactivity of the biomass-derived carbons has been determined. It has been observed that a higher pyridinic-N/quaternary-N ratio favors the onset potential, while a lower quaternary-N/pyrrolic-N ratio favors the number of electrons exchanged during ORR. However, these results are only significant for highly microporous materials, demonstrating that the adequate combination of textural and chemical properties is essential for improving the electroactivity of biomass-derived carbons. In fact, the combination between high surface area, high pyridinic-N/quaternary-N ratio and low quaternary-N/pyrrolic-N ratio resulted in a material with an onset potential value of 0.82 V, a stable number of electrons involved in the reaction mechanism close to four throughout the studied potential range and a production of H_2O_2 lower than 7%.

Experimental
Preparation of carbon materials
Carbon materials were prepared from an initial solution of glucose (HiMedia, >99%) and deionized water (produced by filtration through inverse osmose by a Panice device) in a 1:6 ratio. The solutions were mixed and then closed in a teflon-lined stainless steel autoclave and hydrothermally carbonized during 12 h at 180 °C. The obtained material was washed with deionized water and dried at 100 °C overnight. The dried material was then activated under a CO_2 flow of 80 cm^3 min^{-1} g^{-1} at 900 °C for 1, 3, 4 and 6 h. The samples were labelled AG$_X$, where X is the hours used for activation.

The sample activated for 6 h was also doped with nitrogen by using melamine (≥99%, Sigma-Aldrich) as a precursor. Two different approaches were studied: i) the activated carbon material was mixed with melamine by ball milling and ii) the activated carbon material was manually mixed with melamine, henceforth referred to as the conventional method. The ball milling process was performed in an enclosed flask with two zirconia balls at 15 Hz frequency during 4 h using a Retsch MM200 device. Regardless of the doping method all samples underwent a subsequent thermal treatment under a N_2 atmosphere for 2 h at 700 °C to force the decomposition of melamine

and to incorporate nitrogen atoms into the carbon structure. Additionally, a carbonized sample was prepared under a N_2 flow of 150 cm^3 min^{-1} at 700 °C for 2 h, to isolate the effect of functionalization with respect to the surface area. This sample also underwent the same two doping methods as the activated sample. All treatments were carried out in a vertical furnace with a fixed heating rate of 10 °C min^{-1}. The samples were labelled XG$_Y$ and N-XG$_Y$ for undoped and N-doped samples, respectively, where X can assume the form of A for activated samples and C for carbonized samples and Y is represented by BM for ball milled samples and C for conventionally doped samples. Activated and carbonized samples were also ball-milled in the absence of any precursor for comparison under the same conditions as in doped samples.

Materials characterization
The textural characterization was carried out by N_2 adsorption at −196 °C performed in a Quantachrome Autosorb iQ automated gas sorption analyzer. All samples were degassed under vacuum at 150 °C for 12 h before the analysis. The specific surface area (S_{BET}) was determined according to the Brunauer–Emmett–Teller (BET) equation, the total pore volume (V_p) was calculated as the volume of nitrogen adsorbed at the saturation point (relative pressure of 0.99) and the micropore volume (V_{DR}) was evaluated by the Dubinin–Radushkevich method.

The chemical composition of the samples was determined by elemental analysis. Carbon, hydrogen and nitrogen (C, H and N) were determined in a Vario micro cube analyzer (Elementar GmbH), by combustion of the sample at 1050 °C. The oxygen content was determined using a rapid oxy cube analyzer (Elementar GmbH) in which the sample underwent pyrolysis at 1450 °C. Each sample was analysed in triplicate. X-ray photoelectron spectroscopy (XPS) was employed to study the surface chemical composition of the samples. The analyses were carried out in a Kratos AXIS Ultra HAS spectrometer using monochromatic Al Kα radiation (1486.7 eV) at 15 kV (90 W), in fixed analyzer transmission mode, performing a pass energy of 80 eV for the general spectra and 40 eV for regions of interest. Temperature programmed desorption (TPD) was performed to determine and quantify the surface oxygenated groups of the samples by using an Altamira Instruments AMI-300 device. The samples were heated with a 10 °C min^{-1} ramp until 1050 °C. At the end of each analysis, a calibration of the CO and CO_2 content was carried out, allowing the quantification of the TPD profiles.

Electrochemical characterization
The electrochemical measurements were performed on a PGSTAT 302N potentiostat/galvanostat by using a three-elec-

trode cell configuration. Ag/AgCl (KCl 3 M) and a glassy carbon rod were used as reference and counter electrode, respectively. Working electrodes were prepared by depositing a suspension of the carbon samples on a glassy carbon rotating disk electrode (3 mm of diameter, Metrohm). These suspensions were prepared by dispersing 1 mg of the prepared samples in a solution containing 220 µL of ultrapure water (Millipore), 142 µL of ethanol (≥99%,Valente e Ribeiro) and 96 µL of nafion (5 wt %, Sigma-Aldrich). The suspension was sonicated for 30 min until a homogeneous dispersion was obtained. The mass loading of all samples was ≈0.1 mg cm^{-2}. A rotation speed controller allowed the rotation of the working electrode to be adjusted according to the assessments being done.

The experiments were carried out at room temperature in a 0.1 mol L^{-1} KOH solution saturated with N$_2$ or O$_2$ for 30 min before the cyclic voltammetry (CV) and linear sweep voltammetry (LSV) were performed. The CVs measurements were accomplished at a scan rate of 5, 20, 60 and 100 mV s^{-1} and the LSVs at a scan rate of 5 mV s^{-1} with a rotation speed range from 400 to 3000 rpm, both within a 1.2 V to −0.1 V potential range (vs RHE). The measured current was determined by subtracting the current obtained from the electrolyte saturated with N$_2$ from the current measured in the O$_2$-saturated electrolyte. Electrochemical impedance spectroscopy (EIS) was also applied to the fully discharged cell at 0 V in the frequency region of 10 kHz to 10 mHz with an AC amplitude of 10 mV. EIS was performed in the same type of cell, with N$_2$-saturated electrolyte (KOH 0.1 mol L^{-1}) and with no rotation.

The current density at the disk can be expressed by the Koutecký–Levich equation:

$$\frac{1}{j} = \frac{1}{j_{L}} + \frac{1}{j_{k}} = \frac{1}{B\omega^{1/2}} + \frac{1}{j_{k}}, \tag{1}$$

where j is the measured current density (mA·cm^{-2}), j_{L} is the O$_2$ diffusion-limited current density (mA cm^{-2}), j_{k} is the kinetic current density (mA cm^{-2}), ω is the electrode rotation rate (rpm) and B represents the Levich constant related to the diffusion limiting current density given by Equation 2.

$$B = 0.2nFD^{2/3}\nu^{-1/6}C \tag{2}$$

In Equation 2, F is the Faraday constant (96 486 C mol^{-1}), D is the diffusion coefficient of O$_2$ (1.95 × 10^{-5} cm^2 s^{-1}), ν is the kinematic viscosity of the electrolyte (0.008977 cm^2 s^{-1}) and C is the bulk concentration of O$_2$ (1.15 × 10^{-3} mol L^{-1}).

The number of electrons n was calculated at different potentials for each LSV recorded by applying Equation 1 and Equation 2.

The percentage of hydrogen peroxide (H$_2$O$_2$) produced during the ORR was also measured by using a rotating ring disk electrode (5 mm diameter, 24.9% collection efficiency, Methrom) as a working electrode, which was prepared by depositing a solution of the carbon sample on the disk area. The dispersions were prepared as detailed above and the mass loading was fixed at ≈0.1 mg cm^{-2}. The H$_2$O$_2$ percentage was calculated by Equation 3.

$$H_2O_2\,(\%) = 200 \times \frac{I_{R}\,/\,N}{I_{D} + I_{R}\,/\,N} \tag{3}$$

In Equation 3, I_{R} is the ring current density (mA cm^{-2}), I_{N} is the disk current density of the disk (mA cm^{-2}) and N is the collection efficiency (0.249).

Supporting Information

Supporting Information File 1
Characterization of the carbon materials, electrochemical assessments and relations resulting from this work.
[https://www.beilstein-journals.org/bjnano/content/supplementary/2190-4286-10-109-S1.pdf]

ORCID® iDs
Rafael Gomes Morais - https://orcid.org/0000-0001-9046-5933
Natalia Rey-Raap - https://orcid.org/0000-0002-5003-0035
José Luís Figueiredo - https://orcid.org/0000-0002-0395-8199
Manuel Fernando Ribeiro Pereira - https://orcid.org/0000-0002-5447-2471

References
1. Kirubakaran, A.; Jain, S.; Nema, R. K.
   Renewable Sustainable Energy Rev. **2009,** *13,* 2430–2440.
   doi:10.1016/j.rser.2009.04.004
2. Stacy, J.; Regmi, Y. N.; Leonard, B.; Fan, M.
   Renewable Sustainable Energy Rev. **2017,** *69,* 401–414.
   doi:10.1016/j.rser.2016.09.135
3. Figueiredo, J. L. *Surf. Coat. Technol.* **2018,** *350,* 307–312.
   doi:10.1016/j.surfcoat.2018.07.033
4. Wu, Z.; Song, M.; Wang, J.; Liu, X. *Catalysts* **2018,** *8,* 196.
   doi:10.3390/catal8050196

5. Lee, K.; Zhang, L.; Lui, H.; Hui, R.; Shi, Z.; Zhang, J. *Electrochim. Acta* **2009,** *54,* 4704–4711. doi:10.1016/j.electacta.2009.03.081

6. Kobayashi, M.; Niwa, H.; Saito, M.; Harada, Y.; Oshima, M.; Ofuchi, H.; Terakura, K.; Ikeda, T.; Koshigoe, Y.; Ozaki, J.-i.; Miyata, S. *Electrochim. Acta* **2012,** *74,* 254–259. doi:10.1016/j.electacta.2012.04.075

7. Luo, J.; Tian, X.; Zeng, J.; Li, Y.; Song, H.; Liao, S. *ACS Catal.* **2016,** *6,* 6165–6174. doi:10.1021/acscatal.6b01618

8. Rezaei, B.; Taghipour Jahromi, A. R.; Ensafi, A. A. *Electrochim. Acta* **2018,** *283,* 1359–1365. doi:10.1016/j.electacta.2018.07.105

9. Xue, Y.; Sun, S.; Wang, Q.; Dong, Z.; Liu, Z. *J. Mater. Chem. A* **2018,** *6,* 10595–10626. doi:10.1039/c7ta10569j

10. Borghei, M.; Lehtonen, J.; Liu, L.; Rojas, O. J. *Adv. Mater. (Weinheim, Ger.)* **2018,** *30,* 1703691. doi:10.1002/adma.201703691

11. Huang, H.; Wei, X.; Gao, S. *Electrochim. Acta* **2016,** *220,* 427–435. doi:10.1016/j.electacta.2016.10.108

12. Rocha, I. M.; Soares, O. S. G. P.; Fernandes, D. M.; Freire, C.; Figueiredo, J. L.; Pereira, M. F. R. *ChemistrySelect* **2016,** *1,* 2522–2530. doi:10.1002/slct.201600615

13. Rocha, I. M.; Soares, O. S. G. P.; Figueiredo, J. L.; Freire, C.; Pereira, M. F. R. *Catal. Sci. Technol.* **2017,** *7,* 1868–1879. doi:10.1039/c7cy00020k

14. Wang, C.; Yang, F.; Xu, C.; Cao, Y.; Zhong, H.; Li, Y. *Mater. Lett.* **2018,** *214,* 209–212. doi:10.1016/j.matlet.2017.11.120

15. Wohlgemuth, S.-A.; White, R. J.; Willinger, M.-G.; Titirici, M.-M.; Antonietti, M. *Green Chem.* **2012,** *14,* 1515–1523. doi:10.1039/c2gc35309a

16. Wu, J.; Yang, Z.; Sun, Q.; Li, X.; Strasser, P.; Yang, R. *Electrochim. Acta* **2014,** *127,* 53–60. doi:10.1016/j.electacta.2014.02.016

17. Yang, D.-S.; Bhattacharjya, D.; Inamdar, S.; Park, J.; Yu, J.-S. *J. Am. Chem. Soc.* **2012,** *134,* 16127–16130. doi:10.1021/ja306376s

18. Cheng, Y.; Tian, Y.; Fan, X.; Liu, J.; Yan, C. *Electrochim. Acta* **2014,** *143,* 291–296. doi:10.1016/j.electacta.2014.08.001

19. Yang, L.; Jiang, S.; Zhao, Y.; Zhu, L.; Chen, S.; Wang, X.; Wu, Q.; Ma, J.; Ma, Y.; Hu, Z. *Angew. Chem., Int. Ed.* **2011,** *50,* 7132–7135. doi:10.1002/anie.201101287

20. Lai, L.; Potts, J. R.; Zhan, D.; Wang, L.; Poh, C. K.; Tang, C.; Gong, H.; Shen, Z.; Lin, J.; Ruoff, R. S. *Energy Environ. Sci.* **2012,** *5,* 7936–7942. doi:10.1039/c2ee21802j

21. Wei, W.; Liang, H.; Parvez, K.; Zhuang, X.; Feng, X.; Müllen, K. *Angew. Chem.* **2014,** *126,* 1596–1600. doi:10.1002/ange.201307319

22. Wei, Q.; Tong, X.; Zhang, G.; Qiao, J.; Gong, Q.; Sun, S. *Catalysts* **2015,** *5,* 1574–1602. doi:10.3390/catal5031574

23. Zheng, J.; Guo, C.; Chen, C.; Fan, M.; Gong, J.; Zhang, Y.; Zhao, T.; Sun, Y.; Xu, X.; Li, M.; Wang, R.; Luo, Z.; Chen, C. *Electrochim. Acta* **2015,** *168,* 386–393. doi:10.1016/j.electacta.2015.03.173

24. Niwa, H.; Horiba, K.; Harada, Y.; Oshima, M.; Ikeda, T.; Terakura, K.; Ozaki, J.-i.; Miyata, S. *J. Power Sources* **2009,** *187,* 93–97. doi:10.1016/j.jpowsour.2008.10.064

25. Geng, D.; Chen, Y.; Chen, Y.; Li, Y.; Li, R.; Sun, X.; Ye, S.; Knights, S. *Energy Environ. Sci.* **2011,** *4,* 760–764. doi:10.1039/c0ee00326c

26. Rocha, R.; Soares, O.; Figueiredo, J.; Pereira, M. *C* **2016,** *2,* 17. doi:10.3390/c2030017

27. Lei, Z.; Li, Y.; Zhang, I.; Li, D.-W.; Karpuzov, D.; Long, Y.-T. *Electrocatalytic Oxidation of NADH on Graphene Oxide and Reduced Graphene Oxide Modified Screen-Printed Electrode;* 2011; Vol. 6, pp 819–829.

28. Tian, X.; Zhou, M.; Tan, C.; Li, M.; Liang, L.; Li, K.; Su, P. *Chem. Eng. J.* **2018,** *348,* 775–785. doi:10.1016/j.cej.2018.05.007

29. Li, R.; Shao, X.; Li, S.; Cheng, P.; Hu, Z.; Yuan, D. *Nanotechnology* **2016,** *27,* 505402. doi:10.1088/0957-4484/27/50/505402

30. Fang, J.; Fan, H.; Li, M.; Long, C. *J. Mater. Chem. A* **2015,** *3,* 13819–13826. doi:10.1039/c5ta02257f

31. Zhang, B.; Wen, Z.; Ci, S.; Mao, S.; Chen, J.; He, Z. *ACS Appl. Mater. Interfaces* **2014,** *6,* 7464–7470. doi:10.1021/am5008547

32. Li, X.; Fang, Y.; Zhao, S.; Wu, J.; Li, F.; Tian, M.; Long, X.; Jin, J.; Ma, J. *J. Mater. Chem. A* **2016,** *4,* 13133–13141. doi:10.1039/c6ta04187f

33. Ferrero, G. A.; Fuertes, A. B.; Sevilla, M.; Titirici, M.-M. *Carbon* **2016,** *106,* 179–187. doi:10.1016/j.carbon.2016.04.080

34. Jain, A.; Balasubramanian, R.; Srinivasan, M. P. *Chem. Eng. J.* **2016,** *283,* 789–805. doi:10.1016/j.cej.2015.08.014

35. Gu, D.; Ma, R.; Zhou, Y.; Wang, F.; Yan, K.; Liu, Q.; Wang, J. *ACS Sustainable Chem. Eng.* **2017,** *5,* 11105–11116. doi:10.1021/acssuschemeng.7b03046

36. Baskar, S.; Murugesan, C.; Barpanda, P. *ECS Trans.* **2017,** *80* (10), 425–430. doi:10.1149/08010.0425ecst

37. Gu, D.; Zhou, Y.; Ma, R.; Wang, F.; Liu, Q.; Wang, J. *Nano-Micro Lett.* **2018,** *10,* 29. doi:10.1007/s40820-017-0181-1

38. Liu, F.; Peng, H.; You, C.; Fu, Z.; Huang, P.; Song, H.; Liao, S. *Electrochim. Acta* **2014,** *138,* 353–359. doi:10.1016/j.electacta.2014.06.098

39. Borghei, M.; Lehtonen, J.; Liu, L.; Rojas, O. J. *Adv. Mater. (Weinheim, Ger.)* **2018,** *30,* 1703691. doi:10.1002/adma.201703691

40. Sibul, R.; Kibena-Põldsepp, E.; Ratso, S.; Kook, M.; Käärik, M.; Merisalu, M.; Paiste, P.; Leis, J.; Sammelselg, V.; Tammeveski, K. *Electrochem. Commun.* **2018,** *93,* 39–43. doi:10.1016/j.elecom.2018.05.027

41. Lefevre, M.; Jaouen, F.; Dodelet, J.-P.; Li, X. H.; Chen, K.; Hay, A. *ECS Trans.* **2006,** *3* (1), 201–210. doi:10.1149/1.2356138

42. Marsh, H.; Rodríguez-Reinoso, F. Activation Processes (Thermal or Physical). In *Activated Carbon;* March, H.; Rodríguez-Reinoso, F., Eds.; Elsevier Science Ltd: Oxford, United Kingdom, 2006; pp 243–321. doi:10.1016/b978-008044463-5/50019-4

43. Zhou, J.-H.; Sui, Z.-J.; Zhu, J.; Li, P.; Chen, D.; Dai, Y.-C.; Yuan, W.-K. *Carbon* **2007,** *45,* 785–796. doi:10.1016/j.carbon.2006.11.019

44. Figueiredo, J. L.; Pereira, M. F. R.; Freitas, M. M. A.; Órfão, J. J. M. *Carbon* **1999,** *37,* 1379–1389. doi:10.1016/s0008-6223(98)00333-9

45. Prauchner, M. J.; Rodríguez-Reinoso, F. *Microporous Mesoporous Mater.* **2012,** *152,* 163–171. doi:10.1016/j.micromeso.2011.11.040

46. Amorós-Pérez, A.; Cano-Casanova, L.; Ouzzine, M.; Rufete-Beneite, M.; Romero-Anaya, A. J.; Lillo-Ródenas, M. Á.; Linares-Solano, Á. *Materials* **2018,** *11,* 770. doi:10.3390/ma11050770

Porous N- and S-doped carbon–carbon composite electrodes by soft-templating for redox flow batteries

Maike Schnucklake[1], László Eifert[2], Jonathan Schneider[1], Roswitha Zeis[2,3] and Christina Roth[*1]

Abstract

Highly porous carbon–carbon composite electrodes for the implementation in redox flow battery systems have been synthesized by a novel soft-templating approach. A PAN-based carbon felt was embedded into a solution containing a phenolic resin, a nitrogen source (pyrrole-2-carboxaldehyde) and a sulfur source (2-thiophenecarboxaldehyde), as well as a triblock copolymer (Pluronic® F-127) acting as the structure-directing agent. By this strategy, highly porous carbon phase co-doped with nitrogen and sulfur was obtained inside the macroporous carbon felt. For the investigation of electrode structure and porosity X-ray photoelectron spectroscopy (XPS), scanning electron microscopy (SEM), and nitrogen sorption (BET) were used. The electrochemical performance of the carbon felts was evaluated by cyclic voltammetry (CV) and electrochemical impedance spectroscopy (EIS). The N- and S-doped carbon electrodes show promising activity for the positive side reaction and could be seen as a significant advance in the design of carbon felt electrodes for use in redox flow batteries.

Introduction

In recent years, vanadium redox flow batteries (VRFBs) have attracted significant attention as a promising large-scale system for storing excess energy from renewable sources like wind or solar energy [1-3]. The energy is stored in the form of vanadium containing electrolytes, which consist of $V^{2+/3+}$ at the negative and $V^{4+/5+}$ at the positive side. These are flowed through carbon materials, which are usually porous felts or carbon paper electrodes [4]. Carbon electrodes exhibit good stability and electrochemical conductivity in the acidic and corrosive electrochemical environment of the battery system. Moreover, they are comparatively inexpensive [5]. One disadvantage is their poor electrochemical activity, which makes an activation step necessary [6].

A common way to achieve higher activities is the thermal treatment of the commercial felts (400 °C, up to 30 h) [7]. Also acid

treatment [8], electrochemical activation [9], catalytic decoration with metal oxides [10,11], as well as methods to increase the surface area of the felts [12,13] have been reported as possible ways to obtain enhanced activity. Several works described heteroatom doping that should provide more active centres for the vanadium redox reactions, and hence lead to a higher electrochemical activity [14-17]. But still details of the mechanism are lacking and contradictory suggestions can be found in the literature, as to which functional group promotes the VO^{2+}/VO_2^+ redox reaction the most [18].

The application of templates is a commonly used strategy to introduce porosity into carbon materials. Depending on the utilized template one can distinguish between a hard-templating and a soft-templating approach [19]. In both cases, the template acts as a structure-directing agent forming an inverse copy of the template morphology. Much higher surface areas can be achieved through this procedure, which offers many benefits in the later application, for instance increased adsorption due to more active sites leading to a better electrocatalytic activity. A disadvantage of the hard-templating approach is the requirement of harsh conditions that are needed to remove, e.g., SiO_2 spheres used as templates [20]. In this respect, the soft-templating approach is a good alternative. The procedure is facile, with just two steps needed, and it is possible to scale-up the method to industrial standards [21]. In earlier studies we reported on a salt-templating method, where we embedded a PAN-based carbon felt into a eutectic mixture containing zinc chloride and sodium chloride mixed with an ionic liquid as the carbon source [22].

Herein, we present novel composite electrodes that were synthesized utilizing the soft-template method inspired by Martinez de Yuso et al. from 2017 [23]. With this method we are able to reduce the cost for the precursor materials significantly. We are able to use pyrrole-2-carboxyaldehyde, instead of ionic liquids, as nitrogen source. Also it is much more environmentally friendly, since zinc chloride is no longer needed and replaced by the structure-directing agent Pluronic® F-127. Pluronic is a self-assembly block copolymer, which has already been widely

used as template in the synthesis of porous carbons [24]. Strong interactions between phloroglucinol and the surfactant lead to the formation of hydrogen bonds to the polyethylene chains of the polymer. In this fashion the porogen initiates a porous structure. It will be removed during the subsequent carbonization step [25].

The new composite materials have great potential to serve as electrodes in the VRFB, since they combine the desired properties of the two components, namely good electron conductivity and high surface area. The carbon fibers as supporting material possess a high electron conductivity, while the amorphous carbon coating provides the catalytic functionality.

Results and Discussion

For the synthesis of nitrogen-doped carbon composite electrodes phloroglucinol was suggested as a carbon source whereas pyrrole-2-carboxaldehyde was utilized as a nitrogen source and the block copolymer Pluronic® F-127 was used as porogen. In the co-doping process additional 2-thiophenecarboxaldehyde was employed as a sulfur source. The carbon–carbon composite materials were synthesized by soaking the felts in a solution containing the aforementioned precursors. After thermopolymerization under air a subsequent carbonization step under protective atmosphere, in which the porogen is removed, was performed to obtain highly porous carbon electrodes co-doped with nitrogen and sulfur. But not all of the formed carbon coating sticks to the surface of the felt fibers, some excess co-doped carbon material exists besides. This additional material is referred to as "bulk material" in the following text (Figure 1).

Structural characterization

For a detailed insight into the morphology of the electrode, SEM images of the carbonized sample, N-doped carbon felt and S- and N-doped composite material were taken at two different magnifications (Figure 2).

The fibers of the pristine felt appear arbitrarily oriented with a smooth surface. In comparison to that, the N-doped composite

Figure 1: Schematic illustration of the synthesis route using the soft-templating approach to obtain porous carbon–carbon composite electrodes. The colours represent the changes of the appearance of the materials during the synthesis.
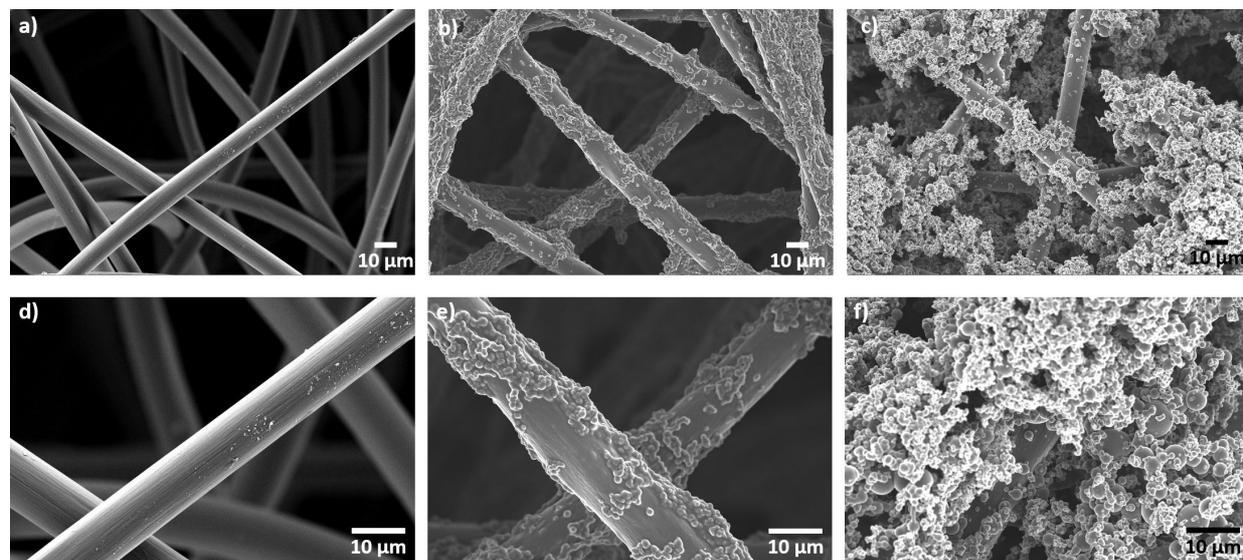
Figure 2: High-resolution images of carbonized carbon felt (left: a,d), N-doped carbon felt (middle: b,e) and S- and N-doped composite material (right: c,f) with 600× (upper row) and 1500× (bottom row) magnification.

material as well as the composite electrode co-doped with nitrogen and sulfur are decorated with patches of agglomerated carbon material. Significant differences in the amount of deposited material can be observed. While the fibers of the co-doped composite electrode are covered completely and the space between fibers is filled up almost completely, the N-doped felt exhibits only partial coverage. It seems as if the

carbon coating sticks more readily to the fibers after co-doping. But so far, we have not come up with a reasonable explanation for this observation.

Elemental mapping by scanning EDS was performed to investigate whether the co-doping was homogeneous and the results are shown in Figure 3.
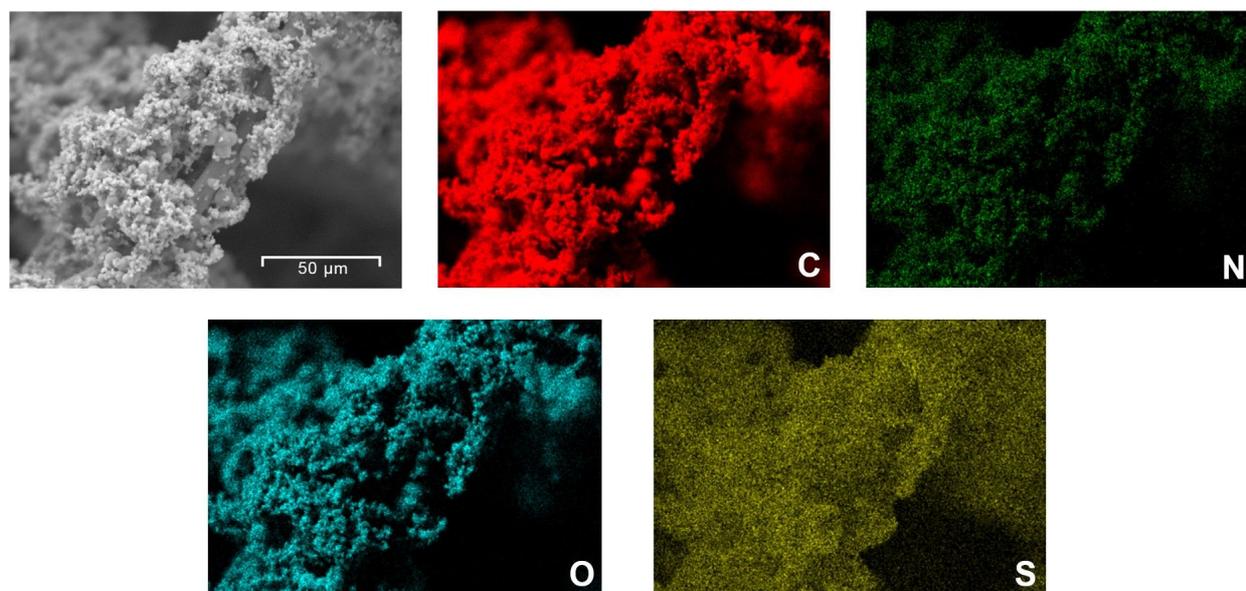
Figure 3: SEM image of the co-doped composite electrode and corresponding colored mappings of carbon, nitrogen, oxygen and sulfur.

The co-doped composite felt contains significant quantities of carbon, nitrogen, oxygen and sulfur. The EDX mappings verify the largely homogeneous distribution of all elements. Nitrogen doping as well as sulfur doping through the proposed soft-templating approach were successful.

BET measurements were carried out to analyze the porosity of the carbon felts. In Figure 4, a comparison between the nitrogen sorption isotherms of the carbonized felt and the N-doped composite electrode is shown. The curves appear distinctively different with a significant hump observed for the doped electrode. With the soft-templating approach it is possible to enhance the surface area of the felts by a factor of up to 20 times in comparison to the undoped felt. The respective BET surface areas are listed in Table 1. It is found that the surface area increases as a result of the doping procedure for all felts heated up to 1000 °C. The enhanced specific surface areas of the synthesized composite electrodes (BET data) in combination with the SEM/EDX mappings indicate the successful functionalization of the pristine felt.
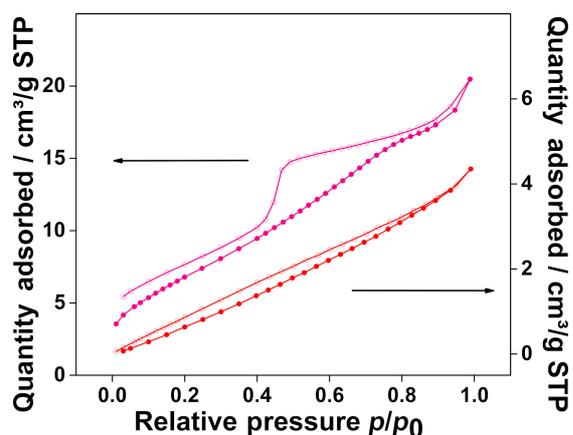
Table 1: BET surface areas of carbonized felt and composite electrodes heated up to 1000 °C.

	$S_{BET}/m^2 \cdot g^{-1}$
carbonized (1000)	6.6
composite (1000 / N)	30.6
composite (1000 / N+S)	130.6

To define the elemental composition of the different carbon felt electrodes and the related bulk materials an elemental analysis was performed, with specific focus on nitrogen and sulfur content. Table 2 summarizes the elemental composition of the different felts. In accordance with our expectations the main component is carbon, followed by nitrogen and sulfur. The felts lose material during the carbonization step, and a trend can be observed that with increasing temperature the remaining nitrogen content as well as the sulfur content become reduced. The composite electrodes, however, contain more nitrogen than the bulk material. Note that the additional nitrogen originates from the PAN fibers.

XPS measurements were carried out to further examine the surface functional groups of the composite materials in contrast to the reference material (Figure 5). In agreement with recent literature the peaks were fitted to the most probable functional groups.

In the C 1s spectrum of the carbonized felt (Figure 5a) five individual peaks could be deconvoluted. There is one dominant peak, which could be assigned to sp^3-hybridized carbon, while the other peaks at higher energy originate from different C–O bonding configurations. Also a small contribution could be allocated to sp^2-hybridized carbon. The C 1s spectrum changes when nitrogen and sulfur atoms are doped into the carbon material (Figure 5c) [26,27]. For the composite electrode an additional peak associated with a C–S functional group could be observed. This additional peak indicates the presence of sulfur on

Figure 4: Nitrogen sorption isotherms of the synthesized composite electrode with nitrogen doping (upper line) and the carbonized carbon felt (lower line).

Table 2: Elemental composition of the pristine and the carbonized felt as well as the composite electrode based on elemental analysis.

	C content/wt %	N content/wt %	S content/wt %	H content/wt %
pristine[a]	58.78	19.18	0.00	4.16
carbonized (800)	77.25	12.67	0.00	1.96
carbonized (1000)	91.77	5.92	0.00	0.04
composite (800 / N+S)	78.36	11.26	2.60	1.66
bulk material (800 / N+S)	84.85	6.37	4.33	1.46
composite (1000 / N+S)	85.59	4.26	2.23	1.18
bulk material (1000 / N+S)	88.95	2.90	2.34	1.28

[a]It is worth mentioning here that the pristine felt consists of only stabilized PAN fibers. The residual mass can be attributed to oxygen content or incomplete combustion of the samples.
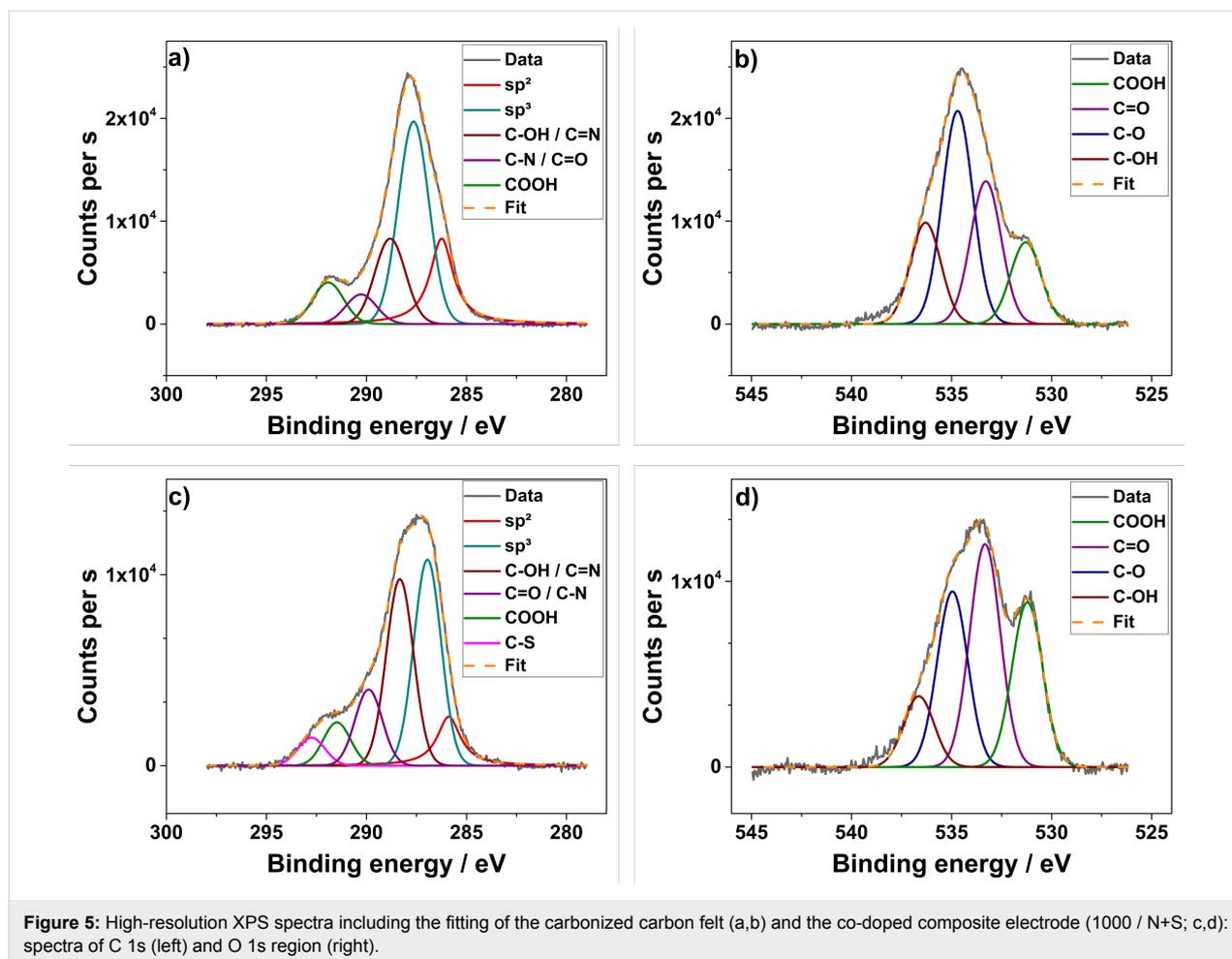
Figure 5: High-resolution XPS spectra including the fitting of the carbonized carbon felt (a,b) and the co-doped composite electrode (1000 / N+S; c,d): spectra of C 1s (left) and O 1s region (right).

the surface of the felt. Moreover, a change in the individual contributions could be noticed for the carbon felt co-doped with nitrogen and sulfur. It can be easily seen that the intensity of the sp^2-hybridized carbon peak is reduced in favor of the peaks attributed to the functional groups.

The high-resolution spectrum of the O 1s region shows four peaks for both materials. The carbonized sample (Figure 5b) has one main contribution with a binding energy at 534.7 eV, corresponding to the C–O functional group. Two additional peaks at 533.3 eV and 536.3 eV could be assigned to C=O and C–OH, while the shoulder peak at 531.3 eV could be attributed to COOH. These signals could also be detected in the O 1s spectra of the composite electrode. However, the intensities of the different contributions change significantly. In contrast to the carbonized sample the co-doped material shows a significant increase in C=O and COOH content, whereas the amount of C–OH is slightly reduced. In the literature, it is frequently found that an increase in the functional groups on the surface of the fibers increases their hydrophilicity and hence their electrochemical performance [28,29]. We refrained, however, from

quantitative analysis due to the inherent restrictions of fitting the rather broad C 1s and O 1s peaks with a multitude of individual contributions.

Electrochemical characterization

The electrocatalytic activity of the composite electrodes for the positive redox reaction VO^{2+}/VO_2^+ was investigated by CV (Table 3) and EIS. The CV curves of the respective carbon samples are shown in Figure 6 and the Nyquist plots are shown in Figure 7.

The pristine felt does not show any catalytic activity for the positive side reaction at all, whereas the carbonized samples exhibit at least poor activity. For the felt carbonized at 800 °C no complete oxidation peak was measured. All samples follow the trend that with increasing temperature an increase in activity is observed (see Figure 6a). In comparison to samples heated up to only 800 °C, the felt carbonized at 1000 °C shows a significant shift of the peak positions resulting in a lower peak separation. In the literature it is often proposed that enhanced electrochemical activity could be ascribed to the presence of abundant

Table 3: Electrochemical data of the VO^{2+}/VO_2^+ redox couple obtained from cyclic voltammograms.

	peak current/mA	peak position E_p/mV	peak separation ΔE_p/mV
carbonized (800)	—	—	—
	−6.0	597	
carbonized (1000)	10.9	982	228
	−6.1	754	
composite (800 / N)	8.2	1000	296
	−6.6	704	
composite (1000 / N)	9.9	906	116
	−7.8	790	
composite (800 / N+S)	8.7	1073	411
	−5.6	662	
composite (1000 / N+S)	14.2	929	149
	10.0	780	
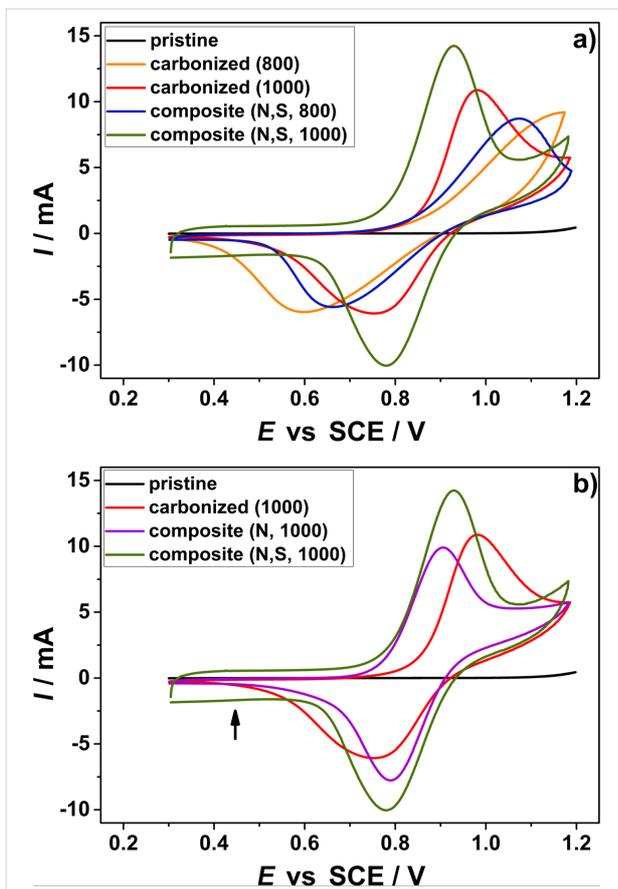
Figure 6: Comparison between the cyclic voltammetry curves of the N-doped (purple) and co-doped (blue, green) composite electrode as well as the carbonized (orange, red) and the pristine (black) felt for the positive half-cell reaction, (a) influence of the temperature used during the treatment and (b) influence of the doping method. The electrolyte consists of 2 M sulfuric acid and additional 0.2 mol/L vanadyl sulfate.

Figure 7: Nyquist plots showing the EIS data for the carbonized felts (orange, red) as well as for the composite electrodes heated up to 800 °C (pink, blue) and 1000 °C (purple, green) in the electrolyte solution. The data were fitted to the circuit model displayed in the graph and the simulated curves are shown as dashed lines. In the inset, the data range from 0 to 30 Ω is enlarged to show details of the N-doped composite electrode (pink, purple) and the co-doped sample (green).

composite material possesses an excellent electrochemical performance. It provides high maximum currents combined with a small peak separation, and the maximum currents appear symmetrical. These parameters indicate a good reversibility, which is beneficial for a reliable and stable cycling of the battery. It is worth mentioning here that the increased double layer capacitance (DLC) in the region between 0.3 and 0.6 V vs SCE is further evidence of an enhanced surface area (marked with an arrow in Figure 6b). This is in good agreement with the BET measurements (Table 1). Due to the enhanced surface area, the amount of vanadium ions that can be adsorbed onto the surface increases, resulting in higher currents compared to the only carbonized samples. The obtained data suggest that the kinetics regarding the VO^{2+}/VO_2^+ redox couple follow the order of

heteroatom-containing functional groups [17,29]. Similar behavior could be noted here, with heteroatoms into the carbon felt an increase in activity is observed. Especially, the co-doped

carbonized < composite (N-doped) < composite (co-doped with N and S). This means that the redox reaction of the vanadium ions proceeds more readily on the composite electrodes than on the undoped reference materials.

Additional electrochemical impedance spectroscopy was performed to study the charge transfer of the VO^{2+}/VO_2^+ redox reaction. The corresponding Nyquist plots are displayed in Figure 7. In the described circuit R_u stands for the solution resistance, which varies with the used electrode. The CPE is the constant-phase element which could be converted into the electric double-layer capacitance (C_{DL}), whereas R_{ct} represents the charge transfer resistance. Compared to the carbonized samples the diameters of the semicircles of the composite materials are significantly reduced, directly reflecting the reduced charge transfer resistances of these electrodes (Table 4). Obviously, the addition of a porous carbon layer decreases the charge transfer resistance, so that the electrochemical reaction can proceed faster. In accordance with the CV measurements, the co-doped electrode possesses the largest double-layer capacity of the electrode/electrolyte interface, which is beneficial for the charge transfer of the positive side reaction [30].

Table 4: Values for the charge transfer resistance and the double-layer capacity received by fitting the impedance data with corresponding circuit model in Figure 7 and converting the CPE parameters following Hirschorn and co-workers [31].

	R_{CT}/Ω	C_{DL}/mF
carbonized (800)	104.0	0.383
carbonized (1000)	93.38	0.143
composite (800 / N+S)	78.19	0.376
composite (1000 / N+S)	53.89	310.0

The combined results of CV and EIS allow for the conclusion that an increased amount of functional groups on the surface of the electrode as well as an increased surface area are favorable for the electrocatalytic activity of the co-doped soft templated carbon felt. Based on current knowledge it seems that the enhancement of the surface has the most significant influence on the performance, but details of this observation have to be analyzed in more detail in the future.

Conclusion

A new method was developed to synthesize carbon–carbon composite materials with an increased surface area and nitrogen and sulfur heteroatom content. These electrodes demonstrated promising activities for the positive half-cell reaction in the all-vanadium redox flow battery. Co-doping with nitrogen and sulfur can introduce a significant number of functional groups, which presumably increases the active sites for the VO^{2+}/VO_2^+

redox couple and therefore substantially contributes to the increase of the battery performance. With the soft-templating approach a porous carbon–carbon composite felt with a significantly enhanced surface area (up to 20 times) was obtained. In case of the co-doped material the electrochemical evaluation exhibited a higher double-layer capacity indicating a higher surface area in contact with the electrolyte. This method does not rely on expensive precursors and thus enables an environmentally friendly way to achieve porous carbon electrode materials without the utilization of zinc chloride or other hazardous substances.

Experimental
Materials
2-Thiophenecarboxaldehyde (98%), pyrrole-2-carboxaldehyde (98%), phloroglucinol (≥99.0%), Pluronic® F-127 and ethanol were purchased from MERCK. Hydrochloric acid (37%, Rotipuran®, p.a.) and ethanol (99.8%, p.a.) were purchased from Carl Roth®. All chemicals were used as obtained without any further purification. As a precursor material PAN-based carbon felts, which were received from Freudenberg Technology Innovation SE & Co. KG (Weinheim, Germany), were used.

Throughout this manuscript the untreated carbon felt is denoted as pristine. All further felts are abbreviated with the maximum temperature used during the carbonization step and the corresponding dopant.

Material synthesis
To produce a suitable reference material, the pristine carbon felt was carbonized at 800 and 1000 °C under inert atmosphere (N_2, 100%). The maximum temperature was held for 1 h before letting the furnace cool down.

To produce composite electrodes a soft-templating approach was utilized, following the synthesis route of Martinez de Yuso and co-workers [23]. Phloroglucinol (1,3,5-benzenetriol, $C_6H_6O_3$; 0.219 g) as carbon source and Pluronic® F-127 ((polyethylene oxide)-(polypropylene oxide)-(polyethylene oxide); 0.437 g) were dissolved in ethanol (40 mL), which was acidified before with HCl (0.3 mL, 37%). Then a solution of pyrrole-2-carboxaldehyde (0.166 g) in ethanol (5.5 mL) was added. In case of the co-doped carbon composite electrode 2-thiophenecarboxaldehyde (0.3 mL) as sulfur source was incorporated as well. The mixture was stirred for 1 min before the felts (size: 3.5 cm × 3.5 cm; average mass: 0.350 g) were soaked homogeneously with the combined solutions (20 mL per felt) in several petri dishes.

The solvent was let to evaporate at room temperature over 6–7 h, followed by thermopolymerisation in a furnace at 80 °C

for at least 13 h, but not more than 15 h. Afterwards the carbon felt was thoroughly separated from the bulk material, which was scraped carefully off the petri dish. For the purpose of carbonization both materials were heated in incinerating dishes up to maximum temperatures of 800 and 1000 °C under a constant flow of nitrogen and with a heating rate of 2.5 °C/min. The tube furnace was allowed to cool down to room temperature after the maximum temperature was kept for 1 h. The composite electrodes were obtained with different mechanical stabilities. In comparison to the flexible pristine felt they appear rigid. With respect to their application in RFB batteries this could be a positive asset as this feature might generate a better contact between electrode and bipolar plate and reduce electrical resistances. All felts were covered with a visible black glossy layer.

Structural characterizations

A scanning electron microscope (SmartSEM Supra 55VP, Carl Zeiss SMT Ltd.) with an acceleration voltage of 5–10 kV and an in-lens detector was utilized to obtain details of the surface structure. High-resolution images (Figure 2) were captured at several magnifications to investigate features at the microscale and the nanoscale. Energy-dispersive X-ray spectroscopy (EDX) analyses were performed with an X-Max 50 silicon drift detector (Oxford Instruments) at an acceleration voltage of 10 kV.

Nitrogen adsorption and desorption isotherms were recorded at 77 K using a high-resolution Micromeritics 3Flex instrument. Prior to the measurement the samples were degassed under vacuum at 120 °C for 4 h. The surface area was calculated according to the Brunauer–Emmett–Teller (BET) model.

Elemental analyses were accomplished using the VarioEL Organic Elemental Analyzer from Elementar Analysensysteme GmbH to determine the carbon, nitrogen, sulfur and hydrogen content. The average of the measured values was determined and listed in Table 2.

The elemental composition and the chemical state of the elements in the sample surfaces were determined by X-ray photoelectron spectroscopy (XPS) measurements (CLAM4 electron analyzer from Thermo VG scientific), using a Mg Kα source (1253.6 eV). For analysis, the peaks were fitted using Gaussian and Lorentzian functions with identical FWHM for each component of the same element after manual background subtraction [32].

Electrochemical characterization

All electrochemical measurements were carried out with a Reference 600 potentiostat from Gamry Instruments operating in a three-electrode setup. A saturated calomel electrode (SCE) was used as reference electrode (243 ± 2 mV vs SHE) and a platinum electrode consisting of a 1 mm thick platinum piece (0.6 cm × 0.7 cm) represented the counter electrode. The respective carbon felts served as working electrodes and were pierced in their center with a 1 mm thick glassy carbon rod for contacting. For studying the VO^{2+}/VO_2^+ redox reaction the electrolyte consisting of 100 mL of 0.2 mol/L vanadylsulfate ($VOSO_4$, Sigma-Aldrich) dissolved in 2.0 mol/L sulfuric acid (H_2SO_4, for analysis, 96%) was utilized from Acros Organics. Prior to each measurement the electrolyte was purged with nitrogen for at least 15 min to make sure that there was no remaining dissolved oxygen in the solution. The homogeneous wetting of the felts was ensured by dipping them into the electrolyte solution for at least 30 min before measuring the samples. CV curves were measured with a scan rate of 2 mV/s and the scan limits were set to 0.3 and 1.2 V. The potentiostatic EIS experiments were implemented in a frequency range from 10^5 to 10^{-1} Hz with an ac amplitude of 10 mV and a dc potential of 0.75 V vs SCE. The EIS data were fitted in the frequency range between 10^3 and 10^0 Hz. The value of the CPE was converted to C_{DL}.

ORCID® iDs

Maike Schnucklake - https://orcid.org/0000-0002-0493-1633
László Eifert - https://orcid.org/0000-0002-9583-0220
Jonathan Schneider - https://orcid.org/0000-0003-4654-7055
Roswitha Zeis - https://orcid.org/0000-0001-8379-0578
Christina Roth - https://orcid.org/0000-0003-1159-2956

References

1. Fabjan, C.; Garche, J.; Harrer, B.; Jörissen, L.; Kolbeck, C.; Philippi, F.; Tomazic, G.; Wagner, F. *Electrochim. Acta* **2001,** *47,* 825–831. doi:10.1016/s0013-4686(01)00763-0
2. Cunha, Á.; Martins, J.; Rodrigues, N.; Brito, F. P. *Int. J. Energy Res.* **2015,** *39,* 889–918. doi:10.1002/er.3260
3. Alotto, P.; Guarnieri, M.; Moro, F. *Renewable Sustainable Energy Rev.* **2014,** *29,* 325–335. doi:10.1016/j.rser.2013.08.001

4. Chakrabarti, M. H.; Brandon, N. P.; Hajimolana, S. A.; Tariq, F.; Yufit, V.; Hashim, M. A.; Hussain, M. A.; Low, C. T. J.; Aravind, P. V. *J. Power Sources* **2014,** *253,* 150–166. doi:10.1016/j.jpowsour.2013.12.038

5. Kear, G.; Shah, A. A.; Walsh, F. C. *Int. J. Energy Res.* **2012,** *36,* 1105–1120. doi:10.1002/er.1863

6. Eifert, L.; Banerjee, R.; Jusys, Z.; Zeis, R. *J. Electrochem. Soc.* **2018,** *165,* A2577–A2586. doi:10.1149/2.0531811jes

7. Sun, B.; Skyllas-Kazacos, M. *Electrochim. Acta* **1992,** *37,* 1253–1260. doi:10.1016/0013-4686(92)85064-r

8. Di Blasi, A.; Di Blasi, O.; Briguglio, N.; Aricò, A. S.; Sebastián, D.; Lázaro, M. J.; Monforte, G.; Antonucci, V. *J. Power Sources* **2013,** *227,* 15–23. doi:10.1016/j.jpowsour.2012.10.098

9. Zhang, W.; Xi, J.; Li, Z.; Zhou, H.; Liu, L.; Wu, Z.; Qiu, X. *Electrochim. Acta* **2013,** *89,* 429–435. doi:10.1016/j.electacta.2012.11.072

10. Schneider, J.; Bulczak, E.; El-Nagar, G. A.; Gebhard, M.; Kubella, P.; Schnucklake, M.; Fetyan, A.; Derr, I.; Roth, C. *Batteries* **2019,** *5,* 16. doi:10.3390/batteries5010016

11. Fetyan, A.; El-Nagar, G. A.; Derr, I.; Kubella, P.; Dau, H.; Roth, C. *Electrochim. Acta* **2018,** *268,* 59–65. doi:10.1016/j.electacta.2018.02.104

12. He, Z.; Liu, L.; Gao, C.; Zhou, Z.; Liang, X.; Lei, Y.; He, Z.; Liu, S. *RSC Adv.* **2013,** *3,* 19774–19777. doi:10.1039/c3ra22631j

13. Zhang, Z. H.; Zhao, T. S.; Bai, B. F.; Zeng, L.; Wei, L. *Electrochim. Acta* **2017,** *248,* 197–205. doi:10.1016/j.electacta.2017.07.129

14. Li, C.; Xie, B.; Chen, J.; He, J.; He, Z. *RSC Adv.* **2017,** *7,* 13184–13190. doi:10.1039/c6ra27734a

15. Flox, C.; Rubio-García, J.; Skoumal, M.; Andreu, T.; Morante, J. R. *Carbon* **2013,** *60,* 280–288. doi:10.1016/j.carbon.2013.04.038

16. Shi, L.; Liu, S.; He, Z.; Shen, J. *Electrochim. Acta* **2014,** *138,* 93–100. doi:10.1016/j.electacta.2014.06.099

17. Kiciński, W.; Szala, M.; Bystrzejewski, M. *Carbon* **2014,** *68,* 1–32. doi:10.1016/j.carbon.2013.11.004

18. Kim, J.; Lim, H.; Jyoung, J.-Y.; Lee, E.-S.; Yi, J. S.; Lee, D. *Electrochim. Acta* **2017,** *245,* 724–733. doi:10.1016/j.electacta.2017.06.008

19. Liang, C.; Li, Z.; Dai, S. *Angew. Chem., Int. Ed.* **2008,** *47,* 3696–3717. doi:10.1002/anie.200702046

20. Thomas, A.; Goettmann, F.; Antonietti, M. *Chem. Mater.* **2008,** *20,* 738–755. doi:10.1021/cm702126j

21. Chuenchom, L.; Kraehnert, R.; Smarsly, B. M. *Soft Matter* **2012,** *8,* 10801–10812. doi:10.1039/c2sm07448f

22. Schnucklake, M.; Kuecken, S.; Fetyan, A.; Schmidt, J.; Thomas, A.; Roth, C. *J. Mater. Chem. A* **2017,** *5,* 25193–25199. doi:10.1039/c7ta07759a

23. Martínez de Yuso, A.; De Fina, M.; Nita, C.; Fioux, P.; Parmentier, J.; Matei Ghimbeu, C. *Microporous Mesoporous Mater.* **2017,** *243,* 135–146. doi:10.1016/j.micromeso.2016.12.001

24. Liang, C.; Dai, S. *J. Am. Chem. Soc.* **2006,** *128,* 5316–5317. doi:10.1021/ja060242k

25. Tintula, K. K.; Sahu, A. K.; Shahid, A.; Pitchumani, S.; Sridhar, P.; Shukla, A. K. *J. Electrochem. Soc.* **2011,** *158,* B622–B631. doi:10.1149/1.3568004

26. Yang, Z.; Dai, Y.; Wang, S.; Cheng, H.; Yu, J. *RSC Adv.* **2015,** *5,* 78017–78025. doi:10.1039/c5ra15360c

27. El-Nagar, G. A.; Hassan, M. A.; Fetyan, A.; Kayarkatte, M. K.; Lauermann, I.; Roth, C. *Appl. Catal., B* **2017,** *214,* 137–147. doi:10.1016/j.apcatb.2017.05.030

28. Di Blasi, O.; Briguglio, N.; Busacca, C.; Ferraro, M.; Antonucci, V.; Di Blasi, A. *Appl. Energy* **2015,** *147,* 74–81. doi:10.1016/j.apenergy.2015.02.073

29. Li, W.; Liu, J.; Yan, C. *Electrochim. Acta* **2011,** *56,* 5290–5294. doi:10.1016/j.electacta.2011.02.083

30. Huang, Y.; Deng, Q.; Wu, X.; Wang, S. *Int. J. Hydrogen Energy* **2017,** *42,* 7177–7185. doi:10.1016/j.ijhydene.2016.04.004

31. Hirschorn, B.; Orazem, M. E.; Tribollet, B.; Vivier, V.; Frateur, I.; Musiani, M. *Electrochim. Acta* **2010,** *55,* 6218–6227. doi:10.1016/j.electacta.2009.10.065

32. Lauermann, I.; Steigert, A. *J. Large-Scale Res. Facil.* **2016,** *2,* A67. doi:10.17815/jlsrf-2-84

License and Terms

Playing with covalent triazine framework tiles for improved CO$_2$ adsorption properties and catalytic performance

Giulia Tuci[1], Andree Iemhoff[2], Housseinou Ba[3], Lapo Luconi[1], Andrea Rossin[1], Vasiliki Papaefthimiou[3], Regina Palkovits[2], Jens Artz[*2], Cuong Pham-Huu[*3] and Giuliano Giambastiani[*1,3,4]

Full Research Paper

Address:
[1]Institute of Chemistry of OrganoMetallic Compounds, ICCOM-CNR and Consorzio INSTM, Via Madonna del Piano 10-50019, Sesto F.no, Florence, Italy, [2]Institut für Technische und Makromolekulare Chemie RWTH Aachen University, Worringerweg 2, D-52074, Aachen, Germany, [3]Institut de Chimie et Procédés pour l'Energie l'Environnement et la Santé (ICPEES) UMR 7515 CNRS University of Strasbourg (UdS) 25 rue Becquerel 67087, Strasbourg Cedex 02, France and [4]Kazan Federal University, Kremlyovskaya Str. 18, 420008 Kazan, Russia

Email:
Jens Artz[*] - artz@itmc.rwth-aachen.de; Cuong Pham-Huu[*] - cuong.pham-huu@unistra.fr; Giuliano Giambastiani[*] - giambastiani@unistra.fr

* Corresponding author

Keywords:
covalent triazine frameworks; CO$_2$ adsorption; CO$_2$/N$_2$ selectivity; dehydrogenation catalysis; ionothermal conditions

Abstract

The rational design and synthesis of covalent triazine frameworks (CTFs) from defined dicyano-aryl building blocks or their binary mixtures is of fundamental importance for a judicious tuning of the chemico-physical and morphological properties of this class of porous organic polymers. In fact, their gas adsorption capacity and their performance in a variety of catalytic transformations can be modulated through an appropriate selection of the building blocks. In this contribution, a set of five CTFs (**CTF1–5**) have been prepared under classical ionothermal conditions from single dicyano-aryl or heteroaryl systems. The as-prepared samples are highly micro-mesoporous and thermally stable materials featuring high specific surface area (up to 1860 m^2·g^{-1}) and N content (up to 29.1 wt %). All these features make them highly attractive samples for carbon capture and sequestration (CCS) applications. Indeed, selected polymers from this series rank among the CTFs with the highest CO$_2$ uptake at ambient pressure reported so far in the literature (up to 5.23 and 3.83 mmol·g^{-1} at 273 and 298 K, respectively). Moreover, following our recent achievements in the field of steam- and oxygen-free dehydrogenation catalysis using CTFs as metal-free catalysts, the new samples with highest N contents have been scrutinized in the process to provide additional insights to their complex structure–activity relationship.

Introduction

Recent years have witnessed an increasing interest in carbon-based nanomaterials as functional devices for energy-related applications [1]. Their unique properties, such as their semiconducting behaviour, their inherent porosity, high specific surface area, chemical versatility, including their thermal and chemical resistance make them ideal candidates for a number of energy storage and conversion technologies [2,3]. The scope of carbon-based nanomaterials therefore covers a wide range of applications in (photo-/electro-)catalysis, gas storage and separation technologies as well as energy storage devices. Among nanocarbons, (nano)porous organic polymers (POPs) have gained a significant popularity because of their unique features [4-8]. Indeed, the use of a wide variety of rigid and sterically demanding organic building blocks to synthesize POPs allows for a fine control of their morphological and chemical properties [9-11]. Thus, POPs provide a permanent porosity (with high accessible specific surface area), combined with a facile chemical modification, e.g., the inclusion of heterocycles and light elements within the organic functional units.

Covalent triazine frameworks (CTFs) represent a POP subclass of highly crosslinked porous polymers, generated by the cyclotrimerization of dicyano-(hetero)aryl building blocks [12,13]. Under ionothermal conditions, in molten zinc chloride, the rational combination of dicyano-substituted organic moieties can be used to provide stable carbon nanomaterials with diverse morphologies (i.e., porosity and specific surface area) along with variable chemical composition (i.e., content and type of light elements such as N, S and O) [14,15]. Major application fields of CTFs are represented by energy storage and conversion [16-18], gas storage and separation (e.g., H_2, CO_2 and CH_4) [19-21] as well as various catalytic uses [22-30].

The exceptional performance of CTFs in capture and storage of CO_2 has prompted us to further exploit their potentiality in that direction through a judicious tuning of their ultimate structural and chemical properties. While the gas-storage capacity of a solid is mainly influenced by its porosity and accessible surface area [31,32], the Lewis basicity of its surface generates preferential interactions with Lewis acids such as CO_2 [33]. The rational selection of monomers featured by Lewis-basic sites, eventually combined with structural directing co-monomers can be used to tune the surface basicity and morphology of the materials and, consequently, optimize their gas-adsorption capacity. In addition, the control of the chemico-physical properties (i.e., pore-size distribution, specific surface area (SSA) and surface basicity) of the target samples is known to play a fundamental role in the control of their performance (activity and stability) as metal-free catalysts in gas-phase processes. Our recent achievements in the use of highly porous and N-rich car-

bon nanomaterials as metal-free catalysts for the steam- and oxygen-free dehydrogenation catalysis (DDH) of ethylbenzene (EB) to styrene (ST) have shown unique outcomes in terms of specific process rate (λ) and ST selectivity, even under operative conditions close to those of industrial plants [34]. Among these, CTFs have unambiguously exhibited superior activity and selectivity in the process [30] compared to carbon-based and metal-based state-of-the-art systems [35-44]. Most importantly, the rational balance between morphological and basic material surface properties has been claimed to control the catalyst stability on stream: the higher the "chemically accessible" surface basicity, the lower the sample deactivation/passivation due to the generation of coke deposits [30].

This contribution describes the synthesis and characterization of two model CTFs based on 1,4-dicyanobenzene (*p*-DCB) and 4,4′-dicyanobiphenyl (DCBP) and their comparative analysis in terms of chemico-physical properties with newly synthesized samples derived from 4,5-dicyanoimidazole (DCI) or its equimolar mixtures with the aforementioned dicyanoaryl units (see Scheme 1 below) [45]. The as-prepared samples have been investigated as CO_2 storage materials as well as metal-free catalysts for the gas-phase DDH of EB to ST. Notably, mixed CTF samples from this series have shown CO_2 adsorption capacities that rank among the highest reported so far in the literature. Furthermore, an ideal combination of material morphology and chemical composition has provided a sample that largely outperforms the classical benchmark carbon materials in terms of DDH catalytic performance (activity and ST selectivity) as well as stability on stream.

Results and Discussion
Synthesis and characterization of **CTF1–5**

CTF samples have been prepared under ionothermal conditions, using molten $ZnCl_2$ as reaction medium and Lewis acid cyanotrimerization catalyst [14]. As $ZnCl_2$ is supposed to act as a porogene, it was used in large excess with respect to the monomer ($ZnCl_2$/monomer = 5:1 molar ratio). After a sequential heating of the monomer/salt mixture at 400 °C and 600 °C for 10 + 10 h in sealed quartz ampules, CTFs have been isolated as amorphous and partially carbonized frameworks. The as-prepared samples feature high specific surface areas showing variable N loadings and N configurations as a function of the type of monomer(s) used. X-ray powder diffraction analyses have confirmed, as expected, the substantially amorphous nature [19,33] of all CTF samples from this series (Supporting Information File 1, Figure S1). Scheme 1 summarizes the different building blocks employed for the synthesis of CTFs in this work, while Table 1 lists all their main chemico-physical and morphological properties. Materials obtained from 1,4-

Scheme 1: Idealized ionothermal synthesis of **CTF1–5** from 1,4-dicyanobenzene (*p*-DCB, **I**), 4,4′-dicyanobiphenyl (DCBP, **II**), 4,5-dicyanoimidazole (DCI, **III**) as well as from their equimolar mixtures (*p*-DCB/DCI, **IV**, and DCBP/DCI, **V**).
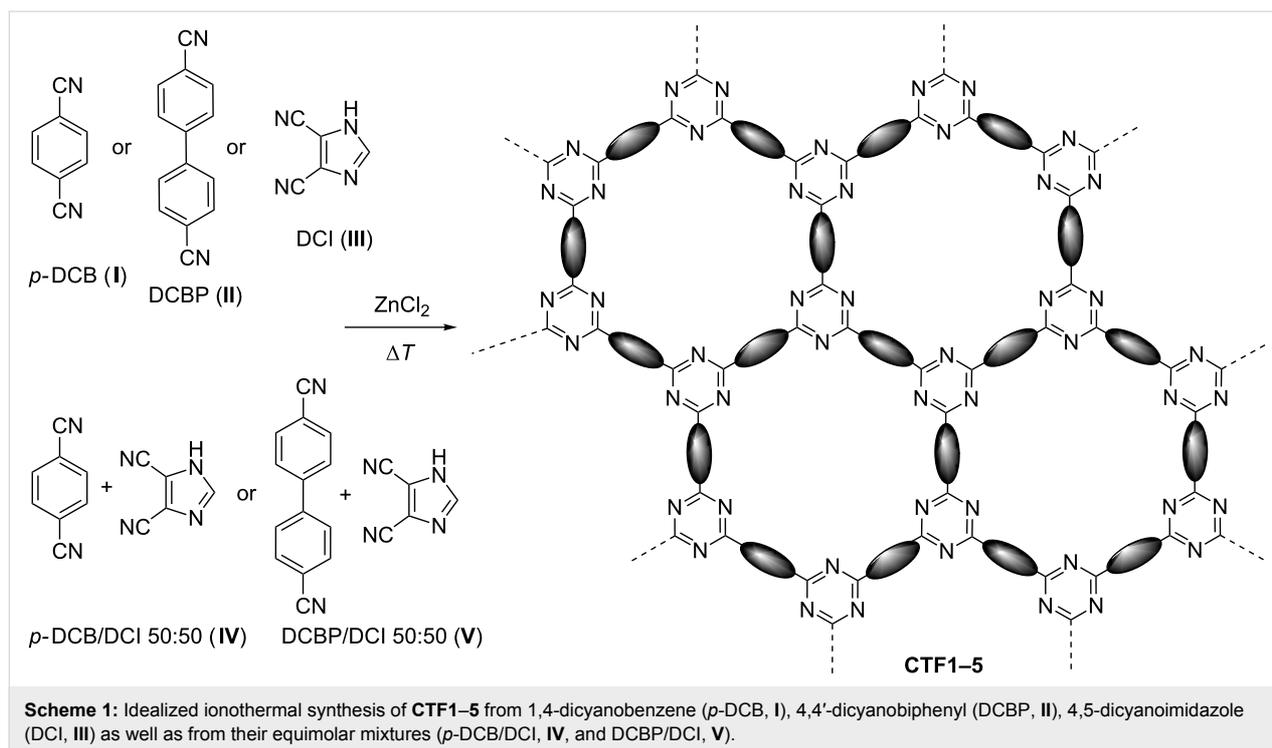
Table 1: Specific surface area, pore size distribution and N content (wt % loading and % of each N configuration) as measured for **CTF1–5**.

entry	sample	SSA^a $[m^2\ g^{-1}]$	$V_{p(total)}^b$ $[cm^3\ g^{-1}]$	$V_{p(micro)}^c$ $[cm^3\ g^{-1}]$	$V_{p(micro)}^c$ [%]	$N^{d,e}$ [wt %]	pyridinic N $\%^f$	pyrrolic N $\%^f$	oxidic N $\%^f$
1	**CTF1**	1654	1.06	0.42	40	7.5	39	51	10
2	CTF2	1863	1.31	0.33	25	3.6	42	50	8
3	CTF3	352	0.19	0.19	100	29.1	58	36	6
4	CTF4	784	0.41	0.30	73	18.1	51	42	7
5	CTF5	1489	0.80	0.44	55	11.4	43	46	11

^{a}Brunauer–Emmett–Teller (BET) specific surface area (SSA) measured at 77 K. ^{b}Total pore volume determined by using the adsorption branch of N_2 isotherm at $p/p_0 = 0.98$. ^{c}Micropore volume calculated by a NLDFT model. ^{d}Determined by elemental analysis as average values from three independent measurements. ^{e}Complete CHN elemental analyses of the five CTF samples are given in Supporting Information File 1, Table S1. ^{f}Determined by XPS analyses.

dicyanobenzene (*p*-DCB, **I**→**CTF1**) and 4,4`-dicyanobiphenyl (DCBP, **II**→**CTF2**) show isotherm profiles typical of bimodal micro-mesoporous materials with complex and ill-defined pore networks (see Supporting Information File 1, Figures S2A,A′ and S2B,B′). As found for related CTF samples previously synthesized by us under similar reaction conditions [30], **CTF2** presents a type-IV isotherm profile with a distinctive H2 hysteresis loop in the range of $p/p_0 = 0.4–0.6$. As expected from its longer linker, **CTF2** shows an increase of mesoporosity with respect to **CTF1** (mesopore volume from 60% to 75% of the total pore volume).

Both samples present a high and comparable specific surface area and a total pore volume up to 1.31 $cm^3 \cdot g^{-1}$ (Table 1,

entries 1 and 2). Although their structural properties sound promising for gas-adsorption applications, their N content remains moderate. As N content and related surface basicity play a key role in the CO_2 adsorption capacity of CTF samples, we have focussed on 4,5-dicyanoimidazole (DCI, **III**) as a novel and highly N-rich monomer to be used for CTF synthesis as such (**III**→**CTF3**), or in equimolar mixture with one of the two other building blocks (**IV**→**CTF4**; **V**→**CTF5**).

N_2 physisorption isotherms recorded on **CTF3–5** present classical type-I(b) profiles [46] that basically account for samples with a prevalent microporous structure (see Table 1, entries 3–5 and Supporting Information File 1, Figure S2C–E and Figure S2C′–E′). In spite of its purely microporous nature and moder-

ate SSA (352 m^2·g^{-1}), **CTF3** holds one of the highest N contents (29.1 wt %) reported so far in the literature for CTF prepared via ionothermal synthesis. Accordingly, the use of DCI monomer (**III**) in combination with **I** or **II** has been exploited to obtain materials that combine high specific surface area, high mesopore density and high N loading. For both mixed CTFs (**CTF4** and **CTF5**), monomer **III** has been used in equimolar amount with either **I** or **II**, while keeping the ZnCl$_2$/monomer(s) molar ratio constant at 5:1. Isotherms recorded on mixed CTFs (**CTF4,5**) account for materials with markedly higher gas-uptake capacities compared to **CTF3**. Indeed, the use of a co-monomer for **III** in the cyanotrimerization step is found to double or quadruple the specific surface areas and total pore volumes on the corresponding CTFs (Table 1, entry 3 vs entries 4 and 5). Moreover, **CTF4,5** show a N content that is much higher than that of materials prepared from pure monomers **I** and **II**. As expected, the greater the size of the *para*-dicyano aryl co-monomer, the greater the share of mesopores (%) and their size distribution in the target material. Indeed, **CTF5** (DCBP/DCI) holds a percentage of mesopores up to 18% higher than its counterpart **CTF4** (*p*-DCB/DCI) and mesopore sizes up to 40 Å (Table 1 and Supporting Information File 1, Figures S2D–E and D′–E′).

The N 1s XPS spectra recorded for all new CTF samples are fitted with two main components and a minor shoulder at binding energies (BE) between 398.5 ± 0.2, and 402.5 ± 0.5 eV. (see Supporting Information File 1, Figure S3A–E and Figure S4). While the former component at lower BEs is unambiguously ascribed to pyridinic N atoms from both triazine frameworks and the pyridinic N sites of the imidazole groups, peaks centred at 400.5 ± 0.2 are likely due to pyrrolic N species mostly deriving from a partial decomposition/rearrangement of the

samples during thermal treatment [30,47-49]. Minor shoulders at higher binding energies for all N 1s profiles are finally attributed to a certain extent of N–O species in the samples [50] (Table 1). Notably, all materials prepared from the DCI (**III**) monomer as such (**CTF3**) or in mixture with *p*-DCB (**I**) (**CTF4**) or DCBP (**II**) (**CTF5**) maintain a relatively high percentage of pyridinic nitrogen (Table 1 and Supporting Information File 1, Figure S3A–E). Such a result is reasonably ascribed to a higher thermal stability of the *ortho*-dicyano monomer **III** compared to the *para*-dicyano aryl systems **I** and **II** under the ionothermal conditions.

CO$_2$ adsorption properties of **CTF1–5**

The wide morphological and chemical diversity of the as-synthesized CTF samples prompted us to evaluate their CO$_2$ adsorption and separation capacities. To this aim, all materials were firstly activated under ultrahigh vacuum and CO$_2$ isotherms were recorded at T = 273 K and T = 298 K, in order to calculate the CO$_2$ heat of adsorption (Q_{st}). All these data are summarized in Table 2 and systematically compared with those reported in the literature for related CTF systems. As Figure 1 shows, neither purely microporous, although highly N-rich, samples (**CTF3**) nor mesoporous and N-poor solids (**CTF2**) were ideal candidates for the CO$_2$ capture and storage.

Among the prepared CTFs, **CTF1** and **CTF4** exhibit a CO$_2$ adsorption uptake at ambient pressure as high as 5.23 and 3.83 mmol·g^{-1} at 273 and 298 K, respectively. A comparative analysis with the current literature data (according to samples analyzed under similar pressure and temperature conditions, see Table 2) reveals that **CTF1** and **CTF4** rank among the samples with the highest CO$_2$ uptake capacity reported up to now in the literature both at T = 273 and 298 K. With the exception of the
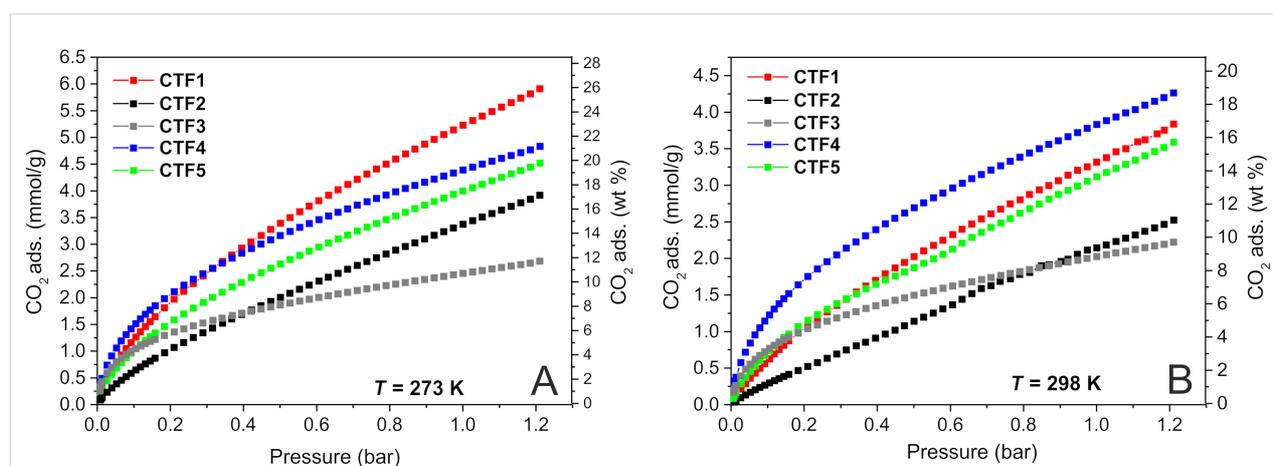

Figure 1: Low-pressure CO$_2$ isotherms for **CTF1** (red), **CTF2** (black), **CTF3** (grey), **CTF4** (blue) and **CTF5** (green) measured at A) T = 273 K and B) T = 298 K. CO$_2$ desorption curves are not reported in here for the sake of clarity. Complete adsorption–desorption isotherms are reported in Supporting Information File 1, Figure S5A,B.

Table 2: CO_2 adsorption uptake, isosteric heat of adsorption (Q_{st}) and CO_2/N_2 selectivity values measured for **CTF1–5** at comparison with the most representative CTF systems from the literature.

entry	sample	CO_2 uptake (mmol·g^{-1})				Q_{st} (kJ·mol^{-1})	CO_2/N_2 selectivity		ref.
		T = 273 K		T = 298 K					
		0.1 bar	1 bar	0.1 bar	1 bar		Henry	IAST	
1	**CTF1**	1.27	**5.23**	0.62	3.32	34.0	13	11	this work
2	**CTF2**	0.65	3.37	0.30	2.14	32.8	10	9	this work
3	**CTF3**	1.05	2.46	0.77	2.03	25.8	59	65	this work
4	**CTF4**	1.51	4.39	**1.23**	**3.83**	21.5	75	46	this work
5	**CTF5**	1.05	4.00	0.74	3.12	24.9	25	19	this work
6	CTF-ph	1.13	4.54	0.58	3.05	33.2	20	—	[30]
7	CTF-ph^{HT}	0.66	4.17	0.36	2.69	25.4	11	—	[30]
8	CTF-py	2.03	5.08	1.12	3.79	35.1	45	—	[30]
9	CTF-py^{HT}	1.04	5.97	0.61	4.22	27.1	29	—	[30]
10	*bipy*-CTF500	—	5.34	—	3.07	34.2	61	42	[33]
11	*bipy*-CTF600	—	5.58	—	2.95	34.4	37	24	[33]
12	*fl*-CTF350	—	4.28	—	2.29	32.7	27	23	[19]
13	F-CTF-1	1.76	4.67	0.92	3.21	35.0	—	31	[53]
14	F-CTF-1-600	1.40	5.53	0.68	3.41	32.0^b	—	19	[53]
15	HAT-CTF-450/600	3.0^a	6.3	2.0^a	4.8	27.1	126	110	[51]
16	caCTF-1-700	—	6.00	—	3.55	30.6	—	—	[59]
17	PHCTF-4	—	2.34	—	1.57	34.5^b	40	35	[54]
18	PHCTF-5	—	2.18	—	1.34	32.5^b	67	138	[54]
19	CTF-20-400	—	3.48	—	2.09	22	19	—	[60]
20	CTF-5-500	—	3.02	—	1.90	26	36	—	[60]
21	F-DCBP-CTF-1	2.15^a	5.98	1.19^a	3.82	33.1	—	31	[61]
22	bpim-CTF400	—	–	—	2.46	31	—	32	[55]
23	bpim-CTF500	—	–	—	2.77	28	—	24	[55]
24	CTF-CSU41	—	2.34	—	1.80^b	44.6	—	35.3	[56]
25	PHCTF-8(650)	1.30^a	4.00	—	2.54	28	56	89	[57]
26	CTF-BIB-1	—	4.35	—	—	35.2	—	29.3	[62]
27	acac-CTF-5-500	—	3.30	—	1.97	28.6	46	—	[58]
28	*df*-TzCTF600	2.17^a	6.79	—	4.60	34	21	30	[52]
29	CTF-TPC	—	4.24	—	2.69	32	20^c	30^c	[20]
30	MM2	—	4.70	—	3.13	32	23^c	44^c	[21]

^{a}Measured at 0.15 bar. ^{b}Estimated value from the low-pressure CO_2 isotherms in the original paper. ^{c}Calculated at 273 K.

CFT-py^{HT} sample [30] (featured by a markedly higher specific surface area of 3040 m^2·g^{-1}; Table 2, entry 9), the highly N/O co-doped HAT-CTF material [51] (1090 m^2·g^{-1}; Table 2, entry 15) and the perfluorinated *df*-TzCTF600 [52] (1720 m^2·g^{-1}; Table 2, entry 28), **CTF4** outperforms the CO_2 adsorption capacity of many benchmark systems from this class of porous organic polymers. With 1.23 mmol·g^{-1} and 3.83 mmol·g^{-1} of adsorbed CO_2 at room temperature and 0.1 bar and 1 bar pressure, respectively (Table 2, entry 4), **CTF4** surpasses the adsorption ability of samples such as bipy-CTFs (3.07–2.95 mmol·g^{-1}; Table 2, entries 10, 11) [33], F-CTF (3.21–3.41 mmol·g^{-1}; Table 2, entries 13, 14) [53], PHCTFs (1.57–1.34 mmol·g^{-1}; Table 2, entries 17, 18) [54], bpim-CTFs (2.46–2.77 mmol·g^{-1}; Table 2, entries 22, 23) [55] CTF-CSU41 (1.80 mmol·g^{-1}; Table 2, entry 24) [56], PHCTF-8(650)

(2.54 mmol·g^{-1}; Table 2, entry 25) [57] and acac-CTF-5-500 (1.97 mmol·g^{-1}; Table 2, entry 27) [58].

CTF1 presents the highest CO_2 adsorption capacity at 1 bar pressure among the samples of this series when analyses are carried out at the lower temperature (273 K). Under these conditions, the adsorption gap with related samples from the literature (Table 2, entry 1 vs entries 6–28) appears somewhat reduced. Anyhow, the relatively high SSA and N content of **CTF1** together with its micro-mesoporous morphology (see Table 1, entry 1) keep it among the samples with the highest CO_2 uptake values claimed so far for this class of materials.

To better specify the binding affinity between **CTF1–5** and CO_2, the isosteric heat of adsorption (Q_{st}) has been calculated

from the CO_2 isotherms recorded for each material at $T = 298$ and 273 K, using a variant of the Clausius–Clapeyron equation [63] (see Supporting Information File 1, Figure S6). Such a measurement strongly relies on the morphological and chemical properties of the material and it is generally claimed to reflect the interaction strength between CO_2 and the sorbent samples [30]. However, the Q_{st} values and the CO_2 adsorption capacity on porous samples do not always coherently correlate [64]. Indeed, the literature presents several examples of materials featuring very high Q_{st} values but only moderate CO_2 uptake [54,56]. The Q_{st} value of **CTF3** is relatively high because of its exceptionally high N content. However, its adsorption capacity is markedly reduced compared to **CTF1** and **CTF2** (Table 1, entry 3 vs entries 1 and 2) because of its markedly decreased pore volume (the total pore volume of **CTF3** is roughly reduced to one tenth compared to **CTF1** and **CTF2**). At odds with its high adsorption capacity (3.83 mmol·g^{-1}, $T = 298$ K, 1 bar of CO_2), the Q_{st} value of **CTF4** (21.5 kJ·mol^{-1}) is lower compared to its congeners. Similarly, the pore volume of **CTF5** is higher than that of **CTF4** while the N loading is smaller; this translates in comparable Q_{st} values for the two mixed samples (Table 2, entries 4 and 5). Overall, Q_{st} values measured for CTF samples from this series fall in the ideal range for CO_2 storage materials (<40 kJ·mol^{-1}) [52], which ensures lower regeneration cost compared to widely used amine solutions (>40 kJ·mol^{-1}) [65] for CCS targets.

Given the CO_2 affinity of the materials, and in view of their practical application as CO_2 adsorbents from gas mixtures, the competitive CO_2 uptake over N_2 has been determined for each sample using the ratio of the initial slopes in the Henry region of the adsorption isotherms (CO_2 and N_2) at $T = 298$ K (see Supporting Information File 1, Figure S7). The resulting values (listed in Table 2) generally come from the combination of two distinct material features: (i) adsorption selectivity and (ii) uptake capacity [52]. Accordingly, the values range from moderate (**CTF1**,**2** and **CTF5**) to relatively high in the case of **CTF3** and **CTF4**. For the sake of completeness, the selective CO_2 capture from CO_2/N_2 mixtures was additionally calculated using the simplified ideal adsorbed solution theory (IAST) model [66]. Accordingly, ideal selectivity values of CO_2 over N_2 were calculated (Table 2) at an equilibrium partial pressure of 85% N_2 and 15% CO_2 in the bulk phase by combining the experimental single-component isotherms. Among the CTFs of this study, the DCI derivative (**CTF3**) gives an ideal selectivity value of 65 that is the highest calculated for this material series. This result is in line with the pure microporous nature of the sample whose channels match better with the CO_2 dimensions providing a higher kinetic selectivity for CO_2 separation from CO_2/N_2 mixtures [56].
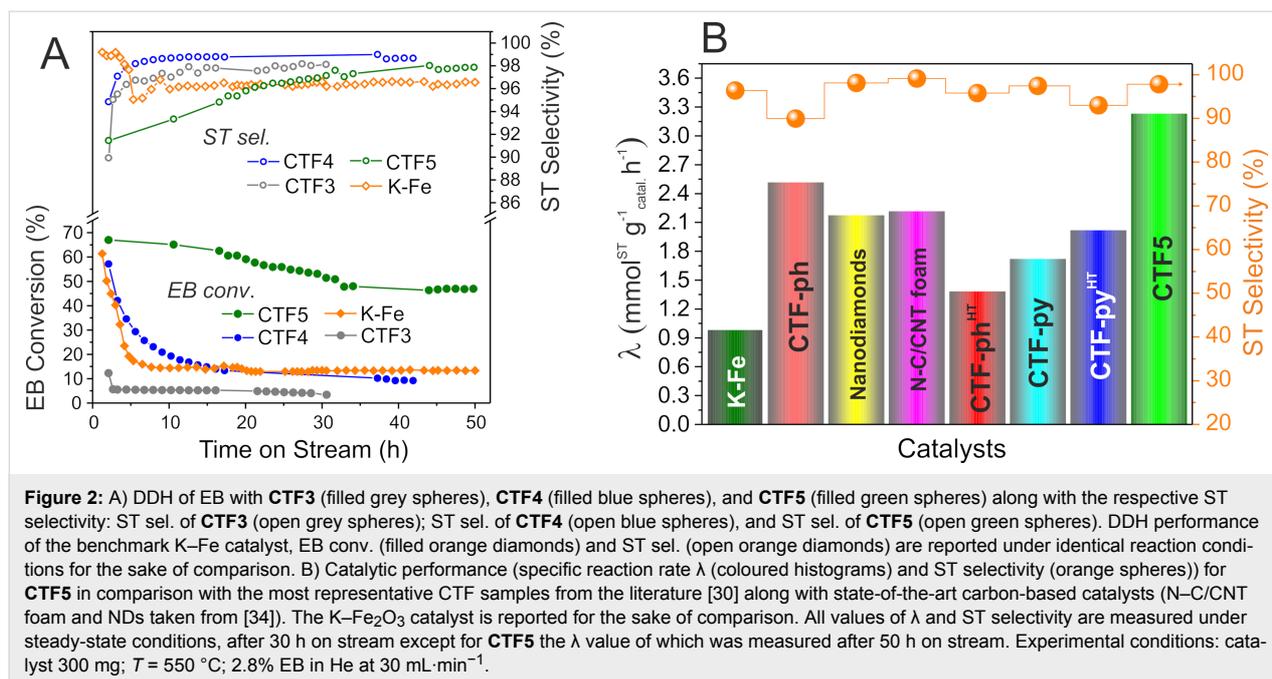
CTF1–5 as metal-free catalysts

From the viewpoint of sustainable technologies, the heterogeneous catalysis with complex carbon networks as metal-free systems, including carbon matrices hetero-doped with light elements, has received a great deal of interest from several research groups operating in the area of industrially relevant transformations. CTFs have been recently reported by some of us as highly stable and effective heterogeneous systems for promoting a challenging transformation such as the steam- and oxygen-free dehydrogenation (DDH) of ethylbenzene (EB) to styrene (ST) [30]. We demonstrated how the unique DDH performance of selected CTFs was the result of a compromise between morphological and accessible basic surface properties of the samples. In particular, the higher the chemically accessible basic surface of the catalytic materials, the higher their stability (as catalysts) on stream. Indeed, from the comparative analysis of CTFs featuring different chemical and morphological properties, we postulated the existence of a close relationship between the rate of cracking side reactions leading to catalyst deactivation (formation of coke deposits) and the kinetic desorption of reagents and products from the catalyst surface. The higher the basic surface properties of the CTF, the higher the desorption rate of reagents and products and the higher the catalyst lifetime on stream. This evidence is in line with other findings from the literature where basic properties of the material are crucial in preventing the occurrence of side cracking reactions of EB [34,35,37,38,67-70].

With a view to the N loading and N configuration of the newly synthesized samples, **CTF3**–**5** offer a variety of morphological properties (from purely microporous to micro-mesoporous samples) along with high charges of nitrogen (up to 29.1 wt %) and, in particular, basic N sites (N$_{Py}$) (from 43 to 58%) (Table 1, entries 3–5). Hence, the three CTF samples have been scrutinized for the DDH of EB to ST and their performance, in terms of EB conversion (filled circles) and ST selectivity (empty circles), are outlined in Figure 2 and compared to the industrially used K–Fe catalyst under identical conditions (550 °C, 2.8 vol % EB diluted in He, total flow rate: 30 mL/min).

CTF5 outperformed the other two metal-free systems as well as the benchmark K–Fe catalyst under steady-state conditions. Despite its remarkably high N content, **CTF3** shows a very moderate performance on stream with an EB conversion that roughly lies around 5% and a ST selectivity close to 98%. Such a result is likely ascribed to its purely microporous nature that largely prevents the regular EB uptake to the bulk active sites for the process to occur.

CTFs featuring larger mesopore domains (Table 1, entry 3 vs entries 4 and 5), albeit providing a lower number of N sites

Figure 2: A) DDH of EB with **CTF3** (filled grey spheres), **CTF4** (filled blue spheres), and **CTF5** (filled green spheres) along with the respective ST selectivity: ST sel. of **CTF3** (open grey spheres); ST sel. of **CTF4** (open blue spheres), and ST sel. of **CTF5** (open green spheres). DDH performance of the benchmark K–Fe catalyst, EB conv. (filled orange diamonds) and ST sel. (open orange diamonds) are reported under identical reaction conditions for the sake of comparison. B) Catalytic performance (specific reaction rate λ (coloured histograms) and ST selectivity (orange spheres)) for **CTF5** in comparison with the most representative CTF samples from the literature [30] along with state-of-the-art carbon-based catalysts (N–C/CNT foam and NDs taken from [34]). The K–Fe$_2$O$_3$ catalyst is reported for the sake of comparison. All values of λ and ST selectivity are measured under steady-state conditions, after 30 h on stream except for **CTF5** the λ value of which was measured after 50 h on stream. Experimental conditions: catalyst 300 mg; *T* = 550 °C; 2.8% EB in He at 30 mL·min^{-1}.

(**CTF4** and **CTF5**), show good to excellent catalyst performance. **CTF4** performs similarly to K–Fe in terms of EB conversion, showing a largely superimposable profile to that of the benchmark system under identical conditions. Despite a higher ST selectivity compared to its metallic counterpart (98.5 vs 96.4% after 40 h on stream), **CTF4** shows a rapid deactivation already within the first hours on stream that progressively continues (although more slowly) after 20 h on stream, thus revealing its rather moderate stability. Such a moderate EB conversion (at the steady-state) and rapid catalyst deactivation on stream is ascribed to pore clogging caused by the formation of coke deposits that progressively reduces the access of EB to the active sites. With an increased volume of the mesoporous component (Table 1, entry 5 vs entry 4) and a relatively high N content (up to 11.4 wt %), **CTF5** largely outperforms all CTFs from this series and exhibits a catalytic performance that is the highest reported so far for a metal-free catalyst in DDH under steam- and O$_2$-free conditions. The absence of a marked deactivation of this sample in the first hours on stream is distinctive for an open-cell pore structure where the chemically accessible basic character of the material (due to the presence of a relatively high fraction of basic N sites) is supposed to reduce the occurrence of side processes responsible for the progressive catalyst passivation on stream. The catalyst stabilizes in the first 30 h on stream during which EB conversion gradually decreases (although it always remains over 50%) and then floats almost constantly around (43 ± 0.5)% for the remaining time (till 50 h). ST selectivity gradually increases to approximately 98% after 50 h on stream. Under these conditions, the measured specific reaction rate (λ), expressed as the amount of ST obtained

per gram of catalyst per hour at the steady state is 3.24 (mmolST·g^{-1}$_{Catal}$·h^{-1}). Such a value certainly ranks among the highest rates claimed so far for CTFs as well as for various metal-free C-networks applied to the process (Figure 2B). The λ value measured for **CTF5** is even higher than that recorded for selected classes of mesoporous carbon nanomaterials, i.e., nanodiamonds (NDs) [39,40] and 3D foams (N–C/CNT) [34], that are commonly quoted as benchmark metal-free systems for DDH. Finally, temperature-programmed oxidation (TPO) analyses have been conducted on the fresh and spent CTF samples used in long-term catalytic DDH runs. As Supporting Information File 1, Figure S8 shows, the TPO profiles of **CTF5** before and after catalysis (see Figure 2A, after 50 h on stream and Figure S8B, Supporting Information File 1) are largely superimposable with a slight increase of the low-temperature component only. On the other hand, the TPO profile of the spent **CTF4** presents (see Figure 2A, after 40 h on stream and Figure S8A, Supporting Information File 1) an evident peak enlargement due to a non-negligible formation of low-temperature carbon deposits (coke). These results mirror the different catalytic behaviour of the two CTF systems at work in DDH and highlight the higher stability of the highly basic and open-cell-structured **CTF5** sample under operative conditions.

Conclusion

The rational combination of highly N-rich building blocks for the bottom-up synthesis of highly porous organic polymers with improved CO$_2$ adsorption properties has prompted us to explore the generation of mixed covalent triazine frameworks. The ionothermal synthesis of mixed CTFs from equimolar mixtures

of 4,5-dicyanoimidazole (DCI, **III**) and 1,4-dicyanobenzene (*p*-DCB, **I**) or 4,4′-dicyanobiphenyl (DCBP, **II**), has provided amorphous polymers with variable (from moderate to high) specific surface areas and bimodal micro-mesoporous morphologies. In particular, the greater the size of the *para*-dicyano aryl co-monomer (**I** or **II**), the greater the mesopore component (%) in the target mixed material. The use of a co-monomer for **III** in the cyanotrimerization step doubles or quadruples the specific surface area and total pore volume of the resulting mixed-CTF samples compared to the material prepared from the unique monomer **III**. In addition, mixed CTFs exhibit a higher N loading than the samples obtained from the pure monomers **I** and **II**. With 1.23 mmol·g^{-1} and 3.83 mmol·g^{-1} of adsorbed CO_2 at room temperature and 0.1 bar and 1 bar pressure, respectively, **CTF4** ranks among the benchmark systems for this class of materials. In addition, the mesoporous nature of the N-rich mixed sample **CTF5** has been found to fulfil ideally the key morphological and chemical requirements for a highly robust and active catalyst for the dehydrogenation of ethylbenzene to styrene. **CTF5** has shown excellent performance as a metal-free catalyst in the process, working under steam-and O_2-free conditions. With a specific reaction rate, λ, of 3.24 (mmolST·g^{-1}$_{Catal}$·h^{-1}) under steady-state conditions and with a markedly high stability on stream, **CTF5** outperforms materials from the same sample series as well as various doped and undoped C-networks reported so far as metal-free catalysts in the same process.

Experimental
Materials and methods

Synthesis of CTF1–5. CTF materials have been synthesized via ionothermal synthesis in quartz glass ampules according to literature procedures [22]. In a general procedure, **CTF1–3** were prepared as follows: 3 g of the selected monomer (**I**, **II** or **III**) were thoroughly mixed and finely ground with 5 equiv of $ZnCl_2$ within a glovebox and transferred into a quartz ampule (12 cm height and 3 cm diameter). After drying the material under vacuum for at least 3 h, the ampule was flame-sealed, placed inside a furnace and heated up to 400 °C with a heat rate of 10 °C·min^{-1}. Afterwards, it was kept at 400 °C for 10 h before raising the temperature to 600 °C (second heating phase) and keeping the sample at that temperature for further 10 h. After cooling to room temperature, the ampules were opened (**caution:** after high-temperature treatment the ampules are under pressure, which is released during opening) and the monolithic solids were ground and thoroughly washed with water and diluted HCl (0.1 M). Finally, the solids were finely ground using a laboratory ball mill (Fritsch Pulverisette 23, 5 min, 30 Hz) to get black powders, which are carefully washed in sequence with water, diluted HCl, diluted NaOH, water and THF. At the end of each work-up, materials were

dried under vacuum to constant weight (at least 12 h at 60 °C). Mixed CTFs (**CTF4,5**) were obtained following an identical procedure except for the use of a 50:50 molar ratio of the two starting monomers (DCI (**III**)/*p*-DCB (**I**) or DCI (**III**)/ DCBP(**II**)) while keeping constant the 1:5 molar ratio between monomer(s) and $ZnCl_2$ [21,71]. All materials (**CTF1–5**) were isolated in nearly quantitative yield (≥90% after work-up). To prevent bursting within the furnace, ampules were charged to a maximum of half of their volume.

Elemental analyses were performed using a Thermo FlashEA 1112 Series CHNS-O elemental analyzer and elemental average values for each sample were calculated over three independent runs.

X-ray photoelectron spectroscopy (XPS) measurements were performed in an ultrahigh vacuum (UHV) Thermo-VG scientific spectrometer equipped with a CLAM4 (MCD) hemispherical electron analyser. The Al Kα line (1486.6 eV) of a dual anode X-ray source was used as incident radiation. Survey and high-resolution spectra were recorded in constant pass energy mode (100 and 20 eV, respectively). Elemental semi-quantitative atomic percentages were calculated by fitting the spectra with mixed Gaussian–Lorentzian peaks applying tabulated sensitivity factors.

Temperature-programmed oxidation (TPO-MS) analyses were carried out on a Hiden Analytical CATLAB instrument coupled with a quadrupole mass spectrometer (detection limit = 2×10^{-14} Torr). In a typical analysis, 5–8 mg of CTF were charged in the sample holder and flushed at room temperature for 30 min under a stream of 10% O_2 in Ar (flow rate: 25 mL/min). Afterwards, the temperature was raised up to 900 °C at a heating rate of 10 °C/min and the evolved volatile species (m/z 2 (H_2), 18 (H_2O), 28 (CO) and 44 (CO_2)) were monitored through a mass spectrometer connected at the furnace outlet.

X-ray powder diffraction (PXRD) qualitative measurements were carried out with a Panalytical X'PERT PRO powder diffractometer equipped with a mirror on the incident beam, a beam knife and a PIXcel$^{©}$ solid state detector in the 4–60° 2θ region, operating with Cu Kα radiation (λ = 1.5418 Å). Anti-scatter slits were used both on the incident (0.25° and 0.5° divergence) and the diffracted (7.5 mm height) beam.

Gas adsorption measurements. In a similar manner as described before [22], nitrogen physisorption experiments were conducted on a Micromeritics ASAP 2010 instrument. Samples were degassed for at least 15 h at 150 °C using a FloVacDegasser. Static volumetric measurements were carried out at

77 K. The empty volume of the cell was determined with helium. The specific surface area (SSA) for each sample was determined by the Brunauer–Emmet–Teller method (BET) using data points at a relative pressure p/p_0 between 0.05 and 0.3. The total pore volume was determined at a relative pressure of 0.98. The pore size distribution was calculated via Micro-Active (version 1.01) using the density functional theory (DFT) N_2 model for slit geometry at optimal goodness of fit vs regularization (0.01) values for both RMS error of fit and roughness of distribution. The cumulative pore volume at the pore width of 2 nm was used to determine the micropore volume of the samples.

Low pressure adsorption isotherms were recorded on an ASAP 2020 Micromeritics instrument after activation of CTF samples at 200 °C for 12 h. CO_2 adsorption isotherms were recorded at 273 K and 298 K up to 1.2 bar, while N_2 adsorption isotherms for the determination of the CO_2/N_2 selectivity were measured at 298 K up to 1.2 bar.

The isosteric heat of adsorption (Q_{st}) was calculated from the measured CO_2 isotherms at 273 and 298 K using a variant of the Clausius–Clapeyron equation (Equation 1) [51,63]:

$$\ln\left(\frac{P_1}{P_2}\right) = Q_{st} \times \frac{T_2 - T_1}{R \times T_1 \times T_2} \qquad (1)$$

where P_n ($n = 1$ or 2) is the pressure value for isotherm n; T_n ($n = 1$ or 2) is the temperature value for isotherm n; R is the gas constant, $R = 8.314$ J·K^{-1}·mol^{-1}. CO_2/N_2 selectivity was calculated on the basis of the Henry model, taking into account the initial slopes of the adsorption isotherms (Supporting Information File 1, Figure S7). The IAST selectivity for a 15:85 CO_2/N_2 mixture at a total pressure of 1 bar was determined from Equation 2:

$$S_{CO_2/N_2} = \frac{\left[\chi_{CO_2}/\chi_{N_2}\right]_{ads}}{\left[\chi_{CO_2}/\chi_{N_2}\right]_{mix}} \qquad (2)$$

where $(\chi_i)_{ads}$ represent the adsorbed molar fractions of the two gases [72] as derived from the application of the free python software pyIAST (https://github.com/CorySimon/pyIAST) to the experimental N_2 and CO_2 isotherms of **CTF1–5** collected at 298 K, while $(\chi_i)_{mix}$ are the molar fractions of the two gases in the starting mixture (0.85 and 0.15 for N_2 and CO_2, respectively). A BET (CO_2) and a Henry (N_2) model were employed for the isotherms fitting. For a detailed explanation of these methods, see the pyIAST webpage and documentation.

Catalytic oxygen- and steam-free direct dehydrogenation of ethylbenzene to styrene

The catalytic reaction was carried out in a fixed-bed continuous flow reactor under atmospheric pressure. 300 mg of CTF were loaded into a quartz fritted disk located inside a tubular quartz reactor (i.d. × length 8 × 800 mm). Helium was fed into the reactor (30 mL·min^{-1}) through a mass flow controller (BROOKS MFC) and passed through a glass evaporator filled with liquid EB maintained at constant temperature with a regulated thermal bath. The reaction system was heated to 550 °C and kept for 2 h under He. The reactant flow (2.8 vol % EB diluted in He, total flow rate of 30 mL·min^{-1}) was then fed to the reactor. The reactant and the products (styrene (ST), benzene (BZ) and toluene (TOL)) getting out from the reactor were analyzed on line with a PERICHROM (PR 2100) gas chromatograph equipped with a flame detector (FID) and a previously calibrated CP WAX S2CB column. In order to avoid any possible condensation of the reactant or the products, all the tube lines were wrapped with a heating wire kept at 110 °C. The ethylbenzene conversion (X_{EB}) and styrene selectivity (S_{ST}) were evaluated using Equation 3 and Equation 4:

$$X_{EB} = \frac{F_0 C_{EB,inlet} - F C_{EB,outlet}}{F_0 C_{EB,inlet}} \times 100\% \qquad (3)$$

$$S_{ST} = \frac{C_{ST,outlet}}{C_{ST,outlet} + C_{TOL,outlet} + C_{BZ,outlet}} \times 100\% \qquad (4)$$

where F and F_0 are the flow rates of the outlet and inlet, respectively, while C_{EB}, C_{ST}, C_{TOL} and C_{BZ} correspond to the concentration of ethylbenzene, styrene, toluene and benzene. The carbon balances amounted to about 100% in all trials.

Supporting Information

Complementing material characterization, such as CHN elemental analysis, nitrogen adsorption−desorption isotherms, differential pore volume distributions, survey spectra and N 1s, O 1s core region XPS analyses, low-pressure CO_2 adsorption–desorption isotherms, heats of adsorption (Q_{st}), CO_2 and N_2 adsorption isotherms at 298 K, TPO and PXRD analyses.

Supporting Information File 1
Additional experimental data.
[https://www.beilstein-journals.org/bjnano/content/supplementary/2190-4286-10-121-S1.pdf]

Acknowledgements

ORCID® iDs

Giulia Tuci - https://orcid.org/0000-0002-3411-989X
Andrea Rossin - https://orcid.org/0000-0002-1283-2803
Vasiliki Papaefthimiou - https://orcid.org/0000-0001-8341-6658
Jens Artz - https://orcid.org/0000-0001-6172-7690
Giuliano Giambastiani - https://orcid.org/0000-0002-0315-3286

References

1. Dai, L.; Chang, D. W.; Baek, J.-B.; Lu, W. *Small* **2012,** *8,* 1130–1166. doi:10.1002/smll.201101594
2. De Volder, M. F. L.; Tawfick, S. H.; Baughman, R. H.; Hart, A. J. *Science* **2013,** *339,* 535–539. doi:10.1126/science.1222453
3. Zhang, Q.; Uchaker, E.; Candelaria, S. L.; Cao, G. *Chem. Soc. Rev.* **2013,** *42,* 3127–3171. doi:10.1039/c3cs00009e
4. Thomas, A. *Angew. Chem., Int. Ed.* **2010,** *49,* 8328–8344. doi:10.1002/anie.201000167
5. Vilela, F.; Zhang, K.; Antonietti, M. *Energy Environ. Sci.* **2012,** *5,* 7819–7832. doi:10.1039/c2ee22002d
6. Rose, M. *ChemCatChem* **2014,** *6,* 1166–1182. doi:10.1002/cctc.201301071
7. Chaoui, N.; Trunk, M.; Dawson, R.; Schmidt, J.; Thomas, A. *Chem. Soc. Rev.* **2017,** *46,* 3302–3321. doi:10.1039/c7cs00071e
8. Rogge, S. M. J.; Bavykina, A.; Hajek, J.; Garcia, H.; Olivos-Suarez, A. I.; Sepúlveda-Escribano, A.; Vimont, A.; Clet, G.; Bazin, P.; Kapteijn, F.; Daturi, M.; Ramos-Fernandez, E. V.; Llabrés i Xamena, F. X.; Van Speybroeck, V.; Gascon, J. *Chem. Soc. Rev.* **2017,** *46,* 3134–3184. doi:10.1039/c7cs00033b
9. Dawson, R.; Cooper, A. I.; Adams, D. J. *Prog. Polym. Sci.* **2012,** *37,* 530–563. doi:10.1016/j.progpolymsci.2011.09.002
10. Xu, Y.; Jin, S.; Xu, H.; Nagai, A.; Jiang, D. *Chem. Soc. Rev.* **2013,** *42,* 8012–8031. doi:10.1039/c3cs60160a
11. Zou, X.; Ren, H.; Zhu, G. *Chem. Commun.* **2013,** *49,* 3925–3936. doi:10.1039/c3cc00039g
12. Puthiaraj, P.; Lee, Y.-R.; Zhang, S.; Ahn, W.-S. *J. Mater. Chem. A* **2016,** *4,* 16288–16311. doi:10.1039/c6ta06089g
13. Artz, J. *ChemCatChem* **2018,** *10,* 1753–1771. doi:10.1002/cctc.201701820
14. Kuhn, P.; Antonietti, M.; Thomas, A. *Angew. Chem., Int. Ed.* **2008,** *47,* 3450–3453. doi:10.1002/anie.200705710
15. Kuhn, P.; Thomas, A.; Antonietti, M. *Macromolecules* **2009,** *42,* 319–326. doi:10.1021/ma802322j
16. Sakaushi, K.; Hosono, E.; Nickerl, G.; Zhou, H.; Kaskel, S.; Eckert, J. *J. Power Sources* **2014,** *245,* 553–556. doi:10.1016/j.jpowsour.2013.07.007
17. Talapaneni, S. N.; Hwang, T. H.; Je, S. H.; Buyukcakir, O.; Choi, J. W.; Coskun, A. *Angew. Chem., Int. Ed.* **2016,** *55,* 3106–3111. doi:10.1002/anie.201511553
18. Liu, J.; Zan, W.; Li, K.; Yang, Y.; Bu, F.; Xu, Y. *J. Am. Chem. Soc.* **2017,** *139,* 11666–11669. doi:10.1021/jacs.7b05025
19. Hug, S.; Mesch, M. B.; Oh, H.; Popp, N.; Hirscher, M.; Senker, J.; Lotsch, B. V. *J. Mater. Chem. A* **2014,** *2,* 5928–5936. doi:10.1039/c3ta15417c
20. Dey, S.; Bhunia, A.; Esquivel, D.; Janiak, C. *J. Mater. Chem. A* **2016,** *4,* 6259–6263. doi:10.1039/c6ta00638h
21. Dey, S.; Bhunia, A.; Breitzke, H.; Groszewicz, P. B.; Buntkowsky, G.; Janiak, C. *J. Mater. Chem. A* **2017,** *5,* 3609–3620. doi:10.1039/c6ta07076k
22. Artz, J.; Delidovich, I.; Pilaski, M.; Niemeier, J.; Kübber, B. M.; Rahimi, K.; Palkovits, R. *RSC Adv.* **2018,** *8,* 22392–22401. doi:10.1039/c8ra04254c
23. Artz, J.; Mallmann, S.; Palkovits, R. *ChemSusChem* **2015,** *8,* 672–679. doi:10.1002/cssc.201403078
24. Artz, J.; Palkovits, R. *ChemSusChem* **2015,** *8,* 3832–3838. doi:10.1002/cssc.201501106
25. Bavykina, A. V.; Goesten, M. G.; Kapteijn, F.; Makkee, M.; Gascon, J. *ChemSusChem* **2015,** *8,* 809–812. doi:10.1002/cssc.201403173
26. Chan-Thaw, C. E.; Villa, A.; Wang, D.; Santo, V. D.; Orbelli Biroli, A.; Veith, G. M.; Thomas, A.; Prati, L. *ChemCatChem* **2015,** *7,* 2149–2154. doi:10.1002/cctc.201500055
27. Katekomol, P.; Roeser, J.; Bojdys, M.; Weber, J.; Thomas, A. *Chem. Mater.* **2013,** *25,* 1542–1548. doi:10.1021/cm303751n
28. Palkovits, R.; Antonietti, M.; Kuhn, P.; Thomas, A.; Schüth, F. *Angew. Chem., Int. Ed.* **2009,** *48,* 6909–6912. doi:10.1002/anie.200902009
29. Pilaski, M.; Artz, J.; Islam, H.-U.; Beale, A. M.; Palkovits, R. *Microporous Mesoporous Mater.* **2016,** *227,* 219–227. doi:10.1016/j.micromeso.2016.03.010
30. Tuci, G.; Pilaski, M.; Ba, H.; Rossin, A.; Luconi, L.; Caporali, S.; Pham-Huu, C.; Palkovits, R.; Giambastiani, G. *Adv. Funct. Mater.* **2017,** *27,* 1605672. doi:10.1002/adfm.201605672
31. Wright, P. A. *Microporous Framework Solids;* Royal Society of Chemistry: Cambridge, United Kingdom, 2008. doi:10.1039/9781847557971
32. Ben, T.; Pei, C.; Zhang, D.; Xu, J.; Deng, F.; Jing, X.; Qiu, S. *Energy Environ. Sci.* **2011,** *4,* 3991–3999. doi:10.1039/c1ee01222c
33. Hug, S.; Stegbauer, L.; Oh, H.; Hirscher, M.; Lotsch, B. V. *Chem. Mater.* **2015,** *27,* 8001–8010. doi:10.1021/acs.chemmater.5b03330
34. Ba, H.; Liu, Y.; Truong-Phuoc, L.; Duong-Viet, C.; Nhut, J.-M.; Nguyen, D. L.; Ersen, O.; Tuci, G.; Giambastiani, G.; Pham-Huu, C. *ACS Catal.* **2016,** *6,* 1408–1419. doi:10.1021/acscatal.6b00101
35. Zhao, Z.; Dai, Y.; Lin, J.; Wang, G. *Chem. Mater.* **2014,** *26,* 3151–3161. doi:10.1021/cm5005664
36. Zhao, Z.; Dai, Y. *J. Mater. Chem. A* **2014,** *2,* 13442–13451. doi:10.1039/c4ta02282c
37. Zhao, Z.; Dai, Y.; Ge, G.; Guo, X.; Wang, G. *Green Chem.* **2015,** *17,* 3723–3727. doi:10.1039/c5gc00971e
38. Zhao, Z.; Dai, Y.; Ge, G. *Catal. Sci. Technol.* **2015,** *5,* 1548–1557. doi:10.1039/c4cy01415d

39. Ba, H.; Liu, Y.; Mu, X.; Doh, W.-H.; Nhut, J.-M.; Granger, P.; Pham-Huu, C. *Appl. Catal., A* **2015,** *499,* 217–226. doi:10.1016/j.apcata.2015.04.022
40. Zhang, J.; Su, D. S.; Blume, R.; Schlögl, R.; Wang, R.; Yang, X.; Gajović, A. *Angew. Chem., Int. Ed.* **2010,** *49,* 8640–8644. doi:10.1002/anie.201002869
41. Zhao, Z.; Dai, Y.; Ge, G.; Wang, G. *ChemCatChem* **2015,** *7,* 1135–1144. doi:10.1002/cctc.201402934
42. Liu, H.; Diao, J.; Wang, Q.; Gu, S.; Chen, T.; Miao, C.; Yang, W.; Su, D. *Chem. Commun.* **2014,** *50,* 7810–7812. doi:10.1039/c4cc01693a
43. Wang, R.; Sun, X.; Zhang, B.; Sun, X.; Su, D. *Chem. – Eur. J.* **2014,** *20,* 6324–6331. doi:10.1002/chem.201400018
44. Zhao, Z.; Dai, Y.; Ge, G.; Wang, G. *AIChE J.* **2015,** *61,* 2543–2561. doi:10.1002/aic.14853
45. **CTF1** and **CTF2** have been previously discussed by some of us and reported elsewhere (see refs. [23] and [29]). They have been discussed and completely characterized in here for the sake of comparison while describing the newly synthesized samples **CTF3-5**.
46. Thommes, M.; Kaneko, K.; Neimark, A. V.; Olivier, J. P.; Rodriguez-Reinoso, F.; Rouquerol, J.; Sing, K. S. W. *Pure Appl. Chem.* **2015,** *87,* 1051–1069. doi:10.1515/pac-2014-1117
47. Wang, K.; Huang, H.; Liu, D.; Wang, C.; Li, J.; Zhong, C. *Environ. Sci. Technol.* **2016,** *50,* 4869–4876. doi:10.1021/acs.est.6b00425
48. Schwinghammer, K.; Hug, S.; Mesch, M. B.; Senker, J.; Lotsch, B. V. *Energy Environ. Sci.* **2015,** *8,* 3345–3353. doi:10.1039/c5ee02574e
49. Bhunia, A.; Vasylyeva, V.; Janiak, C. *Chem. Commun.* **2013,** *49,* 3961–3963. doi:10.1039/c3cc41382a
50. Osadchii, D. Y.; Olivos-Suarez, A. I.; Bavykina, A. V.; Gascon, J. *Langmuir* **2017,** *33,* 14278–14285. doi:10.1021/acs.langmuir.7b02929
51. Zhu, X.; Tian, C.; Veith, G. M.; Abney, C. W.; Dehaudt, J.; Dai, S. *J. Am. Chem. Soc.* **2016,** *138,* 11497–11500. doi:10.1021/jacs.6b07644
52. Mukherjee, S.; Das, M.; Manna, A.; Krishna, R.; Das, S. *J. Mater. Chem. A* **2019,** *7,* 1055–1068. doi:10.1039/c8ta08185a
53. Zhao, Y.; Yao, K. X.; Teng, B.; Zhang, T.; Han, Y. *Energy Environ. Sci.* **2013,** *6,* 3684–3692. doi:10.1039/c3ee42548g
54. Yuan, K.; Liu, C.; Zong, L.; Yu, G.; Cheng, S.; Wang, J.; Weng, Z.; Jian, X. *ACS Appl. Mater. Interfaces* **2017,** *9,* 13201–13212. doi:10.1021/acsami.7b01783
55. Park, K.; Lee, K.; Kim, H.; Ganesan, V.; Cho, K.; Jeong, S. K.; Yoon, S. *J. Mater. Chem. A* **2017,** *5,* 8576–8582. doi:10.1039/c6ta11226a
56. Fu, Y.; Wang, Z.; Li, S.; He, X.; Pan, C.; Yan, J.; Yu, G. *ACS Appl. Mater. Interfaces* **2018,** *10,* 36002–36009. doi:10.1021/acsami.8b13417
57. Yuan, K.; Liu, C.; Liu, C.; Zhang, S.; Yu, G.; Yang, L.; Yang, F.; Jian, X. *Polymer* **2018,** *151,* 65–74. doi:10.1016/j.polymer.2018.07.061
58. Jena, H. S.; Krishnaraj, C.; Wang, G.; Leus, K.; Schmidt, J.; Chaoui, N.; Van Der Voort, P. *Chem. Mater.* **2018,** *30,* 4102–4111. doi:10.1021/acs.chemmater.8b01409
59. Lee, Y. J.; Talapaneni, S. N.; Coskun, A. *ACS Appl. Mater. Interfaces* **2017,** *9,* 30679–30685. doi:10.1021/acsami.7b08930
60. Wang, G.; Leus, K.; Zhao, S.; Van Der Voort, P. *ACS Appl. Mater. Interfaces* **2018,** *10,* 1244–1249. doi:10.1021/acsami.7b16239
61. Wang, G.; Leus, K.; Jena, H. S.; Krishnaraj, C.; Zhao, S.; Depauw, H.; Tahir, N.; Liu, Y.-Y.; Van Der Voort, P. *J. Mater. Chem. A* **2018,** *6,* 6370–6375. doi:10.1039/c7ta08913a
62. Du, J.; Liu, Y.; Krishna, R.; Yu, Y.; Cui, Y.; Wang, S.; Liu, Y.; Song, X.; Liang, Z. *ACS Appl. Mater. Interfaces* **2018,** *10,* 26678–26686. doi:10.1021/acsami.8b08625
63. Zhu, X.; Mahurin, S. M.; An, S.-H.; Do-Thanh, C.-L.; Tian, C.; Li, Y.; Gill, L. W.; Hagaman, E. W.; Bian, Z.; Zhou, J.-H.; Hu, J.; Liu, H.; Dai, S. *Chem. Commun.* **2014,** *50,* 7933–7936. doi:10.1039/c4cc01588f
64. Bae, Y.-S.; Snurr, R. Q. *Angew. Chem., Int. Ed.* **2011,** *50,* 11586–11596. doi:10.1002/anie.201101891
65. Haszeldine, R. S. *Science* **2009,** *325,* 1647–1652. doi:10.1126/science.1172246
66. Liebl, M. R.; Senker, J. *Chem. Mater.* **2013,** *25,* 970–980. doi:10.1021/cm4000894
67. Zhao, Z.; Dai, Y.; Ge, G.; Mao, Q.; Rong, Z.; Wang, G. *ChemCatChem* **2015,** *7,* 1070–1077. doi:10.1002/cctc.201500074
68. Kissin, Y. V. *Catal. Rev.: Sci. Eng.* **2001,** *43,* 85–146. doi:10.1081/cr-100104387
69. Jin, X.; Balasubramanian, V. V.; Selvan, S. T.; Sawant, D. P.; Chari, M. A.; Lu, G. Q.; Vinu, A. *Angew. Chem., Int. Ed.* **2009,** *48,* 7884–7887. doi:10.1002/anie.200903674
70. Gounder, R.; Iglesia, E. *J. Am. Chem. Soc.* **2009,** *131,* 1958–1971. doi:10.1021/ja808292c
71. Dey, S.; Bhunia, A.; Boldog, I.; Janiak, C. *Microporous Mesoporous Mater.* **2017,** *241,* 303–315. doi:10.1016/j.micromeso.2016.11.033
72. Schell, J.; Casas, N.; Pini, R.; Mazzotti, M. *Adsorption* **2012,** *18,* 49–65. doi:10.1007/s10450-011-9382-y

Alloyed Pt$_3$M (M = Co, Ni) nanoparticles supported on S- and N-doped carbon nanotubes for the oxygen reduction reaction

Stéphane Louisia[1,2], Yohann R. J. Thomas[2], Pierre Lecante[3], Marie Heitzmann[2], M. Rosa Axet[1], Pierre-André Jacques[*2] and Philippe Serp[*1]

Abstract

Sulfur- (S-CNT) and nitrogen-doped (N-CNT) carbon nanotubes have been produced by catalytic chemical vapor deposition (c-CVD) and were subject to an annealing treatment. These CNTs were used as supports for small (≈2 nm) Pt$_3$M (M = Co or Ni) alloyed nanoparticles that have a very homogeneous size distribution (in spite of the high metal loading of ≈40 wt % Pt), using an ionic liquid as a stabilizer. The electrochemical surface area, the activity for the oxygen reduction reaction and the amount of H$_2$O$_2$ generated during the oxygen reduction reaction (ORR) have been evaluated in a rotating ring disk electrode experiment. The Pt$_3$M/N-CNT catalysts revealed excellent electrochemical properties compared to a commercial Pt$_3$Co/Vulcan XC-72 catalyst. The nature of the carbon support plays a key role in determining the properties of the metal nanoparticles, on the preparation of the catalytic layer, and on the electrocatalytic performance in the ORR. On N-CNT supports, the specific activity followed the expected order Pt$_3$Co > Pt$_3$Ni, whereas on the annealed N-CNT support, the order was reversed.

Introduction

Proton exchange membrane fuel cells (PEMFCs) convert chemical energy from the hydrogen oxidation reaction (HOR) and the oxygen reduction reaction (ORR) into electrical energy. PEMFCs are one of the most promising technologies in the field of renewable energy (and especially for transport applications), but the cost and lifetime are factors still to be improved in order to achieve widespread dissemination of this technology [1,2]. Due to the sluggish reaction kinetics for the ORR, the cathode active layer contains generally four times more catalyst than the anodic layer, which explains why most of the research is focused on the optimization of the cathodic catalytic layer. Platinum nanoparticles (NPs) supported on carbon black (CB),

especially Vulcan XC-72 [3,4], are usually used as the catalyst. To meet the performance and durability requirements for transport applications, a metal loading of 0.4 $mg_{Pt} \cdot cm^{-2}$ for the cathode side is commonly used, which explains the high cost of these systems [5]. One lever to reduce the cost of this technology is the reduction of the cathode Pt loading, but this must be done without compromise to the catalyst layer performance and durability.

It is known that catalyst degradation via platinum dissolution and carbon corrosion plays an important role in the voltage degradation of PEMFCs [6-8]. CB, which is widely used, particularly for its low cost, suffers from thermochemical instability and corrosion in fuel cell applications. In the cathodic layer, the oxidizing, wet and acidic environment, the high electrochemical potential, and the high platinum loading all lead to the oxidation of the carbon surface, and occasionally to the formation of CO_2 [9]. This carbon corrosion modifies the mass transport properties of the active layer, especially for the water management, and accelerates the degradation of the Pt NPs [10,11].

One way to reduce the Pt content is to use more active, tailored NPs [12,13], for example, bimetallic NPs with a core–shell structure [14,15]: a Pt shell can be deposited on a low-cost transition metal such as Co [16-18], Ni [19,20] or Cu [21] or their nitrides [22]. Kristian et al. have described a redox–transmetalation method for the synthesis of Co_{core}–Pt_{shell} particles with a high activity for the ORR [23]. Platinum-based alloys can also been used [24,25]. Therefore, it seems important to develop nanostructured catalysts supported on a material with electronic conductivity and surface area close to the common CB but with more resistance towards corrosion. Interestingly, it has recently been shown that the introduction of small amounts of ionic liquids (ILs), which are known as NP stabilizers, including on carbon supports [26], into Pt-based catalysts can further improve the ORR performance. This is likely due to the high O_2 solubility in the IL phase [27]. It was also demonstrated that the choice of the carbon support, in combination with ILs, is also important to achieve high Pt dispersion, and functionalized carbons should be preferred, presumably because of their stronger interaction with the IL [28].

Carbon nanotubes (CNTs) are well known for their remarkable chemical and physical properties and appear to be an interesting alternative to replace CB in fuel cell applications [29,30]. It has been described that CNTs could be used as resistant material to support nanostructured PtNi hollow particles, but it appears that the structure of the used CNT might be responsible for the large external diameter of the deposited particles, which is close to 25 nm [31]. Previous works have shown the possibility to dope CNTs with nitrogen (N-CNT) or sulfur (S-CNT) in

order to modify properties such as electronic conduction and surface chemistry [32-34]. This strategy contributes to improve the metal dispersion and to increase the performance of the catalyst for the ORR due to the structural and electronic properties of the doped CNT [34,35]. Additionally, the amount of heteroatom in the doped structure has an effect on the hydrophobicity of the material, which could provide a solution to facilitate the water management in the active layer. In fact, water management in the cathodic layer is a key challenge: the electrolytic membrane has to be hydrated enough to favor the proton conduction, but an excess of water in the cathodic layer will decrease the oxygen accessibility to the active sites. Thermal treatment can be used to improve the carbon corrosion resistance of the CNT. In fact, annealing at high temperature (above 1000 °C) is used to remove structural defects from the CNT in order to obtained more stable [36] and more conductive [37] structures. In the case of the N-CNTs, the thermal annealing can also modify the ratio of the different nitrogen groups at the surface [38], and consequently, the metal–support interaction.

This work proposes: i) to reduce the amount of Pt on the catalyst by using Pt alloyed compounds, and ii) to increase the support corrosion resistance using heat-treated carbon materials. Several CNT materials have been synthetized, fully characterized (structural and surface properties) and used as catalyst supports. CNT-supported bimetallic Pt_3Co or Pt_3Ni NPs were synthetized. To evaluate catalyst performance, electrochemical characterization was performed using a rotating ring disk electrode (RRDE) experiment to determine the active surface and the activity for the ORR of each catalyst. Finally, membrane electrode assemblies (MEAs) of 25 cm^2 active area, integrating the synthesized catalysts, have been prepared and tested. The one giving the best beginning-of-life performance has been aged following a recommended accelerated stress test (AST) cycle for catalyst support corrosion.

Results and Discussion
Synthesis and characterization of the CNTs and Pt_3M/CNT

Three kinds of CNTs have been produced by catalytic chemical vapor deposition (c-CVD): undoped (CNTs), N-doped (N-CNTs) and S-doped CNT (S-CNTs). To further increase the corrosion resistance and the electrical conductivity of the N-CNTs, they were annealed at 1000 °C to produce N-CNT$_{HT}$.

The introduction of nitrogen or sulfur into the CNT structure has an effect on the structural properties of the prepared materials. High resolution transmission electron microscopy (HRTEM) analysis shows a remarkable difference between the carbon structures synthetized (Figure 1).
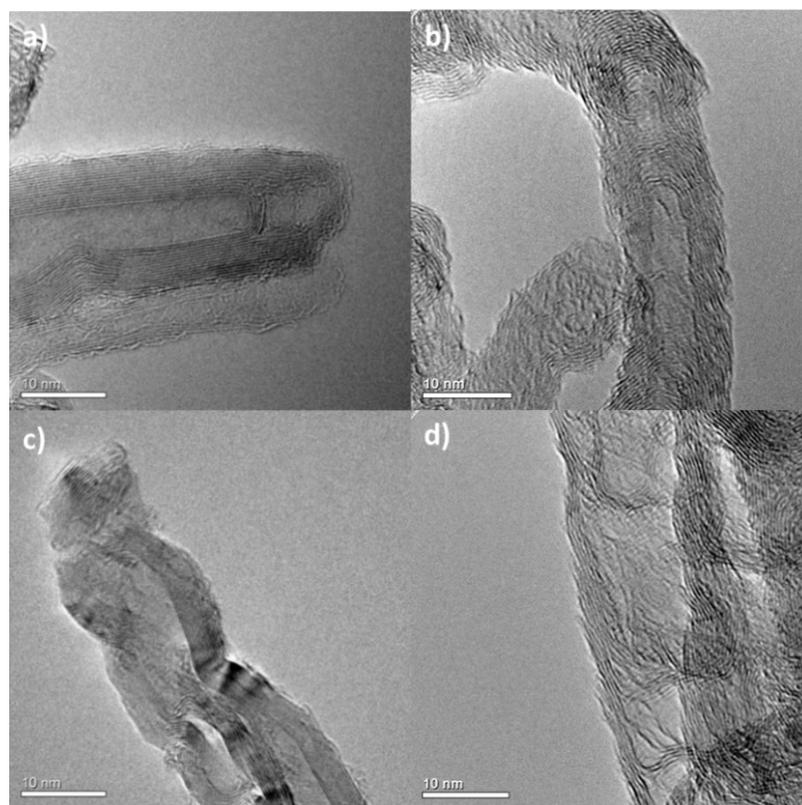
Figure 1: HRTEM micrographs of: a) CNTs; b) N-CNTs; c) S-CNTs, and d) N-CNTs$_{HT}$. (Scale bar = 10 nm).

Very regular structures were obtained for the CNT sample (Figure 1a), while the N-CNT sample presented a "bamboo-like" structure typically found in N-doped CNTs (Figure 1b) [39], and the structure of the S-doped CNTs presents some alterations (bulbous segments, Figure 1c), which are different than those observed for the N-CNTs (bamboo structure). The N-CNTs$_{HT}$ show similar structure to the HRTEM observations (Figure 1d). Low magnification TEM micrographs of the carbon supports are given in Supporting Information File 1, Figure S1. The CNTs, N-CNTs and S-CNTs have mean external diameters of 15 ± 5, 18 ± 8, and 15 ± 7 nm, respectively. The specific surface area (SSA) of these materials ranged between 150 m^2/g (CNTs) and 190 m^2/g (S-CNTs).

Structural characterization was performed using Raman spectroscopy and X-ray diffraction (XRD, see Table 1 and Supporting Information File 1, Figure S2 for Raman spectra). In Raman spectroscopy, a useful parameter for carbon nanotubes is the ratio between the D band (I_D) at ≈1380 cm^{-1}, attributed to the defects of the CNT structure, and the G band (I_G) at ≈1580 cm^{-1}, the first-order Raman band of all sp^2 carbon materials. The presence of disorder in CNTs can also impact: i) the intensity of other bands, such as the G' band at ≈2700 cm^{-1}, and ii) the position and shape of the peaks [40]. The G' band is

indicative of long-range order in a sample. Finally, another parameter, measurable by Raman spectroscopy that is relevant to catalyst preparation, is the L_D: L_D is a typical inter-defect distance that we have measured as described in [41]. A lower I_D/I_G (and higher L_D) is obtained for the CNT sample and a higher I_D/I_G (and lower L_D) for the N-CNT sample, which is in accordance with the TEM observations. The N-CNT$_{HT}$ sample shows a decrease in the number of defects compared to N-CNT, as expected after the high temperature treatment. S-CNTs constitute an intermediate situation. The d$_{002}$ inter-planar spacing results obtained with XRD are presented in Table 1.

All the values are larger than that of graphite (3.334 Å), and the smallest value is obtained for N-CNT$_{HT}$, indicating a higher level of graphitization for this sample.

The elemental composition as well as the surface chemistry is also affected by heteroatom doping. Elemental and X-ray photoelectron spectroscopy (XPS) analysis results are shown in Table 1. The elemental analysis confirmed the efficiency of the doping, and showed that S-CNT contains a significant amount of residual catalyst (iron, encapsulated in the structure of the tubes). An effect of heat treatment on the N-CNTs (besides the reduction of disorder) is to decrease the amount of nitrogen,

Table 1: Chemical, textural, and crystalline properties of the carbon supports.

Supports	XPS analysis				Textural properties		Elemental analysis		
	C (%)	O (%)	N (%)	S (%)	BET surface area ($m^2 \cdot g^{-1}$)	Pore volume ($cm^3 \cdot g^{-1}$)	C (%)	N (%)	S (%)
CNT	98.4	1.6	–	–	151	2.6	92.3	–	–
N-CNT	91.2	4.9	3.9	0.2	182	2.7	92.3	2.9	–
N-CNT$_{HT}$	94.1	3.5	2.4	–	168	2.4	95.6	1.6	–
S-CNT	95.6	2.8	–	1.3	190	1.1	78.6	–	5.0

	Raman analysis				Crystallite properties	
	I_D/I_G	I_D/I_G	I_D/I_G	I_D/I_G	d$_{002}$ (nm)	d$_{002}$ (nm)
CNT	0.87	0.87	0.87	0.87	0.3444	0.3444
N-CNT	1.02	1.02	1.02	1.02	0.3436	0.3436
N-CNT$_{HT}$	0.95	0.95	0.95	0.95	0.3379	0.3379
S-CNT	0.99	0.99	0.99	0.99	0.3422	0.3422

which decreases from 2.9 to 1.6%. XPS analysis confirmed the bulk analyses and showed that the S-CNT sample also contains a significant amount of surface oxygen groups. The introduction of oxygen may correspond to the oxidation of the sulfur species introduced during the doping during the purification step in H_2SO_4. As the S 2p peaks are typically presented in spin–orbit doublets of S 2p$_{3/2}$ and S 2p$_{1/2}$ (splitting magnitude ≈1.18 eV), four S 2p$_{3/2}$ peaks representing sulfur bonding of FeS$_2$ (≈162.5 eV), H–S–C (≈163.5 eV), R–S–C (≈164.5 eV), and S–O (≈168.0 eV) were observed (Supporting Information File 1, Figure S3) [42,43]. The intense peak at 163.5 eV indicated the doping of CNTs with mainly thiol surface groups (Table 2). The peak at 164.5 eV could arise from the presence of sulfur in the carbon matrix, while the oxidation of surface thiols should produce S–O bonds (peak at 168 eV). The presence of pyrite could arise from the significant amount of remaining iron catalyst in this sample. Different nitrogen groups are present in N-CNT, and the proportion of these groups was determined by deconvolution of the main N 1s peak: pyridinic nitrogen, pyrrolic nitrogen, quaternary nitrogen and nitrogen-

oxidized species were identified (Table 2, and Supporting Information File 1, Figure S4). XPS analysis also showed the presence of sulfonic acid groups on the surface of N-doped CNTs (Supporting Information File 1, Figure S4b), and the S content increases with the nitrogen content. This functionalization occurs during the purification step with sulfuric acid. In the N-CNT$_{HT}$ sample, we measured a clear decrease of the nitrogen-oxidized species.

Electrocatalyst support materials are crucial to both the performance and durability of PEM fuel cells [44,45]. These materials should combine some key characteristics such as: i) an adapted surface chemistry to allow high dispersion of the metallic phase at very high metal loading, ii) a good balance between hydrophobicity and hydrophilicity to allow water management and interaction with the electrolyte, iii) a good dispersibility in the ink to limit mass transfer, and iv) structural features allowing high conductivity and chemical stability. As some of these characteristics are not compatible (e.g., a high metal dispersion should be favored on defective carbon

Table 2: Contribution of species detected by deconvolution of XPS spectra for several N-CNT samples.

Sample	Surface groups			
S-doped	S$_{FeS2}$ (%)	S$_{thiol}$ (%)	S$_{sulphide/thioether}$ (%)	S$_{ox}$ (%)
S-CNT	5.0	64.9	22.8	7.3
N-doped	N$_{pyridinic}$ (%)	N$_{quaternary}$ (%)	N$_{pyrrolic}$ (%)	N$_{oxidized}$ (%)
N-CNT	23.9	23.4	9.1	43.6
N-CNT$_{HT}$	30.9	54.3	10.3	4.5

supports but this should be detrimental to the stability and electronic conduction), some compromises have to be made.

Figure 2 shows the evolution of the I_D/I_G ratio from Raman spectroscopy and the percent of surface heteroatoms from XPS in the investigated supports. The I_D/I_G ratio reflects the concentration of defects in these supports, where a high ratio favors metal dispersion. A high percentage of surface heteroatoms should favor metal dispersion and interaction with the electrolyte but may have negative impacts on the electronic conductivity, the stability, and can modify the metal/support interactions and thus the electrocatalytic performance. From this figure, we can see that the CNTs and S-CNTs constitute the extremes and that the compromise could lie in the N-doped nanotubes, particularly the N-CNT$_{HT}$.

Figure 2: Evolution of the I_D/I_G ratio (from Raman spectroscopy) and the percent of surface heteroatoms (from XPS) in the investigated CNT supports.
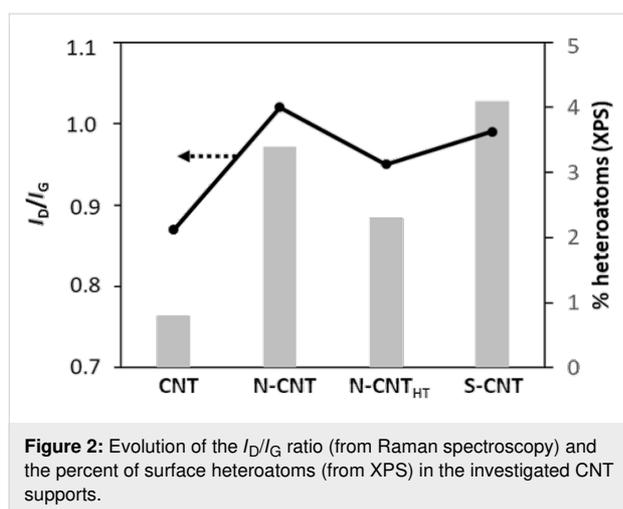
These CNTs have been used to support Pt$_3$M (M = Co, Ni) NPs. The bimetallic NPs were prepared using the transmetalation method described by Kristian et al. [23]. The redox couple used for the transmetalation is Co^{2+}(II)/Co(0) ($E° = −0.77$ V/RHE) and PtCl$_4{}^{2−}$/Pt(0) ($E° = 0.67$ V/RHE) for Pt$_3$Co NPs. In our procedure, the ammonium salt used as a stabilizer has been replaced by an ionic liquid in order to obtain a better distribution of NPs at the surface of the CNTs [46]. Indeed, the use of hexadecyl trimetyl ammonium bromide leads to the formation of small NPs (1.90 ± 0.77 nm) that are not well-dispersed on the support (see Supporting Information File 1, Figure S5a for the Pt$_3$Co/CNT sample). In order to improve the NP distribution on the support, [bmim][Tf$_2$N] was chosen as stabilizer. It is known that imidazolium salts show good interaction with CNTs due to π–π interactions and could also be used as a stabilization agent for NPs [46-48]. The TEM images of sample Pt$_3$Co/CNT (Supporting Information File 1, Figure S5b) show that the use of ILs does not result in well-dispersed NPs on this support. The presence of heteroatoms in the CNTs significantly affects the

distribution of the NPs on the CNT surface (Figure 3a–c). N-doped or S-doped structures are known to be more reactive due to the presence of different functional groups at the surface of the CNTs, while un-doped CNTs are relatively inert. With nitrogen or sulfur groups acting as nucleation centers, the distribution of NPs on the CNT walls is better on N-CNTs and S-CNTs than on CNTs. A decrease of the nitrogen content was observed with annealing of the N-CNTs. This could explain why the NP distribution is better for Pt$_3$Co/N-CNT compared to Pt$_3$Co/N-CNT$_{HT}$. Non-annealed CNTs seem to have better interaction with the Co precursor and the as-obtained catalysts show a better NP distribution. Nevertheless, the mean size of the NPs is around 2 nm for all the prepared catalysts (Table 3 and Supporting Information File 1, Figure S6).

Pt$_3$Ni/N-CNT catalysts were prepared using the same procedure. The redox couple used for the transmetalation is Ni^{2+}(II)/Ni(0) ($E° = −0.257$ V/RHE) and PtCl$_4{}^{2−}$/Pt(0) ($E° = 0.67$ V/RHE). A poor metal distribution was obtained on the CNTs, thus Pt$_3$Ni NPs were further studied only on N-CNTs and S-CNTs. For the Pt$_3$Ni catalysts, the mean size of the NPs is around 2 nm as observed for Pt$_3$Co (Figure 3d–f and Supporting Information File 1, Figure S6). From these syntheses, we can estimate the influence of the metal precursor on the NP distribution. Regardless of the carbon support, much better distribution on the CNT walls was obtained with the Ni precursor. The affinity between the metal precursor and the carbon surface seems to play a role on the active phase distribution. The higher affinity of Ni compared to Co for graphene [49,50] and N-doped carbon [51,52] surfaces has already been reported in the literature and could hint at the origin of our results. The annealing of the N-CNTs has also an impact, since the Pt$_3$Ni/N-CNT$_{HT}$ catalyst shows a better distribution than the Pt$_3$Ni/N-CNT one. We suspect that the annealing of the N-CNTs and the as-obtained modifications of the chemical surface causes an important change in the adsorption and diffusion of the metal. It has been shown that the binding energy between a transition metal and a carbon support depends on the nature of the metal but also on the carbon material composition [53].

Particularly, Kattel showed that the binding energy of several transition metals could change if they are bound to two carbon atoms (M–C$_2$), one carbon atom and one nitrogen atom (M–CN) or two nitrogen atoms (M–N$_2$) [52]. Good metal distribution was also obtained on the S-CNT sample; in this case, however, the Pt loading is rather low (≈23%) compared to the N-CNTs. A recent study has shown that good metal distribution can be obtained on S-CNTs in the case of Pt catalysts (Pt loading = 20%, Pt NP size = 2.4 nm) [32,33]. The mean particle size for the Pt$_3$Ni series is also around 2 nm, highlighting
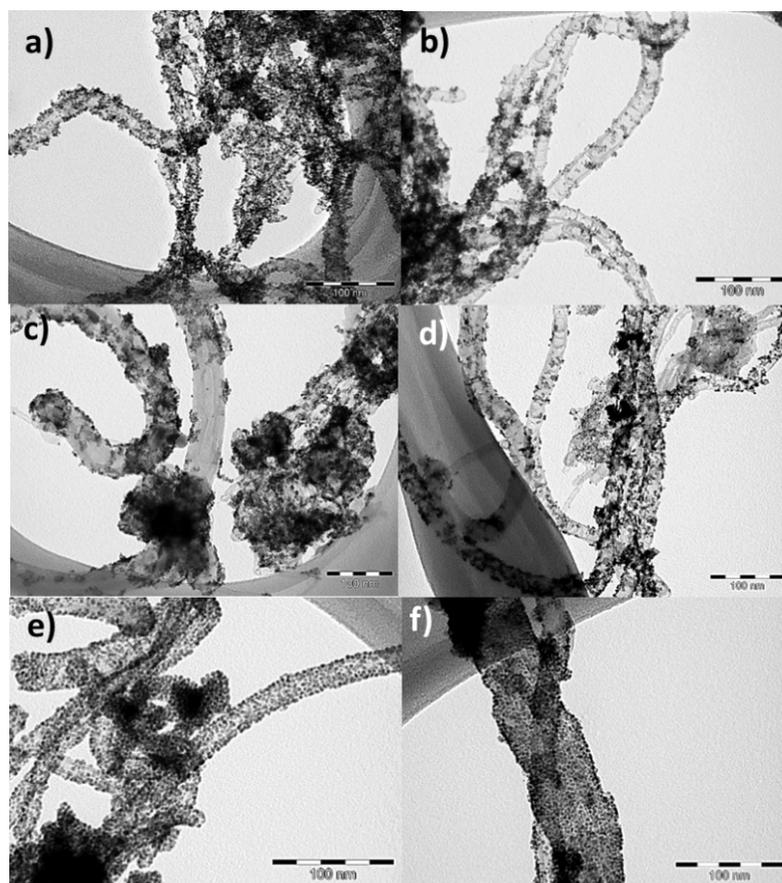
Figure 3: TEM micrographs of: a) Pt₃Co/N-CNT; b) Pt₃Co/N-CNT$_{HT}$; c) Pt₃Co/S-CNT; d) Pt₃Ni/N-CNT; e) Pt₃Ni/N-CNT$_{HT}$, and f) Pt₃Ni/S-CNT. Scale bar = 100 nm.

Table 3: Mean nanoparticle size and metal loading for PtM/CNT catalysts.

Sample	Particle size (nm)	M (wt %)	Pt (wt %)
Pt₃Co/CNT	2.28 ± 0.82	12.5	33.5
Pt₃Co/N-CNT	1.71 ± 0.73	15.4	41.5
Pt₃Co/N-CNT$_{HT}$	2.08 ± 0.90	7.9	40.2
Pt₃Co/S-CNT	2.00 ± 0.71	15.4	33.0
Pt₃Ni/N-CNT	2.42 ± 1.24	15.3	40.3
Pt₃Ni/N-CNT$_{HT}$	1.87 ± 0.86	18.3	42.3
Pt₃Ni/S-CNT	2.30 ± 0.80	14.8	23.3

the effectiveness of the synthetic procedure followed in this work.

Moreover, these binding energies are also dependent on the nature of the metal. These observations could explain the strong differences between Pt₃Co and Pt₃Ni catalysts. In both cases, the theoretical Pt loading (50 wt %) is never reached, while the Co (or Ni) loading is higher than expected (theoretical content

≈7 wt %), strongly suggesting the presence of residual Co (or Ni) in these catalysts.

RRDE measurements of electrochemical surface area (ECSA) and ORR activity and selectivity

In order to proceed to a first screening of the as-prepared catalysts, their electrochemical properties were evaluated by RRDE measurements. It is worth noting that electrocatalyst investigations are usually performed with a rotating ring-disk electrode (RRDE) in acidic or alkaline media. Previous works have shown that the ORR activities of Pt catalysts are strongly dependent on the electrolyte [54]. According to these studies, activities were found to increase from H_2SO_4 to $HClO_4$ due to the specific effect of the adsorbed anion on different Pt(*hkl*) sites. Furthermore, the thin film RRDE method, with a low Nafion amount, is recommended to avoid diffusion resistance into the deposited active layer [55]. Therefore, low catalyst loadings are known to give higher activities, but these conditions are not always representative of the true working of the PEMFC [56]. Furthermore, the difficulty of dispersing CNTs in a highly

diluted ink without using a dispersing agent is a real issue, which is why we have preferred to use a higher catalyst loading ($100 \ \mu g_{Pt} \cdot cm^{-2}$).

For Pt_3Ni and Pt_3Co catalysts, the typical specific activities (expressed as kinetic current densities) for ORR at 25 °C are in the range 2.5–4.5 $mA \cdot cm^{-2}$ in $HClO_4$ [57-59] and around 0.3–0.7 $mA \cdot cm^{-2}$ in H_2SO_4 [59-61]. Interestingly, it was also reported that for Pt_3Ni and Pt_3Co catalysts in H_2SO_4, the activity increases in the order $Pt_3Ni > Pt_3Co$, and in $HClO_4$ the order of activity at 25 °C was PtCo > PtNi [59]. However, these tendencies can also be particle size dependent. Thus, it was demonstrated that in H_2SO_4, this order ($Pt_3Ni > Pt_3Co$) is respected for particles >6 nm, whereas the opposite order prevails for particle sizes smaller than 6 nm [60]. In our work, the electrochemical properties were evaluated in H_2SO_4 and compared with a commercial $Pt_3Co/Vulcan$ XC-72 (Pt_3Co/CB) catalyst. This commercial reference has shown excellent activity in RRDE and during single cell tests [5]. Figure 4a,b shows the cyclic voltammetry (CV) curves obtained in N_2-purged 0.5 M H_2SO_4 for Pt_3Co/N-CNT, Pt_3Co/N-CNT$_{HT}$, Pt_3Co/S-CNT, Pt_3Ni/N-CNT, Pt_3Ni/N-CNT$_{HT}$, Pt_3Ni/S-CNT and the commercial Pt_3Co/CB samples. For all the catalysts characterized, two small peaks at 0.14 and 0.24 V/RHE were observed, corresponding to the adsorption of H^+ on the (110) and the (100) crystallographic faces of platinum, respectively [62]. Figure 4c,d represents the current–potential curves obtained by RRDE experiments in O_2-saturated electrolyte at 900 rpm. These voltammograms are used to measure the ORR specific current density at 0.9 V/RHE. All the RRDE results are shown in Table 4.

The electrochemical surface area (ECSA) of the Pt_3Co/N-CNT and Pt_3Ni/N-CNT catalysts were higher than that of Pt_3Co/CB (NP size ≈5 nm), probably due to the smaller size of the NPs (NP size ≈2 nm). These values (23–55 $m^2 \cdot g^{-1}$) are consistent with values reported in the literature for PtCo and PtNi catalysts on CNT [31,63-66], but showing larger particle size. These values are also lower than that obtained for Pt_3Co particles with a slightly larger diameter (3.2–4.2 nm) (but on other carbon supports) where the ECSA values between 50 and 74 $m^2 \cdot g^{-1}$ were reported [67-70]. We think that remaining traces of ionic liquid adsorbed on the NP surface could be at the origin of this phenomenon. Indeed, it is not uncommon to observe an ECSA loss for Pt/C catalysts after IL modification [27].

Furthermore, we recently showed that when CNTs are used as catalyst supports, they show a tendency to form aggregates, making the accessibility of the electrolyte difficult, which could lead to a Pt utilization of 40%. For Pt_3Co/S-CNT catalysts (and

particularly the Pt_3Ni/S-CNT catalyst), a much lower ECSA was obtained.

The specific activity has been calculated for each catalyst at 0.9 V/RHE. It appears that this value is mainly driven by the ECSA. The catalyst with the lower ESCA presents a higher specific activity and the catalyst with the higher ECSA has the lowest specific activity. This effect has been previously reported in the literature [71]. Nevertheless, we need to mention that the relatively high thickness of our prepared electrodes enhances the O_2 diffusion resistance, which might enhance the surface activity for a material with lower ECSA.

This highlights the influence of the carbon support on the performance obtained in RRDE measurement. With 25.0 $A \cdot g_{Pt}^{-1}$, the activity measured for PtCo/S-CNT is slightly higher than that of the commercial reference. The value obtained for PtNi/S-CNT is significantly lower (7.9 $A \cdot g_{Pt}^{-1}$). A possible explanation could be linked to the Pt_3Ni NP–support interaction. As Pt_3Ni catalysts on S-doped carbon materials have already shown good performance for the ORR [72,73], we suspect that the explanation arises from an excessive amount of carbon support during the measurement. Indeed, the measurements were made with an equivalent Pt loading on the electrode; however, the Pt loading in PtNi/S-CNT is rather low, which should have led to a thicker active layer during RRDE measurements. This could explain the low activity of this catalyst.

The two highest ECSAs were measured for Pt_3Co/N-CNT and Pt_3Ni/N-CNT$_{HT}$ at 55.5 $m^2 \cdot g_{Pt}^{-1}$ and 46 $m^2 \cdot g_{Pt}^{-1}$, respectively. For the RRDE characterization, a thin film of the catalyst was formed at the surface of the working electrode. For each carbon support used in this study, there was a modification of the properties of the catalytic layer and certainly a strong change of the mass transfer limitation. The proton transport should be better at the surface of the N-CNT due to the nitrogen doping and the hydrophilic behavior of these carbon supports [74]. For both metals, the catalysts with the best NP distribution on the CNT walls presented the higher ECSA. In these cases, we can assume that the interactions between Nafion®, NPs and N-CNTs are optimum to allow for high activity for the ORR. It should be noted that all the catalysts synthesized on N-doped CNTs outperformed the commercial Pt_3Co/CB (22.3 $m^2 \cdot g_{Pt}^{-1}$ and 19.6 $A \cdot g_{Pt}^{-1}$) material. The highest mass densities were calculated for Pt_3Co/N-CNT, Pt_3Ni/N-CNT and Pt_3Ni/N-CNT$_{HT}$, with 50.3 $A \cdot g_{Pt}^{-1}$, 32.9 $A \cdot g_{Pt}^{-1}$ and 29.1 $A \cdot g_{Pt}^{-1}$, respectively. Different hypotheses could explain the excellent results for these two catalysts. First, the well-distributed NPs are the result of the good interaction between the transition metal and the nitrogen-doped CNT. It is known that high binding energies between the transition metal and the car-
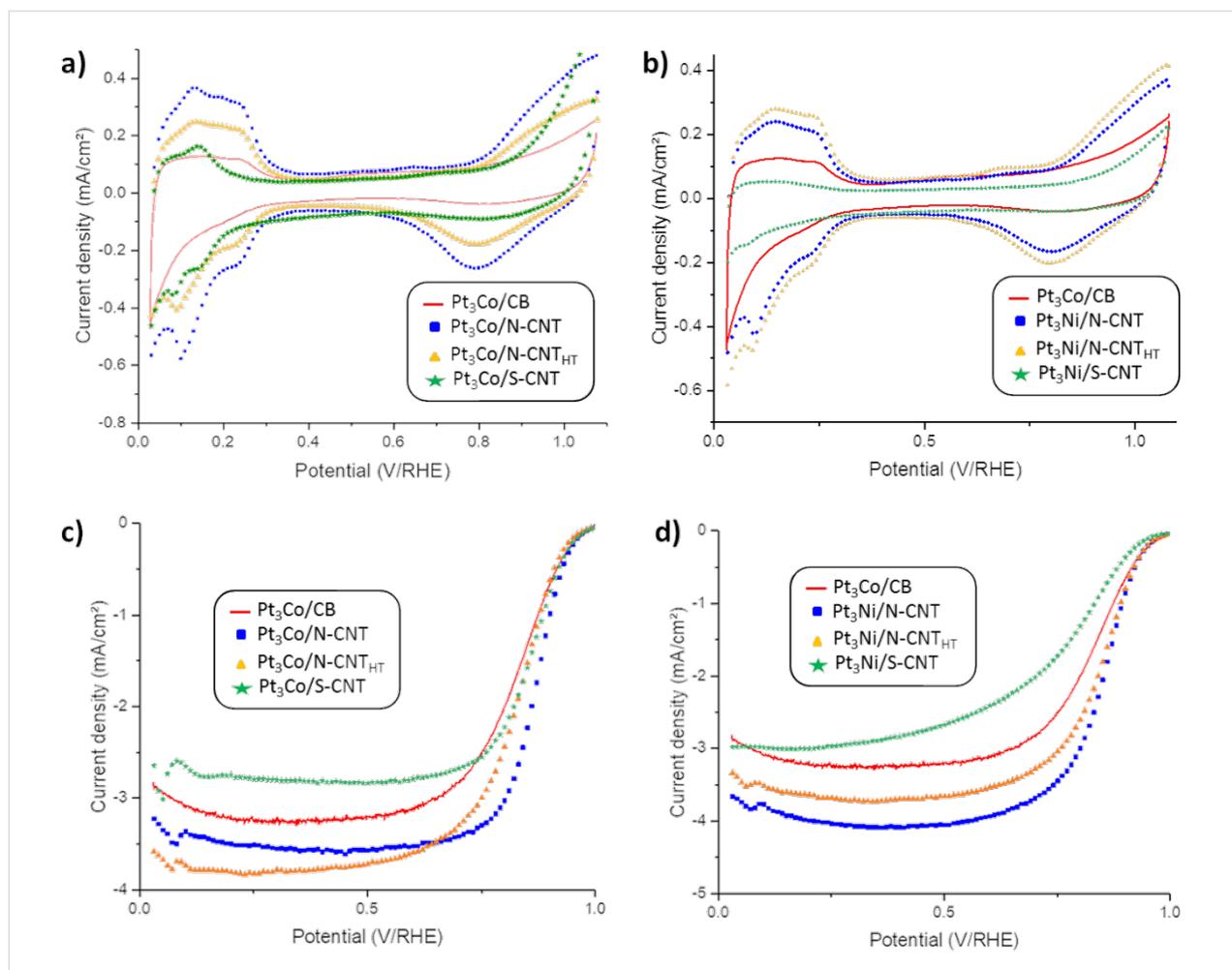
Figure 4: CVs from an RRDE experiment for the catalysts in 0.5 M H_2SO_4 at 5 mV·s^{-1} under N_2 at 25 °C for a) the Pt_3Co/CB and Pt_3Co/CNT series and b) the Pt_3Co/CB and Pt_3Ni/CNT series. Background of linear sweep voltammetry (LSV) with RRDE experiment for the catalysts in 0.5 M H_2SO_4 at 5 mV·s^{-1} at 900 rpm under O_2 at 25 °C for the c) Pt_3Co/CNT and d) Pt_3Ni/CNT series.

Table 4: Electrochemical surface area (ECSA), current density and i_K at 0.9 V/RHE for Pt_3M catalysts using RRDE experiments.

Sample	Pt loading (μg_{Pt} cm^{-2})	ECSA (m^2·g$_{Pt}^{-1}$)	Current density at 0.9 V/RHE (mA·cm^{-2})	Kinetic current at 0.9 V/RHE (mA·cm^{-2})	Specific activity at 0.9 V/RHE (A/m$^2_{Pt}$)	Mass activity at 0.9 V/RHE (A·g$_{Pt}^{-1}$)
Pt_3Co/CB	100	22.3	1.22	1.96	0.88	19.6
Pt_3Co/N-CNT	106	55.5	2.12	5.33	0.91	50.3
Pt_3Co/N-CNT$_{HT}$	100	34.9	1.29	1.97	0.56	19.7
Pt_3Co/S-CNT	99	23.1	1.30	2.47	1.08	25.0
Pt_3Ni/N-CNT	106	34.7	1.85	3.49	0.95	32.9
Pt_3Ni/N-CNT$_{HT}$	106	46.4	1.66	3.09	0.63	29.1
Pt_3Ni/S-CNT	94	5.6	0.58	0.74	1.41	7.9

bon support modify the electronic properties of the NPs and can facilitate the adsorption of the O_2. However, XPS data (vide infra) do not support this hypothesis, since the binding energy of Pt 4f electrons is consistent with Pt(0) in these two catalysts. Another hypothesis could be the particle proximity effect.

Speder et al. show the influence of the distance of the neighboring particles on the ORR activity [75]. In fact, catalysts with small inter-particles distance with no agglomeration display excellent activity. Computational investigations have shown that decreasing the inter-particle distances causes an overlap of

the electrochemical double layer. This overlap could reduce the oxide coverage of the NPs and thus increase the activity of the catalyst. Moreover, the synergetic effect of a Pt_3CO catalyst supported on Co containing N-doped carbon material has recently been demonstrated [76].

It is worth noting that the effect of support annealing is not the same for the PtCo and PtNi catalysts. On the non-heat-treated support N-CNT the activity order follows that expected from the literature for 2 nm NPs in H_2SO_4 electrolyte: $Pt_3Co > Pt_3Ni$ [58]. However, this order is reversed for the $N-CNT_{HT}$ support since the specific activity (SA) is 1.66 and 1.29 $mA \cdot cm^{-2}$ for Pt_3Ni and Pt_3Co catalysts, respectively. On Pt_3Co catalysts, the support annealing induces a pronounced decrease of both the ECSA and SA, whereas on Pt_3Ni catalysts, the annealing induces an increase of the ECSA and a slight decrease of the SA. It is thus demonstrated that the specific activity of Pt_3Ni and Pt_3Co electrocatalysts for the ORR is electrolyte- and particle-size-dependent, as is already known, but also support-dependent, at least for small (2 nm) nanoparticles. For such smaller NPs, it is plausible that a modification of the d-band center occurs upon modification of the support [77].

The ORR selectivity is also a critical issue for a PEMFC catalyst. A well-known phenomenon of catalyst degradation is due to the formation of hydrogen peroxide near the electrolyte membrane [78]. Moreover, it was shown that in aqueous KNO_3 solutions, nitrogen-doped carbon structures were active for ORR with lower H_2O_2 selectivity than Pt/C [79]. During the CV measurements in O_2-saturated electrolyte, the amount of hydrogen peroxide produced during the ORR was monitored to compare its production for each catalyst. Figure 5 presents the hydrogen peroxide yield during the ORR for all the catalysts shown before.

First, between 1 and 0.7 V/RHE the fractions of H_2O_2 produced are below 1% for all catalysts. In this voltage region, the ORR occurs only through the four electron process. The H_2O_2 production is significantly higher at low potential, between 0.05 and 0.4 V/RHE, because of the oxygen reduction on carbon [80]. The amount of H_2O_2 produced by the reference Pt_3Co/CB is higher than for all the Pt_3Co samples and most of the Pt_3Ni catalysts prepared in this study. Thus, the H_2O_2 production is not an obstacle for using these catalysts for PEMFC applications.

Structural characterization of the best catalysts

For a better understanding of the structure of these catalysts, additional characterization was carried out on the $Pt_3Co/N-CNT$ and $Pt_3Ni/N-CNT_{HT}$ samples, which presented the best perfor-
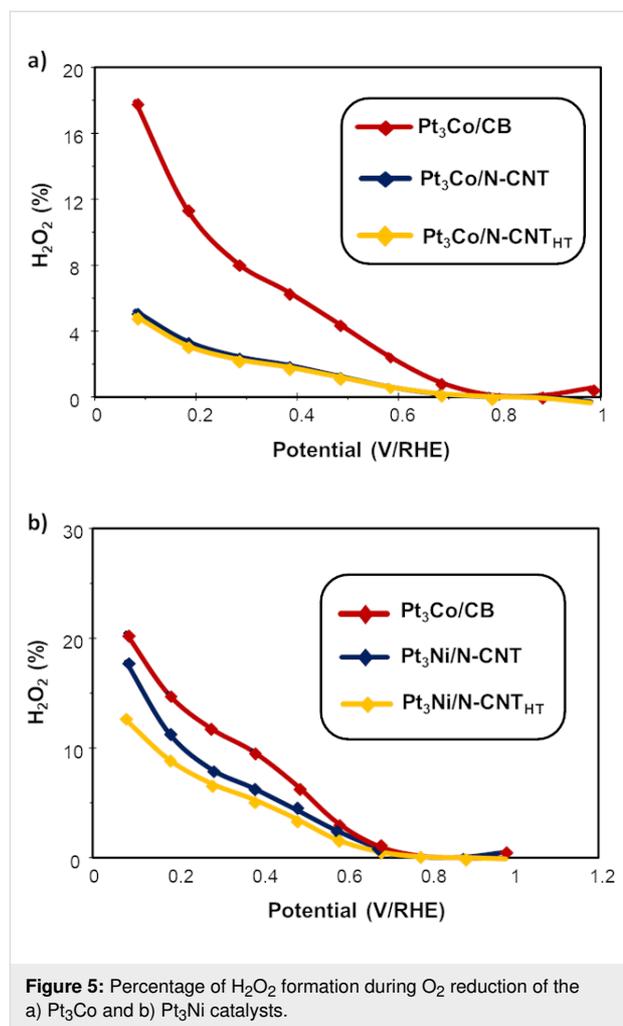
Figure 5: Percentage of H_2O_2 formation during O_2 reduction of the a) Pt_3Co and b) Pt_3Ni catalysts.

mance in the ORR. We first used HRTEM to analyze the product resulting from the first step of the catalyst preparation, i.e., the reduction of the cobalt and nickel salts. The HRTEM images of Co/N-CNT samples are depicted in Figure 6a,b.

First, no residual IL can be observed. Surprisingly, despite a high cobalt loading (52% w/w), Co NPs were also not observed on the surface of the N-CNTs. Instead, Co atoms (Figure 6a,b) and a few non-crystallized Co islands (Supporting Information File 1, Figure S7a,b) were identified using the scanning transmission electron microscopy/high-angle annular dark-field imaging (STEM-HAADF) technique. Energy-dispersive X-ray spectroscopy (EDX) analysis on the N-CNT surface or in the Co aggregates confirmed the presence of Co. The same analysis was made on the sample $Ni/N-CNT_{HT}$. There also, despite the high Ni loading (48% w/w), no Ni NPs were observed (Figure 6c,d). STEM-HAADF analysis shed light into the presence of non-crystallized Ni at the surface of the carbon support. EDX analysis confirmed the presence of Ni at the surface of the N-CNTs.

Figure 6: HRTEM images of a) Co/N-CNT and c) Ni/N-CNT$_{HT}$; and STEM-HAADF images of b) Co/N-CNT and d) Ni/N-CNT$_{HT}$.

Figure 7: HRTEM images of a) Pt$_3$Co/N-CNT and c) Pt$_3$Ni/N-CNT$_{HT}$, and STEM-HAADF images of b) Pt$_3$Co/N-CNT and d) Pt$_3$Ni/N-CNT$_{HT}$.
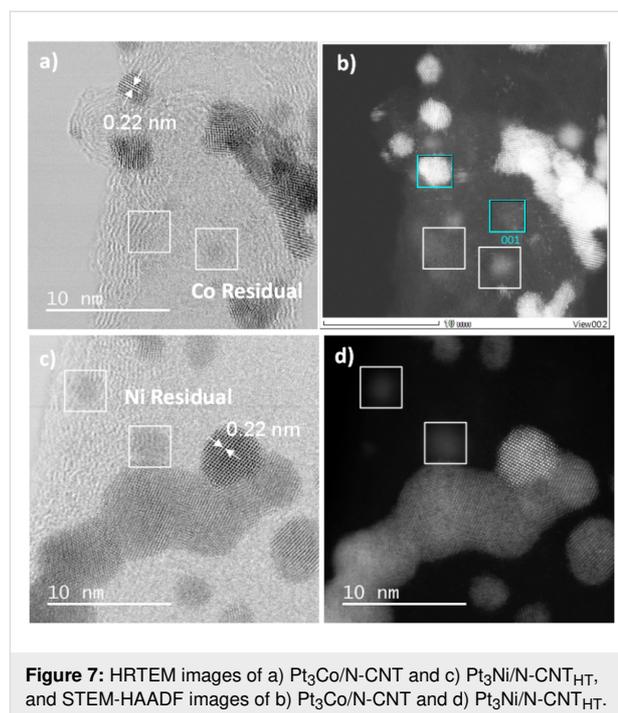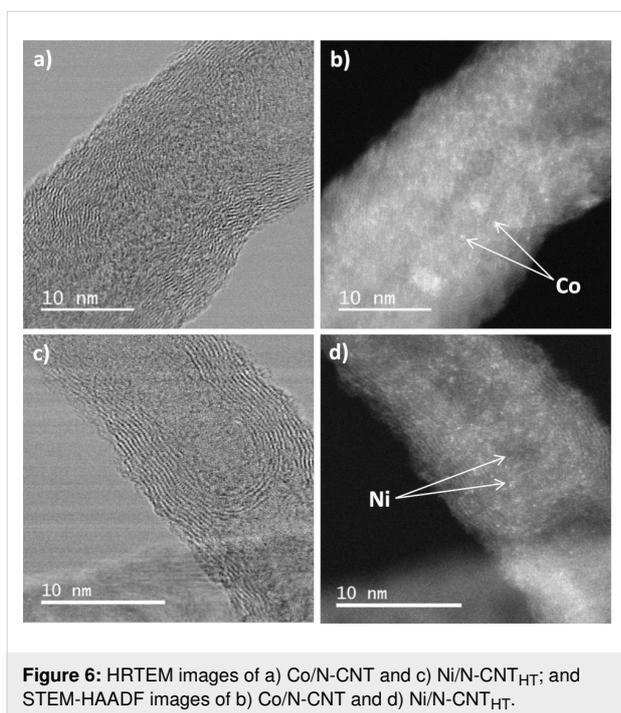
HRTEM images of the bimetallic catalysts Pt$_3$Co/N-CNT and Pt$_3$Ni/N-CNT$_{HT}$ do not evidence the formation of core–shell NPs (Figure 7). The interplanar distance of 0.22 nm was found for Pt$_3$Co/N-CNT NPs and Pt$_3$Ni/N-CNT$_{HT}$ NPs (Figure 7), which is slightly smaller than the common distance found for d$_{111}$ in Pt (0.23 nm) [81]. The slight contraction of the crystalline structure is probably due to the presence of Co (or Ni) atoms in the Pt structure. EDX spectra (Supporting Information File 1, Figure S8) reveal the presence of Co and Pt in the individual NPs (Figure 7b, 001 selected area) displaying a Pt$_3$Co composition. The absence of Co NPs in the Co/N-CNT sample, and the composition and structure of the Pt$_3$Co/N-CNTs, indicate that the Pt$_3$Co/N-CNT is more likely an alloy than a core–shell structure. The presence of residual cobalt atoms or clusters on the CNT surface was also evidenced by STEM-HAADF images of Pt$_3$Co/N-CNT (Figure 7b, 001 selected area). In the same way, the Pt$_3$Ni composition was determine by EDX analysis for the sample Pt$_3$Ni/N-CNT$_{HT}$ (Supporting Information File 1, Figure S9). This sample also displays some residual nickel atoms or clusters.

Interestingly, Co single atoms on nitrogen-doped carbon have been reported to be active for the ORR in acidic media [82-85], and Ni single atoms on nitrogen-doped carbon are known to be active for some electro-reduction reactions [86,87]. Thus, the involvement of these species in ORR cannot be discarded. Wide angle X-ray scattering (WAXS) analysis was performed on Pt$_3$Co/N-CNT and Pt$_3$Ni/N-CNT$_{HT}$ (Figure 8). After corrections and taking a Fourier transform of the scattering data, the

related pair distribution function (PDF) is well defined, with a low structural disorder. For Pt$_3$Co/N-CNT, the coherence length is close to 2.3 nm, which gives a measurement of the average size of crystalline domains.

Figure 8: WAXS analysis – red: experimental PDF from a) Pt$_3$Co/N-CNT and b) Pt$_3$Ni/N-CNT$_{HT}$, green: simulation from a spherical pure Pt model.
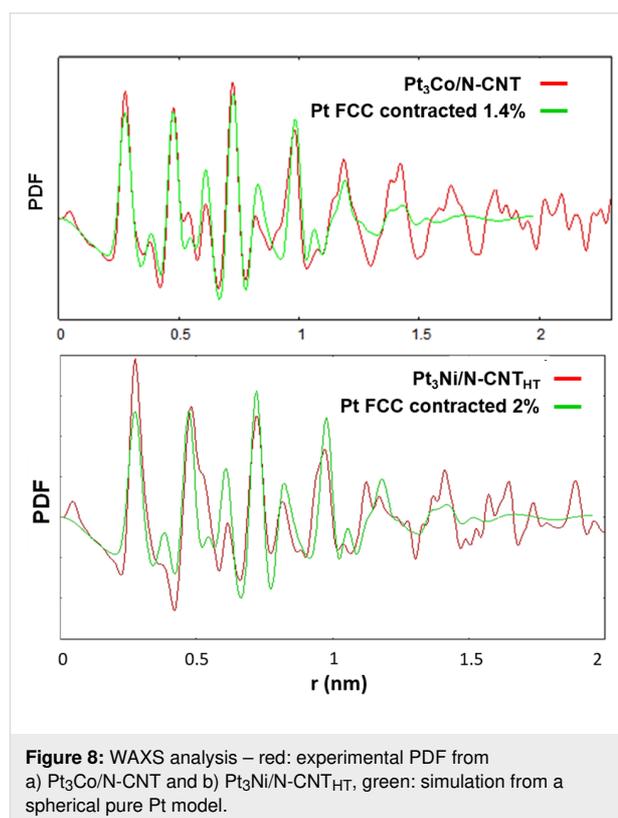
To accurately evaluate the actual cell parameter, thus the average composition, a simulation was performed from a model derived from pure Pt (spherical NPs, 2 nm in diameter).

To obtain a good agreement with the experimental data, a contraction factor of 1.4% was required, leading to a metallic bond length of 0.2721 nm, significantly shorter than in pure Pt (0.2760 nm – JCPDS 04–0802) but very close to the value in Pt_3Co also crystallized in the Fm-3m system (0.2725 nm – JCPDS 29-0499) [88]. These results indeed point to an alloyed structure since in similar studies of core–shell NPs, the bond length obtained from the PDF was clearly related to the nature of the compact core [89]. The relatively poor agreement in amplitude for longer distances indicates that most crystalline domains are close to 2 nm but that some size and/or shape dispersion compared to the model is likely. The same conclusions can be made for the sample $Pt_3Ni/N-CNT_{HT}$. To obtain a good correlation with experimental data, a contraction factor of 2% was required. Concerning the NP size, most crystalline domains are close to 2 nm, which is consistent with the TEM result (1.86 nm).

XPS analysis was performed on the $Pt_3M/N-CNT$ catalysts in order to study the electronic structure of Pt, Co and Ni (Table 5 and below in Table 6).

Table 5: Binding energies and ratio of Pt and Co species obtained from XPS spectra.

Pt₃Co/N-CNT	Species	Binding energy (eV)		Ratio (%)
		Pt 4f$_{7/2}$	Pt 4f$_{5/2}$	
Pt	Pt(0)	71.1	74.3	64.3
	PtO	72.1	75.2	12.8
	Pt(OH)$_2$	73.1	76.6	22.9
		Co 2p$_{3/2}$	Co 2p$_{1/2}$	
Co	Co(0)	778.0	792.0	3.9
	CoO	779.8	785.0	60.4
	Co(OH)$_2$	781.4	796.9	35.7

The Pt 4f region of the XPS spectrum is shown in Supporting Information File 1, Figure S10a. The spectrum was deconvoluted in three pairs of doublets (corresponding to Pt 4f$_{7/2}$ and Pt 4f$_{5/2}$). The first doublet at 71.08/74.3 eV corresponds to metallic Pt(0) [90]. The Pt surface is mainly in the metallic state (64.3 wt %). The doublets at 72.1/75.2 eV and 73.1/76.6 eV are assigned respectively to Pt(II) and Pt(IV) oxidation state species. The presence of Pt oxide and hydroxide is common for ultrafine Pt NPs [90-92]. The Co 2p region of the XPS spec-

trum (Supporting Information File 1, Figure S10b) reveals the presence of Co on the surface of the catalyst. The Co is mainly observed under oxidized state. In this area, peaks corresponding to CoO and Co(OH)$_2$ can be observed at 779.8/785.0 eV and 781.4/796.9 eV, respectively. Considering the easy oxidation of cobalt in air, cobalt is always observed under these forms when PtCo alloys are studied [60,93,94]. As far as Co single atoms on nitrogen-doped carbon materials, it has been shown that nitrogen doping of the carbon provides sites for Co incorporation. On such supports, cobalt is usually found in the ionic state in a CoN$_4$ environment. XPS characterization of Co single atoms on nitrogen-doped carbon has shown two peaks for Co at a binding energy of 781.1 and 796.2 eV [95]. However, the CoN$_4$ single atoms are usually prepared by high temperature pyrolysis, and in our case, the synthesis is conducted at room temperature. It is very unlikely that CoN$_4$ species will be formed under these conditions.

The results of the XPS analysis performed on $Pt_3Ni/N-CNT_{HT}$ revealed the species detailed in Table 6.

Table 6: Binding energies and ratio of Pt and Ni species obtained from XPS spectra.

Pt₃Ni/N-CNT$_{HT}$	Species	Binding energy (eV)		Ratio (%)
		Pt 4f$_{7/2}$	Pt 4f$_{5/2}$	
Pt	Pt(0)	71.2	74.4	60.1
	PtO	72.1	75.2	19.2
	Pt(OH)$_2$	73.1	76.3	20.7
		Ni 2p$_{3/2}$	Ni 2p$_{1/2}$	
Ni	Ni(0)	852.8	869.9	4.4
	NiO	854.3	873.3	16.4
	Ni(OH)$_2$	856.0	874.3	51.6
	NiOOH	857.6	874.6	27.6

The Pt 4f region of the XPS spectrum is shown in Supporting Information File 1, Figure S11a. The deconvolution shows three pairs of doublets (corresponding to Pt 4f$_{7/2}$ and Pt 4f$_{5/2}$). The first doublet at 71.2/74.4 eV corresponds to metallic Pt(0). The metallic state represents 60.1 wt % of the sample. The doublets at 72.1/75.2 eV and 73.1/76.6 eV are assigned to PtO and Pt(OH)$_2$ oxidation state species, respectively. The Ni 2p region of the XPS spectrum is presented in Supporting Information File 1, Figure S11b. The deconvoluted spectrum indicates that most of the Ni is present under oxidized states. In this area, doublets corresponding to NiO, Ni(OH)$_2$ and Ni(OOH) can be observed at 854.3/873.3 eV, 856.0/874.3 eV, and 857.6/874.6 eV, respectively [96]. The important concentration

of oxidized species is generally observed when PtNi alloys are studied [96,97]. As far as Ni single atoms on nitrogen-doped carbon as concerned, oxidized species have also been reported [98].

Taking into account all these results, we propose the following mechanism for the synthesis of Pt_3M NPs supported on N-CNTs. During the first step of the synthesis, the transition metal, M, will anchor the carbon surface in atomic form after reduction of the metal salt. Cobalt and nickel atoms are well-dispersed due to the use of the ILs. The addition of water for the hydrolysis of the $NaBH_4$ may explain the partial oxidation of the transition metal and the presence of residual metal in the final product, as oxidized species cannot undergo the galvanic displacement. During the galvanic replacement, the M atoms in metallic form can react with the platinum salt. After washing the catalyst and removing of the IL, Pt_3M NPs supported on N-CNTs are obtained with unreacted M atoms (and clusters) at the surface of the carbon support.

Catalyst treatment: EDTA washing

The previous characterization revealed a large amount of unalloyed cobalt or nickel species on the support surface, which can be easily dissolved in acidic media, which then poisons the protonic group of the ionomer and the proton exchange membrane [5]. The impact of dissolved Co or Ni will be much more important in MEA configuration than in RRDE testing, specifically because the poisoned sulfonic groups could not be washed by liquid electrolyte in MEA, as it could be in RRDE setup. In order to minimize the impact of the treatment on both the catalyst and its support, we avoid the classically used acid leaching method [99], but preferred using and internally developed method, based on washing the material with a solution of ethylenediaminetetraacetic acid (EDTA). This consists of dispersing the Pt_3Co/N-CNT or Pt_3Ni/N-CNT_{HT} in a 0.1 M EDTA solution and using ultrasonication. For the Pt_3Co/N-CNT catalyst, the solution become purple in a few seconds, indicating the fast and easy dissolution of the Co; while for Pt_3Ni/N-CNT_{HT}, the solution become blue after a few hours. One can suppose there is a better interaction between the Ni and the N-CNT_{HT} than the Co and the N-CNT. The catalysts were then filtered, washed with deionized water and dried for 24 hours at 80 °C.

The same structural characterization was performed on the washed Pt_3Co/N-CNT catalyst. The results of the XPS analysis are reported in Supporting Information File 1, Table S1. The data do not show significant variations of the $Pt^{(0)}/PtO/Pt(OH)_2$ and $Co^{(0)}/CoO/Co(OH)_2$-CoN_4 values, except a low decrease of the metallic content for both Pt and Co after the EDTA washing. TEM and STEM-HAADF images are reported in

Figure 9. The same interplanar distance of 0.22 nm for the NPs as before washing has been found by HRTEM (Figure 9a). The STEM-HAADF image in Figure 9b shows an important decrease of Co atoms clusters on the surface of the N-CNT, and the EDX analysis shows an important decrease of the Co amount after the washing (Supporting Information File 1, Figure S12).
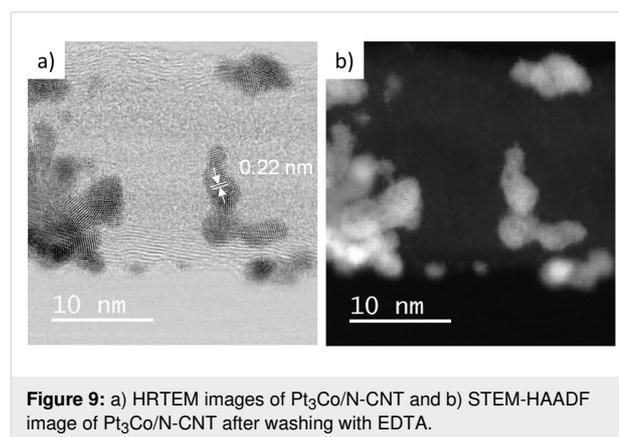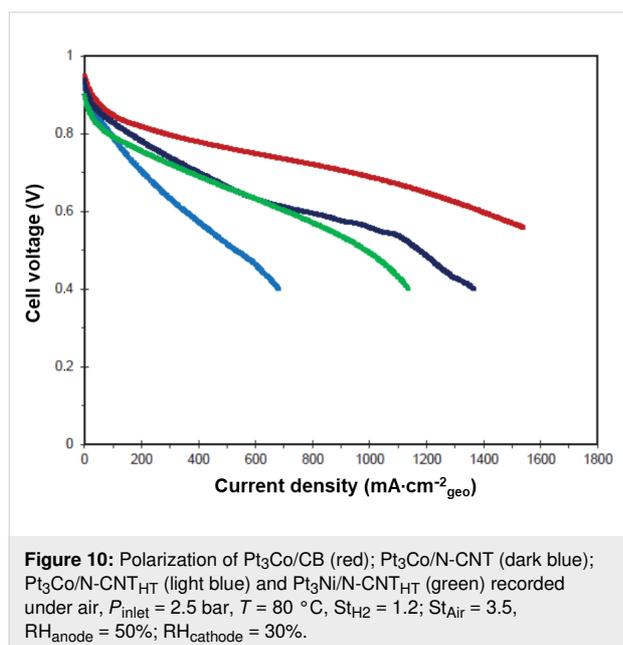

Figure 9: a) HRTEM images of Pt_3Co/N-CNT and b) STEM-HAADF image of Pt_3Co/N-CNT after washing with EDTA.

WAXS analysis was also performed. The superimposition of the PDF after and before washing is shown in Supporting Information File 1, Figure S13. The results show that the nanoparticles are metallic and well crystalized but with a mean diameter slightly larger after washing (2.6 nm) than before washing (2.3 nm). In that case, a correction factor of 1.5% should be applied to obtain a good agreement between the experimental results and a simulation performed from a model derived from pure Pt (spherical NP, 2 nm in diameter). From the TEM images, the mean diameter was calculated to be 2.4 ± 1 nm. The inductively coupled plasma optical emission spectrometry (ICP-OES) analysis give a weight ratio of 3.8% for Co and 45.5% for Pt. These results show that this new washing procedure is efficient to removed unalloyed non noble metals. Its impact on the structure of the catalyst particles is limited and, in the case of Co, it takes just a few minutes. One can assume that the conditions are mild enough to avoid damaging the catalyst support. Nevertheless, after this treatment, the catalyst composition seems to be closer to Pt_4Co than Pt_3Co.

Single cell testing and accelerated stress tests

First, the washed catalysts Pt_3Co/N-CNT, Pt_3Co/N-CNT_{HT} and Pt_3Ni/N-CNT_{HT} were integrated into the MEA with a platinum loading of 0.26, 0.24 and 0.3 mg_{Pt}/cm^2, respectively. A reference MEA, integrating the commercial reference catalyst Pt_3Co/CB with a loading of 0.3 $mg_{Pt}·cm^{-2}$, has been prepared and used as a reference. The polarization curves registered under air are reported in Figure 10. Focusing on the activation
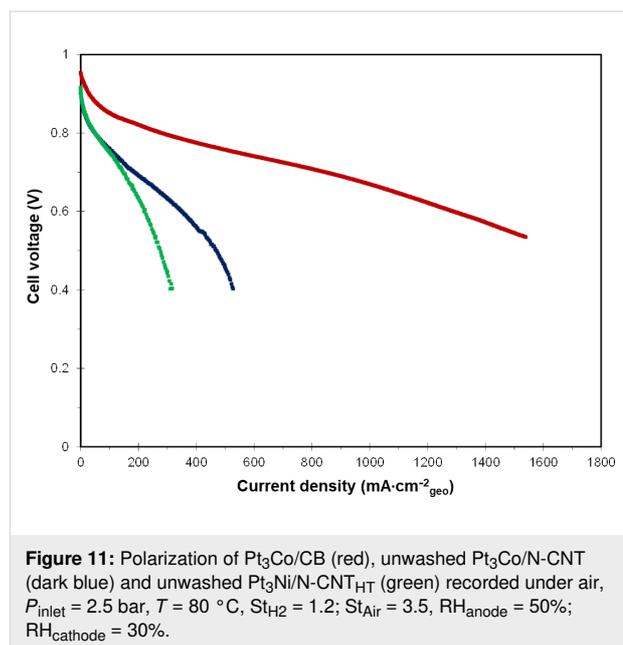
part of the curve, and as expected thanks to the RDE screening, $Pt_3Co/N\text{-}CNT$ is more active than $Pt_3Co/N\text{-}CNT_{HT}$ and $Pt_3Ni/N\text{-}CNT_{HT}$. The performance obtained under air was shown to achieve 574 mW·cm^{-2} for $Pt_3Co/N\text{-}CNT$, 278 mW·cm^{-2} for $Pt_3Co/N\text{-}CNT_{HT}$ and 494 mW·cm^{-2} for $Pt_3Ni/N\text{-}CNT_{HT}$. When the $Pt_3Co/N\text{-}CNT$ is tested under pure O_2 the power density obtained at 1.5 A·cm^{-2} is 996 mW·cm^{-2}, which is higher than the results previously reported on an MEA integrating catalysts supported on CNTs [100,101].

Figure 10: Polarization of Pt_3Co/CB (red); $Pt_3Co/N\text{-}CNT$ (dark blue); $Pt_3Co/N\text{-}CNT_{HT}$ (light blue) and $Pt_3Ni/N\text{-}CNT_{HT}$ (green) recorded under air, P_{inlet} = 2.5 bar, T = 80 °C, St_{H2} = 1.2; St_{Air} = 3.5, RH_{anode} = 50%; $RH_{cathode}$ = 30%.

The polarization curves recorded under O_2 are shown in Supporting Information File 1, Figure S14. Even this performance is still lower than the performance of the reference MEA, 863 mW·cm^{-2} under air and 1118 mW·cm^{-2} under O_2 at 1.5 A/cm^2.

To evidence the added value of the EDTA washing protocol, an MEA integrating the catalysts not treated with a solution of EDTA are shown in Figure 11. One can see that, even at very low current, the beneficial impact of the developed washing protocol is clear. We suspect that for the unwashed catalyst the non-alloyed Co or Ni could be leached during the ink preparation and then trapped by the ionomer.

Based on the quantitative analysis of the catalyst composition, it can be calculated that for the unwashed $Pt_3Co/N\text{-}CNT$, 1.5 µmol of Co^{2+} is released into the ink, for each square centimeter of prepared MEA. As the cathode contain 20% weigh ratio of Nafion (equivalent weight: 1000), each square centimeter of cathodic active layer contains 0.18 µmol of sulfonic acid site. The anode is composed of 0.2 mg$_{Pt}$·cm^{-2} and

Figure 11: Polarization of Pt_3Co/CB (red), unwashed $Pt_3Co/N\text{-}CNT$ (dark blue) and unwashed $Pt_3Ni/N\text{-}CNT_{HT}$ (green) recorded under air, P_{inlet} = 2.5 bar, T = 80 °C, St_{H2} = 1.2; St_{Air} = 3.5, RH_{anode} = 50%; $RH_{cathode}$ = 30%.

a Nafion content of 25%, which leads to 0.13 µmol of sulfonic acid site per square centimeter of MEA. According to the membrane thickness (20 µm) the Nafion density (1.02 g·mL^{-1}), and disregarding the impact of the reinforcement, it can be considered that 1 cm^2 of HP membrane contains around 2 µmol of sulfonic acid site. Therefore, the total amount of sulfonic acid group in the MEA is around 2.31 µmol·cm$^{-2}_{geo}$, which is less than two times the theoretical amount of released Co. As one Co^{2+} cation can neutralize two sulfonic acid groups, the proton transport in the MEA integrating unwashed catalyst is almost impossible, which explains such low performance, even at low current.

Electrochemical impedance spectra (EIS) were collected on single cell containing an MEA based on $Pt_3Co/N\text{-}CNT$ and Pt_3Co/CB at 0.1 A/cm^2, under air and in the same conditions as the polarization experiments. The high frequency resistance was 4.6 and 3.2 mΩ, respectively (see Supporting Information File 1, Figure S15). The higher value for the MEA integrating the catalyst supported on CNTs might be due to worse dispersion of the ionomer into the active layer and worse interface of the active layer with the membrane than with the reference catalyst. Indeed, it is known that CNTs tend to form aggregates and worsen dispersion than Vulcan-like carbon black. This was also observed in SEM images of the prepared MEA (Figure 12).

Next, the catalyst support stability was evaluated using an AST for this purpose [102]. The evolution of the polarization registered during the AST is shown is Figure 13 for both the reference MEA and the MEAs integrating the $Pt_3Co/N\text{-}CNT$ catalysts.
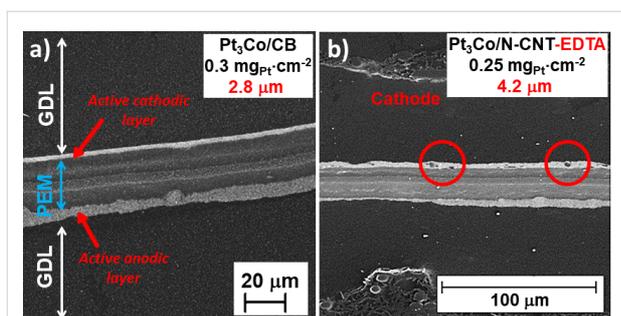
Figure 12: SEM micrographs of MEA sections prepared with Pt_3Co/CB at 0.3 $mg_{Pt} \cdot cm^{-2}$ and Pt_3Co/CNT-N at 0.25 $mg_{Pt} \cdot cm^{-2}$.
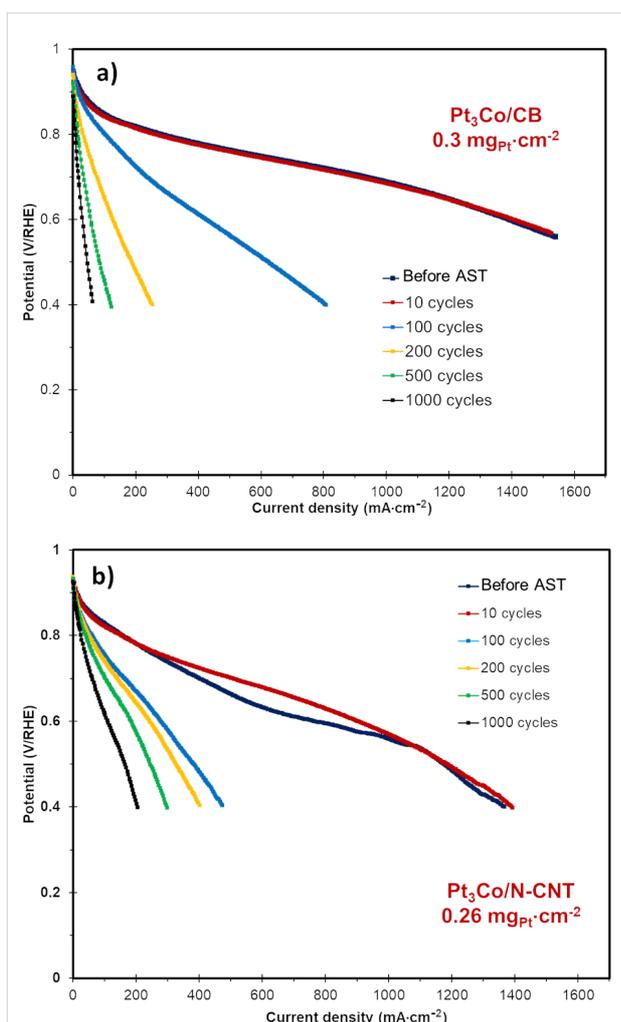

Figure 13: Polarization curves performed on MEAs integrating: a) Pt_3Co/CB; and b) Pt_3Co/N-CNT. Dark blue: after conditioning, red: after 10 cycles, light blue: after 100 cycles, yellow: after 200 cycles, green: after 500 cycles and black: after 1000 cycles.

It can be observed that the degradation rate for the catalyst supported on N-CNTs is slower than the reference commercial catalyst. Indeed, even if the beginning-of-life performance of

the reference MEA is better, after only 200 cycles, the performance of the Pt_3Co/N-CNT MEA is then better. This validates the robustness of the synthesized catalyst.

Conclusion

In summary, a series of undoped, S- and N-doped CNTs have been synthetized by c-CVD. These carbon materials have been used together with an ionic liquid as a support structure for bimetallic Pt_3Co and Pt_3Ni NPs by a transmetalation method. The nature of the support significantly produced the NP distribution on the supports. For Pt_3Co catalysts, a high metal loading (>45% w/w) and small NP size (<2 nm) was obtained on the support presenting the higher nitrogen content. Surprisingly, for Pt_3Ni catalysts, a higher loading and smaller particle size was obtained on N-doped CNTs that were submitted to a high temperature treatment, which decreased the nitrogen content. HRTEM, WAXS and XPS analyses of the Pt_3Co and Pt_3Ni samples revealed that bimetallic Pt_3M NP alloys were obtained with this method. Residual cobalt or nickel atoms were also present on the N-CNT surface. The experimental results showed enhanced catalytic performance for catalysts prepared with N-CNTs compared to the S-CNTs and commercial $Pt_3Co/$CB catalysts. The best results were obtained for Pt_3Co that used the more hydrophilic supports (N-CNT), and for Pt_3Ni with the heat-treated N-CNT$_{HT}$ supports. Interestingly, our study shows that the catalytic performance is support-dependent. For the N-CNT support, the SA followed the trend $Pt_3Co > Pt_3Ni$, in accordance with literature reports; whereas for N-CNT$_{HT}$, the SA followed the opposite order.

The use of Pt_3M/N-CNT catalysts results in the reduction in the quantity of H_2O_2 produced during the ORR compared to the commercial Pt_3Co/CB catalyst. After ex situ validation of the catalyst, the treatment with EDTA solution to remove unalloyed non noble metals (Co or Ni) was employed. The electrochemical characterization of the MEA containing washed and unwashed catalysts validated this new protocol. The ageing tests (AST), characterizing the catalyst support degradation, showed better resistance toward degradation of the Pt_3Co/N-CNT than the reference Pt_3Co/CB catalyst. Beyond these results, our future works will focus on the end-of-life analysis on the aged MEA and on the integration of catalysts supported on CNTs in the active layer to increase the beginning-of-life performance of the MEA.

Experimental

The metal precursors used for the syntheses were purchased from Strem Chemicals Inc., the ionic liquid was purchased from Solvionic, and the other chemicals were purchased from Sigma-Aldrich. All operations were carried out under argon atmosphere using standard Schlenk techniques or in an MBraun

glovebox. For comparison purpose, the commercial catalyst Pt_3Co/CB consists of 6 wt % Co, 46.7 wt % Pt on carbon black from Tanaka Kikinzoku Kogyo (reference TEC36V52) with NPs of around 5 nm.

CNT synthesis and functionalization

CNTs were grown using a catalytic-CVD process: ethylene as a carbon source, acetonitrile as a nitrogen/carbon source and thiophene as a sulfur/carbon source were decomposed at 650 °C on a Fe/Al_2O_3 catalyst in a vertical oven to produce CNTs and N-CNTs. First, the catalyst was reduced under argon/hydrogen (Ar/H_2 (1.5/1): 375 mL·min^{-1}) during 30 min at 650 °C. Undoped structures (called CNTs) were prepared from ethylene/H_2 (375 mL·min^{-1} (1.5/1)) mixtures, N-doped structures (called N-CNTs) from acetonitrile/Ar/H_2 (375 mL·min^{-1}, Ar/H_2 (1.5/1) bubbling through acetonitrile at 35 °C, 0.19 bar vapor pressure), and S-doped structures (called S-CNTs) according to a published procedure [103]. All CNTs were purified with a refluxing mixture of H_2O/H_2SO_4 (50/50 v/v) for 3 h to remove the catalyst. The annealing of the N-CNTs was carried out at 1000 °C. 0.5 g of sample was placed in the chamber of a horizontal oven under Ar (200 mL·min^{-1}). The annealing temperature was reached with a rate of 10 °C·min^{-1} and held for 2 h. Finally, the sample was cooled down to room temperature under Ar to obtain N-CNT$_{HT}$.

Catalyst preparation

The Pt_3Co/CNT catalysts were prepared following a modified procedure reported elsewhere [23]. Here, the ionic liquid, 1-butyl-3-methylimidazolium bis(trifluoromethanesulfonyl)imide ([bmim][Tf$_2$N]) was used as a stabilizer in order to increase the interaction between the carbon support and the metallic salt and favor the formation of small nanoparticles. 2.04 mmol of $CoCl_2·6H_2O$ were dissolved in 60 mL of ethanol and added in a 30 mL ethanol solution containing 0.2 g of CNTs and 0.48 mmol of [bmim][Tf$_2$N]. The reaction mixture was sonicated for 20 min and then stirred vigorously. A freshly prepared $NaBH_4$ solution in ethanol (0.15 mol·L^{-1}) was added to the reaction mixture and allowed to react for 30 min. Afterwards, 100 mL of deionized water were added and the suspension was stirred for 3 h. Next, 1.27 mmol of K_2PtCl_4 was dissolved in 60 mL of deionized water added to the solution. After stirring overnight, the solution was filtered; the product was washed with ethanol and deionized water, and finally dried at 80 °C. The Pt_3Ni/CNT catalysts were prepared using the same procedure using $NiCl_2·6H_2O$ as the metal precursor.

Characterization

The samples were characterized using transmission electron microscopy (TEM, JEOL, JEM-1011 at 100 kV) and high-resolution TEM (HRTEM, JEM-ARM200F Cold FEG, STEM-EDX CENTURIO-X, GATAN Gif quantum ER), chemical analysis (CHN Perkin Elmer elemental analyzer), Raman spectroscopy at 633 nm (SmartsSPM-1000 AIST-NT) and thermal analysis under air (thermobalance Perkin Elmer Diamond TG). The textural characterization (BET surface area, S_{BET}) of the material was evaluated by N_2 adsorption–desorption analysis at −196 °C using a Quantachrome autosorb device. X-ray photoelectron spectroscopy (XPS) was performed on a ThermoScientific XPS K-alpha apparatus, which operated with an achromatized Mg K source (1253.6 eV). Pt and Co loadings were determined by inductively coupled plasma optical emission spectrometry (ICP-OES) analysis (Thermo Scientific, ICAP 6300 instrument). Wide angle X-ray scattering (WAXS) measurements were performed on a diffractometer dedicated to pair distribution function (PDF) analyses: graphite-monochromatized molybdenum radiation (0.07169 nm), solid state detection and low background setup. The samples were sealed in Lindemann glass capillaries (diameter 1.5 mm).

The MEA cross-sections were prepared by first cutting MEA samples (8 × 8 mm^2) and embedding them in epoxy resin. Then, the MEA cross-sections were prepared by mechanical polishing until a mirror-like surface was achieved and were observed using a Zeiss FEG-SEM LEO1530.

Electrochemical measurements
RRDE measurements

The electrochemical properties of the prepared catalysts were investigated in a three-electrode system in 0.5 M H_2SO_4 solution at room temperature using a RRDE. A saturated mercury sulfate electrode (MSE, Bioanalytical system Inc., RE-2C) was used as the reference electrode and a platinum wire as the counter electrode (CE). All the potentials are presented to the reversible hydrogen electrode (RHE). The measurements were carried out using a BIOLOGIC VSP potentiostat. The used RRDE is the model AFE7R9GCPT from PINE research, and the disk is glassy carbon with an area of 0.2475 cm^2. The ring is in Pt with a collection factor of 37%. The electrode is polished with 1 μm diamond paste and 0.05 μm alumina paste before use. The RRDE electrodes were prepared from a suspension of PtCo/CNT catalyst in 4 mL of isopropanol/DI water/Nafion® dispersion (type D-2020 from Dupont Fluoroproduct, 20% Nafion® dissolved in aliphatic alcohol) (80/19.5/0.5), and sonicated for 30 min. 30 μL of the prepared ink was deposited three times onto the polished glassy carbon disk electrode. A thin catalytic layer with a Pt loading of 100 μgPt/cm^2 was obtained after evaporation of the solvent under air at room temperature. The electroactive surface area (ECSA) was calculated from the second cyclic voltammetry (CV) curves using an electrolyte saturated with N_2 at 5 mV·s^{-1}, from 0.04 to 1.08 V/RHE. The ECSA was estimated by integrating the current in the hydrogen

desorption region between 0.04 and 0.4 V/RHE on the positive-going potential scan, corrected by the double layer current at 0.4 V/RHE and assuming 210 μC·cm^{-2}$_{(Pt)}$ (Table 5). The activity was measured on the cyclic voltamograms using an electrolyte saturated with O_2 at 5 mV·s^{-1} from 0.04 to 1.08 V/RHE fixing the rotation speed to 900 rpm The rotation is controlled by a PINE Research Instrumentation/model AFMSRCE device. The current density is normalized to the geometric surface area of the glassy carbon (0.247 cm^2). The kinetic current is calculated following the equation:

$$\frac{1}{|i|} = \frac{1}{|i_d|} + \frac{1}{i_k},$$

where i is the measured current at 0.9 V/RHE under O_2 and corrected by a reference measurement made under N_2 at the same potential and i_d is the measured current at 0.4 V/RHE under O_2 and corrected by a reference measurement made under N_2 at the same potential. There is no internal resistance correction.

The mass activity is finally obtained using the kinetic current density and the mass of the Pt loaded on the electrode. While the ORR occurs on the disk, the ring current was recorded, corresponding to H_2O_2 oxidation. This method was already reported elsewhere [104].

Single cell testing and accelerated stress tests

The single cell tests were performed using a Green Light (GL-40) test station. A graphite monopolar plate with a single serpentine flow field and 1 mm channel and landing dimensions were used. The active areas were 25 cm^2. The polarization curves were recorded under current control, from open-circuit voltage (OCV) to high current with a ramping of 2 A·min^{-1}. The polarization curves were recorded at 80 °C, with a pressure inlet of 2.5 bar on both sides, a stoichiometry of 1.2 at the anode side and 3.5 at the cathode side when air was used, or 5 when pure O_2 was used. The relative humidity was managed by boilers and the values are 50% at the anode and 30% at the cathode. The conditioning is performed under air by maintaining the cell voltage at 0.5 V for 8 h, the operating conditions are similar but the relative humidity fixed at 100% on both sides.

For the ASTs, the cell was maintained at 80 °C, and the inlet pressure was 2.5 bar. The anode and cathode were fed with H_2 and N_2, respectively, both with 100% relative humidity. The cell voltage was controlled by a Gamry Instruments reference 3000 potentiostat. The cell voltage was cycled between 1.0 V and 1.5 V with a scan rate of 500 mV·s^{-1}. The polarization curves were registered under air after 10, 100, 200, 500 and 1000 cycles. The MEAs were prepared by hot pressing gas diffusion electrodes on a reinforced HP Nafion$^®$ membrane. The cathodes were prepared by manually spraying the cathodic active layer on the gas diffusion layer (GDL) (SGL-sigracet$^®$ 24 BC). The used ionomer was Nafion$^®$ D2020, its dry extract in the active layer is 20% for the synthesized catalysts and 25% for the commercial catalyst. The anode catalyst is Pt/CB 50% weight ratio from TKK, the loading of the anode is 0.2 mg$_{Pt}$/cm^2 and the gas diffusion electrode was prepared by screen printing.

Supporting Information

Supporting Information File 1
Additional experimental data.
[https://www.beilstein-journals.org/bjnano/content/supplementary/2190-4286-10-125-S1.pdf]

ORCID$^®$ iDs
Yohann R. J. Thomas - https://orcid.org/0000-0002-9100-2583
Pierre Lecante - https://orcid.org/0000-0001-6337-6855
Marie Heitzmann - https://orcid.org/0000-0003-4394-9219
Philippe Serp - https://orcid.org/0000-0003-1424-2724

References
1. Wilberforce, T.; Alaswad, A.; Palumbo, A.; Dassisti, M.; Olabi, A. G. *Int. J. Hydrogen Energy* **2016**, *41*, 16509–16522. doi:10.1016/j.ijhydene.2016.02.057
2. Gallo, A. B.; Simões-Moreira, J. R.; Costa, H. K. M.; Santos, M. M.; Moutinho dos Santos, E. *Renewable Sustainable Energy Rev.* **2016**, *65*, 800–822. doi:10.1016/j.rser.2016.07.028
3. Antolini, E. *J. Mater. Sci.* **2003**, *38*, 2995–3005. doi:10.1023/a:1024771618027
4. Marković, N. M.; Ross, P. N. *Surf. Sci. Rep.* **2002**, *45*, 117–229. doi:10.1016/s0167-5729(01)00022-x
5. Gasteiger, H. A.; Kocha, S. S.; Sompalli, B.; Wagner, F. T. *Appl. Catal., B* **2005**, *56*, 9–35. doi:10.1016/j.apcatb.2004.06.021
6. Pavlišič, A.; Jovanovič, P.; Šelih, V. S.; Šala, M.; Hodnik, N.; Gaberšček, M. *J. Electrochem. Soc.* **2018**, *165*, F3161–F3165. doi:10.1149/2.0191806jes
7. Bodner, M.; Senn, J.; Hacker, V. Chapter 7 - Degradation Mechanisms and Their Lifetime. In *Fuel Cells and Hydrogen*; Hacker, V.; Mitsushima, S., Eds.; Elsevier, 2018; pp 139–154. doi:10.1016/b978-0-12-811459-9.00007-4

8. Meier, J. C.; Galeano, C.; Katsounaros, I.; Topalov, A. A.; Kostka, A.;
    Schüth, F.; Mayrhofer, K. J. J. *ACS Catal.* **2012,** *2,* 832–843.
    doi:10.1021/cs300024h

9. de Bruijn, F. A.; Dam, V. A. T.; Janssen, G. J. M. *Fuel Cells* **2008,** *8,*
    3–22. doi:10.1002/fuce.200700053

10. Macauley, N.; Papadias, D. D.; Fairweather, J.; Spernjak, D.;
    Langlois, D.; Ahluwalia, R.; More, K. L.; Mukundan, R.; Borup, R. L.
    J. Electrochem. Soc. **2018,** *165,* F3148–F3160.
    doi:10.1149/2.0061806jes

11. Roen, L. M.; Paik, C. H.; Jarvi, T. D. *Electrochem. Solid-State Lett.*
    2004, *7,* A19–A22. doi:10.1149/1.1630412

12. Lv, H.; Li, D.; Strmcnik, D.; Paulikas, A. P.; Markovic, N. M.;
    Stamenkovic, V. R. *Nano Energy* **2016,** *29,* 149–165.
    doi:10.1016/j.nanoen.2016.04.008

13. Kulkarni, A.; Siahrostami, S.; Patel, A.; Nørskov, J. K. *Chem. Rev.*
    2018, *118,* 2302–2312. doi:10.1021/acs.chemrev.7b00488

14. Shao, M.; Chang, Q.; Dodelet, J.-P.; Chenitz, R. *Chem. Rev.* **2016,**
    116, 3594–3657. doi:10.1021/acs.chemrev.5b00462

15. Hwang, S. J.; Yoo, S. J.; Shin, J.; Cho, Y.-H.; Jang, J. H.; Cho, E.;
    Sung, Y.-E.; Nam, S. W.; Lim, T.-H.; Lee, S.-C.; Kim, S.-K. *Sci. Rep.*
    2013, *3,* 1309. doi:10.1038/srep01309

16. Wang, L.; Gao, W.; Liu, Z.; Zeng, Z.; Liu, Y.; Giroux, M.; Chi, M.;
    Wang, G.; Greeley, J.; Pan, X.; Wang, C. *ACS Catal.* **2018,** *8,* 35–42.
    doi:10.1021/acscatal.7b02501

17. Wang, D.; Xin, H. L.; Hovden, R.; Wang, H.; Yu, Y.; Muller, D. A.;
    DiSalvo, F. J.; Abruña, H. D. *Nat. Mater.* **2013,** *12,* 81–87.
    doi:10.1038/nmat3458

18. Lin, R.; Cao, C.; Zhao, T.; Huang, Z.; Li, B.; Wieckowski, A.; Ma, J.
    J. Power Sources **2013,** *223,* 190–198.
    doi:10.1016/j.jpowsour.2012.09.073

19. Chen, Y.; Liang, Z.; Yang, F.; Liu, Y.; Chen, S. *J. Phys. Chem. C*
    2011, *115,* 24073–24079. doi:10.1021/jp207828n

20. Zhao, X.; Takao, S.; Higashi, K.; Kaneko, T.; Samjeskè, G.;
    Sekizawa, O.; Sakata, T.; Yoshida, Y.; Uruga, T.; Iwasawa, Y.
    ACS Catal. **2017,** *7,* 4642–4654. doi:10.1021/acscatal.7b00964

21. Zhu, H.; Li, X.; Wang, F. *Int. J. Hydrogen Energy* **2011,** *36,*
    9151–9154. doi:10.1016/j.ijhydene.2011.04.224

22. Kuttiyiel, K. A.; Sasaki, K.; Choi, Y.; Su, D.; Liu, P.; Adzic, R. R.
    Nano Lett. **2012,** *12,* 6266–6271. doi:10.1021/nl303362s

23. Kristian, N.; Yu, Y.; Lee, J.-M.; Liu, X.; Wang, X. *Electrochim. Acta*
    2010, *56,* 1000–1007. doi:10.1016/j.electacta.2010.09.073

24. Zhang, C.; Shen, X.; Pan, Y.; Peng, Z. *Front. Energy* **2017,** *11,*
    268–285. doi:10.1007/s11708-017-0466-6

25. Bing, Y.; Liu, H.; Zhang, L.; Ghosh, D.; Zhang, J. *Chem. Soc. Rev.*
    2010, *39,* 2184–2202. doi:10.1039/b912552c

26. Tunckol, M.; Durand, J.; Serp, P. *Carbon* **2012,** *50,* 4303–4334.
    doi:10.1016/j.carbon.2012.05.017

27. Zhang, G.-R.; Wolker, T.; Sandbeck, D. J. S.; Munoz, M.;
    Mayrhofer, K. J. J.; Cherevko, S.; Etzold, B. J. M. *ACS Catal.* **2018,** *8,*
    8244–8254. doi:10.1021/acscatal.8b02018

28. Guo, S.; Dong, S.; Wang, E. *Adv. Mater. (Weinheim, Ger.)* **2010,** *22,*
    1269–1272. doi:10.1002/adma.200903379

29. Luo, C.; Xie, H.; Wang, Q.; Luo, G.; Liu, C. *J. Nanomater.* **2015,**
    560392. doi:10.1155/2015/560392

30. Akbari, E.; Buntat, Z. *Int. J. Energy Res.* **2017,** *41,* 92–102.
    doi:10.1002/er.3600

31. Asset, T.; Job, N.; Busby, Y.; Crisci, A.; Martin, V.; Stergiopoulos, V.;
    Bonnaud, C.; Serov, A.; Atanassov, P.; Chattot, R.; Dubau, L.;
    Maillard, F. *ACS Catal.* **2018,** *8,* 893–903.
    doi:10.1021/acscatal.7b03539

32. Ayala, P.; Arenal, R.; Rümmeli, M.; Rubio, A.; Pichler, T. *Carbon*
    2010, *48,* 575–586. doi:10.1016/j.carbon.2009.10.009

33. Kiciński, W.; Szala, M.; Bystrzejewski, M. *Carbon* **2014,** *68,* 1–32.
    doi:10.1016/j.carbon.2013.11.004

34. Fan, J.-J.; Fan, Y.-J.; Wang, R.-X.; Xiang, S.; Tang, H.-G.; Sun, S.-G.
    J. Mater. Chem. A **2017,** *5,* 19467–19475. doi:10.1039/c7ta05102f

35. Chen, Y.; Wang, J.; Liu, H.; Banis, M. N.; Li, R.; Sun, X.; Sham, T.-K.;
    Ye, S.; Knights, S. *J. Phys. Chem. C* **2011,** *115,* 3769–3776.
    doi:10.1021/jp108864y

36. Chen, J.; Shan, J. Y.; Tsukada, T.; Munekane, F.; Kuno, A.;
    Matsuo, M.; Hayashi, T.; Kim, Y. A.; Endo, M. *Carbon* **2007,** *45,*
    274–280. doi:10.1016/j.carbon.2006.09.028

37. Fujisawa, K.; Tojo, T.; Muramatsu, H.; Elías, A. L.; Vega-Díaz, S. M.;
    Tristán-López, F.; Kim, J. H.; Hayashi, T.; Kim, Y. A.; Endo, M.;
    Terrones, M. *Nanoscale* **2011,** *3,* 4359–4364.
    doi:10.1039/c1nr10717h

38. Liu, H.; Zhang, Y.; Li, R.; Sun, X.; Abou-Rachid, H. *J. Nanopart. Res.*
    2012, *14,* 1016. doi:10.1007/s11051-012-1016-0

39. Podyacheva, O. Y.; Cherepanova, S. V.; Romanenko, A. I.;
    Kibis, L. S.; Svintsitskiy, D. A.; Boronin, A. I.; Stonkus, O. A.;
    Suboch, A. N.; Puzynin, A. V.; Ismagilov, Z. R. *Carbon* **2017,** *122,*
    475–483. doi:10.1016/j.carbon.2017.06.094

40. Cançado, L. G.; Jorio, A.; Martins Ferreira, E. H.; Stavale, F.;
    Achete, C. A.; Capaz, R. B.; Moutinho, M. V. O.; Lombardo, A.;
    Kulmala, T. S.; Ferrari, A. C. *Nano Lett.* **2011,** *11,* 3190–3196.
    doi:10.1021/nl201432g

41. DiLeo, R. A.; Landi, B. J.; Raffaelle, R. P. *J. Appl. Phys.* **2007,** *101,*
    064307. doi:10.1063/1.2712152

42. Serp, P.; Machado, B. CHAPTER 4 Surface Chemistry of
    Nanostructured Carbon Materials and Preparation of Nanocarbon
    Supported Catalysts. *Nanostructured Carbon Materials for Catalysis;*
    The Royal Society of Chemistry, 2015; pp 163–222.
    doi:10.1039/9781782622567-00163

43. Mattila, S.; Leiro, J. A.; Laajalehto, K. *Appl. Surf. Sci.* **2003,** *212–213,*
    97–100. doi:10.1016/s0169-4332(03)00413-6

44. Shahgaldi, S.; Hamelin, J. *Carbon* **2015,** *94,* 705–728.
    doi:10.1016/j.carbon.2015.07.055

45. Du, L.; Shao, Y.; Sun, J.; Yin, G.; Liu, J.; Wang, Y. *Nano Energy* **2016,**
    29, 314–322. doi:10.1016/j.nanoen.2016.03.016

46. Wu, B.; Hu, D.; Yu, Y.; Kuang, Y.; Zhang, X.; Chen, J.
    Chem. Commun. **2010,** *46,* 7954–7956. doi:10.1039/c0cc02956d

47. Wang, J.; Chu, H.; Li, Y. *ACS Nano* **2008,** *2,* 2540–2546.
    doi:10.1021/nn800510g

48. Janiak, C. *Z. Naturforsch., B: J. Chem. Sci.* **2013,** *68,* 1059–1087.
    doi:10.5560/znb.2013-3140

49. Cao, C.; Wu, M.; Jiang, J.; Cheng, H.-P. *Phys. Rev. B* **2010,** *81,*
    205424. doi:10.1103/physrevb.81.205424

50. Sessi, V.; Stepanow, S.; Rudenko, A. N.; Krotzky, S.; Kern, K.;
    Hiebel, F.; Mallet, P.; Veuillen, J.-Y.; Šipr, O.; Honolka, J.;
    Brookes, N. B. *New J. Phys.* **2014,** *16,* 062001.
    doi:10.1088/1367-2630/16/6/062001

51. Makaremi, M.; Mortazavi, B.; Singh, C. V. *J. Phys. Chem. C* **2017,**
    121, 18575–18583. doi:10.1021/acs.jpcc.7b04511

52. Kattel, S. *RSC Adv.* **2013,** *3,* 21110–21117. doi:10.1039/c3ra43810d

53. Hu, L.; Hu, X.; Wu, X.; Du, C.; Dai, Y.; Deng, J.
    Phys. B (Amsterdam, Neth.) **2010,** *405,* 3337–3341.
    doi:10.1016/j.physb.2010.05.001

54. Nesselberger, M.; Ashton, S.; Meier, J. C.; Katsounaros, I.;
    Mayrhofer, K. J. J.; Arenz, M. *J. Am. Chem. Soc.* **2011,** *133,*
    17428–17433. doi:10.1021/ja207016u

55. Paulus, U. A.; Schmidt, T. J.; Gasteiger, H. A.; Behm, R. J.
    J. Electroanal. Chem. **2001,** *495,* 134–145.
    doi:10.1016/s0022-0728(00)00407-1

56. Shih, Y.-H.; Sagar, G. V.; Lin, S. D. *J. Phys. Chem. C* **2008,** *112,*
    123–130. doi:10.1021/jp071807h

57. Stamenkovic, V. R.; Mun, B. S.; Mayrhofer, K. J. J.; Ross, P. N.;
    Markovic, N. M. *J. Am. Chem. Soc.* **2006,** *128,* 8813–8819.
    doi:10.1021/ja0600476

58. Wang, C.; van der Vliet, D.; Chang, K.-C.; You, H.; Strmcnik, D.;
    Schlueter, J. A.; Markovic, N. M.; Stamenkovic, V. R.
    J. Phys. Chem. C **2009,** *113,* 19365–19368. doi:10.1021/jp908203p

59. Stamenković, V.; Schmidt, T. J.; Ross, P. N.; Marković, N. M.
    J. Phys. Chem. B **2002,** *106,* 11970–11979. doi:10.1021/jp021182h

60. Loukrakpam, R.; Luo, J.; He, T.; Chen, Y.; Xu, Z.; Njoki, P. N.;
    Wanjala, B. N.; Fang, B.; Mott, D.; Yin, J.; Klar, J.; Powell, B.;
    Zhong, C.-J. *J. Phys. Chem. C* **2011,** *115,* 1682–1694.
    doi:10.1021/jp109630n

61. Xu, Y.; Hou, S.; Liu, Y.; Zhang, Y.; Wang, H.; Zhang, B.
    Chem. Commun. **2012,** *48,* 2665–2667. doi:10.1039/c2cc16798k

62. Yamamoto, K.; Kolb, D. M.; Kötz, R.; Lehmpfuhl, G.
    J. Electroanal. Chem. Interfacial Electrochem. **1979,** *96,* 233–239.
    doi:10.1016/s0022-0728(79)80380-0

63. Vinayan, B. P.; Ramaprabhu, S. *Nanoscale* **2013,** *5,* 5109–5118.
    doi:10.1039/c3nr00585b

64. Du, S.; Lu, Y.; Malladi, S. K.; Xu, Q.; Steinberger-Wilckens, R.
    J. Mater. Chem. A **2014,** *2,* 692–698. doi:10.1039/c3ta13608f

65. Rosado, G.; Verde, Y.; Valenzuela-Muñiz, A. M.; Barbosa, R.;
    Miki Yoshida, M.; Escobar, B. *Int. J. Hydrogen Energy* **2016,** *41,*
    23260–23271. doi:10.1016/j.ijhydene.2016.07.098

66. Huang, H.; Fan, Y.; Wang, X. *Electrochim. Acta* **2012,** *80,* 118–125.
    doi:10.1016/j.electacta.2012.06.129

67. Choi, D. S.; Robertson, A. W.; Warner, J. H.; Kim, S. O.; Kim, H.
    Adv. Mater. (Weinheim, Ger.) **2016,** *28,* 7115–7122.
    doi:10.1002/adma.201600469

68. Oezaslan, M.; Hasché, F.; Strasser, P. *J. Electrochem. Soc.* **2012,**
    159, B394–B405. doi:10.1149/2.075204jes

69. Vinayan, B. P.; Imran Jafri, R.; Nagar, R.; Rajalakshmi, N.;
    Sethupathi, K.; Ramaprabhu, S. *Int. J. Hydrogen Energy* **2012,** *37,*
    412–421. doi:10.1016/j.ijhydene.2011.09.069

70. Rao, C. V.; Reddy, A. L. M.; Ishikawa, Y.; Ajayan, P. M. *Carbon* **2011,**
    49, 931–936. doi:10.1016/j.carbon.2010.10.056

71. Jayasayee, K.; Rob Van Veen, J. A.; Manivasagam, T. G.; Celebi, S.;
    Hensen, E. J. M.; de Bruijn, F. A. *Appl. Catal., B* **2012,** *111–112,*
    515–526. doi:10.1016/j.apcatb.2011.11.003

72. Xu, C.; Hoque, M. A.; Chiu, G.; Sung, T.; Chen, Z. *RSC Adv.* **2016,** *6,*
    112226–112231. doi:10.1039/c6ra19924k

73. Higgins, D.; Hoque, M. A.; Seo, M. H.; Wang, R.; Hassan, F.;
    Choi, J.-Y.; Pritzker, M.; Yu, A.; Zhang, J.; Chen, Z. *Adv. Funct. Mater.*
    2014, *24,* 4325–4336. doi:10.1002/adfm.201400161

74. Martin-Martinez, M.; Machado, B. F.; Serp, P.; Morales-Torres, S.;
    Silva, A. M. T.; Figueiredo, J. L.; Faria, J. L.; Gomes, H. T.
    Catal. Today **2019,** in press. doi:10.1016/j.cattod.2019.03.014

75. Speder, J.; Altmann, L.; Bäumer, M.; Kirkensgaard, J. J. K.;
    Mortensen, K.; Arenz, M. *RSC Adv.* **2014,** *4,* 14971–14978.
    doi:10.1039/c4ra00261j

76. Chong, L.; Wen, J.; Kubal, J.; Sen, F. G.; Zou, J.; Greeley, J.;
    Chan, M.; Barkholtz, H.; Ding, W.; Liu, D.-J. *Science* **2018,** *362,*
    1276–1281. doi:10.1126/science.aau0630

77. Hammer, B.; Nørskov, J. K. Theoretical surface science and
    catalysis—calculations and concepts. *Advances in Catalysis;*
    Academic Press, 2000; Vol. 45, pp 71–129.
    doi:10.1016/s0360-0564(02)45013-4

78. Goellner, V.; Armel, V.; Zitolo, A.; Fonda, E.; Jaouen, F.
    J. Electrochem. Soc. **2015,** *162,* H403–H414.
    doi:10.1149/2.1091506jes

79. Maldonado, S.; Stevenson, K. J. *J. Phys. Chem. B* **2005,** *109,*
    4707–4716. doi:10.1021/jp044442z

80. Hasché, F.; Oezaslan, M.; Strasser, P.; Fellinger, T.-P.
    J. Energy Chem. **2016,** *25,* 251–257.
    doi:10.1016/j.jechem.2016.01.024

81. Mukerjee, S.; Srinivasan, S.; Soriaga, M. P.; McBreen, J.
    J. Electrochem. Soc. **1995,** *142,* 1409–1422. doi:10.1149/1.2048590

82. Wang, X. X.; Cullen, D. A.; Pan, Y.-T.; Hwang, S.; Wang, M.; Feng, Z.;
    Wang, J.; Engelhard, M. H.; Zhang, H.; He, Y.; Shao, Y.; Su, D.;
    More, K. L.; Spendelow, J. S.; Wu, G. *Adv. Mater. (Weinheim, Ger.)*
    2018, *30,* 1706758. doi:10.1002/adma.201706758

83. Cheng, Q.; Yang, L.; Zou, L.; Zou, Z.; Chen, C.; Hu, Z.; Yang, H.
    ACS Catal. **2017,** *7,* 6864–6871. doi:10.1021/acscatal.7b02326

84. Dilpazir, S.; He, H.; Li, Z.; Wang, M.; Lu, P.; Liu, R.; Xie, Z.; Gao, D.;
    Zhang, G. *ACS Appl. Energy Mater.* **2018,** *1,* 3283–3291.
    doi:10.1021/acsaem.8b00490

85. Han, Y.; Wang, Y.-G.; Chen, W.; Xu, R.; Zheng, L.; Zhang, J.; Luo, J.;
    Shen, R.-A.; Zhu, Y.; Cheong, W.-C.; Chen, C.; Peng, Q.; Wang, D.;
    Li, Y. *J. Am. Chem. Soc.* **2017,** *139,* 17269–17272.
    doi:10.1021/jacs.7b10194

86. Su, P.; Iwase, K.; Nakanishi, S.; Hashimoto, K.; Kamiya, K. *Small*
    2016, *12,* 6083–6089. doi:10.1002/smll.201602158

87. Zhao, C.; Dai, X.; Yao, T.; Chen, W.; Wang, X.; Wang, J.; Yang, J.;
    Wei, S.; Wu, Y.; Li, Y. *J. Am. Chem. Soc.* **2017,** *139,* 8078–8081.
    doi:10.1021/jacs.7b02736

88. Jen, S. U. *J. Alloys Compd.* **1996,** *234,* 231–234.
    doi:10.1016/0925-8388(95)02046-2

89. Bergounhou, C.; Blandy, C.; Choukroun, R.; Lecante, P.; Lorber, C.;
    Pellegatta, J.-L. *New J. Chem.* **2007,** *31,* 218–223.
    doi:10.1039/b614910c

90. Kim, K. S.; Winograd, N.; Davis, R. E. *J. Am. Chem. Soc.* **1971,** *93,*
    6296–6297. doi:10.1021/ja00752a065

91. Anumol, E. A.; Kundu, P.; Deshpande, P. A.; Madras, G.;
    Ravishankar, N. *ACS Nano* **2011,** *5,* 8049–8061.
    doi:10.1021/nn202639f

92. Tian, Z. Q.; Jiang, S. P.; Liang, Y. M.; Shen, P. K. *J. Phys. Chem. B*
    2006, *110,* 5343–5350. doi:10.1021/jp056401o

93. Li, D.; Wang, H.; Shi, C.; Xu, X. *RSC Adv.* **2016,** *6,* 35340–35347.
    doi:10.1039/c6ra04818h

94. Duong, H. T.; Rigsby, M. A.; Zhou, W.-P.; Wieckowski, A.
    J. Phys. Chem. C **2007,** *111,* 13460–13465. doi:10.1021/jp072586i

95. Fei, H.; Dong, J.; Arellano-Jiménez, M. J.; Ye, G.; Dong Kim, N.;
    Samuel, E. L. G.; Peng, Z.; Zhu, Z.; Qin, F.; Bao, J.; Yacaman, M. J.;
    Ajayan, P. M.; Chen, D.; Tour, J. M. *Nat. Commun.* **2015,** *6,* 8668.
    doi:10.1038/ncomms9668

96. Luo, B.; Xu, S.; Yan, X.; Xue, Q. *J. Electrochem. Soc.* **2013,** *160,*
    F262–F268. doi:10.1149/2.056303jes

97. Zignani, S. C.; Baglio, V.; Sebastián, D.; Saccà, A.; Gatto, I.;
    Aricò, A. S. *Materials* **2017,** *10,* 317. doi:10.3390/ma10030317

98. Yang, H. B.; Hung, S.-F.; Liu, S.; Yuan, K.; Miao, S.; Zhang, L.;
    Huang, X.; Wang, H.-Y.; Cai, W.; Chen, R.; Gao, J.; Yang, X.;
    Chen, W.; Huang, Y.; Chen, H. M.; Li, C. M.; Zhang, T.; Liu, B.
    Nat. Energy **2018,** *3,* 140–147. doi:10.1038/s41560-017-0078-8

99. Mani, P.; Srivastava, R.; Strasser, P. *J. Phys. Chem. C* **2008,** *112,* 2770–2778. doi:10.1021/jp0776412
100. Berber, M. R.; Hafez, I. H.; Fujigaya, T.; Nakashima, N. *Sci. Rep.* **2015,** *5,* 16711. doi:10.1038/srep16711
101. Higgins, D. C.; Meza, D.; Chen, Z. *J. Phys. Chem. C* **2010,** *114,* 21982–21988. doi:10.1021/jp106814j
102. Park, Y.-C.; Kakinuma, K.; Uchida, M.; Uchida, H.; Watanabe, M. *Electrochim. Acta* **2014,** *123,* 84–92. doi:10.1016/j.electacta.2013.12.120
103. Louisia, S.; Contreras, R. C.; Heitzmann, M.; Rosa Axet, M.; Jacques, P.-A.; Serp, P. *Catal. Commun.* **2018,** *109,* 65–70. doi:10.1016/j.catcom.2018.02.024
104. Sethuraman, V. A.; Weidner, J. W.; Haug, A. T.; Motupally, S.; Protsailo, L. V. *J. Electrochem. Soc.* **2008,** *155,* B50–B57. doi:10.1149/1.2801980

Warped graphitic layers generated by oxidation of fullerene extraction residue and its oxygen reduction catalytic activity

Machiko Takigami[1], Rieko Kobayashi[1,2], Takafumi Ishii[1], Yasuo Imashiro[1,2] and Jun-ichi Ozaki[*1]

Address:
[1]Graduate School of Science and Technology, Gunma University, 1-5-1 Tenjin-cho, Kiryu, Gunma 376-8515, Japan and [2]R & D Center, Nissinbo Holdings Inc, 1-2-3 Onodai, Midori-ku, Chiba 267-0056, Japan

Email:
Jun-ichi Ozaki[*] - jozaki@gunma-u.ac.jp

* Corresponding author

Abstract

Carbon-based oxygen reduction reaction (ORR) catalysts are regarded as a promising candidate to replace the currently used Pt catalyst in polymer electrolyte fuel cells (PEFCs); however, the active sites remain under discussion. We predicted that warped graphitic layers (WGLs) are responsible for the ORR catalytic activity in some carbon catalysts (i.e., carbon alloy catalysts (CACs)). To prove our assumption, we needed to use WGLs consisting of carbon materials, but without any extrinsic catalytic elements, such as nitrogen, iron, or cobalt, which effectively enhance ORR activity. The present study employed a fullerene extraction residue as a starting material to construct WGLs. The oxidation of the material at 600 °C exposed the WGLs by removing the surrounding amorphous moieties. Transmission electron microscopy (TEM) observations revealed the formation of WGLs by oxidation treatment at 600 °C in an O_2/N_2 stream. Extending the oxidation time increased the purity of the WGL phase, but also simultaneously increased the concentration of oxygen-containing surface functional groups as monitored by temperature programmed desorption (TPD). The specific ORR activity increased with oxidation up to 1 h and then decreased with the intensive oxidation treatment. Correlations between the specific ORR activity and other parameters confirmed that the development of the WGL and the increase in the O/C ratio are the competing factors determining specific ORR activity. These results explain the maximum specific ORR activity after 1 h of oxidation time. WGLs were found to lower the heat of adsorption for O_2 and to increase the occurrence of heterogeneous electron transfer.

Introduction

Polymer electrolyte fuel cells (PEFCs) are used as the power supply for automobiles and stationary devices. Cost reduction, specifically the cost reduction of cathode catalysts, is imperative to apply PEFCs for practical use [1]. Increasing the specific activity of platinum catalysts is the most realistic approach; for example, by creating alloys [2] or core–shell structures [3]

or by activating the Pt particles through metal support interactions [4]. Developing non-precious-metal catalysts is a fascinating, but ultimately speculative, technology for material scientists. Many studies have reported on the preparation of active non-precious catalysts; however, few mention the principles of the catalytic activity. All the studies reporting on the ORR activity suggest dependence on the following three principles: (1) formation of M–N$_4$ surface complexes (M = Fe, Co) and its analog on carbon substrates [5-8]; (2) change in the electronic distribution by doping with nitrogen and other elements [9-22]; and (3) activation of the carbon surface by encapsulated metal particles [23-28].

Our non-precious-metal ORR catalysts are based on carbon alloy catalysts (CACs) [29]. CACs are carbon-based catalysts with active sites consisting of mainly carbon atoms. The sites are constructed by controlling the crystallographic and chemical states of carbon atoms through careful carbonization. Controlling carbonization by metal catalysts such as iron or cobalt produces nanoshell-containing carbon (NSCC) with ORR activity [30-35]. This activity is thought to originate from surface defects formed on the nanoshell carbons, including edges and warped graphitic layers (WGLs) [31,36]. Improving an ORR catalyst by altering the catalyst design and preparation successfully led to the world's first commercialization of a portable fuel cell with a non-precious-metal catalyst [37,38]. Building on this success, we ultimately aim to apply our CACs to automobile and stationary device uses. These applications require more active and more durable catalysts. The identification of the active sites of these CACs is an important issue for improving their activity and durability.

Active CACs commonly include WGLs [31]. We consider WGLs to be the basic structure responsible for the ORR activity of CACs. The ORR activity of the WGLs was examined using onion-like carbon (OLC) produced by the heat treatment of a nanodiamond [39]. The results showed the highest ORR activity for OLC heat-treated at 1400 °C among the prepared samples (HTT = 1000 °C to 1800 °C). The material formed OLCs composed of WGLs, but also included untransformed diamond. The residual diamond prevented us from confirming that WGLs are the active sites of the CACs.

The ideal carbon material to confirm our assumption that WGLs are responsible for the ORR active sites should not include foreign atoms, known as promoters, such as a diamond phase, nitrogen, boron, phosphorus, sulfur, and transition metals like iron and cobalt. Such WGLs can be obtained from fullerene-related materials. We selected a commercial carbon, Nanom Black, which is a fullerene extraction residue from a fullerene soot prepared by a combustion method [40]. The combustion

method produces a large amount of fullerenes by partial thermal oxidation of hydrocarbons. The residue is essentially amorphous but should include WGLs containing a non-benzenoid structure due to some incomplete formation of fullerenes [41,42].

Our previous study on extracting nanoshell structures from a nanoshell-containing carbon (NSCC) by using H$_2$O$_2$ oxidation showed that extracting oxidation works well to produce WGLs from Nanom Black [43]. Here, we describe the formation of WGLs from Nanom Black by oxidation and show that the ORR activity of the obtained WGLs is related to their development in the material. Finally, we show that the WGLs are responsible for the catalytic activity of CACs.

Experimental
Sample preparation
Nanom Black (NB-ORG) is a residual carbon found after extracting fullerenes (e.g., C$_{60}$ and C$_{70}$) from a fullerene soot produced by a combusting method. It is commercially available from Frontier Carbon Inc. (Japan). From inductively coupled plasma atomic emission spectroscopy (ICP-AES) measured by Shimadzu Techno-Research, Inc., it can be concluded that the carbon possesses no ORR promoting metal elements. NB-ORG was heat-treated at 600 °C in an oxygen-containing stream (O$_2$ [Vol.]/N$_2$ [Vol.] = 6:94) for a duration ranging from 0.5 to 5 h. The oxidized NBs are referred to as ONB-*t* (*t* = 0.5, 1, 2, 3, 5) according to their oxidation time. A control was also prepared from NB-ORG by heating it at 600 °C in a nitrogen stream for 2 h (NNB).

Characterization techniques
The structure of the prepared carbons was studied by transmission electron microscopy (TEM) and X-ray diffraction (XRD). The transmission electron microscope (JEM-2010, JEOL Inc.) was operated at an accelerating voltage of 200 kV. The X-ray diffractometer (XRD6100, Shimadzu Corp.) was equipped with a Cu Kα X-ray source (40 kV, 30 mA) and was operated by scanning the diffraction angles from 5° to 90° at a scanning speed of 1 °/min. Corrections for atomic scattering, Lorentz, and polarization factors [44] were made to the diffraction profile for detailed analysis of the 002 diffractions.

An automatic surface area analyzer (BELSORP MINI, Microtrak BEL Inc., Japan) was used to measure the N$_2$ adsorption isotherms at 77 K after evacuating the sample at 200 °C for 2 h under a dynamic vacuum. The Brunauer–Emmett–Teller (BET) theory was applied to determine the surface area (BET-SSAs) of the samples as calculated from the isotherms. An automatic static adsorption analyzer (BELSORP Max, Microtrac BEL Inc., Japan) was used to measure the O$_2$ adsorption isotherms at

−80 °C with a pressure range of 5 to 100 kPa. A differential scanning calorimeter (DSC8500, Perkin-Elmer) was used to measure the heat of O_2 adsorption of the carbons, and was operated by monitoring the heat-flux change when the stream was switched from nitrogen to oxygen. A laboratory-constructed temperature programmed desorption (TPD) apparatus recorded the TPD spectra of H_2O, CO, CO_2, and H_2. The spectra were used to calculate the amount of surface functional groups. The details of this technique are described elsewhere [45,46].

Electrochemical techniques

Cyclic voltammetry was used to evaluate the heterogeneous electron transfer rate of the carbons in an aqueous solution consisting of 6×10^{-3} mol/L $K_3[Fe(CN)_6]$ and 1 mol/L KNO_3. The carbons, bound by using a polyvinylidene fluoride (PVDF) resin solution (KF polymer L, #7305, NMP solution, Kureha Co. Ltd.) with a composition of carbon/PVDF = 1/0.5, served as a working electrode with round shape. A potentiostat system (ALS700 series, BAS Japan) was used to record the cyclic voltammograms in a potential range of 0.6 to −0.1 V vs Ag/AgCl at different sweep rates (1 to 50 mV/s).

Linear sweep voltammetry with a rotating disk electrode was used to evaluate the ORR activity of the prepared carbons. The carbons were used to form a working electrode by using a Nafion (Nafion perfluorinated resin solution, Aldrich) solution on a 4 mm glass-like carbon disk electrode (0.2 mg [carbon]/cm^2, 0.1 mg [binder]/cm^2). The reference electrode was a reversible hydrogen electrode (RHE). The electrolyte was a 0.5 mol/L H_2SO_4 aqueous solution. A voltammogram obtained in a N_2-saturated electrolyte was subtracted from a voltammogram in an O_2-saturated electrolyte giving a net ORR voltammogram. The electrochemical system consisted of a rotation apparatus (RRDE-3A, BAS Japan) and a potentiostat (ALS700 series, BAS Japan). The potential sweep was started from 1 V to 0 V vs RHE, at a potential sweep rate of 1 mV/s and a rotating speed of 1500 rpm.

Results
Carbon structure

Figure 1 shows selected TEM images of the prepared carbons. NB-ORG did not show a stacking structure, even at higher magnification, but it did show dot-like structures. These results indicate the amorphous nature of this carbon material. WGLs started to appear in ONB-0.5, and they occupied the entire TEM field in ONB-1. Further increases in the oxidation time to 3 h did not yield noticeable changes in the structure of the graphitic layers. The 5 h oxidation resulted in thick graphitic layers forming multilayer onion-like carbons, as shown in Figure 1d. A TEM image of NNB showed similarities to that of NB-ORG, meaning that the heat treatment of NB-ORG in an inert atmo-
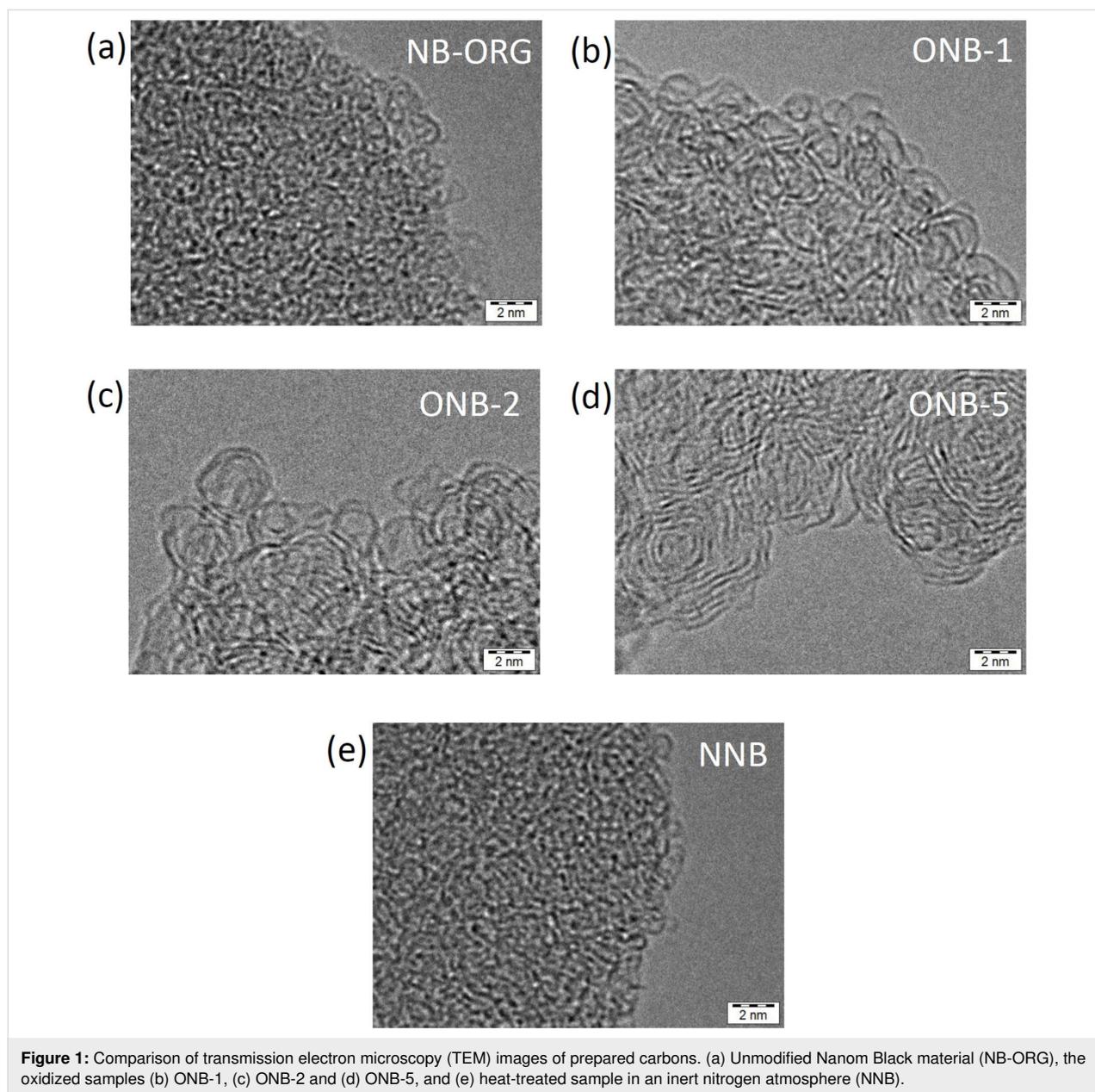
sphere did not cause any structural changes under TEM observation.

Figure 2a shows the dependence of the yield on treatment time; there is a rapid decrease in the yield with oxidation time up to 2 h, but no significant decrease for the heat treatment in an inert atmosphere (Figure 2e). Figure 2b shows the XRD profiles of the prepared samples. NB-ORG appeared to have two diffraction peaks in the carbon 002 region: one at $2\theta = 17°$ another at $2\theta = 23°$. The former was present in other types of fullerene soot, but the origin is not clear [47]. Scanlon et al. reported encapsulated fullerene even in extraction residues [41]. NB-ORG did not show the diffraction characteristics of fullerene crystals, indicating no fullerene nanocrystallites remained in the material. The oxidation treatment to NB-ORG diminished the intensity of the peak at $2\theta = 17°$, as can be observed in ONB-1 (Figure 2b). This trend was more apparent with extended oxidation treatment time. The peak at around $2\theta = 23°$ became dominant in ONB-2. The results confirm the multicomponent feature of the region in vicinity of 002-diffraction. The diffraction peaks were retrieved by assuming three Gaussian curves. The fraction of the peak at 26.5°, denoted as peak W in Figure 2c, against the total diffraction peaks in this region was defined as f_W. The calculated fraction indicated how dominant the peak W (f_W) is in the material. The change of the fraction f_W is presented as a function of oxidation time in Figure 2d. The fraction f_W increased with time up to 2 h of oxidation and then reached unity, as shown in Figure 2d. Comparing this feature with the TEM images, we concluded that the peak W corresponds to the warped graphitic layers. The samples ONB-2, 3, and 5 contained only the structure corresponding to peak W.

Surface chemical properties

TPD is a useful method to evaluate the amount and type of surface oxygen groups present. Ishii et al. [45,46] extended the analysis temperature up to 1800 °C, which enabled complete desorption of CO-emitting and H_2-emitting groups, which requires temperatures above 1000 °C. Figure 3a shows the emitted oxygen-containing gases detected by the TPD technique. Oxidation for 1 h did not change the concentration of the surface functional groups, but further oxidation resulted in excess surface oxygen groups and increasing f_W.

The techniques used to study the oxygen adsorption properties were a static adsorption technique to measure the amount of adsorbed oxygen and a dynamic adsorption technique to measure the heat of adsorption. Figure 4a and Figure 4b present the changes in the amount of adsorption and the heat of adsorption with oxidation time, respectively. The amount of O_2 adsorption increased in the first 1 h of oxidation time and then reached saturation. The heat of adsorption showed an abrupt de-

Figure 1: Comparison of transmission electron microscopy (TEM) images of prepared carbons. (a) Unmodified Nanom Black material (NB-ORG), the oxidized samples (b) ONB-1, (c) ONB-2 and (d) ONB-5, and (e) heat-treated sample in an inert nitrogen atmosphere (NNB).

crease for the 0.5 h oxidation treatment, followed by gradual decrease. NNB did not show such a decrease.

Figure 5a shows the cyclic voltammograms of the selected samples using a $Fe(CN)_6^{3-}/ Fe(CN)_6^{4-}$ redox couple. The cyclic voltammograms showed two peaks, upward (oxidation to $Fe(CN)_6^{3-}$) and downward (reduction to $Fe(CN)_6^{4-}$). The potential difference between the oxidation peak and the reduction peak was defined as ΔE_P, an indicator of the heterogeneous electron transfer rate. When the ΔE_P value is close to 57 mV, the system is reversible, meaning that the electron transfer at the interface between the electrode and the electrolyte is very high. On the other hand, the increases in ΔE_P cor-

respond to slow electron transfer. Figure 5b shows a plot of ΔE_P as a function of oxidation time; the ΔE_P value decreased rapidly with oxidation time up to 1 h. NNB did not show such a decrease in ΔE_P. The oxidized carbons, ONBs, showed smaller values than NB-ORG and NNB, indicating an accelerated electron transfer process.

ORR catalytic activity

Figure 6a presents the ORR voltammograms of the prepared carbons obtained in a 0.5 mol/L H_2SO_4 solution. NB-ORG showed the lowest ORR activity, as can be recognized from the lowest onset potential and the lowest reduction current. The oxidation treatment increased the ORR activity, as observed in the
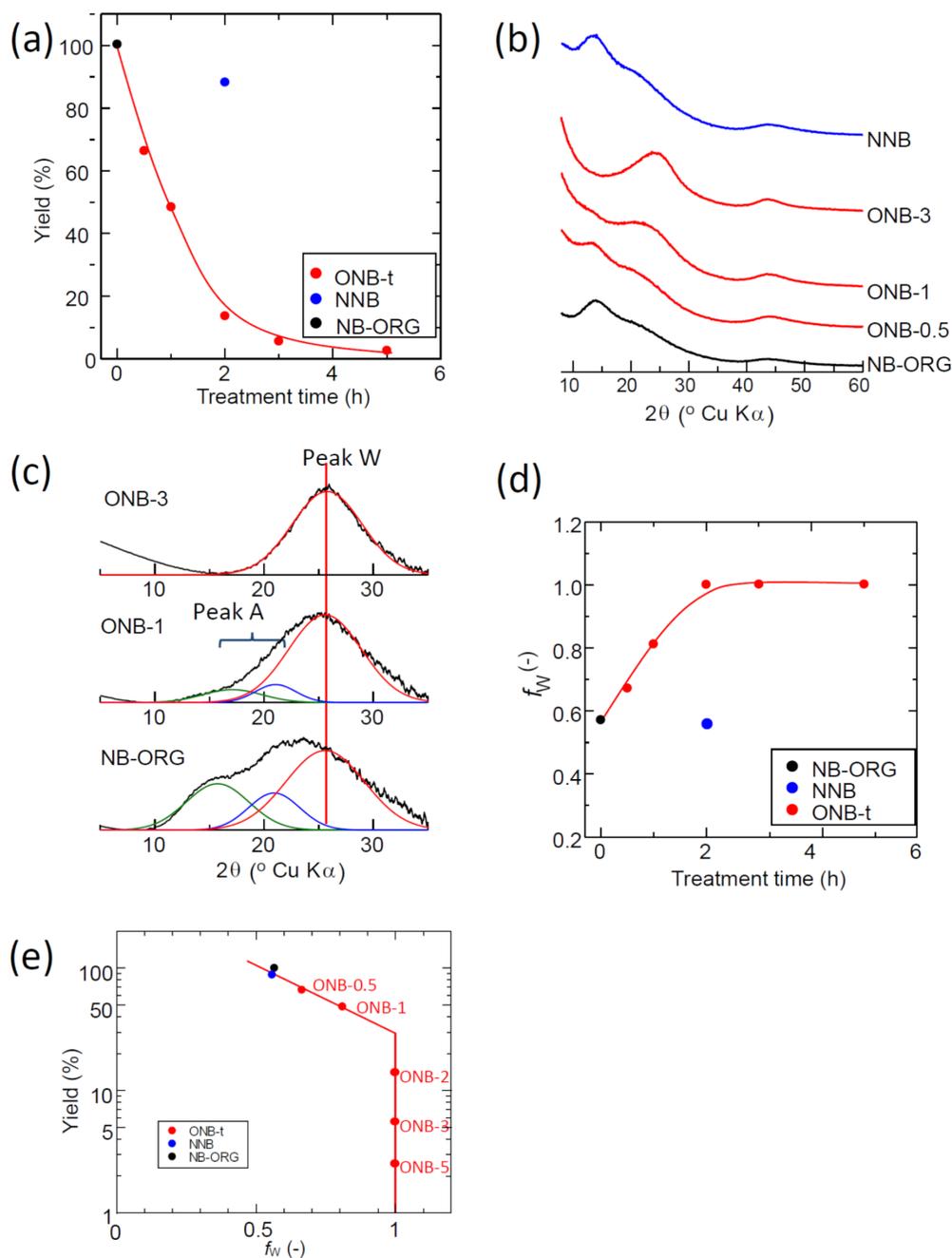
Figure 2: (a) Dependence of the carbon yield on the treatment time. (b) XRD profiles of the prepared carbons. The black line represents the unmodified Namom Black material (NB-ORG), red lines represent the oxidized samples in an O_2/N_2 stream (ONB-t series), and the blue line represents the heat-treated sample in a N_2 stream (NNB). (c) Examples of the peak deconvolution of the 002 XRD profiles of the selected samples; ONB-3, ONB-1 and NB-ORG from top to bottom. The colors of the sub peaks indicate the differences of their origin. The green and blue curves represent amorphous carbon moieties (Peak A) and the red curves the warped graphitic layers (WGLs, Peak W), which were inferred by comparing the XRD profiles and the TEM images shown in Figure 1. (d) Changes of f_W, the fraction of warped graphitic layers (WGLs), calculated as a ratio of the integrated intensity of the peak W in (b) to the total integrated intensity of the 002 region in the vicinity of 002 diffraction with the heat treatment time. (e) Relationship between the yield and f_W.

voltammograms of ONBs. NNB showed slight increases in both the onset potential and current; however, its magnitude was lower than that of the ONBs. Figure 6b shows the change in the specific ORR activity as a function of oxidation time, where the

specific ORR activity was a current density of 0.3 V vs RHE normalized by the corresponding BET-SSA. The ORR activity increased with the oxidation time for the first 1 h and then decreased. Figure 6c shows a plot of the specific ORR activity
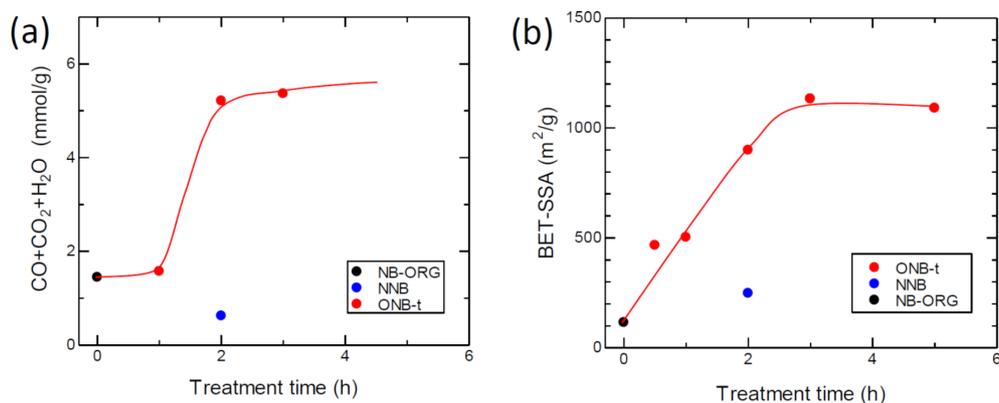
Figure 3: (a) Treatment time dependence of the amount of oxygen-containing surface groups detected by the TPD technique with an upper temperature limit of 1600 °C on the treatment temperature. (b) Dependence of the BET specific surface area of the prepared carbons within the heat-treatment time.
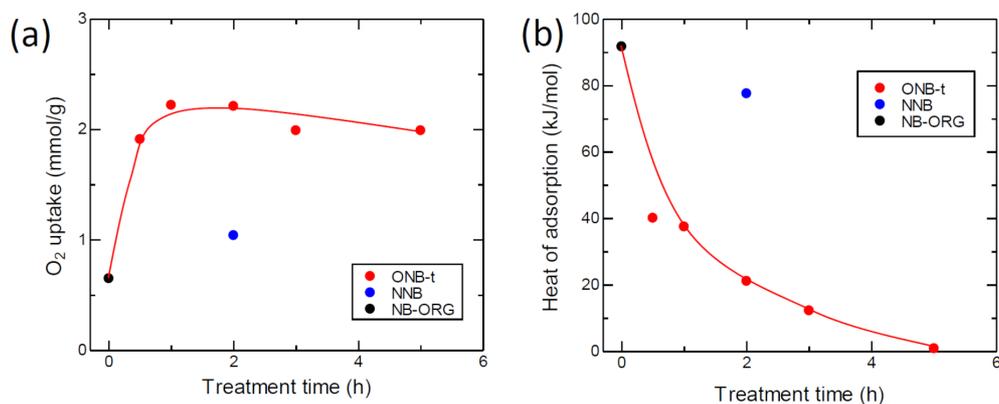

Figure 4: Dependence of the oxygen adsorption properties at −80 °C. (a) O_2 adsorption uptake measured using a static method. (b) Heat of O_2-adsorption measured with a dynamic adsorption method using differential scanning calorimetry (DSC).
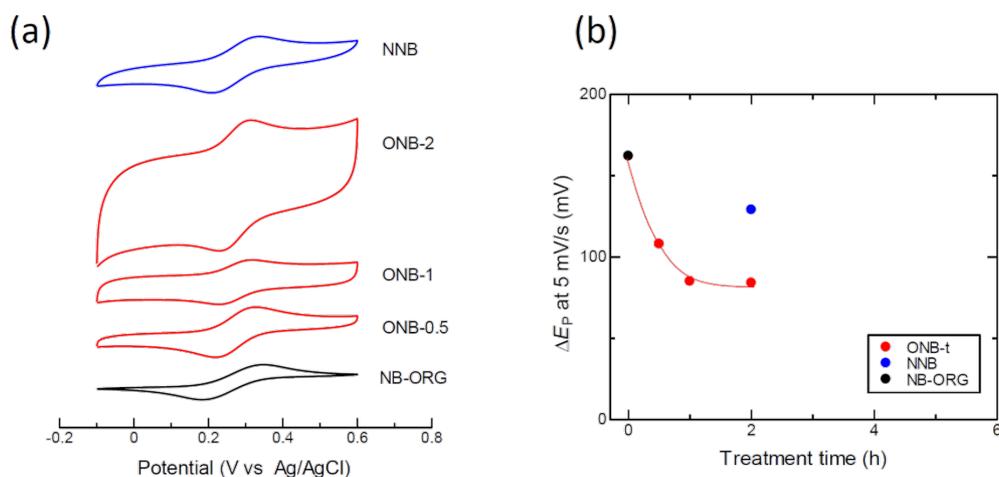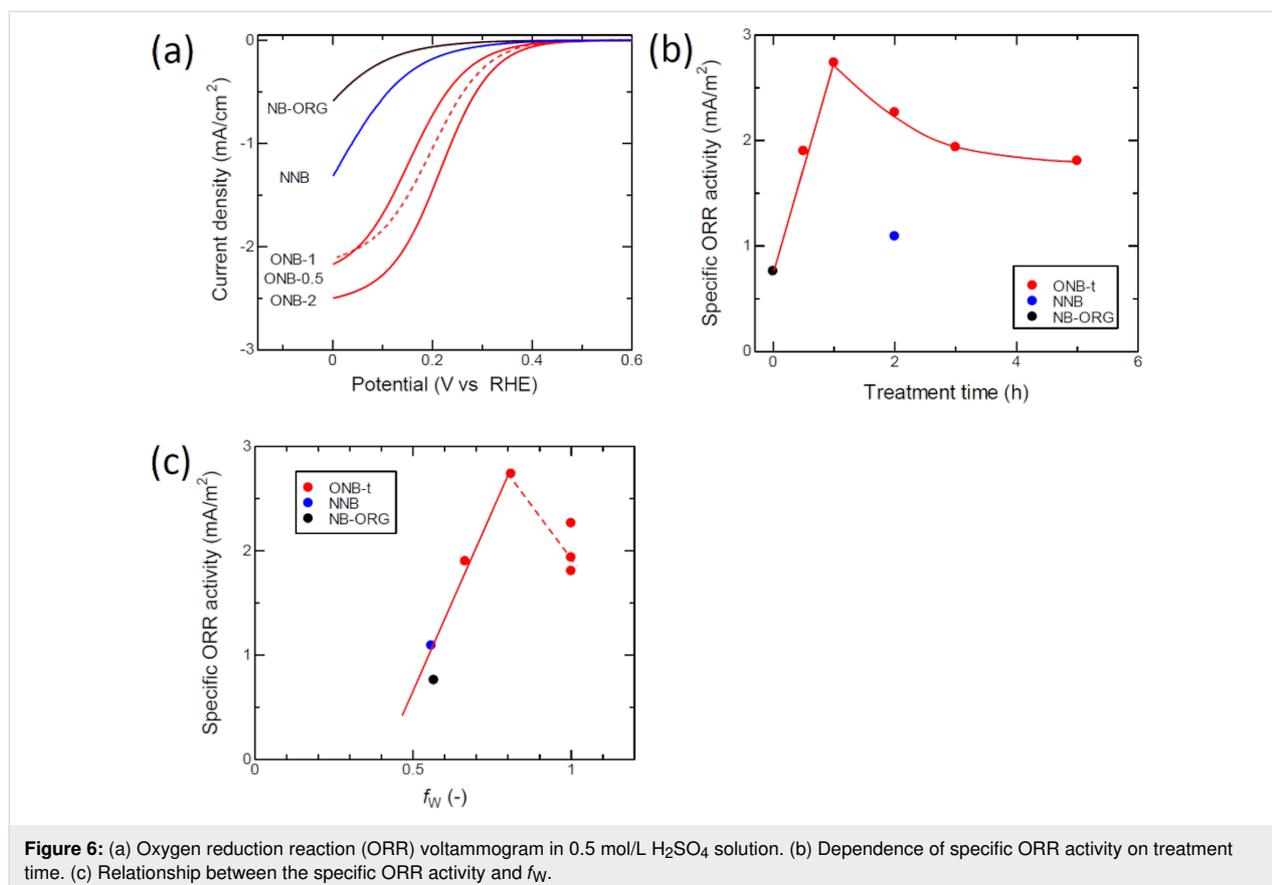

Figure 5: (a) Cyclic voltammograms of the samples for the redox reaction ferricyanide/ferrocyanide (potential sweep rate = 5 mV/s). (b) Dependence of ΔE_P on treatment time.

Figure 6: (a) Oxygen reduction reaction (ORR) voltammogram in 0.5 mol/L H_2SO_4 solution. (b) Dependence of specific ORR activity on treatment time. (c) Relationship between the specific ORR activity and f_W.

against f_W. The specific ORR activity of the ONBs prepared for an oxidation time of less than 2 h correlated well with f_W.

Discussion
Formation of WGLs from NB-ORG by oxidation

We initially expected NB-ORG to include WGLs because of the incomplete formation of the fullerene structure during the manufacturing process. If we can separate WGLs from NB-ORG, the extracted WGLs should be a well-defined model to study the origin of the ORR activity of CACs. We postulated the selective oxidation of amorphous moieties in NB-ORG to separate WGLs. TEM observations confirm the formation of WGLs through the oxidation by removing the amorphous moieties. The changes in the shape of the XRD profiles with treatment also supports our theory. The relationship between the oxidation treatment yield and f_W calculated from the XRD profiles in the vicinity of 002 diffraction illuminates the structural changes with the progression of oxidation. First, amorphous carbons reacted with oxygen to produce and remove CO_2, leaving WGLs behind. Further oxidation results in the formation of oxygen functional groups on WGLs, as observed by TPD. The oxidation treatment also increases the BET-SSA, which corresponds to the removal of amorphous carbon

moieties. The results confirm that NB-ORG originally included WGLs embedded in amorphous moieties. The oxidation treatment resulted in WGLs by the selective oxidation of amorphous moieties. Furthermore, chemical analysis of NB-ORG confirmed the absence of the foreign atoms that are effective at enhancing ORR activity. Therefore, the obtained WGLs were also free from such foreign elements.

Oxygen appears to play an important role in forming the five-membered rings that are necessary to construct WGLs. The reaction of fullerenes with oxygen molecules at elevated temperatures induces cage opening [48-50]. Furthermore, some oxygen compounds can form orifices or holes on fullerene molecules; this is recognized as an important synthesis technique for "molecular surgery" [51]. Blending a biodiesel oil containing oxygen atoms into an ordinary diesel oil resulted in the formation of soot with WGLs [52]; the authors explain this phenomenon by the C_5-forming ability of oxygen included in the biodiesel oil. These two studies reported on the formation of WGLs in commonly included reactions between oxygen and carbon atoms. The results indicate the possibility of that WGLs in the present study formed during the oxidation. The NB-ORG used in this study already included WGLs, as evidenced by the multicomponent feature of the XRD profiles in the vicinity of

002 diffraction, which was supported by TEM observation. Ultimately, the formation of the WGLs by the oxidation of NB-ORG occurred by removing amorphous carbons through oxidation.

Factors determining ORR catalytic activity of carbons

We have shown that the oxidation treatment of NB-ORG brought about the formation of WGLs, the enhancement of the ORR activity, an increase in the specific surface area, and an increase in surface oxygen functional groups. Herein, we discuss the specific ORR activity defined in the previous section, which eliminates the influence of the BET-SSA on the ORR activity. The specific activity increased with oxidation time up to 1 h and then decreased, as shown in Figure 3b. The increasing behavior of the specific activity for the first 1 h agrees with the development of the WGL phase, which is confirmed by the correlation between the specific activity and f_W (Figure 6c). However, the correlation was not maintained for samples with $f_W \approx 1$. This initially seems to disprove our assumption, because the result indicates that the pure WGLs had less activity than the less pure WGLs. Thus, we consider another parameter, the surface concentration of the oxygen surface functional groups. We measured the surface oxygen concentration by using a TPD technique. The obtained concentration of the surface oxygen functional groups increased suddenly between 1 and 2 h of oxidation time. From these results, it can be seen that longer oxidation times result in the two opposite effects on specific ORR activity: the development of WGLs and oxidation to introduce oxygen functional groups to WGLs.

Surface oxidation of carbon is reported to deteriorate ORR activity. Banham et al. studied the degradation of non-precious-metal catalysts and a carbon alloy catalyst [38]. They claim that carbon oxidation (attacked by H_2O_2) is the primary mechanism for performance loss during cell operation. Hence, this conclusion justifies the degrading effect of the specific activity observed for the intensively oxidized NBs. Finally, we have two competing factors to control the ORR activity of carbon with the oxidation treatment – the development of the WGL phase as the promoting factor and the increase in the concentration of surface oxygen groups as the inhibiting factor. The changes in these two factors finally determined the specific ORR activity of the ONBs.

Next, we considered the reason for the ORR activity increase with the development of the WGL phase. Removing the amorphous phase by the oxidation treatment exposed the WGL to the material surface and to contact with the reactants, O_2 and protons. The exposure of the WGL phase by removing the amorphous phase meant a change in the surface property from that governed by the amorphous carbon phase to that governed by the WGL phase. The ORR activity change was a result of the surface change due to the exposure of the WGL phase to the surface of the material; hence, we considered the chemical characteristics of the WGL-exposed NBs (ONBs) by paying special attention to ONBs that did not experience the introduction of oxygen surface groups (i.e., the ONBs obtained by the oxidation for shorter than 1 h).

The oxygen adsorption uptake and heat of oxygen adsorption varied with oxidation time. The oxidation of NB-ORG immediately increased the O_2 adsorption and decreased the heat of adsorption. The increase in adsorption uptake accelerates the following elementary step through the concentration term in the rate equation. The decrease in the heat of adsorption activated the adsorbed state of oxygen molecules. However, lowering the heat too much led to a small interaction between the adsorbent and the adsorbate (i.e., less activation).

Further evidence for the changes in the surface properties due to WGL exposure is the change in the electron transfer rate evaluated by the ΔE_P of $Fe(CN)_6^{3-}/Fe(CN)_6^{4-}$ cyclic voltammograms. The ΔE_P value decreased rapidly in the first 2 h of oxidation, approaching the limit of the fastest electron transfer, $\Delta E_P = 57$ mV. This behavior confirms that the exposure of WGLs to the surface of the material enhances electron transfer. Another interesting point is that the electron transfer was not inhibited by the oxygen surface functional groups. This may be because the redox reaction does not require any adsorption sites, unlike ORR.

Conclusion

In summary, we obtained WGLs by the oxidation of Nanom Black (NB-ORG), a fullerene extraction residue, at 600 °C and tested our assumptions about the ORR activity of WGLs by examining their structure, properties, and ORR activity. First, we clarified the mechanism of the WGL formation from NB-ORG as the removal of an amorphous carbon matrix surrounding the originally included WGLs. The specific ORR activity, defined as an ORR current normalized by the corresponding BET surface area, showed a maximum when the oxidation time was 1 h. The presence of the maximum activity was understood in terms of two competing factors, the development of WGLs and the increase in oxygen surface functionality with oxidation time. The role of WGLs in ORR was also found to lower the heat of O_2-adsorption to a suitable value for O_2 activation and to accelerate heterogeneous electron transfer. The present study highlights important considerations for the design of non-metal carbon-based cathode catalysts for PEFCs and illuminates interesting aspects of carbon materials.

Acknowledgements

References

1. Banham, D.; Choi, J.-Y.; Kishimoto, T.; Ye, S.
   Adv. Mater. (Weinheim, Ger.) **2019,** 1804846.
   doi:10.1002/adma.201804846
2. Toda, T.; Igarashi, H.; Watanabe, M. *J. Electroanal. Chem.* **1999,** *460,*
   258–262. doi:10.1016/s0022-0728(98)00361-1
3. Zhang, J.; Lima, F. H. B.; Shao, M. H.; Sasaki, K.; Wang, J. X.;
   Hanson, J.; Adzic, R. R. *J. Phys. Chem. B* **2005,** *109,* 22701–22704.
   doi:10.1021/jp055634c
4. Inoue, H.; Ishii, T.; Kannari, N.; Ozaki, J.-i. *ChemistrySelect* **2016,** *1,*
   3189–3196. doi:10.1002/slct.201600662
5. Jasinski, R. *Nature* **1964,** *201,* 1212–1213. doi:10.1038/2011212a0
6. Jahnke, H.; Schönborn, M.; Zimmermann, G. Organic dyestuffs as
   catalysts for fuel cells. *Physical and Chemical Applications of
   Dyestuffs;* Topics in Current Chemistry; Springer-Verlag: Berlin,
   Germany, 1976; pp 133–181. doi:10.1007/bfb0046059
7. Lefèvre, M.; Dodelet, J. P.; Bertrand, P. *J. Phys. Chem. B* **2002,** *106,*
   8705–8713. doi:10.1021/jp020267f
8. Lefèvre, M.; Proietti, E.; Jaouen, F.; Dodelet, J.-P. *Science* **2009,** *324,*
   71–74. doi:10.1126/science.1170051
9. Maldonado, S.; Stevenson, K. J. *J. Phys. Chem. B* **2005,** *109,*
   4707–4716. doi:10.1021/jp044442z
10. Ozaki, J.-i.; Kimura, N.; Anahara, T.; Oya, A. *Carbon* **2007,** *45,*
    1847–1853. doi:10.1016/j.carbon.2007.04.031
11. Razmjooei, F.; Singh, K. P.; Song, M. Y.; Yu, J.-S. *Carbon* **2014,** *78,*
    257–267. doi:10.1016/j.carbon.2014.07.002
12. Li, R.; Wei, Z.; Gou, X. *ACS Catal.* **2015,** *5,* 4133–4142.
    doi:10.1021/acscatal.5b00601
13. Gao, J.; Ma, N.; Tian, J.; Shen, C.; Wang, L.; Yu, P.; Chu, Y.; Liu, W.;
    Tan, X.; Li, X.; Yin, Z. *J. Solid State Electrochem.* **2018,** *22,* 519–525.
    doi:10.1007/s10008-017-3785-y
14. Huang, S.-F.; Terakura, K.; Ozaki, T.; Ikeda, T.; Boero, M.; Oshima, M.;
    Ozaki, J.-i.; Miyata, S. *Phys. Rev. B* **2009,** *80,* 235410.
    doi:10.1103/physrevb.80.235410
15. Ozaki, J.-i.; Anahara, T.; Kimura, N.; Oya, A. *Carbon* **2006,** *44,*
    3358–3361. doi:10.1016/j.carbon.2006.08.022
16. Ikeda, T.; Boero, M.; Huang, S.-F.; Terakura, K.; Oshima, M.;
    Ozaki, J.-i.; Miyata, S. *J. Phys. Chem. C* **2010,** *114,* 8933–8937.
    doi:10.1021/jp100045e
17. Matter, P. H.; Wang, E.; Arias, M.; Biddinger, E. J.; Ozkan, U. S.
    J. Mol. Catal. A: Chem. **2007,** *264,* 73–81.
    doi:10.1016/j.molcata.2006.09.008
18. Gong, K.; Du, F.; Xia, Z.; Durstock, M.; Dai, L. *Science* **2009,** *323,*
    760–764. doi:10.1126/science.1168049
19. Mamtani, K.; Jain, D.; Dogu, D.; Gustin, V.; Gunduz, S.; Co, A. C.;
    Ozkan, U. S. *Appl. Catal., B* **2018,** *220,* 88–97.
    doi:10.1016/j.apcatb.2017.07.086
20. Qu, K.; Zheng, Y.; Dai, S.; Qiao, S. Z. *Nano Energy* **2016,** *19,*
    373–381. doi:10.1016/j.nanoen.2015.11.027
21. You, J.-M.; Ahmed, M. S.; Han, H. S.; Choe, J. e.; Üstündağ, Z.;
    Jeon, S. *J. Power Sources* **2015,** *275,* 73–79.
    doi:10.1016/j.jpowsour.2014.10.174
22. Bag, S.; Mondal, B.; Das, A. K.; Raj, C. R. *Electrochim. Acta* **2015,**
    163, 16–23. doi:10.1016/j.electacta.2015.02.130
23. Jiang, H.; Yao, Y.; Zhu, Y.; Liu, Y.; Su, Y.; Yang, X.; Li, C.
    ACS Appl. Mater. Interfaces **2015,** *7,* 21511–21520.
    doi:10.1021/acsami.5b06708
24. Zhang, X.; Lin, J.; Chen, S.; Yang, J.; Song, L.; Wu, X.; Xu, H.
    ACS Appl. Mater. Interfaces **2017,** *9,* 38499–38506.
    doi:10.1021/acsami.7b11120
25. Kim, B. J.; Lee, D. U.; Wu, J.; Higgins, D.; Yu, A.; Chen, Z.
    J. Phys. Chem. C **2013,** *117,* 26501–26508. doi:10.1021/jp410014a
26. Varnell, J. A.; Tse, E. C. M.; Schulz, C. E.; Fister, T. T.; Haasch, R. T.;
    Timoshenko, J.; Frenkel, A. I.; Gewirth, A. A. *Nat. Commun.* **2016,** *7,*
    12582. doi:10.1038/ncomms12582
27. Tan, H.; Li, Y.; Kim, J.; Takei, T.; Wang, Z.; Xu, X.; Wang, J.;
    Bando, Y.; Kang, Y.-M.; Tang, J.; Yamauchi, Y. *Adv. Sci.* **2018,** *5,*
    1800120. doi:10.1002/advs.201800120
28. Wu, Z.-Y.; Xu, X.-X.; Hu, B.-C.; Liang, H.-W.; Lin, Y.; Chen, L.-F.;
    Yu, S.-H. *Angew. Chem., Int. Ed.* **2015,** *54,* 8179–8183.
    doi:10.1002/anie.201502173
29. Ozaki, J.; Imashiro, Y. *Electrochemistry* **2015,** *83,* 319–325.
    doi:10.5796/electrochemistry.83.319
30. Ozaki, J.-i.; Nozawa, K.; Yamada, K.; Uchiyama, Y.; Yoshimoto, Y.;
    Furuichi, A.; Yokoyama, T.; Oya, A.; Brown, L. J.; Cashion, J. D.
    J. Appl. Electrochem. **2006,** *36,* 239–247.
    doi:10.1007/s10800-005-9054-2
31. Ozaki, J.-i.; Tanifuji, S.-i.; Furuichi, A.; Yabutsuka, K. *Electrochim. Acta*
    2010, *55,* 1864–1871. doi:10.1016/j.electacta.2009.10.037
32. Ishii, T.; Maie, T.; Kimura, N.; Kobori, Y.; Imashiro, Y.; Ozaki, J.-i.
    Int. J. Hydrogen Energy **2017,** *42,* 15489–15496.
    doi:10.1016/j.ijhydene.2017.05.003
33. Kannari, N.; Ozaki, J.-i. *Carbon* **2012,** *50,* 2941–2952.
    doi:10.1016/j.carbon.2012.02.063
34. Kannari, N.; Takigami, M.; Maie, T.; Honda, H.; Kusadokoro, S.;
    Ozaki, J.-i. *Smart Grid Renewable Energy* **2013,** *04,* 10–15.
    doi:10.4236/sgre.2013.47a002
35. Maie, T.; Ozaki, J.-i. *J. Electrochem. Soc.* **2016,** *163,* H223–H227.
    doi:10.1149/2.0991603jes
36. Ishii, T.; Maie, T.; Hamano, M.; Kishimoto, T.; Mizushiri, M.;
    Imashiro, Y.; Ozaki, J.-i. *Carbon* **2017,** *116,* 591–598.
    doi:10.1016/j.carbon.2017.02.035
37. Banham, D.; Kishimoto, T.; Sato, T.; Kobayashi, Y.; Narizuka, K.;
    Ozaki, J.-i.; Zhou, Y.; Marquez, E.; Bai, K.; Ye, S. *J. Power Sources*
    2017, *344,* 39–45. doi:10.1016/j.jpowsour.2017.01.086
38. Banham, D.; Kishimoto, T.; Zhou, Y.; Sato, T.; Bai, K.; Ozaki, J.-i.;
    Imashiro, Y.; Ye, S. *Sci. Adv.* **2018,** *4,* eaar7180.
    doi:10.1126/sciadv.aar7180
39. Kannari, N.; Itakura, T.; Ozaki, J.-i. *Carbon* **2015,** *87,* 415–417.
    doi:10.1016/j.carbon.2015.02.050
40. Takehara, H.; Fujiwara, M.; Arikawa, M.; Diener, M. D.; Alford, J. M.
    Carbon **2005,** *43,* 311–319. doi:10.1016/j.carbon.2004.09.017
41. Scanlon, J. C.; Ebert, L. B. *J. Phys. Chem.* **1993,** *97,* 7138–7140.
    doi:10.1021/j100130a004
42. Grieco, W. J.; Howard, J. B.; Rainey, L. C.; Vander Sande, J. B.
    Carbon **2000,** *38,* 597–614. doi:10.1016/s0008-6223(99)00149-9
43. Kannari, N.; Nakamura, Y.; Ozaki, J.-i. *Carbon* **2013,** *61,* 537–542.
    doi:10.1016/j.carbon.2013.04.108

44. Iwashita, N.; Park, C. R.; Fujimoto, H.; Shiraishi, M.; Inagaki, M.
    Carbon **2004**, *42,* 701–714. doi:10.1016/j.carbon.2004.02.008
45. Ishii, T.; Kashihara, S.; Hoshikawa, Y.; Ozaki, J.-i.; Kannari, N.;
    Takai, K.; Enoki, T.; Kyotani, T. *Carbon* **2014**, *80,* 135–145.
    doi:10.1016/j.carbon.2014.08.048
46. Ishii, T.; Kaburagi, Y.; Yoshida, A.; Hishiyama, Y.; Oka, H.;
    Setoyama, N.; Ozaki, J.-i.; Kyotani, T. *Carbon* **2017**, *125,* 146–155.
    doi:10.1016/j.carbon.2017.09.049
47. Werner, H.; Herein, D.; Blöcker, J.; Henschke, B.; Tegtmeyer, U.;
    Schedel-Niedrig, T.; Keil, M.; Bradshaw, A. M.; Schlögl, R.
    Chem. Phys. Lett. **1992**, *194,* 62–66.
    doi:10.1016/0009-2614(92)85743-t
48. Wohlers, M.; Bauer, A.; Rühle, T.; Neitzel, F.; Werner, H.; Schlögl, R.
    Fullerene Sci. Technol. **1997**, *5,* 49–83.
    doi:10.1080/15363839708011973
49. Chen, H. S.; Kortan, A. R.; Haddon, R. C.; Kaplan, M. L.; Chen, C. H.;
    Mujsce, A. M.; Chou, H.; Fleming, D. A. *Appl. Phys. Lett.* **1991**, *59,*
    2956–2958. doi:10.1063/1.105810
50. Wohlers, M.; Werner, H.; Herein, D.; Schedel-Niedrig, T.; Bauer, A.;
    Schlögl, R. *Synth. Met.* **1996**, *77,* 299–302.
    doi:10.1016/0379-6779(96)80106-8
51. Gan, L.; Yang, D.; Zhang, Q.; Huang, H. *Adv. Mater. (Weinheim, Ger.)*
    2010, *22,* 1498–1507. doi:10.1002/adma.200903705
52. Vander Wal, R. L.; Strzelec, A.; Toops, T. J.; Stuart Daw, C.;
    Genzale, C. L. *Fuel* **2013**, *113,* 522–526.
    doi:10.1016/j.fuel.2013.05.104

Hierarchically structured 3D carbon nanotube electrodes for electrocatalytic applications

Pei Wang, Katarzyna Kulp and Michael Bron[*§]

Address:
Martin-Luther-University Halle-Wittenberg, Faculty of Natural Sciences II, Department of Chemistry, 06120 Halle, Germany

Email:
Michael Bron[*] - michael.bron@chemie.uni-halle.de

* Corresponding author
§ Tel: +49 345 55 25900; fax: +49 345 55 27163.

Abstract

Hierarchically structured 3-dimensional electrodes based on branched carbon nanotubes (CNTs) are prepared on a glassy carbon (GC) substrate in a sequence of electrodeposition and chemical vapor deposition (CVD) steps as follows: Primary CNTs are grown over electrodeposited iron by CVD followed by a second Fe deposition and finally the CVD growth of secondary CNTs. The prepared 3-dimensional CNT structures (CNT/CNT/GC) exhibit enhanced double-layer capacitance and thus larger surface area compared to CNT/GC. Pt electrodeposition onto both types of electrodes yields a uniform and homogeneous Pt nanoparticle distribution. Each preparation step is followed by scanning electron microscopy, while the CNTs were additionally characterized by Raman spectroscopy. In this way it is demonstrated that by varying the parameters during the electrodeposition and CVD steps, a tuning of the structural parameters of the hierarchical electrodes is possible. The suitability of the hierarchical electrodes for electrocatalytic applications is demonstrated using the methanol electro-oxidation as a test reaction. The Pt mass specific activity towards methanol oxidation of Pt-CNT/CNT/GC is approximately 2.5 times higher than that of Pt-CNT/GC, and the hierarchical electrode exhibits a more negative onset potential. Both structures demonstrate an exceptionally high poisoning tolerance.

Introduction

Carbon nanotubes (CNTs) have attracted considerable attention since their discovery in 1991 [1] due to their high electrical conductivity, large surface area, good chemical stability, high mechanical strength and high aspect ratio and are considered as promising materials for diverse applications such as field emission displays, energy storage devices, sensors, and so on [2-8]. Besides the above-mentioned applications, CNTs have also been investigated as catalysts or catalyst supports for various electrocatalytic reactions [8-13], including methanol oxidation in direct methanol fuel cells (DMFCs). DMFCs are promising power sources for future energy conversion and storage, since they, in addition to their nonpolluting nature and

low operating temperature, run on an easily handled and cheap liquid fuel.

However, the slow kinetics of methanol oxidation at the anode and the methanol crossover through the electrolyte membrane from anode to cathode are still major obstacles that hinder the broad market implementation of DMFCs. The slow kinetics are mainly caused by incomplete methanol oxidation accompanied by the formation of adsorbed carbonaceous reaction intermediates, which poison the Pt surface [14-19]. Most strategies to solve these issues are focused on the optimization of the catalyst, such as alloying Pt with a second metal such as Ni, Ru and Pd [20-24] or using Pt-metal oxide composites such as Pt/SnO_2 and Pt/CeO_2 [24-28]. Additionally, a variety of catalyst preparation methods, e.g., colloidal synthesis [29-31], a galvanic replacement process [32-35] or microwave-assisted preparation [20,21,36], have been proposed to gain control over the structural features of the active nanoparticles.

However, from heterogeneous catalysis it is generally known that a suitable catalyst support is as important as the active material in order to form an optimum catalyst. For electrocatalytic applications, the support should possess high electrical conductivity, large surface area and good chemical and mechanical stability. Furthermore, the electrode prepared with the catalyst should provide optimized pore structure and retain the high surface area of the catalyst to guarantee a high availability of active sites and unhindered mass transport for high efficiency.

Besides the classical carbon blacks, different carbon-based catalyst supports (e.g., modified CNTs, functionalized reduced graphene oxide, etc.) have been recently studied to improve the reaction performance, enhance stability and thus reduce the cost [37-41]. It was reported that Pt supported on these optimized catalyst supports provides higher electrocatalytical activity towards methanol oxidation and increased tolerance against poisoning in comparison to those supported on carbon blacks and nonmodified catalyst supports. This could be due to improved Pt dispersion owing to a higher amount of functional anchoring sites of the catalyst supports and their high surface area, as well as from a good electrical contact between the conducting components [42-45]. The modification of the electronic and structural properties of Pt due to interaction with the support may also play a role.

To take advantage of the properties of novel carbon materials, and at the same time gain control over the electrode structure, bottom-up synthesis approaches have been suggested, including branching or hierarchical structuring of carbon-based catalyst supports. In these approaches, one-dimensional (1D, e.g., CNTs or nano-/microfibers) or two-dimensional carbon materi-

als (2D, e.g., graphene) are transformed into three-dimensional (3D) structures by attaching other nanofibers or carbon materials. Examples are nanofibers distributed on polymer-based microfibers, CNTs grown on graphene, CNT–carbon black hybrids, graphene- or polymer-coated CNTs, and so on [45-51]. Another approach for hierarchical structuring is the growth of secondary CNTs on primary CNTs [52-56]. It was shown that such nanostructured CNT–CNT composites exhibit enhanced specific surface area as well as increased specific double-layer capacitance. Additionally, the presence of the secondary CNTs can reduce the equivalent series resistance to promote electron transfer. CNT–CNT composites have been successfully employed as catalyst supports. Kundu et al. reported that Pt supported on such hierarchical structures showed enhanced surface atomic concentration, indicating an improved Pt dispersion. The oxygen reduction reaction on Pt/CNT–CNT yielded a much higher diffusion-limited current compared to Pt supported on other carbon-based electrodes [52]. In general, CNT-based hierarchically nanostructured materials can be considered as promising support materials for electrocatalytic applications.
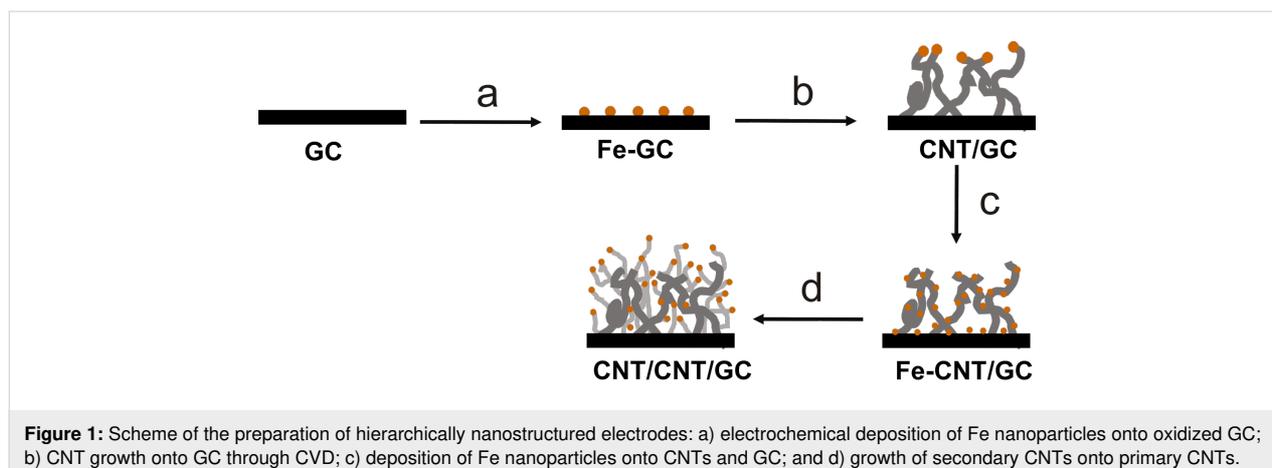
This paper investigates the preparation of hierarchically structured CNTs on glassy carbon (GC) based on a sequential CNT growth over electrodeposited Fe nanoparticles via chemical vapor deposition (CVD) with cyclohexane as the carbon precursor. Pt electrodeposition onto these hierarchical structures leads to active electrocatalysts. The bottom-up synthesis of these nanocomposites was monitored using scanning electron microscopy (SEM) and Raman spectroscopy, and it is demonstrated that the hierarchical structures can be tuned with respect to thickness, length, and density of the CNTs. The activity of the Pt-CNT/CNT/GC electrodes towards methanol oxidation was investigated and compared to that of Pt-CNT/GC and high activity and exceptional poisoning stability were demonstrated.

Results and Discussion
Preparation and characterization of hierarchically nanostructured electrodes
Fe deposition
In Figure 1, the individual steps for the preparation of hierarchically nanostructured electrodes are displayed schematically. First, Fe nanoparticles are electrodeposited onto oxidized GC followed by CVD growth of primary CNTs to form CNT/GC. After a second deposition of Fe nanoparticles, another CVD step leads to the hierarchically structured electrodes (CNT/CNT/GC). Each step has been optimized towards structural control and high reproducibility, as detailed below. The first and critical step is the initial Fe deposition. Fe nanoparticles were electrochemically deposited onto the GC surface using double pulse deposition [57]. This method allows adjustment of nucleation and growth potential to control the distribution and
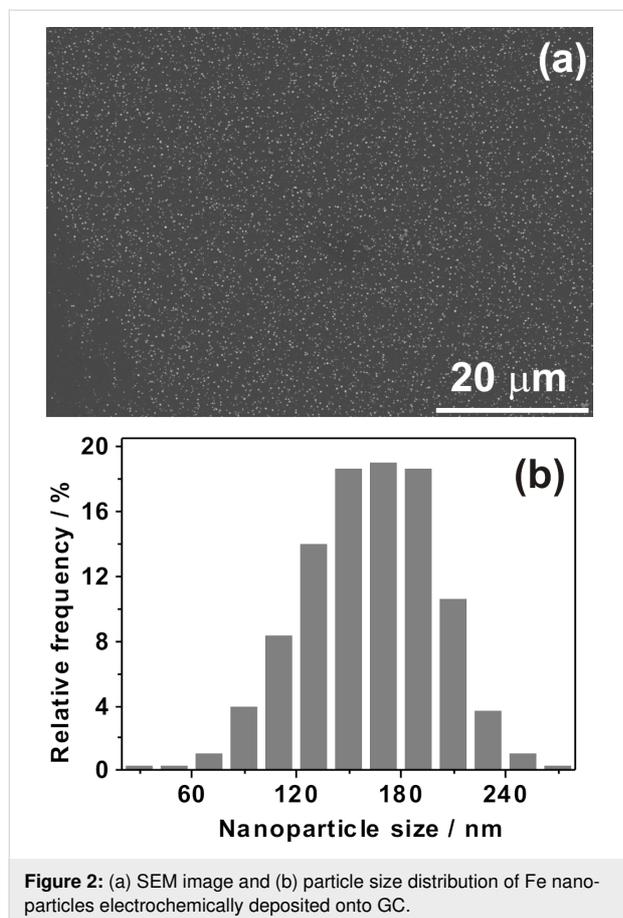
Figure 1: Scheme of the preparation of hierarchically nanostructured electrodes: a) electrochemical deposition of Fe nanoparticles onto oxidized GC; b) CNT growth onto GC through CVD; c) deposition of Fe nanoparticles onto CNTs and GC; and d) growth of secondary CNTs onto primary CNTs.

size of the Fe nanoparticles. A nucleation potential of −1.41 V vs Ag|AgCl|KCl$_{sat.}$ and a growth potential of −1.27 V vs Ag|AgCl|KCl$_{sat.}$ were applied (compare also Figure S1, Supporting Information File 1). Figure 2a shows an SEM image of Fe nanoparticles deposited onto oxidized GC. The particle diameter is in the range from 100–200 nm (Figure 2b), which is considerably large. Recent investigations in our lab, which will be published in the near future, show that particle sizes down to

20 nm and below are possible. Fe deposition onto nonoxidized GC is possible as well but leads to poor reproducibility and inhomogeneous samples with respect to particle size and size distribution. The control over the size of the particles is necessary since it was shown that the diameter of CVD-prepared CNTs can be associated with the size of the catalyst particles [58,59].

Growth of primary CNTs

After the metal catalyst deposition, the CNTs are grown via CVD. During CVD growth, the CNT structure (quality) and yield of CNTs is controlled by many parameters, such as the pressure, temperature, growth time, reactor geometry, carbon precursors, gas flow rate and composition of gas mixtures, as well as the catalyst support and physical and chemical state of the catalyst [59-63]. It is not the aim of this paper to present a detailed study on the influence of all these parameters. However, some of them turned out to be critical for the success or failure of the preparation of hierarchically structured electrodes, as detailed in the following.

The CVD growth of primary CNTs over electrodeposited Fe nanoparticles was carried out with cyclohexane at 750 °C, a temperature that turned out to be suitable in reference experiments (not shown). Cyclohexane is brought into the CVD furnace using a H$_2$/Ar gas mixture saturated at room temperature. To gain control over the CVD process, the influence of growth time, gas flow rate and H$_2$/Ar ratio were studied. In a series of experiments, using a growth time of 120 min and a gas flow rate of 1.7 L h^{-1}, the H$_2$/Ar ratio is varied (which translates into a varied H$_2$/cyclohexane ratio), and the results are represented in Figure 3a and Supporting Information File 1, Figure S2e and f. Using a H$_2$/Ar ratio of 1.1 L h^{-1}/0.6 L h^{-1} (Figure 3a), the primary CNTs were densely and nearly uniformly grown on the surface of GC with a diameter of approximately 40–80 nm. Accordingly, the optical image (Sup-
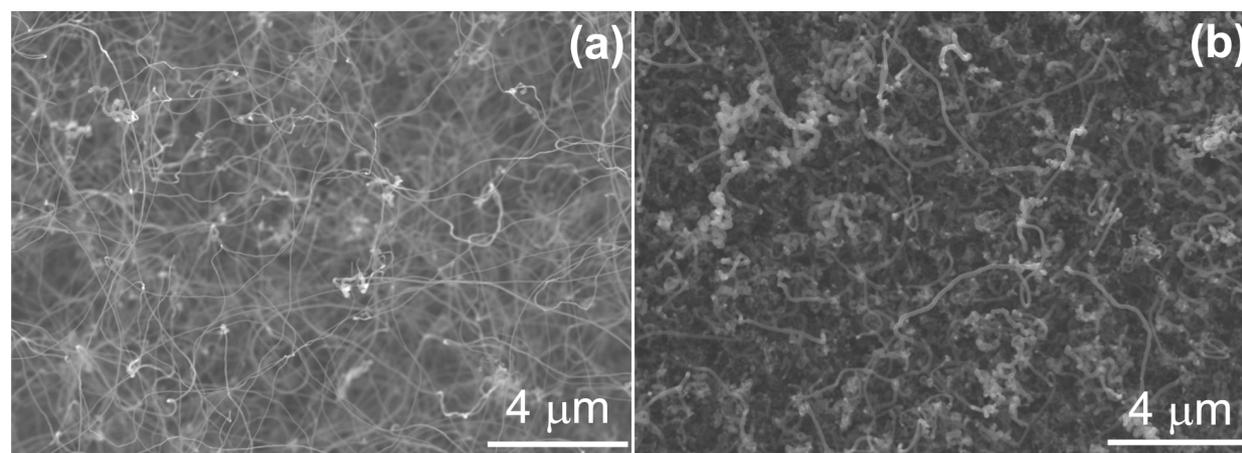

Figure 2: (a) SEM image and (b) particle size distribution of Fe nanoparticles electrochemically deposited onto GC.

Figure 3: SEM images of CNTs deposited onto GC by CVD at 750 °C using cyclohexane and a gas flow rate of 1.7 L h^{-1} for 120 min with an H$_2$/Ar ratio of 1.8 (1.1 L h^{-1}/0.6 L h^{-1}). (b) CNTs grown under the same conditions but with an increased total gas flow rate of 3.9 L h^{-1}.

porting Information File 1, Figure S2g) displays a matt black thin layer at those areas of the GC chips that were covered with Fe particles. However, no CNT growth was observed with a H$_2$/Ar ratio higher than 1.2 L h^{-1}/0.5 L h^{-1} (and thus a higher H$_2$/cyclohexane ratio, Supporting Information File 1, Figure S2f), while Figure S2e shows only few CNTs and large amounts of surrounding (probably amorphous) carbon obtained with a smaller H$_2$/Ar ratio (1.0 L h^{-1}/0.7 L h^{-1}). It was reported that the density and diameter of CNTs synthesized on carbon cloth with ethylene as the carbon precursor over a nickel catalyst at 700 °C decrease with decreasing ratio of H$_2$ to N$_2$ [62], while CNTs grown on an Fe-decorated Si wafer at 825 °C using toluene increased in density and diameter with decreasing ratio of H$_2$/Ar [63]. This demonstrates that the CNT growth strongly depends on the growth conditions. Accordingly, the above-described results reveal the sensitivity of the CNT growth on the H$_2$/cyclohexane ratio under the chosen conditions. During CVD growth, hydrogen molecules or atoms keep the metal catalyst in its active state and avoid catalyst passivation by excess carbon deposition, which would otherwise suppress CNT growth. We assume that with the decreasing ratio of H$_2$/cyclohexane, exactly these processes occur, resulting in suppressed CNT growth and formation of amorphous carbon. In contrast, there is no CNT growth with the increasing ratio of H$_2$/Ar, likely because excess hydrogen hydrogenates carbon structures formed at the catalyst surface into volatile compounds, thus hindering CNT growth.
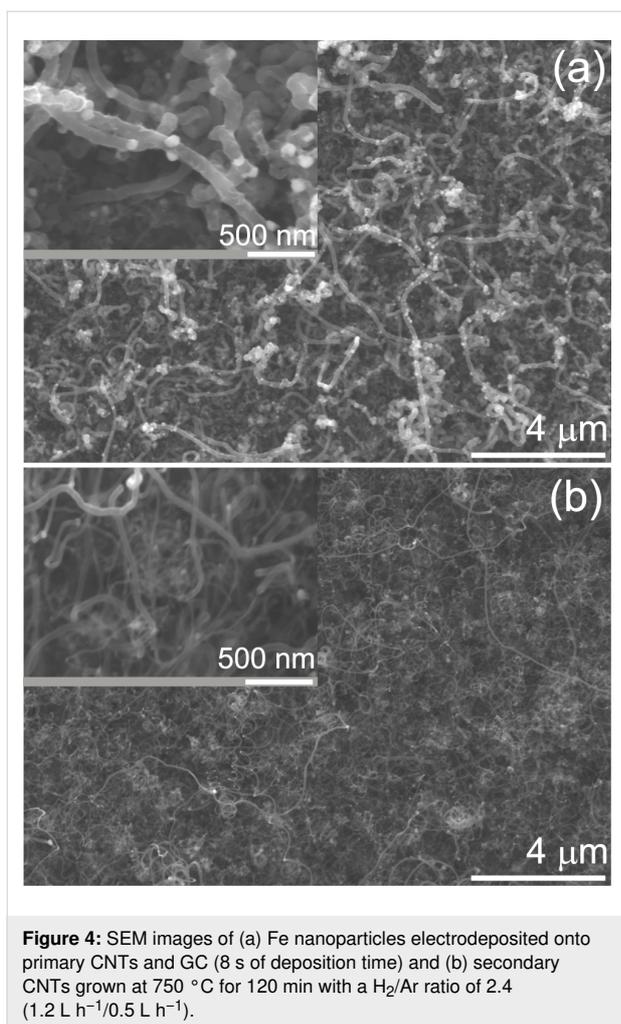
The time dependence of CNT growth was examined for growth times ranging from 30 to 120 min (Figure 3a, Supporting Information File 1, Figure S2a,b). After 30 min of growth, no CNTs can be found, while short CNTs with a diameter of 40–80 nm are formed during 60 min of CVD growth. The diameter is sim-

ilar to that of CNTs grown for 120 min (Figure 3a). From 30 min to 120 min, the density of the CNTs is increased. Obviously there is a considerably long conditioning period, during which the growth catalyst is likely slowly saturated with carbon until the optimum H$_2$/cyclohexane (or carbon) ratio is reached.

Besides varying the H$_2$/Ar ratio and the growth time, the influence of the total gas flow rate and thus the cyclohexane feed on CNT growth was studied using the optimum H$_2$/Ar ratio (1.8) and a growth time of 120 min. Figure 3b shows CNTs grown with a total gas flow rate of 3.9 L h^{-1}. The CNTs grow densely and homogenously with a diameter of approximately 150 nm. This is about twice as thick as the diameter of the CNTs grown with 1.7 L h^{-1}. Most likely, the larger amount of decomposed carbon crystallizing on the Fe nanoparticles to form a cylindrical network is the reason for this observation. Using 6.7 L h^{-1} and 12.1 L h^{-1} as the total gas flow rate, only few CNTs were grown (Supporting Information File 1, Figure S2c,d). We assume that the excess carbon surrounds the Fe nanoparticles, blocking them from further CNT growth. It might be speculated that a higher H$_2$/cyclohexane ratio would allow CNT growth also at higher total gas flow rates, which we have not yet investigated. Regardless, the above results demonstrate that by choosing the appropriate experimental conditions, it is possible to tune the thickness and length of the primary CNTs grown on glassy carbon.

Growth of secondary CNTs and Pt deposition
After the growth of the primary CNTs, a subsequent Fe electrodeposition and growth of secondary CNTs was carried out to form the hierarchical electrodes (CNT/CNT/GC) as shown in the SEM images of Figure 4. These experiments were carried

Figure 4: SEM images of (a) Fe nanoparticles electrodeposited onto primary CNTs and GC (8 s of deposition time) and (b) secondary CNTs grown at 750 °C for 120 min with a H$_2$/Ar ratio of 2.4 (1.2 L h^{-1}/0.5 L h^{-1}).

out with the thicker primary CNTs grown at a gas flow of 3.9 L h^{-1}. Figure 4a shows Fe nanoparticles deposited onto the primary CNTs with quite homogenous distribution. Double pulse deposition, as described above, was utilized but the deposition time was decreased from 12 s to 8 s, resulting in a reduced Fe particle size range from 50–90 nm. The use of thicker CNTs as the primary material and smaller Fe particles for the secondary CNTs was chosen to obtain truly hierarchical structures, facilitating the verification of the growth of secondary CNTs. The particle size can be controlled via the deposition time, as shown in Supporting Information File 1, Figure S3, with average particle sizes of ≈45 nm after 6 s of deposition time and ≈110 nm after 12 s of deposition. Additionally, the Fe nanoparticles seem to prefer to nucleate on cross junctions between primary CNTs, as observed from Figure S3a, which could be caused by improvement of electron transfer or preferential nucleation sites.

The growth of secondary CNTs using the same optimized gas mixture as above and a gas flow rate of 1.7 L h^{-1} yielded unsat-

isfactory results. As exposed in Supporting Information File 1, Figure S4, larger amounts of amorphous carbon are deposited and only few CNTs are grown, indicating the dependence of CNT growth on support and structure. Learning from the results on the growth of primary CNTs, the H$_2$/Ar ratio was adjusted to 1.2 L h^{-1}/0.5 L h^{-1} to avoid formation of amorphous carbon, and the growth of secondary CNTs was successfully achieved, as demonstrated in Figure 4b. The secondary CNTs were grown quite irregularly, which may be caused by the size distribution of the Fe nanoparticles but also by the fact that the gas composition within the 3-dimensional structure of the primary CNTs may change due to cyclohexane consumption by the CVD process. However, the presence of a large number of thinner CNTs compared to the initial structures verifies the growth of secondary CNTs (compare also Supporting Information File 1, Figure S5). It is, however, considerably difficult to identify junctions between the primary and secondary CNTs, probably due to top growth and the high density of CNTs.

Furthermore, to access the generality of our approach, the above designed procedure was successfully employed to prepare nitrogen-doped nanostructured electrodes (N-CNT/N-CNT/GC) using acetonitrile (CH$_3$CN) as the carbon precursors and nitrogen source instead of cyclohexane (see Supporting Information File 1, Figure S6).

Physicochemical characterization

The prepared electrodes (CNT/GC and CNT/CNT/GC) were characterized by Raman spectroscopy (Figure 5) after Fe removal in concentrated HNO$_3$ (before Pt electrodeposition). Both electrodes show the typical D-band at ≈1355 cm^{-1} und the G-band at ≈1600 cm^{-1}, which are associated with structural defects within the carbon lattice and crystalline carbon, respec-
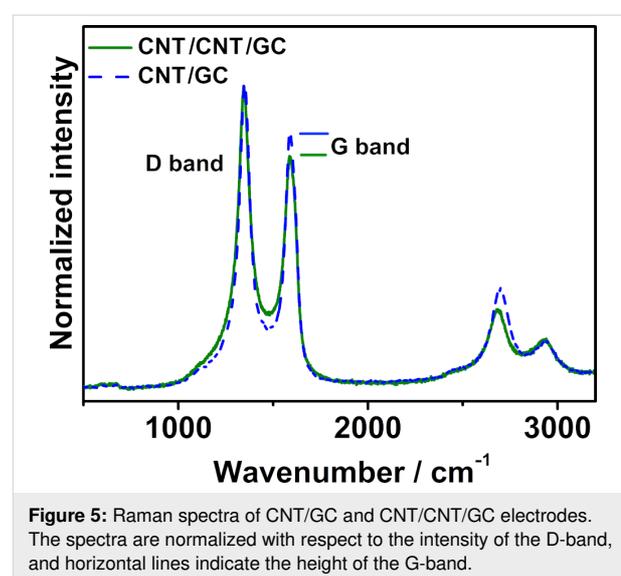

Figure 5: Raman spectra of CNT/GC and CNT/CNT/GC electrodes. The spectra are normalized with respect to the intensity of the D-band, and horizontal lines indicate the height of the G-band.

tively [64]. The intensity ratios of these bands (I_D/I_G) for the CNT/GC und CNT/CNT/GC electrodes are 1.36 und 1.54, respectively. This indicates that the secondary CNTs are less ordered and have a higher defect density than the primary ones.

As the last step in electrode preparation, Pt nanoparticles were electrochemically deposited onto CNT/CNT/GC and CNT/GC using linear-sweep voltammetry from 0 to −0.9 V vs Ag|AgCl|KCl$_{sat.}$. For comparison, Pt deposition onto oxidized GC was carried out in the same manner (compare Supporting Information File 1, Figure S7 for the resulting deposition curves). The very different double-layer capacities above −0.15 V are due to the different surface areas and was subtracted for charge integration. Based on Faraday's Law and the charge consumed during the sweep, the mass of electrodeposited Pt onto the GC, CNT/GC and CNT/CNT/GC electrodes was calculated to be 0.147 mg, 0.101 mg and 0.065 mg, respectively (Table 1). It seems to be surprising that the amount of deposited Pt is highest on the sample with the lowest surface area. The reason for the decreasing Pt amount in the order GC, CNT/GC and CNT/CNT/GC is not clear to us at the moment; however, this was observed in repeated experiments. Similarly it was reported by Rajesh et al. [65] that the amount of electrodeposited Pt on graphene/CNT/GC was less than that on graphene/GC under the same deposition conditions. As shown in the SEM/BSE images in Figure 6 and Supporting Information File 1, Figure S8 and S9, Pt nanoparticles were homogenously and densely distributed onto the CNT/GC and CNT/CNT/GC electrodes with similar particle sizes (≈7 nm). Meanwhile, the Pt nanoparticles deposited on oxidized GC are much larger (≈50 nm, Supporting Information File 1, Figure S9). Besides electrodeposition onto CNTs, it may be assumed that some Pt is directly deposited onto the GC substrate. Furthermore, it cannot be excluded that particles smaller than the mentioned 7 nm form, which are below the detection limit of our SEM.
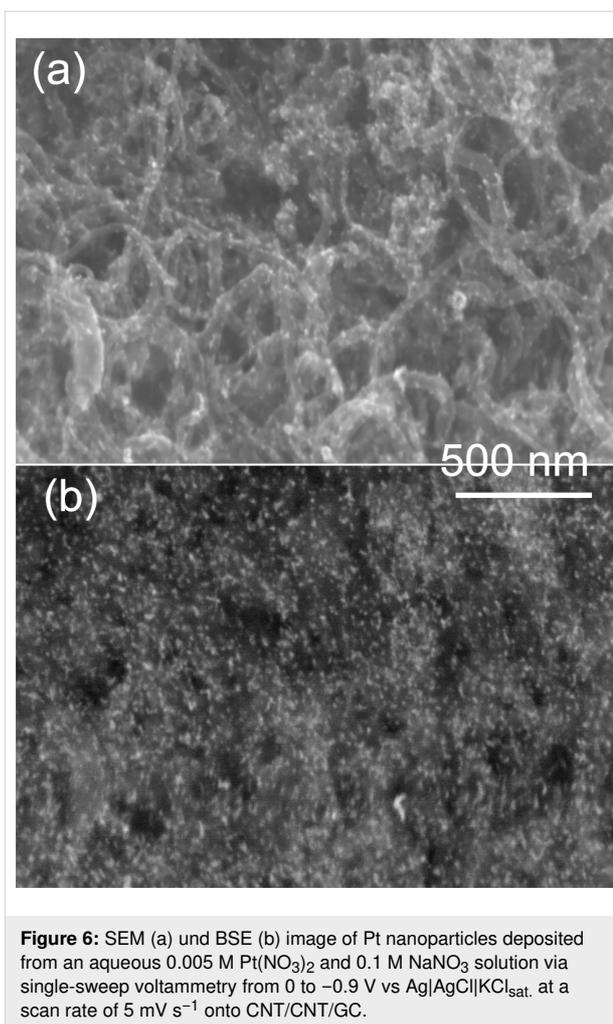

Figure 6: SEM (a) und BSE (b) image of Pt nanoparticles deposited from an aqueous 0.005 M Pt(NO$_3$)$_2$ and 0.1 M NaNO$_3$ solution via single-sweep voltammetry from 0 to −0.9 V vs Ag|AgCl|KCl$_{sat.}$ at a scan rate of 5 mV s^{-1} onto CNT/CNT/GC.

tograms were obtained due to the low overall Pt loading and probably due to the fact that the electrodeposited Pt nanoparticles seem to be quite irregular and might consist of several crystallites that are too small to be detected by XRD (compare Supporting Information File 1, Figure S8).

Electrochemical Investigations
Cyclic voltammetry

A basic electrochemical characterization of the prepared electrodes was carried out using cyclic voltammetry (CV). CVs of GC before and after oxidation in HNO$_3$ as well as after growth of the primary CNTs and additional secondary CNTs are displayed in Figure 7. The currents in the CVs are associated with the charging and decharging of the electrical double layer and denote the double-layer capacity, which can be regarded as an estimation of the surface area for the carbon-only samples. In addition to these currents, in the potential range between 0.5 V and 0.7 V vs RHE, a redox peak pair is observed for all three samples, which is attributed to the presence of oxygen-containing groups (quinone-type) resulting from the necessary treat-

Table 1: Pt mass on the different supports and corresponding electrochemically active surface area (ECSA) determined by H$_{upd}$ and CO$_{ads}$.

	Pt-GC	Pt-CNT/GC	Pt-CNT/CNT/GC
Mass of Pt (mg) via LSV	0.147	0.101	0.065
ECSA from H$_{upd}$ (cm^2/mg)	1.11	6.81	12.39
ECSA from CO (cm^2/mg)	–	10.95	13.87
Ratio of ECSA From CO vs H$_{upd}$	–	1.61	1.12

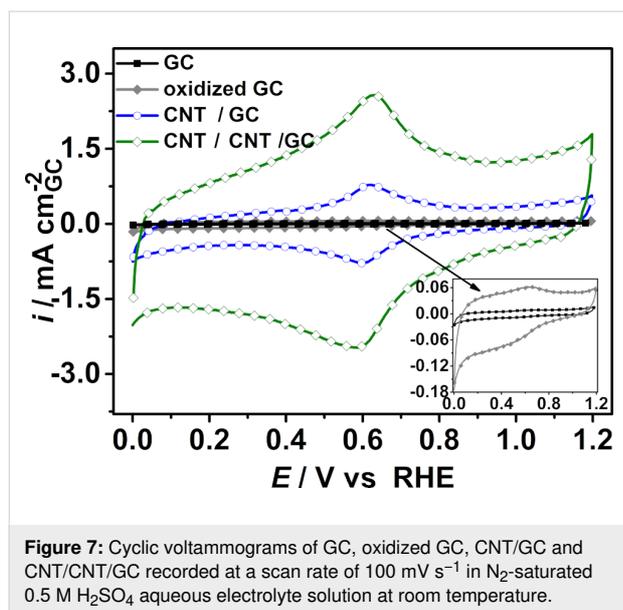In addition to SEM, XRD measurement were perfomed to analyze the Pt nanoparticles, however, no meaningful diffrac-

Figure 7: Cyclic voltammograms of GC, oxidized GC, CNT/GC and CNT/CNT/GC recorded at a scan rate of 100 mV s^{-1} in N$_2$-saturated 0.5 M H$_2$SO$_4$ aqueous electrolyte solution at room temperature.

ment with HNO$_3$ (see experimental, preparation of GC surface or leaching of Fe particles) [66]. The double-layer capacity of oxidized GC is increased compared to GC before oxidation, which may be attributed to a roughening of the surface and probably the formation of oxygen-containing surface groups like –OH or –C=O [66]. After the CVD growth of the primary CNTs and the secondary CNTs, the double-layer capacity is significantly enhanced, demonstrating the successful CNT growth and the concomitant increase in the electrochemically available surface area. Additionally, the functional groups of the primary and secondary CNTs, which are formed in the concentrated HNO$_3$ during the removal of Fe nanoparticles, can also contribute to the increase in the double-layer capacity [67]. The same observation can be made on the above-mentioned nitrogen-doped hierarchically nanostructured electrodes, where N-CNT/N-CNT/GC electrodes have a higher double-layer capacity (Supporting Information File 1, Figure S10). It should be mentioned that N-CNT/N-CNT/GC displays no redox peak attributed to oxygen-containing functional groups since Fe was electrochemically leached out in H$_2$SO$_4$ and not chemically in concentrated HNO$_3$ for the sake of follow-up studies not presented here. Additionally, CNT/CNT/GC is hydrophobic, while N-CNT/N-CNT/GC turned out to be hydrophilic, rendering an oxidative treatment unnecessary.

As described above, Pt nanoparticles were electrodeposited onto the hierarchical electrodes and, for comparison, also onto the surfaces of oxidized GC and CNT/GC. The available cata-lyst surface area (electrochemically active surface area (ECSA)) of Pt on GC, CNT/GC and CNT/CNT/GC was determined from the H$_{upd}$ charge and CO$_{ad}$ stripping voltammograms. The respective cyclic voltammograms of H$_{upd}$ were recorded in

N$_2$-saturated aqueous 0.5 M H$_2$SO$_4$ in the potential range from 0.05 to 1.2 V vs RHE at a scan rate of 100 mV s^{-1} as displayed in Figure 8. The ECSA was calculated from the average coulombic charge obtained via integrating the area under the hydrogen adsorption/desorption peaks after subtracting the double-layer charge in the potential range between 0.05 V and 0.35 V vs RHE [68,69]. As shown in Figure 8, the current den-sity (normalized to Pt mass) of Pt-CNT/CNT/GC for hydrogen adsorption/desorption increases compared to Pt-GC and Pt-CNT/GC, and the determined values are displayed in Table 1. The increase in the ECSA for Pt-CNT/CNT/GC may be explained by the higher CNT surface area of CNT/CNT/GC as compared to CNT/GC, as deduced from the double-layer cur-rent. The secondary CNTs provide a larger number of anchoring sites (e.g., surface functional groups or junction be-tween primary CNTs and secondary CNTs) to form a larger numbers of Pt nuclei during electrodeposition. As a conse-quence, the Pt particles in Pt-CNT/CNT/GC must be smaller than in Pt-CNT/GC. This difference is scarcely observed from the SEM images (Figure 6), which may be attributed to the limited resolution of SEM and non-observable Pt nanoparticles on GC. As described in the literature [52], secondary CNTs ex-hibit decreased charge transfer resistance with respect to the pri-mary CNTs as determined by electrochemical impedance spec-troscopy. Thus, we speculate that the improvement in Pt disper-sion is due to a better conductivity within the 3D network and a facilitated electron transfer, which may facilitate Pt nucleation at the CNT surface. As expected, Pt-GC has a much lower ECSA compared to Pt-CNT/GC or Pt-CNT/CNT/GC, which is associated with the larger Pt nanoparticles (see Supporting Information File 1, Figure S9) resulting from the much lower surface area of GC.
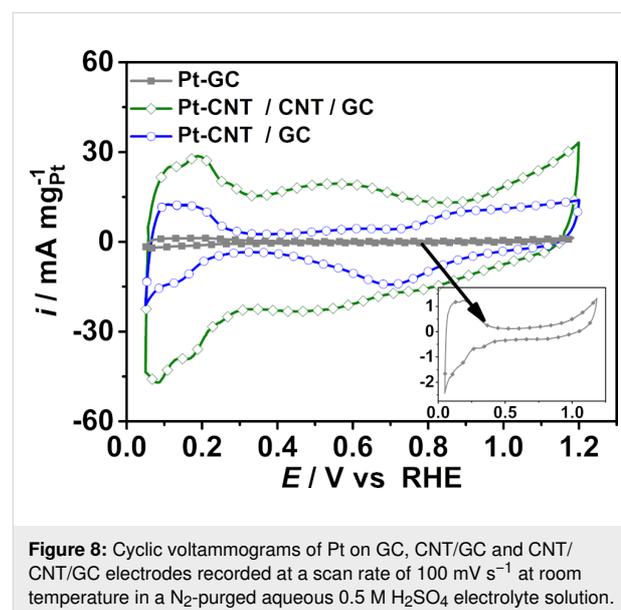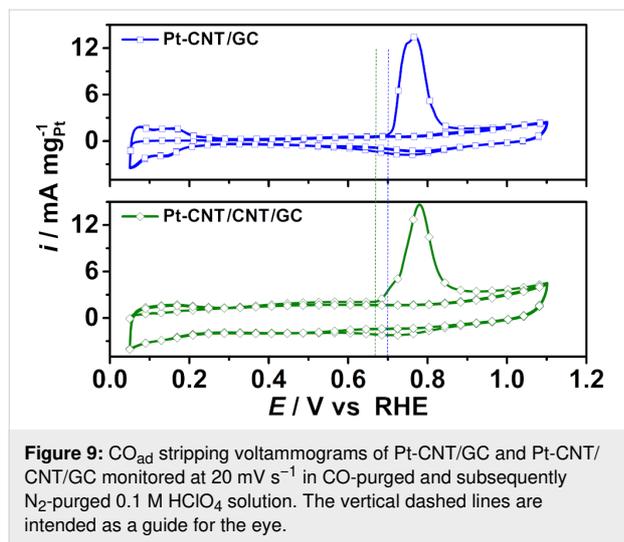

Figure 8: Cyclic voltammograms of Pt on GC, CNT/GC and CNT/CNT/GC electrodes recorded at a scan rate of 100 mV s^{-1} at room temperature in a N$_2$-purged aqueous 0.5 M H$_2$SO$_4$ electrolyte solution.

CO stripping voltammograms

In addition, CO_{ad} stripping voltammograms were recorded at a scan rate of 20 mV s^{-1} in the potential range of 0.05–1.1 V vs RHE after CO adsorption in N$_2$-purged 0.1 M HClO$_4$ solution for ECSA determination as well as investigation of CO tolerance as shown in Figure 9. HClO$_4$ was used as the electrolyte for these investigations instead of H$_2$SO$_4$ for a better comparability with literature values and to avoid disturbance of the CO_{ad} stripping voltamogramms by sulfate/bisulfate adsorption. The charge consumed during CO_{ad} oxidation was used to calculate the ECSA, and the values are 10.95 cm^2 mg^{-1}$_{Pt}$ for Pt-CNT/GC and 13.87 cm^2 mg^{-1}$_{Pt}$ for Pt-CNT/CNT/GC. The ECSAs determined from CO_{ad} stripping are higher than those from H$_{upd}$ (Table 1), and the ratio of ECSA$_{COad}$ to ECSA$_{Hupd}$ is 1.61 for Pt-CNT/GC and 1.12 for Pt-CNT/CNT/GC. This is comparable to values reported by Mayrhofer et al. [69]. The calculated ECSAs of Pt-CNT/GC and Pt-CNT/CNT/GC are lower than the values of 30–80 cm^2 mg^{-1}$_{Pt}$ ECSA for 2–3 nm Pt nanoparticles deposited onto CNTs as reported in the literature [70-72], in accordance with the larger size of the Pt nanoparticles. The differences in the ECSA ratios between both samples originate from the much more difficult baseline determination for the H$_{upd}$ peaks and thus a relatively large error. In this respect, the results on the surface-specific properties (see below) are related to the ECSA determined by CO stripping, which is believed to be much more reliable due to easier baseline correction.
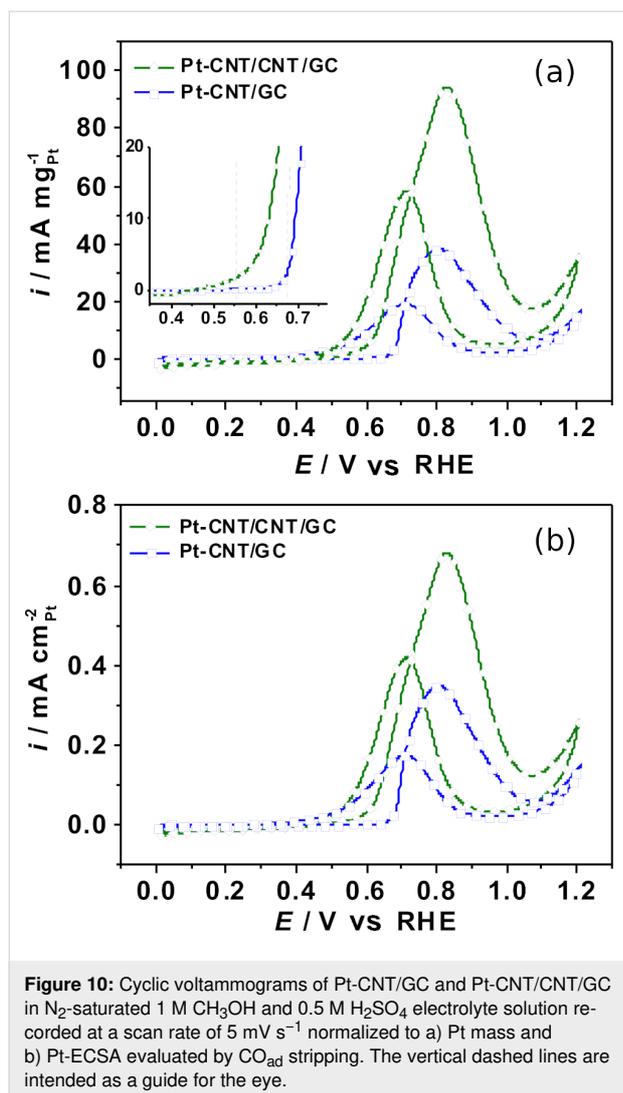

Figure 9: CO_{ad} stripping voltammograms of Pt-CNT/GC and Pt-CNT/CNT/GC monitored at 20 mV s^{-1} in CO-purged and subsequently N$_2$-purged 0.1 M HClO$_4$ solution. The vertical dashed lines are intended as a guide for the eye.

Methanol electro-oxidation

The CVs of the methanol oxidation reaction (MOR) over the Pt-containing nanostructured electrodes were recorded in N$_2$-purged 1 M CH$_3$OH and 0.5 M H$_2$SO$_4$ aqueous solution to investigate their suitability for electrocatalytic applications. Due to the large double-layer capacity of the samples, a slow scan rate of 5 mV s^{-1} was applied. Note that the oxidation current scales with the square root of the scan rate, while the double-layer charging current linearly scales with scan rate. Thus, the slow scan rate allows for a much more reliable determination of peak potentials and currents. The fifth cycle of each measurements is represented in Figure 10. The current response for electrochemical activity towards MOR was quantified to the Pt mass and the Pt ECSA in Figure 10a and Figure 10b, respectively, where the Pt ESCA was calculated from the CO_{ad} stripping voltammograms. Figure 10 represents the typical appearance of the CVs for methanol oxidation over Pt-based catalysts. Methanol is oxidized to CO$_2$ in the forward CV scan until Pt is oxidized, leading to a surface passivation and a sudden decrease in the oxidation current. During the backward CV scan, MeOH oxidation starts as soon as the electrode is liberated from oxides. In the literature, it is often observed that the current during the backward scan is higher and/or extends to less positive potentials than during the forward scan, since in the forward scan the electrode is blocked by intermediate carbonaceous species (e.g., CO) formed at lower potentials. Thus, the peak current ratio between the forward and backward scan (i_f/i_b) is typically used as a qualitative measure of the poisoning tolerance of a catalyst towards carbonaceous poisoning species formed during incomplete methanol oxidation at lower potentials [72-75]. In this regard, the comparably high (i_f/i_b) ratio (see below) indicates very good poisoning tolerance of our nanostructured samples. However, Hofstead-Duffy et al. [76] claimed that the forward and backward scan of methanol oxidation has the same chemical origin and the i_f/i_b ratio is inadequate to be used as a measure for CO tolerance, which is further demonstrated and complemented in [77,78]. Thus, we attempted to obtain additional information on CO tolerance from the CO stripping voltammograms. As shown in Figure 9, the hydrogen adsorption/desorption is suppressed in the potential range from 0.05 to 0.3 V vs RHE, indicating complete coverage of Pt with CO_{ad}. Pt-CNT/CNT/GC provides a more negative onset potential for CO oxidation at around 0.66 V vs RHE compared to Pt-CNT/GC ($\approx$0.7 V). The negative shift of the onset potential indicates that Pt-CNT/CNT/GC is superior for the electro-oxidation of CO_{ad} compared to Pt-CNT/GC The reason for this improved poisoning tolerance is not known to us at the moment. However, it is known from literature that methanol as well as CO oxidation are very sensitive to Pt surface structure. It might be that a defect-rich structure of our Pt nanoparticles formed by electrodeposition is highly active for CO and MeOH oxidation and less prone to poisoning.

The cyclic voltammograms in Figure 10 show differences in terms of the electrocatalytic activity. In the forward scan, Pt-CNT/CNT/GC provides Pt mass specific and Pt surface specific peak currents of 94.46 mA mg^{-1}$_{Pt}$ and 0.68 mA cm^{-2}$_{Pt}$ at

Figure 10: Cyclic voltammograms of Pt-CNT/GC and Pt-CNT/CNT/GC in N_2-saturated 1 M CH_3OH and 0.5 M H_2SO_4 electrolyte solution recorded at a scan rate of 5 mV s^{-1} normalized to a) Pt mass and b) Pt-ECSA evaluated by CO_{ad} stripping. The vertical dashed lines are intended as a guide for the eye.

Such enhancement in specific activity could be attributed to a better distribution of Pt on the high-surface-area secondary nanotubes, while on the primary CNTs, the Pt particles may be more densely packed. Furthermore, the secondary CNTs may increase the contact between GC and primary CNTs and within the CNT network, improving electron transfer pathways. Additionally, differences in particle shape or the presence of small particles invisible to SEM may contribute, however we can only speculate on this.

In the literature, graphene/CNT hybrids were demonstrated to be superior Pt catalyst supports towards MOR with respect to graphene, CNTs or commercial carbons [45,65,79-82]. In [65] electrodeposited Pt nanoparticles were used in a similar fashion as in our paper. Using a Pt-graphene/CNT hybrid material on GC, a mass specific current of 62.02 mA mg$^{-1}_{Pt}$ was found in 1 M methanol solution at a scan rate of 50 mV s^{-1}. It should be pointed that MOR measurements in literature are usually performed at scan rates of 50 or 100 mV s^{-1}, while in our study, we employ 5 mV s^{-1} for reasons explained above, and increased mass-specific peak currents at higher scan rates are expected according to the Randles–Sevcik equation. Furthermore, the Pt-mass specific peak current for Pt-CNT/CNT/GC is similar to that of the Pt-graphene/CNT hybrid material on carbon cloth (101.52 mA mg$^{-1}_{Pt}$), and the Pt-surface specific peak current was two times higher than that of Pt-graphene/CNT on carbon cloth (0.34 mA cm$^{-2}_{Pt}$) reported previously [79], indicating that the introduction of secondary CNTs may provide a similar or superior beneficial effect as graphene on the electrocatalytic activity toward MOR. In general, it can be concluded that Pt-CNT/CNT/GC, as prepared in this paper, performs similar or better compared to literature studies using similar systems.

In [52], similar nanostructures were prepared that showed high activity in the oxygen reduction reaction. Although there are differences in electrode preparation (in the present case, Pt is electrodeposited onto the carbon-based electrodes, probably leading to defect-rich particles (see also below), while in [52], Pt deposition has been deposited by CVD), we think that generally the high surface area and good accessibility of the active sites is a prerequisite for the enhanced electrocatalytic performance of such structures in various electrocatalytic reactions.

Conclusion

The preparation of hierarchically nanostructured electrodes for electrocatalytic applications was achieved via sequential growth of primary CNTs and secondary CNTs by CVD and finally Pt electrodeposition. CNT growth was carried out over electrodeposited iron nanoparticles. By varying the growth time, gas flow rate and ratio of H_2/Ar, it was shown that the structural properties of the primary and secondary CNTs could be tuned

the peak potential of 0.83 V vs RHE, respectively, which is much higher than those for Pt-CNT/GC, which are 38.54 mA mg$^{-1}_{Pt}$ and 0.35 mA cm$^{-2}_{Pt}$ at 0.81 V vs RHE, respectively. Pt-GC provides much lower specific peak currents of 1.88 mA mg$^{-1}_{Pt}$ and 0.17 mA cm$^{-2}_{Pt}$ as expected. The inset in Figure 10a indicates the superior onset potential of Pt-CNT/CNT/GC ($\approx$0.55 V vs RHE) compared to that of Pt-CNT/GC ($\approx$0.68 V vs RHE). Pt mass specific and Pt surface specific peak current ratios of Pt-CNT/CNT/GC related to Pt-CNT/GC are 2.5 and 1.9, respectively. For the backward scans, the values for Pt-CNT/CNT/GC were 58.14 mA mg$^{-1}_{Pt}$ and 0.41 mA cm$^{-2}_{Pt}$, which are again, significantly higher than those for Pt-CNT/GC (19.74 mA mg$^{-1}_{Pt}$ and 0.17 mA cm$^{-2}_{Pt}$). These values indicate that Pt-CNT/CNT/GC provides higher catalytic activity for the methanol oxidation. Similarly, Pt-CNT/CNT/GC exhibits a 1.3 times higher surface specific current density than Pt-CNT/GC for methanol oxidation in alkaline medium as shown in Supporting Information File 1, Figure S11.

to a certain extent. The secondary CNTs were adjusted to be smaller than the primary ones to obtain truly hierarchical structures. Enhanced double-layer capacitance as well changes in the Raman spectra with respect to the primary CNTs indicate the successful growth of secondary CNTs. Pt nanoparticles were homogeneously distributed onto both primary and secondary CNTs by electrodeposition. The Pt-CNT/CNT/GC electrode exhibited increased ECSA and electrochemical activity as well as more negative onset potential for MOR compared with Pt-CNT/GC. Additionally, CO_{ad} stripping indicated improved tolerance towards CO-like carbonaceous species poisoning. The improvement of electrochemical performance is attributed to the homogenous dispersion of Pt nanoparticles on the highly cross-linked 3D network. The prepared carbon electrode was shown to be a competitive catalyst support for methanol oxidation. In general, the applied sequences of electrodeposition and CVD steps may be considered as part of a toolbox enabling the preparation of hierarchically structured electrodes by tuning every step with respect to the requirements of a given electrochemical application.

Experimental
Electrode preparation
The procedure for the preparation of hierarchically structured electrodes is illustrated in Figure 1. Glassy carbon chips (GC, 2×1 cm^2) were oxidized by refluxing in 5 M HNO$_3$ (prepared by diluting ≥65% HNO$_3$, p.a, Roth, Germany) at 100 °C for 2 h to activate their surface and form oxygen functional groups as anchoring sites. Afterwards, Fe nanoparticles were grown on the oxidized GC by double pulse deposition [57] in 0.005 M FeSO$_4$·7H$_2$O (≥99.5%, Roth, Germany) and 0.5 M MgSO$_4$·7H$_2$O (pure, Roth, Germany) aqueous solution. MgSO$_4$ simply serves as a conducting electrolyte to avoid high solution resistance and does not take part in the reaction. A potential sequence consisting of a so-called "no-effect potential" ($E = -0.75$ V vs Ag|AgCl|KCl$_{sat.}$; $t = 5$ s), a nucleation potential ($E = -1.41$ V vs Ag|AgCl|KCl$_{sat.}$; $t = 0.2$ s) and a growth potential ($E = -1.27$ V vs Ag|AgCl|KCl$_{sat.}$; $t = 12$ s) was applied. The potentials were estimated considering linear-sweep voltammograms recorded in the potential range between -0.5 V and -1.75 V vs Ag|AgCl|KCl$_{sat.}$ with a scan rate of 5 mV s^{-1} as shown in Supporting Information File 1, Figure S1. The deposited Fe nanoparticles serve as a catalyst for growth of the so-called "primary CNTs", which was carried out through CVD at 750 °C in H$_2$/Ar mixtures saturated with cyclohexane (Roth) at room temperature, and the resulting structures are labelled as CNT/GC. The influence of growth time (30 min, 60 min and 120 min), gas flow rate and H$_2$/Ar ratio on the CNT growth was investigated, where gas flow rates were adjusted by mass flow controllers (Bronkhorst High-Tech, Germany). Prior to CVD, the Fe catalysts were conditioned at 750 °C for 30 min in a

H$_2$/Ar gas mixture. After the CNT growth, the surface of CNT/GC is highly hydrophobic. To remove remaining Fe nanoparticles, the CNT/GC electrodes were immersed in concentrated HNO$_3$ at room temperature for 12 h, where the CNTs were also oxidized to form anchoring sites for a second Fe deposition, which was carried out in the same way as above but with 8 s of growth time. "Secondary CNTs" were grown on the Fe-CNT/GC material in a gas mixture of H$_2$ (1.2 L h^{-1}) and Ar (0.5 L h^{-1}) at 750 °C for 120 min to form the hierarchical CNT/CNT/GC structure. Afterwards, the Fe nanoparticles were again leached out in concentrated HNO$_3$. Furthermore, the same procedure was performed using acetonitrile as a carbon source to yield N-CNT/N-CNT/GC.

Finally, Pt nanoparticles were electrochemically deposited onto CNT/GC and CNT/CNT/GC in an aqueous 0.005 M Pt(NO$_3$)$_2$ and 0.1 M NaNO$_3$ solution via linear-sweep voltammetry from 0 to -0.9 V vs Ag|AgCl|KCl$_{sat}$ at a scan rate of 5 mV s^{-1} to form Pt-CNT/GC and Pt-CNT/CNT/GC. For comparison, Pt deposition onto GC was performed in the same manner. The amount of deposited Pt was calculated from the charge consumed during the linear sweep voltammetry according to the following faradic reaction (Equation 1) and Faraday's law (Equation 2):

$$Pt^{2+} + 2e^- \rightarrow Pt \tag{1}$$

$$Q_{Pt} = n \times \frac{m_{Pt}}{M_{Pt}} \times F \tag{2}$$

where Q_{Pt} is the charge consumed to reduce Pt ions to Pt, n is the number of transfer electrons, m_{Pt} is the amount of Pt, M_{Pt} is the atomic weight of Pt (195.09 g mol^{-1}), and F is Faraday's constant (96485.31 C mol^{-1}).

Electrochemical characterization
Electrochemical experiments were carried out at room temperature in a one-compartment three-electrode cell employing a Gamry potentiostat PGI 4 controlled by the Gamry Framework 2.67 software. The modified GC, after its various treatment steps, served as working electrode, a Pt mesh (GoodFellow, Germany) as the counter electrode, and an Ag|AgCl|KCl$_{sat.}$ (SE20, Sensortechnik Meinsberg, Germany) for the electrodeposition and methanol oxidation or a reversible hydrogen electrode (RHE) built in-house for characterization as reference electrode. Before Pt deposition, GC, oxidized GC, CNT/GC and CNT/CNT/GC, were cleaned and activated employing CV in the potential range between 0 V and 1.2 V vs RHE at a scan rate of 200 mV s^{-1} for 50–100 cycles in N$_2$-purged 0.5 M H$_2$SO$_4$ (prepared from 98% H$_2$SO$_4$, Roth, Germany) aqueous solution until the CVs did not change any more, while Pt-GC,

Pt-CNT/GC and Pt-CNT/CNT/GC were cycled in the potential range from 0.05 V to 1.2 V vs RHE. After this treatment, the double-layer current of the electrodes without Pt and the hydrogen adsorption/desorption ($H_{ads/des}$) of the electrodes containing Pt were determined by CV at 100 mV s^{-1} in a fresh N$_2$-purged aqueous 0.5 M H$_2$SO$_4$ solution. The average charge during H_{ads} and H_{des} was used to determine the Pt-electrochemical surface area (ECSA). Additionally, the ECSA was determined through CO$_{ad}$ stripping voltammetry measured at a scan rate of 20 mV s^{-1} in the potential range of 0.05–1.1 V vs RHE in 0.1 M HClO$_4$ solution. HClO$_4$ was used as a supporting electrolyte in this case to avoid changes/deviations in the CO stripping peak by sulfate/bisulfate adsorption. The solution was purged with CO for 20 min to allow for CO adsorption on the Pt catalyst, and excess CO was removed by purging the electrolyte with N$_2$ for 20 min. The working electrode was held at 0.05 V during this procedure until the stripping voltammogram was recorded. Afterwards, the activity of the Pt-containing electrodes for methanol oxidation was investigated by CV at a low scan rate of 5 mV s^{-1} in an N$_2$-purged 1 M CH$_3$OH and 0.5 M H$_2$SO$_4$ aqueous solution. The low scan rate was used because of the large double-layer capacity of the hierarchical electrodes.

Structural characterization

The nanostructured electrodes were examined via SEM employing an ESEM XI 30 FEG (Philips, Germany) instrument to characterize the morphology and structural properties. The average particle size and size distribution of Fe nanoparticles were determined by examining the size of 200–300 particles with the software "Lince" (TU Damstadt, Germany) [83]. Raman spectra were measured employing a Renishaw InVia spectrometer with 532 nm excitation wavelength from a Cobolt CW DPSS laser. Due to the considerably thin film of the CNT layers, and thus the low amount of Pt, XRD did not yield useful results regarding the Pt structure and particle size.

Supporting Information

Supporting Information File 1
Additional SEM images and results of electrochemical characterization.
[https://www.beilstein-journals.org/bjnano/content/supplementary/2190-4286-10-146-S1.pdf]

Acknowledgements

ORCID® iDs

Michael Bron - https://orcid.org/0000-0002-3965-5691

References

1. Iijima, S. *Nature* **1991,** *354,* 56–58. doi:10.1038/354056a0
2. Lin, Z.; Zeng, Z.; Gui, X.; Tang, Z.; Zou, M.; Cao, A. *Adv. Energy Mater.* **2016,** *6,* 1600554. doi:10.1002/aenm.201600554
3. Gogotsi, Y. *Nanomaterials Handbook;* CRC Press: Boca Raton, FL, U.S.A., 2017.
4. Chouhan, V.; Noguchi, T.; Kato, S. *J. Appl. Phys.* **2016,** *119,* 134303. doi:10.1063/1.4945581
5. Sun, L.; Wang, X.; Wang, Y.; Zhang, Q. *Carbon* **2017,** *122,* 462–474. doi:10.1016/j.carbon.2017.07.006
6. Gupta, S.; Murthy, C. N.; Prabha, C. R. *Int. J. Biol. Macromol.* **2018,** *108,* 687–703. doi:10.1016/j.ijbiomac.2017.12.038
7. Rana, M. M.; Ibrahim, D. S.; Mohd Asyraf, M. R.; Jarin, S.; Tomal, A. *Sens. Rev.* **2017,** *37,* 127–136. doi:10.1108/sr-10-2016-0230
8. De Volder, M. F. L.; Tawfick, S. H.; Baughman, R. H.; Hart, A. J. *Science* **2013,** *339,* 535–539. doi:10.1126/science.1222453
9. Luo, C.; Xie, H.; Wang, Q.; Luo, G.; Liu, C. *J. Nanomater.* **2015,** *2015,* 1–10. doi:10.1155/2015/560392
10. Yuan, W.; Lu, S.; Xiang, Y.; Jiang, S. P. *RSC Adv.* **2014,** *4,* 46265–46284. doi:10.1039/c4ra05120c
11. Liu, J.; Lai, L.; Sahoo, N. G.; Zhou, W.; Shen, Z.; Chan, S. H. *Aust. J. Chem.* **2012,** *65,* 1213. doi:10.1071/ch12128
12. Nakashima, N., Ed. *Nanocarbons for Energy Conversion: Supramolecular Approaches;* Nanostructure Science and Technology; Springer International Publishing: Cham, Switzerland, 2019. doi:10.1007/978-3-319-92917-0
13. You, P. Y.; Kamarudin, S. K. *Chem. Eng. J.* **2017,** *309,* 489–502. doi:10.1016/j.cej.2016.10.051
14. Gao, W.; Zhao, M.; Jiang, Q. *ChemPhysChem* **2008,** *9,* 2092–2098. doi:10.1002/cphc.200800150
15. Zhang, L. Y.; Zhang, W.; Zhao, Z.; Liu, Z.; Zhou, Z.; Li, C. M. *RSC Adv.* **2016,** *6,* 50726–50731. doi:10.1039/c6ra06517a
16. DeLuca, N. W.; Elabd, Y. A. *J. Polym. Sci., Part B: Polym. Phys.* **2006,** *44,* 2201–2225. doi:10.1002/polb.20861
17. Larminie, J.; Dicks, A. *Fuel Cell Systems Explained,* 2nd ed.; Wiley: New York, NY, U.S.A., 2003. doi:10.1002/9781118878330
18. Liu, H.; Song, C.; Zhang, L.; Zhang, J.; Wang, H.; Wilkinson, D. P. *J. Power Sources* **2006,** *155,* 95–110. doi:10.1016/j.jpowsour.2006.01.030
19. Cheng, X.; Shi, Z.; Glass, N.; Zhang, L.; Zhang, J.; Song, D.; Liu, Z.-S.; Wang, H.; Shen, J. *J. Power Sources* **2007,** *165,* 739–756. doi:10.1016/j.jpowsour.2006.12.012
20. Nassr, A. B. A. A.; Bron, M. *ChemCatChem* **2013,** *5,* 1472–1480. doi:10.1002/cctc.201200742
21. Nassr, A. B. A. A.; Sinev, I.; Pohl, M.-M.; Grünert, W.; Bron, M. *ACS Catal.* **2014,** *4,* 2449–2462. doi:10.1021/cs401140g
22. Zhang, G.; Huang, C.; Qin, R.; Shao, Z.; An, D.; Zhang, W.; Wang, Y. *J. Mater. Chem. A* **2015,** *3,* 5204–5211. doi:10.1039/c4ta06076h
23. Antolini, E. *Energies (Basel, Switz.)* **2017,** *10,* 42. doi:10.3390/en10010042
24. Kakati, N.; Maiti, J.; Lee, S. H.; Jee, S. H.; Viswanathan, B.; Yoon, Y. S. *Chem. Rev.* **2014,** *114,* 12397–12429. doi:10.1021/cr400389f

25. Huang, M.; Zhang, J.; Wu, C.; Guan, L. *ACS Appl. Mater. Interfaces* **2017,** *9,* 26921–26927. doi:10.1021/acsami.7b07866

26. Xu, H.; Wang, A.-L.; Tong, Y.-X.; Li, G.-R. *ACS Catal.* **2016,** *6,* 5198–5206. doi:10.1021/acscatal.6b01010

27. Hameed, R. M. A.; Amin, R. S.; El-Khatib, K. M.; Fetohi, A. E. *Appl. Surf. Sci.* **2016,** *367,* 382–390. doi:10.1016/j.apsusc.2016.01.087

28. Elezovic, N. R.; Radmilovic, V. R.; Krstajic, N. V. *RSC Adv.* **2016,** *6,* 6788–6801. doi:10.1039/c5ra22403a

29. Oliveira Neto, A.; Franco, E. G.; Aricó, E.; Linardi, M.; Gonzalez, E. R. *J. Eur. Ceram. Soc.* **2003,** *23,* 2987–2992. doi:10.1016/s0955-2219(03)00310-8

30. Xu, Y.; Chen, L.; Wang, X.; Yao, W.; Zhang, Q. *Nanoscale* **2015,** *7,* 10559–10583. doi:10.1039/c5nr02216a

31. Bönnemann, H.; Brijoux, W.; Brinkmann, R.; Joußen, T.; Korall, B.; Dinjus, E. *Angew. Chem., Int. Ed. Engl.* **1991,** *30,* 1312–1314. doi:10.1002/anie.199113121

32. Zhao, Z.-G.; Yao, Z.-J.; Zhang, J.; Zhu, R.; Jin, Y.; Li, Q.-W. *J. Mater. Chem.* **2012,** *22,* 16514. doi:10.1039/c2jm32769d

33. Pham, V. V.; Ta, V.-T.; Sunglae, C. *Int. J. Hydrogen Energy* **2017,** *42,* 13192–13197. doi:10.1016/j.ijhydene.2017.01.236

34. Xu, L.; Luo, Z.; Fan, Z.; Yu, S.; Chen, J.; Liao, Y.; Xue, C. *Chem. – Eur. J.* **2015,** *21,* 8691–8695. doi:10.1002/chem.201406677

35. Georgieva, J.; Valova, E.; Mintsouli, I.; Sotiropoulos, S.; Tatchev, D.; Armyanov, S.; Hubin, A.; Dille, J.; Hoell, A.; Raghuwanshi, V.; Karanasios, N.; Malet, L. *J. Electroanal. Chem.* **2015,** *754,* 65–74. doi:10.1016/j.jelechem.2015.07.001

36. Sahin, N. E.; Napporn, T. W.; Dubau, L.; Kadirgan, F.; Léger, J.-M.; Kokoh, K. B. *Appl. Catal., B* **2017,** *203,* 72–84. doi:10.1016/j.apcatb.2016.09.026

37. Huang, H.; Wang, X. *J. Mater. Chem. A* **2014,** *2,* 6266–6291. doi:10.1039/c3ta14754a

38. Liu, J.; Liu, C.-T.; Zhao, L.; Zhang, J.-J.; Zhang, L.-M.; Wang, Z.-B. *Int. J. Hydrogen Energy* **2016,** *41,* 1859–1870. doi:10.1016/j.ijhydene.2015.11.103

39. Zhang, J.; Yi, X.-b.; Liu, S.; Fan, H.-L.; Ju, W.; Wang, Q.-C.; Ma, J. *J. Phys. Chem. Solids* **2017,** *102,* 99–104. doi:10.1016/j.jpcs.2016.11.006

40. Zhang, J.-J.; Wang, Z.-B.; Li, C.; Zhao, L.; Liu, J.; Zhang, L.-M.; Gu, D.-M. *J. Power Sources* **2015,** *289,* 63–70. doi:10.1016/j.jpowsour.2015.04.150

41. Yola, M. L.; Eren, T.; Atar, N.; Saral, H.; Ermiş, İ. *Electroanalysis* **2016,** *28,* 570–579. doi:10.1002/elan.201500381

42. Jiang, H.; Zhao, T.; Li, C.; Ma, J. *Chem. Commun.* **2011,** *47,* 8590–8592. doi:10.1039/c1cc12942b

43. Qian, W.; Hao, R.; Zhou, J.; Eastman, M.; Manhat, B. A.; Sun, Q.; Goforth, A. M.; Jiao, J. *Carbon* **2013,** *52,* 595–604. doi:10.1016/j.carbon.2012.10.031

44. Huang, H.; Wang, X. *J. Mater. Chem.* **2012,** *22,* 22533. doi:10.1039/c2jm33727d

45. Wang, Y.-S.; Yang, S.-Y.; Li, S.-M.; Tien, H.-W.; Hsiao, S.-T.; Liao, W.-H.; Liu, C.-H.; Chang, K.-H.; Ma, C.-C. M.; Hu, C.-C. *Electrochim. Acta* **2013,** *87,* 261–269. doi:10.1016/j.electacta.2012.09.013

46. Su, Z.; Li, C.; Cheng, Y.; Gui, Q.; Xiong, Y.; Tan, Y.; Jiang, H.; Liu, X. *RSC Adv.* **2018,** *8,* 33742–33747. doi:10.1039/c8ra06246c

47. Ma, Y.; Wang, Q.; Miao, Y.; Lin, Y.; Li, R. *Appl. Surf. Sci.* **2018,** *450,* 413–421. doi:10.1016/j.apsusc.2018.04.094

48. Zhang, Z.; Jing, H.-K.; Liu, S.; Li, G.-R.; Gao, X.-P. *J. Mater. Chem. A* **2015,** *3,* 6827–6834. doi:10.1039/c4ta07183b

49. Liu, J.; Zeng, B.; Wang, X.; Wang, W.; Shi, H. *Appl. Phys. Lett.* **2013,** *103,* 053105. doi:10.1063/1.4816751

50. Li, Y.; Huang, Y.; Zhang, Z.; Duan, D.; Hao, X.; Liu, S. *Chem. Eng. J.* **2016,** *283,* 911–921. doi:10.1016/j.cej.2015.08.063

51. Guo, L.; Jiang, W.-J.; Zhang, Y.; Hu, J.-S.; Wei, Z.-D.; Wan, L.-J. *ACS Catal.* **2015,** *5,* 2903–2909. doi:10.1021/acscatal.5b00117

52. Kundu, S.; Nagaiah, T. C.; Chen, X.; Xia, W.; Bron, M.; Schuhmann, W.; Muhler, M. *Carbon* **2012,** *50,* 4534–4542. doi:10.1016/j.carbon.2012.05.037

53. Hsieh, C.-T.; Lin, J.-Y.; Chou, Y.-W. *Chem. Phys. Lett.* **2007,** *444,* 149–154. doi:10.1016/j.cplett.2007.07.001

54. Li, N.; Chen, X.; Stoica, L.; Xia, W.; Qian, J.; Aßmann, J.; Schuhmann, W.; Muhler, M. *Adv. Mater. (Weinheim, Ger.)* **2007,** *19,* 2957–2960. doi:10.1002/adma.200602625

55. Xia, W.; Chen, X.; Kundu, S.; Wang, X.; Grundmeier, G.; Wang, Y.; Bron, M.; Schuhmann, W.; Muhler, M. *Surf. Coat. Technol.* **2007,** *201,* 9232–9237. doi:10.1016/j.surfcoat.2007.05.031

56. Susi, T.; Nasibulin, A. G.; Jiang, H.; Kauppinen, E. I. *J. Nanomater.* **2008,** *2008,* 1–7. doi:10.1155/2008/425195

57. Ueda, M.; Dietz, H.; Anders, A.; Kneppe, H.; Meixner, A.; Plieth, W. *Electrochim. Acta* **2002,** *48,* 377–386. doi:10.1016/s0013-4686(02)00683-7

58. Sato, S.; Kawabata, A.; Nihei, M.; Awano, Y. *Chem. Phys. Lett.* **2003,** *382,* 361–366. doi:10.1016/j.cplett.2003.10.076

59. Kumar, M.; Ando, Y. *J. Nanosci. Nanotechnol.* **2010,** *10,* 3739–3758. doi:10.1166/jnn.2010.2939

60. Li, W. Z.; Wen, J. G.; Tu, Y.; Ren, Z. F. *Appl. Phys. A: Mater. Sci. Process.* **2001,** *73,* 259–264. doi:10.1007/s003390100916

61. Li, W. Z.; Wen, J. G.; Ren, Z. F. *Appl. Phys. A: Mater. Sci. Process.* **2002,** *74,* 397–402. doi:10.1007/s003390201284

62. Cheng, T.-C. *Mater. Chem. Phys.* **2012,** *136,* 140–145. doi:10.1016/j.matchemphys.2012.06.043

63. Raney, J. R.; Misra, A.; Daraio, C. *Carbon* **2011,** *49,* 3631–3638. doi:10.1016/j.carbon.2011.04.066

64. Heise, H. M.; Kuckuk, R.; Ojha, A. K.; Srivastava, A.; Srivastava, V.; Asthana, B. P. *J. Raman Spectrosc.* **2009,** *40,* 344–353. doi:10.1002/jrs.2120

65. Rajesh; Paul, R. K.; Mulchandani, A. *J. Power Sources* **2013,** *223,* 23–29. doi:10.1016/j.jpowsour.2012.08.088

66. Alexeyeva, N.; Tammeveski, K. *Electrochem. Solid-State Lett.* **2007,** *10,* F18. doi:10.1149/1.2713657

67. Steimecke, M.; Rümmler, S.; Bron, M. *Electrochim. Acta* **2015,** *163,* 1–8. doi:10.1016/j.electacta.2015.02.142

68. Ralph, T. R.; Hards, G. A.; Keating, J. E.; Campbell, S. A.; Wilkinson, D. P.; Davis, M.; St-Pierre, M.; Johnson, M. C. *J. Electrochem. Soc.* **1997,** *144,* 3845. doi:10.1149/1.1838101

69. Mayrhofer, K. J. J.; Strmcnik, D.; Blizanac, B. B.; Stamenkovic, V.; Arenz, M.; Markovic, N. M. *Electrochim. Acta* **2008,** *53,* 3181–3188. doi:10.1016/j.electacta.2007.11.057

70. Chen, S.; Wei, Z.; Guo, L.; Ding, W.; Dong, L.; Shen, P.; Qi, X.; Li, L. *Chem. Commun.* **2011,** *47,* 10984–10986. doi:10.1039/c1cc14261e

71. Tong, X.; Zhang, J.; Zhang, G.; Wei, Q.; Chenitz, R.; Claverie, J. P.; Sun, S. *Chem. Mater.* **2017,** *29,* 9579–9587. doi:10.1021/acs.chemmater.7b04221

72. Bedolla-Valdez, Z. I.; Verde-Gómez, Y.; Valenzuela-Muñiz, A. M.; Gochi-Ponce, Y.; Oropeza-Guzmán, M. T.; Berhault, G.; Alonso-Núñez, G. *Electrochim. Acta* **2015,** *186,* 76–84. doi:10.1016/j.electacta.2015.10.084

73. Mancharan, R.; Goodenough, J. B. *J. Mater. Chem.* **1992,** *2,* 875. doi:10.1039/jm9920200875

74. Lu, S.; Eid, K.; Ge, D.; Guo, J.; Wang, L.; Wang, H.; Gu, H. *Nanoscale* **2017,** *9,* 1033–1039. doi:10.1039/c6nr08895c

75. Huang, L.; Zhang, X.; Wang, Q.; Han, Y.; Fang, Y.; Dong, S. *J. Am. Chem. Soc.* **2018,** *140,* 1142–1147. doi:10.1021/jacs.7b12353

76. Hofstead-Duffy, A. M.; Chen, D.-J.; Sun, S.-G.; Tong, Y. J. *J. Mater. Chem.* **2012,** *22,* 5205. doi:10.1039/c2jm15426a

77. Zhao, Y.; Li, X.; Schechter, J. M.; Yang, Y. *RSC Adv.* **2016,** *6,* 5384–5390. doi:10.1039/c5ra24249e

78. Chung, D. Y.; Lee, K.-J.; Sung, Y.-E. *J. Phys. Chem. C* **2016,** *120,* 9028–9035. doi:10.1021/acs.jpcc.5b12303

79. Wang, P.; Kottakkat, T.; Bron, M. *ChemElectroChem* **2015,** *2,* 1396–1402. doi:10.1002/celc.201500044

80. Ye, F.; Cao, X.; Yu, L.; Chen, S.; Lin, W. *Int. J. Electrochem. Sci.* **2012,** *7,* 1251–1265.

81. Jhan, J.-Y.; Huang, Y.-W.; Hsu, C.-H.; Teng, H.; Kuo, D.; Kuo, P.-L. *Energy* **2013,** *53,* 282–287. doi:10.1016/j.energy.2013.03.002

82. Zhang, X.; Zhang, J.; Huang, H.; Jiang, Q.; Wu, Y. *Electrochim. Acta* **2017,** *258,* 919–926. doi:10.1016/j.electacta.2017.11.142

83. *Lince Software;* Department of Material Science, TU Darmstadt: Darmstadt, Germany, 1999.

Synthesis of P- and N-doped carbon catalysts for the oxygen reduction reaction via controlled phosphoric acid treatment of folic acid

Rieko Kobayashi[1,2], Takafumi Ishii[1], Yasuo Imashiro[1,3] and Jun-ichi Ozaki[*1]

Abstract

Herein, we synthesized P- and N-doped carbon materials (PN-doped carbon materials) through controlled phosphoric acid treatment (CPAT) of folic acid (FA) and probed their ability to catalyze the oxygen reduction reaction (ORR) at the cathode of a fuel cell. Precursors obtained by heating FA in the presence of phosphoric acid at temperatures of 400–1000 °C were further annealed at 1000 °C to afford PN-doped carbon materials. The extent of precursor P doping was maximized at 700 °C, and the use of higher temperatures resulted in activation and increased porosity rather than in increased P content. The P/C atomic ratios of PN-doped carbon materials correlated well with those of the precursors, which indicated that CPAT is well suited for the preparation of PN-doped carbon materials. The carbon material prepared using a CPAT temperature of 700 °C exhibited the highest ORR activity and was shown to contain $-C-PO_2$ and $-C-PO_3$ moieties as the major P species and pyridinic N as the major N species. Moreover, no N–P bonds were detected. It was concluded that the presence of $-C-PO_2$ and $-C-PO_3$ units decreases the work function and thus raises the Fermi level above the standard O_2/H_2O reduction potential, which resulted in enhanced ORR activity. Finally, CPAT was concluded to be applicable to the synthesis of PN-doped carbon materials from N-containing organic compounds other than FA.

Introduction

The widespread application of fuel cells as clean energy sources is the most desirable way of realizing a low-CO_2-emission society. In conventional polymer electrolyte fuel cells (PEFCs), both anode and cathode reactions are catalyzed by Pt. Com- pared to the anode reaction, the cathode reaction, namely the oxygen reduction reaction (ORR), is rather slow and hence requires the use of larger amounts of Pt [1], which increases the cost of PEFCs and prevents their wide application as domestic,

back-up, and vehicle power sources. The cost of cathode catalysts can be reduced in a number of ways, e.g., by alloying Pt with base metals [2], forming core–shell particles with base-metal cores covered by thin Pt layers [3], and developing non-Pt catalysts. In particular, the implementation of non-Pt or non-precious-metal cathode catalysts is the ultimate goal of PEFC development.

Since the discovery of the ORR activity of cobalt phthalocyanine in 1964 [4], numerous studies have focused on the synthesis of non-precious metal ORR catalysts such as those based on carbon [5]. The thermal treatment of carbon materials impregnated with N_4–M complexes was found to afford highly active and durable ORR catalysts. Since then, much effort has been directed at clarifying the nature of the active sites in these catalysts and the ORR activity has been predominantly ascribed to N_x–M (M = Co, Fe) moieties on the surface of the carbon supports [6,7]. Our research group has identified and characterized different types of non-Pt ORR catalysts, the so-called carbon alloy catalysts (CACs) [8]. We prepared two types of CACs (nanoshell-containing carbon materials [9,10] and BN-doped carbon materials [11]) and further improved their ORR activity and durability to afford a commercial CAC [12,13] and thus realized the world's first portable PEFC cell containing a non-precious-metal cathode catalyst [14,15].

Much effort has been directed at the development of transition-metal-free carbon catalysts for the ORR, with the best practical performance so far observed for N-doped carbon materials [16]. For example, a recently reported metal-free catalyst based on N-doped carbon nanotubes showed high ORR activity even under acidic conditions and allowed for facile electricity generation when employed as a single-cell cathode [17]. The ORR activity of carbon-based catalysts can be substantially improved by their simultaneous doping with N and other elements. In 2007, we reported that carbon prepared by carbonization of a N- and B-doped furan resin exhibited an increased ORR activity in sulfuric acid solution [11], and since then, much attention has been directed at the activation of carbon catalysts through co-doping [18]. The concept of co-doping has been even extended to three-component catalysts, as exemplified by studies on N, P, S-doped and N, P, F-doped carbon materials [19,20]. Strelko et al. used theoretical methods to establish an interesting relationship between the bandgap energy of a given catalyst and its ability to promote reactions involving electron transfer [21]. Moreover, P-doping of graphitic layers was revealed to have an effect similar to that of N-doping and hence, co-doping with P and N was found to be an effective way of increasing the ORR activity of carbon materials [22-26]. Most of the reported PN-doping techniques involve the carbonization of [N-containing polymer + P-containing compound] mixtures or of ionic liquids containing both N and P, i.e., employ special compounds or their combinations as starting materials.

Herein, to establish a more generalized PN-doping method allowing for the use of more common compounds, we developed the technique of controlled phosphoric acid treatment (CPAT) that is potentially applicable to non-special N-containing organic compounds and applied it to folic acid (FA) as a commonly occurring N-containing organic compound. During CPAT, phosphoric acid (PA) acts as both a P-doping agent [20,27-31] and a chemical activator to introduce pores [32,33]. The CPAT method, we used here, includes pretreatment with phosphoric acid at various temperatures to alter the properties of the precursors of carbon materials. In the present study, PN-doped precursors synthesized at CPAT temperatures of 400–800 °C were carbonized at 1000 °C to prepare PN-doped carbon materials, and factors influencing the ORR catalytic activity of these carbon materials were investigated in detail.

Results
Structure, chemical composition and ORR activity of precursors

The CPAT temperature affected both the BET specific surface area (BET-SSA) and surface elemental composition of the precursors, as exemplified by values derived from X-ray photoelectron spectra of P-series precursors (Table 1, for the naming scheme of the samples see section "Experimental"). The N_2 adsorption isotherms together with the micropore size distribution curves are given in Figure S1 (Supporting Information File 1). The BET specific surface area values were calculated from these isotherms. The BET-SSAs of samples prepared at CPAT temperatures below 700 °C were estimated to be of

Table 1: Surface properties of H- and P-type precursors (for the naming scheme of the samples see section "Experimental").
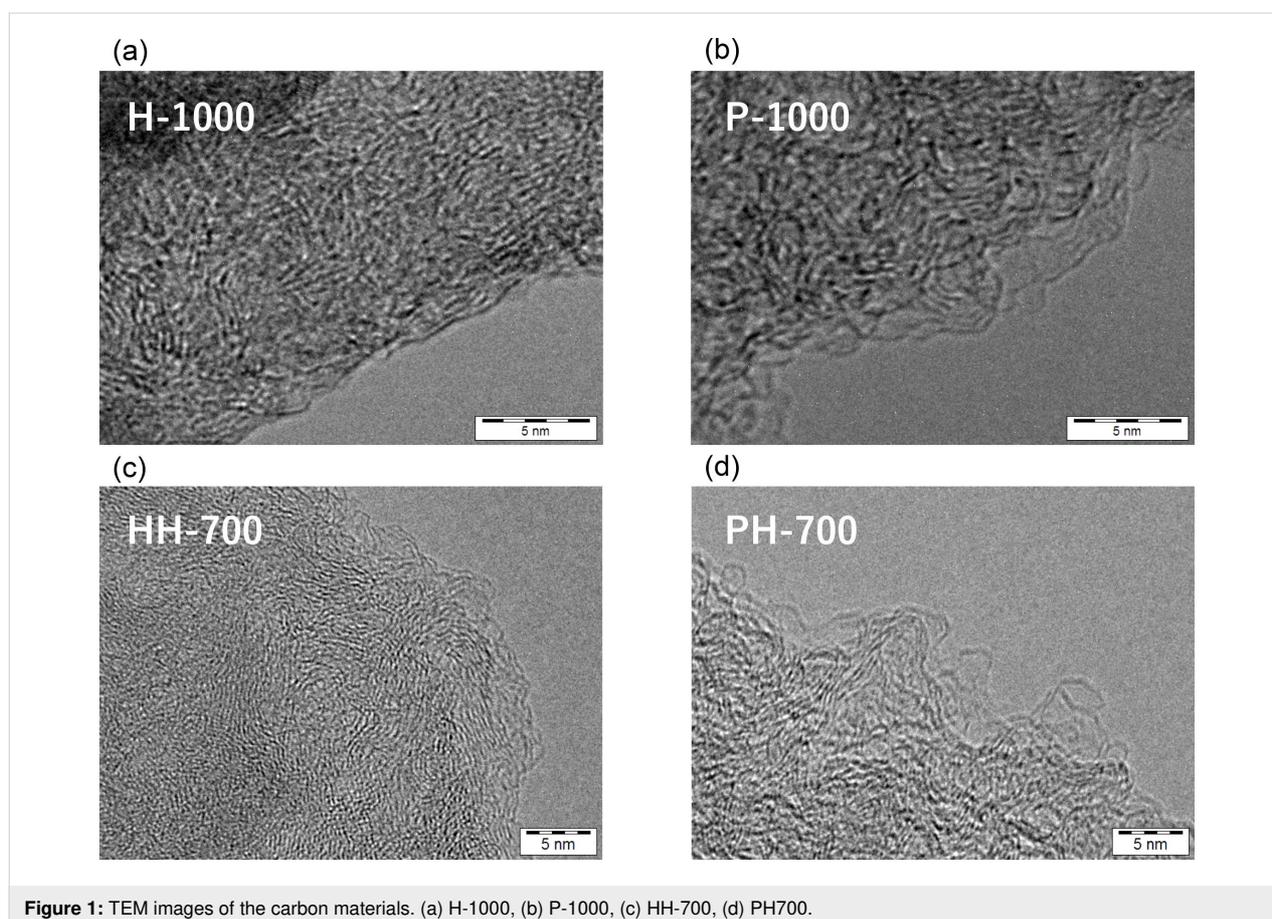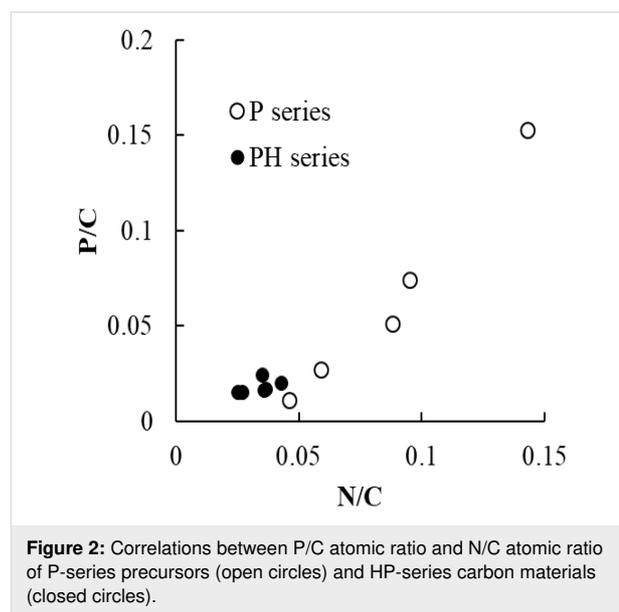
sample	BET-SSA ($m^2 \cdot g^{-1}$)	surface composition		
		C (atom %)	N/C	O/C	P/C
H-400	20	61.7	0.206	0.415	—
H-500	65	67.2	0.243	0.246	—
H-600	115	61.4	0.213	0.415	—
H-700	56	79.2	0.091	0.172	—
H-1000	84	81.5	0.055	0.172	—
P-400	2	76.0	0.046	0.258	0.011
P-500	7	72.6	0.059	0.292	0.027
P-600	8	70.2	0.088	0.286	0.051
P-700	6	50.0	0.143	0.702	0.153
P-800	277	68.2	0.095	0.296	0.074
P-1000	1014	84.0	0.043	0.125	0.022

several square meters per gram but rapidly increased at CPAT temperatures above 800 °C, with maximum values obtained at 1000 °C. This behavior was different from that of H-series precursors.

Figure 1a,b shows the transmission electron microscopy (TEM) images of the selected samples. Comparing the images of (a) H-1000 and (b) P-1000 revealed differences in the carbon structure. P-1000 is less dense than H-1000 and exhibits a round surface composed of graphitic layers.
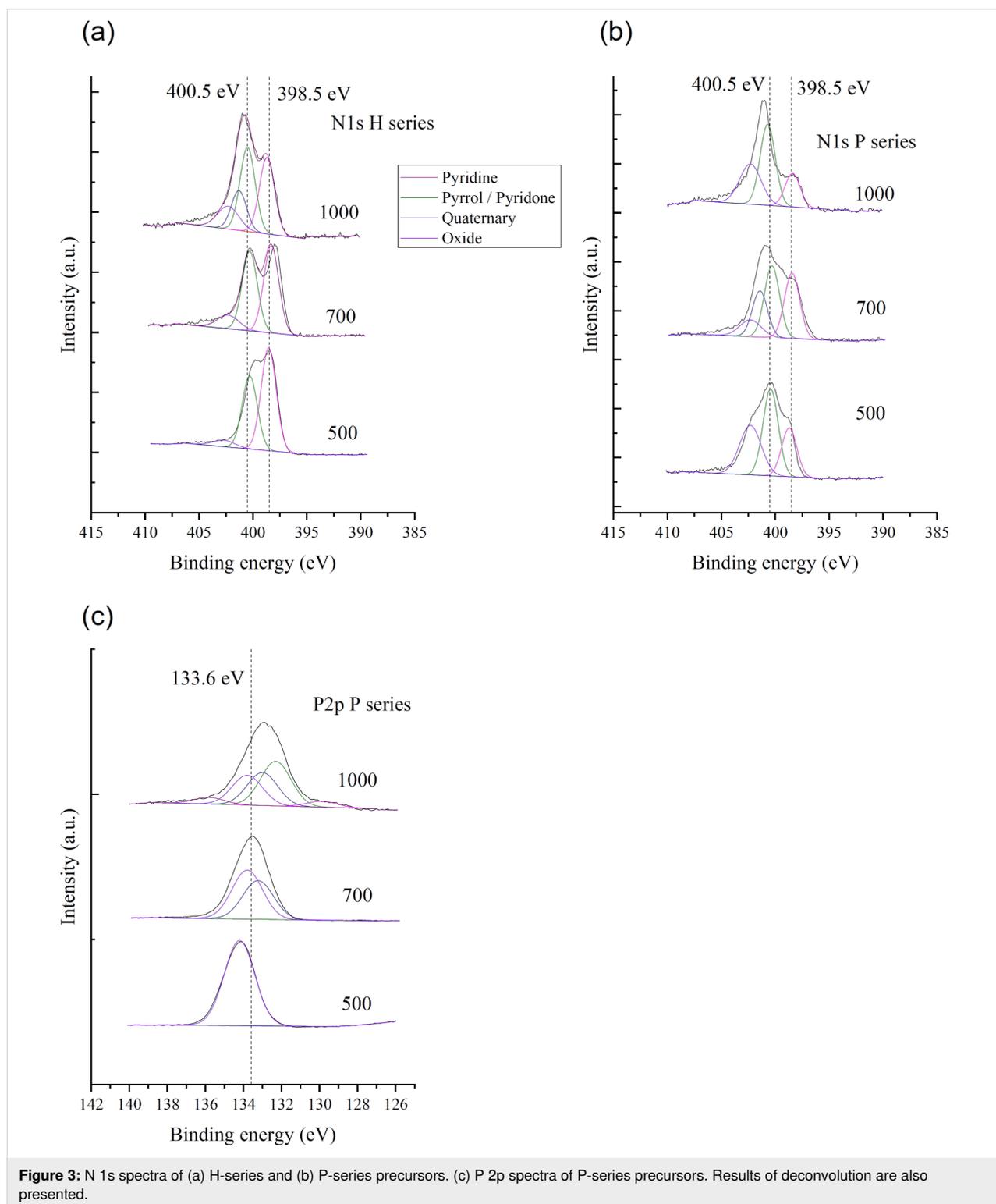
The results of X-ray photoelectron spectroscopy (XPS) analysis demonstrated that when pretreatment was performed in the absence of PA, the N content of the carbon materials decreased with increasing temperature. On the other hand, in the presence of PA, the N/C atomic ratio initially increased with increasing CPAT temperature, reaching a maximum at 700 °C, and then decreased again. The O/C ratio behaved similarly to the N/C ratio regardless of the presence of PA but could not be accurately estimated because of the effects of atmospheric moisture and oxygen. The P/C ratio of P-series precursors was maximal at a CPAT temperature of 700 °C, i.e., it behaved similarly to the N/C ratio. Thus, CPAT promoted both the development of

specific surface area and P doping, and the relative contributions of these roles were determined by temperature, i.e., P-doping was dominant below 700 °C, while chemical activation was dominant at higher temperatures [34]. Figure 2 shows

Figure 2: Correlations between P/C atomic ratio and N/C atomic ratio of P-series precursors (open circles) and HP-series carbon materials (closed circles).

Figure 1: TEM images of the carbon materials. (a) H-1000, (b) P-1000, (c) HH-700, (d) PH700.

the correlation between P/C ratio and N/C ratio in P-series precursors and HP-series carbon materials. It indicates the presence of some chemical interactions between the nitrogen in folic acid and the phosphorus in phosphoric acid, which will be discussed in the "Discussion" section.

The chemical states of N in P-series precursors were studied by XPS (Figure 3a,b), which revealed that the shapes of N 1s spectra depended on the pretreatment temperature and the presence/absence of PA. H-series precursors featured N 1s spectra with two peaks, the positions of which were affected by CPAT tem-

Figure 3: N 1s spectra of (a) H-series and (b) P-series precursors. (c) P 2p spectra of P-series precursors. Results of deconvolution are also presented.

perature (Figure 3a). For FA pretreated at 500 °C (H-500), these peaks were located at 398.5 and 400.0 eV, while for H-700, peaks at 397.9 and 400.5 eV were observed, and for H-1000, signals were detected at 398.5 and 401.1 eV. The broad N 1s spectra (Figure 3b) of P-series precursors prepared at 500 and 700 °C were assumed to be a superposition of several peaks; the results of its deconvolution are also presented in Figure 3a,b. For example, the spectrum of P-500 was deconvoluted into peaks at 398.5, 400.5, and 402.5 eV, while that of P-700 was deconvoluted into peaks at 398.5, 399.8, and 401.0 eV. In contrast, the N 1s spectrum of P-1000 featured two overlapping peaks centered at 398.5 and 401.7 eV.

Conventionally, peaks at 398.5, 400.5, 401, and 402 eV in the N 1s spectra of N-doped carbon materials are assigned to pyridinic, pyrrole/pyridone-type, quaternary, and oxygen-bonded (oxidized) N, respectively (Table 2). Thus, P-700 contained quaternary N incorporated into graphite layers, as exemplified by the corresponding peaks at 401–400.7 eV. The peak of pyridinic N (398.5 eV), clearly observed for H-series precursors, was less pronounced in the case of P-series precursors, e.g., the intensity of this peak was higher for H-1000 than for P-1000.

Table 2: Distribution of the N species in H-type and P-type precursors.

sample	N/C	$N_{pyridine}$	N_{pyrrol}	$N_{quaternary}$	N_{oxides}
H400	0.207	0.43	0.40	0.00	0.18
H500	0.243	0.56	0.39	0.00	0.05
H600	0.214	0.47	0.42	0.00	0.12
H700	0.091	0.47	0.43	0.00	0.10
H1000	0.055	0.33	0.36	0.17	0.14
P400	0.046	0.14	0.53	0.00	0.33
P500	0.059	0.33	0.42	0.00	0.25
P600	0.088	0.44	0.40	0.00	0.16
P700	0.143	0.32	0.35	0.22	0.12
P800	0.095	0.34	0.32	0.21	0.13
P1000	0.043	0.12	0.47	0.00	0.33

The P 2p XPS spectra of the P-series precursors are presented in Figure 3c. The peak shifted from 134.2 to 133.0 eV with the increase of the CPAT temperature. The figure also includes the results of peak deconvolution by assuming the presences of the five species given in the legend. The P-species varied with the CPAT temperature.

The ORR voltammograms of the precursors are presented in Figure S4 (Supporting Information File 1). Both H-series and P-series precursors showed increased ORR activity with the CPAT temperature. The temperature-dependence of ORR activ-

ity is remarkably large for P-series precursors. The highest ORR activity among the precursors was achieved by P-1000.

Structure, chemical composition, and electronic properties of carbonized FA

PH-series carbon materials were prepared by thoroughly rinsing P-series precursors with water to remove excess PA and subjecting them to carbonization at 1000 °C. The same operation was also performed for H-series precursors to afford HH-series carbon materials. The N_2 adsorption isotherms are presented in Figure S5 (Supporting Information File 1) with the micropore size distribution calculated by the MP-method. The BET-SSAs of these two carbon series exhibited different behaviors (Table 3), e.g., those of HH-series carbon materials were almost constant (ca. 30 $m^2 \cdot g^{-1}$) even though the corresponding precursors showed different BET-SSA values, whereas the BET-SSA of PH-series carbon materials increased with increasing CPAT temperature. Specifically, the samples with CPAT temperature above 700 °C showed remarkable increases of BET-SSA. This might be caused by desorption or destruction of instable compounds formed by CPAT at these temperatures.

Table 3: BET-SSAs and XPS-determined elemental surface compositions of HH- and PH-series carbon materials.

sample	BET-SSA ($m^2 \cdot g^{-1}$)	surface composition			
		C (atom %)	N/C	O/C	P/C
HH-400	34	83.7	0.054	0.141	—
HH-500	32	81.6	0.043	0.183	—
HH-600	30	81.2	0.033	0.199	—
HH-700	32	81.3	0.043	0.187	—
H-1000	84	81.5	0.055	0.172	—
PH-400	48	83.0	0.027	0.164	0.015
PH-500	243	82.3	0.036	0.164	0.016
PH-600	311	82.4	0.025	0.174	0.015
PH-700	674	81.6	0.035	0.166	0.024
PH-800	564	80.4	0.043	0.181	0.020
PH-900	1008	82.6	0.036	0.157	0.017
P-1000	1014	84.0	0.043	0.125	0.022

Table 3 also lists N/C and P/C atomic ratios determined by XPS, demonstrating that for HH- and PH-series carbon materials. The former ratio showed no clear dependence on the pretreatment temperature and was in the range of 0.03–0.05. Conversely, the P/C atomic ratio of PH-series carbon materials varied in the range of 0.015–0.024, with a maximum value obtained at 700 °C. Figure 4 shows the relationship between the elemental composition of the precursors and that of the carbon materials, revealing that the N content of the precursors had no

influence on that of the carbon materials, while the P content of PH-series carbon materials was positively correlated with that of P-series precursors with a linear correlation coefficient of $r = 0.943$. These results confirmed the viability of the CPAT method and demonstrated that carbon materials with a high extent of P-doping can be prepared from precursors with a high P/C atomic ratio.

Figure 5a,b shows that although the N 1s spectra of both HH- and PH-series carbon materials comprise two peaks, the relative intensities of these two peaks were different, as exemplified by the spectra of H-1000 and P-1000. The shapes of the N 1s spectra of other HH- and PH-series carbon materials were similar to those of H-1000 and P-1000 spectra, respectively, and did not depend on the pretreatment temperature. The N 1s spectra were deconvoluted into the four abovementioned peaks (pyridinic, pyrrole/pyridone-type, quaternary, and oxidized N) as shown in Figure 5, with the results presented in Table 4. Notably, the spectra of PH-series carbon materials were dominated by peaks of non-pyridinic N, while those of HH-series

carbon materials featured signals of pyridinic and pyrrole/pyridone-type N of comparable intensities.

The P 2p spectra of all PH-series carbon materials featured broad asymmetric signals at 132.5 eV (Figure 5c) that were deconvoluted into five components (Table 5). The most and second-most abundant moieties were identified as $-C-PO_2$ (P2) and $-C-PO_3$ (P3), respectively, and the contributions of other components (P1 (C–P): P bonded only to carbon atoms, P4 ($-C-O-PO_3$: P bonded to carbon via oxygen, P5 (P_2O_5): P without any bonds to carbon) were found to be minor [35].

The above observations revealed that carbonization at 1000 °C attenuated the differences in the chemical states of P and N observed in the precursors. However, the effects of CPAT such as changes in the chemical states of N and the amount of P were retained.

The work function of PH-series carbon materials was determined by the vibration capacitance (Kelvin) method and fluctu-
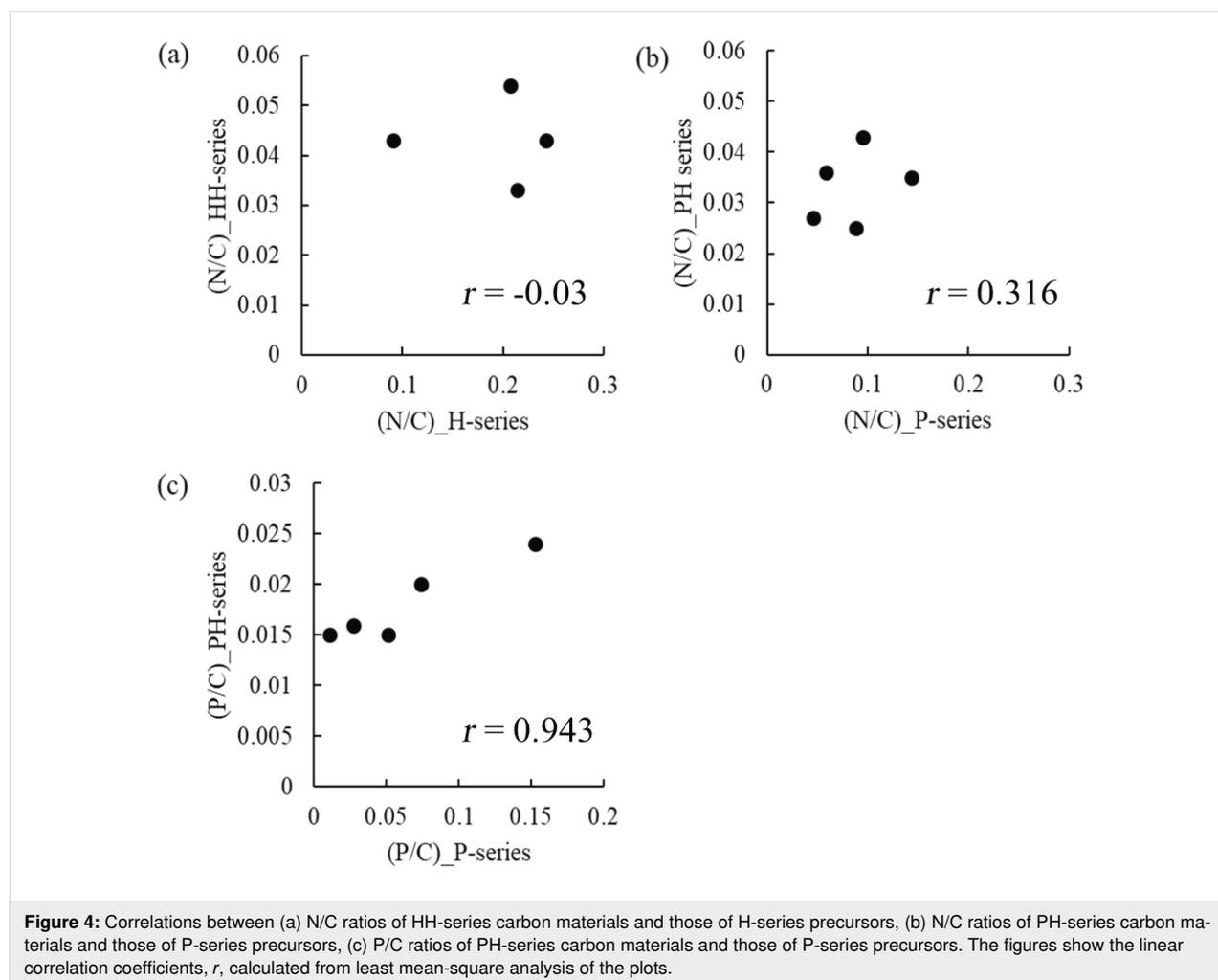

Figure 4: Correlations between (a) N/C ratios of HH-series carbon materials and those of H-series precursors, (b) N/C ratios of PH-series carbon materials and those of P-series precursors, (c) P/C ratios of PH-series carbon materials and those of P-series precursors. The figures show the linear correlation coefficients, *r*, calculated from least mean-square analysis of the plots.

Figure 5: N 1s spectra of (a) HH- and (b) PH-series carbon materials. (c) P 2p spectra of PH-series carbon materials.
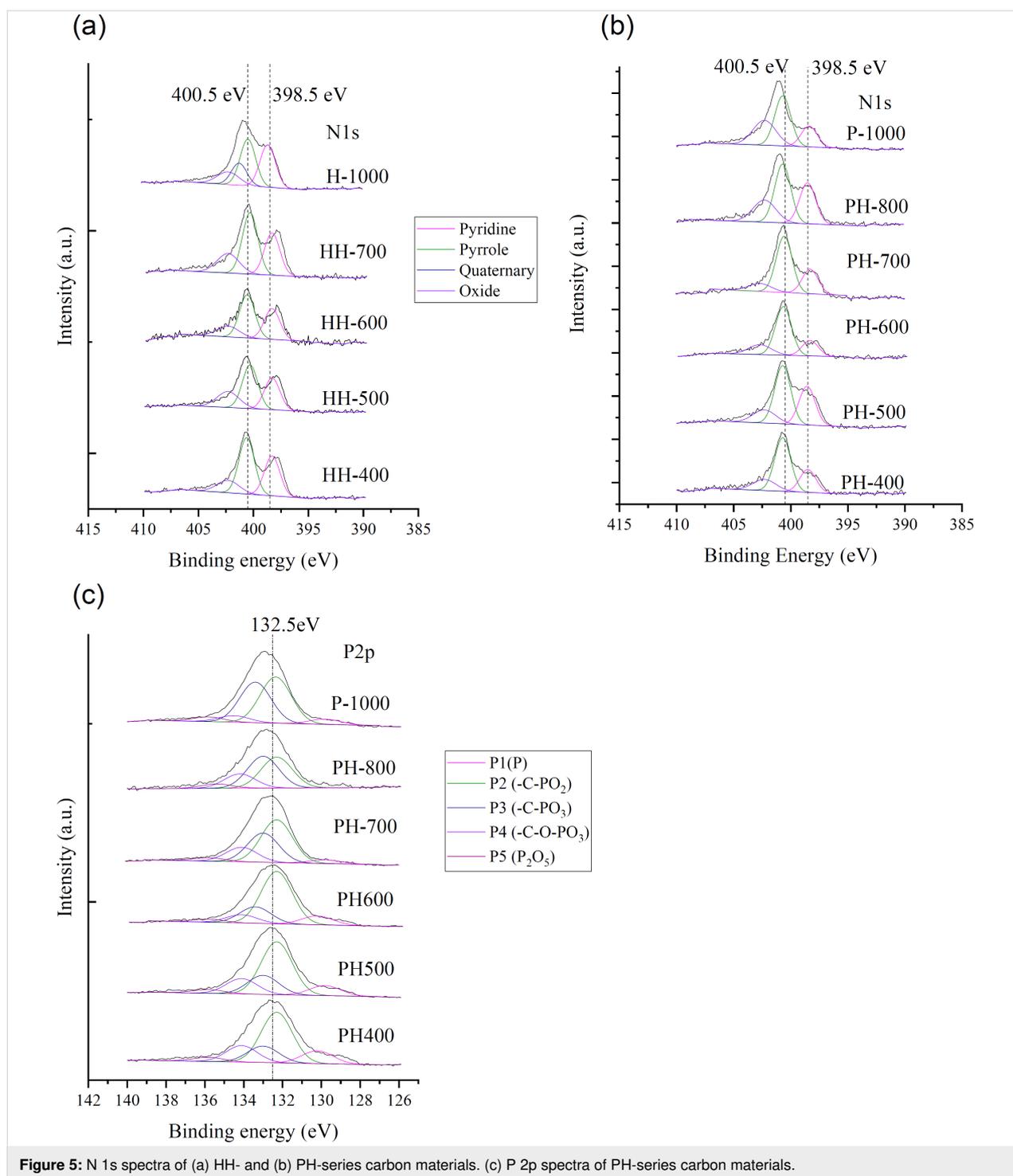
ated in the range of 5.4–5.6 eV (Figure 6a), decreasing with increasing CPAT temperature in the range of 400–700 °C and increasing with increasing CPAT temperature above 700 °C. As a result, the smallest work function was observed for PH-700. Figure 6b shows the relationship between the ORR activity and the work function. These two values exhibited a good correlation with *r* = −0.853.

ORR activity of the carbon materials

Figure 7a shows representative ORR voltammograms of PH- and HH-series carbon materials recorded in O₂-saturated aqueous H_2SO_4. The voltammograms of HH-500 and HH-700 were almost identical, i.e., pretreatment had no effect on ORR activity, while the voltammogram of H-1000 was different, showing a larger increase of ORR current density below 0.4 V

**Table 4:** Distribution of N-species in HH- and PH-series carbon materials.

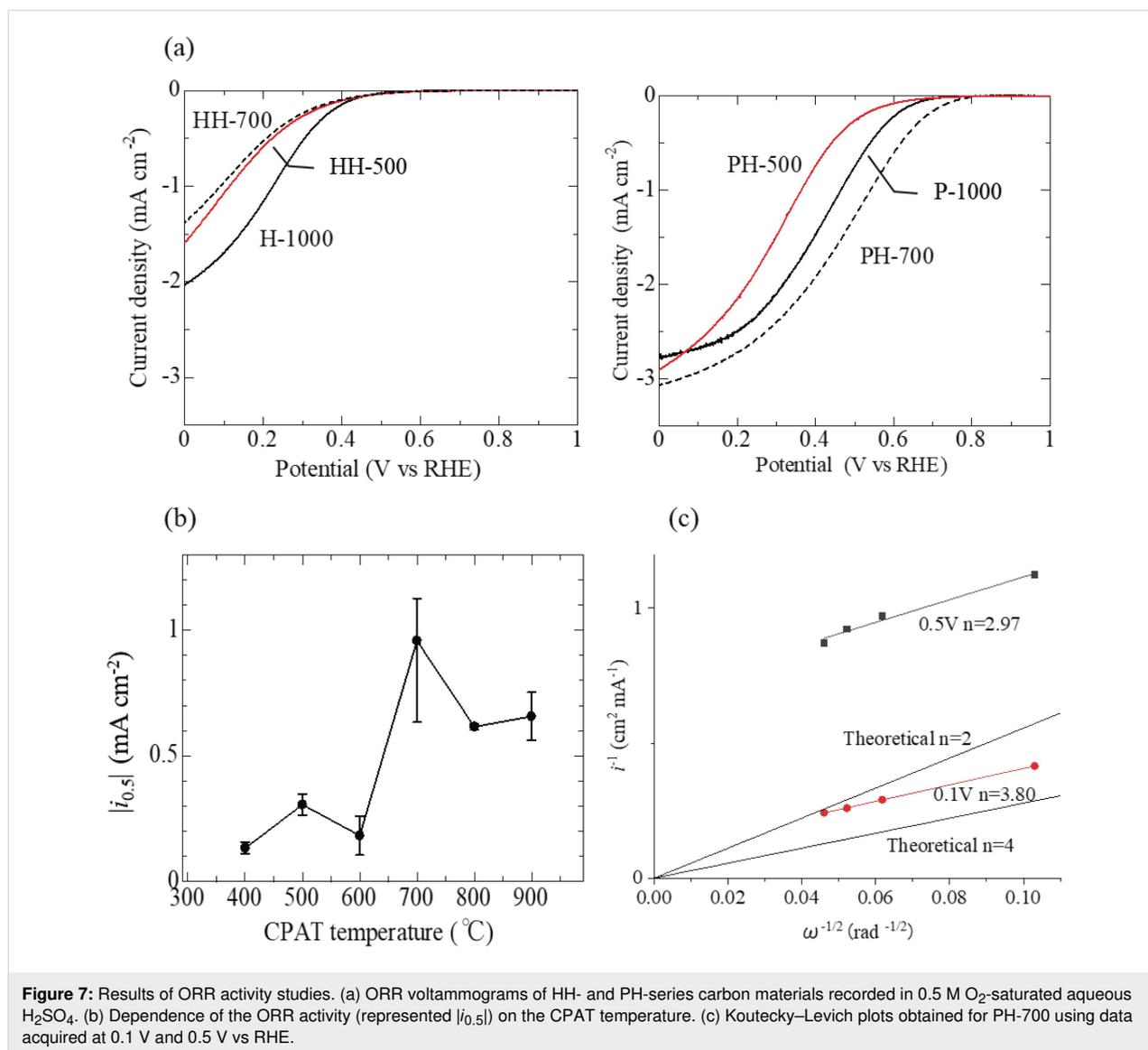| sample	N/C	$N_{pyridine}$	N_{pyrrol}	$N_{quaternary}$	N_{oxide}
HH-400	0.054	0.37	0.63	0.00	0.01
HH-500	0.043	0.32	0.44	0.00	0.23
HH-600	0.033	0.34	0.48	0.00	0.17
HH-700	0.043	0.32	0.47	0.00	0.21
H-1000	0.055	0.33	0.36	0.17	0.14
PH-400	0.027	0.23	0.60	0.00	0.17
PH-500	0.036	0.31	0.52	0.00	0.17
PH-600	0.025	0.20	0.62	0.00	0.18
PH-700	0.035	0.24	0.61	0.00	0.15
PH-800	0.043	0.31	0.45	0.00	0.24
PH-900	0.036	0.19	0.44	0.00	0.37
P-1000	0.043	0.20	0.47	0.00	0.33

vs RHE. At a given potential, higher current densities were observed for PH-series carbon materials than for HH-series carbon materials, which was ascribed to the influence of CPAT. Figure 7b shows the dependence of ORR activity ($|i_{0.5}|$, defined as the current corresponding to a potential of 0.5 V) on the CPAT temperature. The $|i_{0.5}|$ values of HH-series carbon materials ranged from 0.02 to 0.03 mA·cm^{-2} regardless of the pretreatment temperature, while the $|i_{0.5}|$ value of PH-series carbon materials reached 0.96 mA·cm^{-2} at 700 °C and then decreased, i.e., was maximal for PH-700. Figure 7c shows Koutecky–Levich plots obtained for PH-700, revealing that at 0.5 V vs RHE, the number of electrons transferred during the ORR approximately equaled three and approached a value of four at 0.1 V vs RHE.

Notably, PN-doped (PH-series) carbon materials exhibited higher ORR activity than N-doped (HH-series) carbon materials. As N-free P-doped carbon materials could not be prepared

Table 5: Distribution of P-species in PH-series carbon materials.

| sample	P/C	P1 (P) (130 eV)	P2 (–C–PO$_2$) (132.5 eV)	P3 (–C–PO$_3$) (133.2 eV)	P4 (–C–O–PO$_3$) (134.2 eV)	P5 (P$_2$O$_5$) (135.6 eV)
PH-400	0.015	0.13	0.50	0.16	0.16	0.04
PH-500	0.016	0.10	0.52	0.19	0.15	0.04
PH-600	0.015	0.10	0.59	0.18	0.09	0.04
PH-700	0.024	0.04	0.46	0.31	0.16	0.04
PH-800	0.020	0.04	0.47	0.32	0.08	0.08
PH-900	0.017	0.03	0.41	0.32	0.16	0.08
P-1000	0.022	0.05	0.45	0.39	0.06	0.04
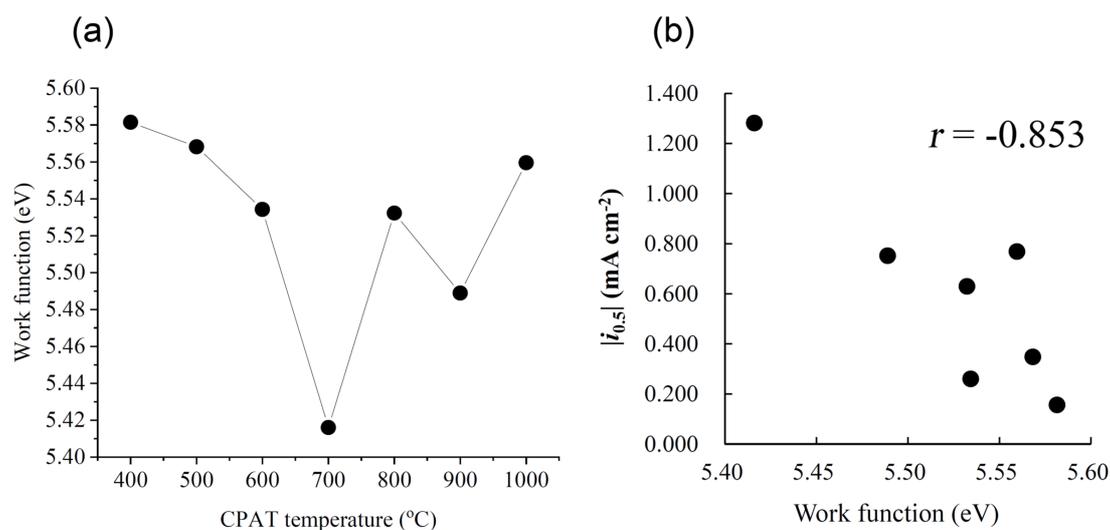
Figure 6: (a) Effect of CPAT temperature on the work function of PH-series carbon materials, (b) relationship between the ORR activity and the work function of carbonized samples.

Figure 7: Results of ORR activity studies. (a) ORR voltammograms of HH- and PH-series carbon materials recorded in 0.5 M O_2-saturated aqueous H_2SO_4. (b) Dependence of the ORR activity (represented $|i_{0.5}|$) on the CPAT temperature. (c) Koutecky–Levich plots obtained for PH-700 using data acquired at 0.1 V and 0.5 V vs RHE.

from FA, a P-doped carbon material was prepared from poly(furyl alcohol) (PFA) to examine the effects of P-only doping on the ORR activity. The ORR activity of P-doped PFA-derived carbon material was higher than that of a non-doped PFA-derived carbon material (Figure 8).

Next, we correlated the ORR activity with BET-SSA, XPS-determined contents of N and P, and the work function. Notably, ORR activity is not fully correlated with BET-SSA (Figure S6, Supporting Information File 1) but was correlated with the relative contents of P2 (Figure 9a) and P3 (Figure 9b) species, with an even better correlation obtained between ORR activity and the sum of P2 and P3 contents (Figure 9c).

Finally, the result of a single-cell test using PH-700, the catalyst with the maximum ORR activity, as the cathode catalyst
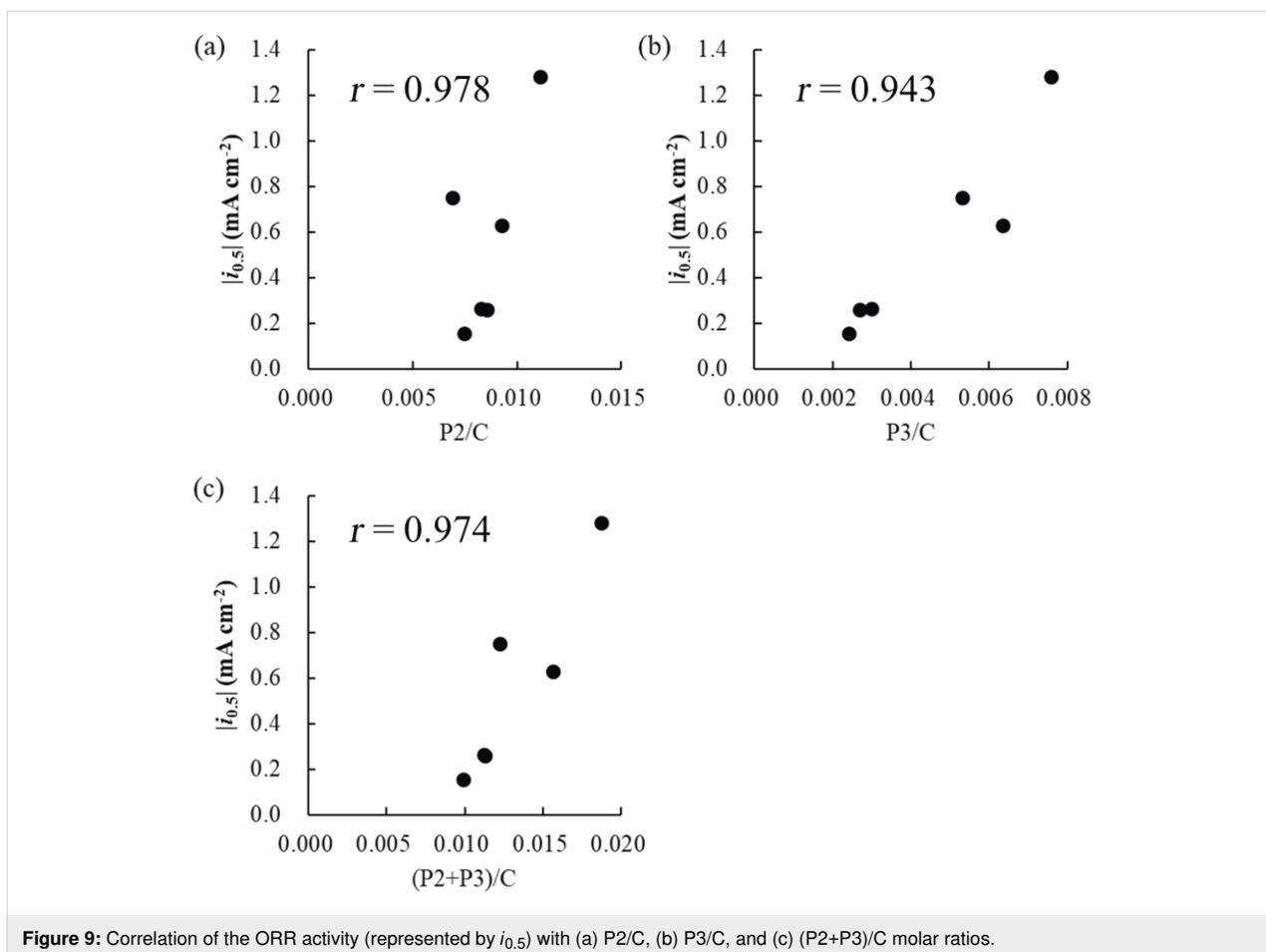

Figure 8: ORR voltammograms of two different PFA-derived carbon materials.
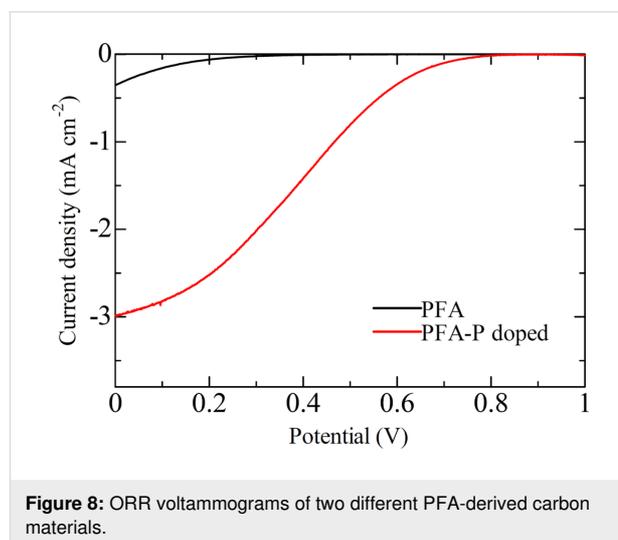
Figure 9: Correlation of the ORR activity (represented by $i_{0.5}$) with (a) P2/C, (b) P3/C, and (c) (P2+P3)/C molar ratios.

and a commercial Pt/C catalyst as the anode catalyst is presented in Figure 10. The initial voltage was 0.86 V and the cell voltage decreased the current density. The red curve indicated the power density of the cell, which showed a maximum value of 141 mW/cm^2.
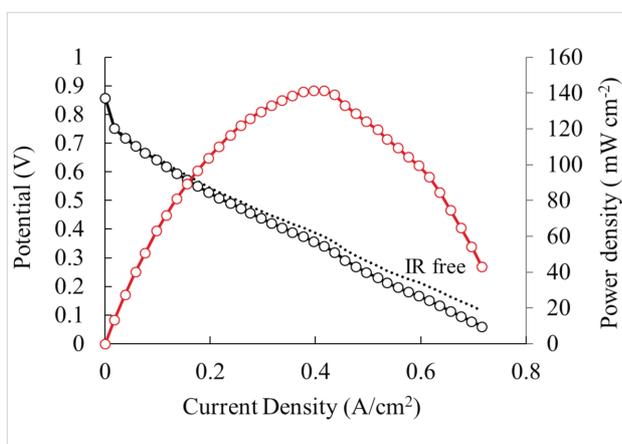

Figure 10: The result of a single-cell test using PH-700 as the cathode catalyst. Current density (black solid line), IR free current density (black dotted line), red solid line (power density).

Discussion
Doping of P into FA by CPAT

Differences between the N chemical states of P- and H-series precursors can be understood by considering the chemical interactions (possibly of the acid–base type) of PA with N atoms in FA, as evidenced by the correlation between P/C and N/C ratios (Figure 2). The N 1s spectra of P-series precursors prepared at temperatures above 400 °C had a shape different from that of the corresponding H-series precursor spectra, and 400 °C was thus taken as the onset of PA action. Interestingly, the nature of this action depended on the CPAT temperature, i.e., N loss was promoted at 400 °C, precursor co-doping with N and P atoms was promoted at 400–700 °C, and the increase of BET-SSA accompanied by the decrease of N and P content was promoted above 800 °C. As a result, maximum N and P contents were obtained at a CPAT temperature of 700 °C. This behavior agreed with the results of a previous study, where the increase of BET-SSA was shown to be accompanied by the sublimation of elemental P above 800 °C [34]. As the initial aim of CPAT was to introduce P into carbon materials rather than to increase their BET-SSAs, the temperature of 700 °C was considered to be optimal. Finally, it was concluded that PN-doped carbon pre-

cursors can be obtained by applying CPAT to other N-containing organic compounds if a proper CPAT temperature is selected.

Chemical aspects of PN-doped carbon materials

The disappearance of the correlation between P/C and N/C ratios (Figure 2) after carbonization indicated that the latter process irreversibly destroyed interactions between N and P atoms. Additionally, the P/C ratios of PH-series carbon materials were correlated with those of P-series precursors, whereas no such correlation was observed for N/C ratios, which highlighted the need for an in-depth investigation of the chemistry involved at different preparation stages.

PN-doped (PH-series) carbon materials had a lower content of pyridinic N than HH-series carbon materials (Figure 5a,b), i.e., P-doping suppressed the formation of this type of N moieties. This behavior contradicted the results of previous studies on PN-doped carbon materials, which reported the facile formation of pyridinic N upon P-doping. For example, Gao et al. prepared a PN-doped carbon material by carbonization of an ionic liquid synthesized from *N*-methylimidazole and PA and reported the selective formation of pyridinic N due to the introduction of P [36]. Li et al. reported that a carbon material obtained by carbonization of P-doped aniline-coated single-wall carbon nanotubes was rich in pyridinic N [26], while Razmjooei et al. described the influence of P-doping on the formation of pyridinic and pyrrole-type N in N, S, P-doped carbon materials [24].

The 400.5 eV peak observed in the N 1s spectra of the PH-series carbon materials has traditionally been assigned to pyrrole/pyridone-type N. The electron configuration of pyridinic N can be described as follows: Two out of five N valence electrons are used for σ-bond formation, two more electrons form an unshared electron pair, and the remaining electron is donated to the π-electron system. Conversely, in the case of pyrrolic N, two valence electrons are used to form C–N–C σ-bonds, one electron is used to form the N–H bond, and the remaining two electrons are donated to the π-electron system. These differences in the number of electrons supplied to the π-electron system result in differences in the N 1s peak binding energies. Strelko et al. conducted quantum chemical calculations to characterize N-doped graphene, revealing that the electronic states of hydrogenated pyridinic N and the three-coordinated N located in the valley at the zigzag edge of graphene are similar to that of pyrrolic N [21].

Detailed analysis of N 1s and P 2p spectra showed that the presence of N–P bonds in carbonized products can be excluded and

demonstrated that P was mainly present as –C–PO$_2$. However, it was difficult to prove the presence of P–N and P=N bonds by analysis of N 1s spectra, as the similar binding energy values of N–P moieties (398.5 eV) and pyridinic N, and of N=P moieties (401.3 eV) and quaternary N made unambiguous assignments impossible [37,38]. Thus, as the N 1s spectra of PH-series carbon materials indicated the absence of N–P and N=P bonds, we concluded that these carbon materials did not contain the above moieties. Regarding P 2p spectra, the main species were identified as P2 (132.5 eV; –C–PO$_2$) and P3 (133.2 eV; –C–PO$_3$). As the P–N signal usually appears at 133.5 eV and overlaps with that of P3, PH-series carbon materials were concluded to contain P2 and P3 as major species and feature no N–P moieties.

Factors determining ORR activity

As electrocatalytic ORR is a heterogeneous reaction occurring on solid surfaces, the overall catalytic activity is governed by the surface area involved in the reaction and the type and surface density of active sites. Herein, the ORR activity of PH-series carbon materials was found to be only weakly influenced by the BET-SSA values (Figure S6, Supporting Information File 1) but was rather determined by the abundances of P2 and P3 species, i.e., by the contents of P atoms directly bonded to one or two carbon atoms as shown in Figure 9.

Previously, the enhanced ORR activity of PN-doped carbon materials was ascribed to an increase of asymmetric spin density [24,25,39], electron transfer from N or P to C [36], changes of oxygen adsorption ability [26,40], and the formation of pyridinic N active sites due to P-doping [26]. In our case, the last reason, namely the formation of pyridinic N, can be ruled out, while further studies are required to confirm/disprove the influence of oxygen adsorption properties. At this point, it is worth noting that our previous investigations of the relationship between the ORR activity and oxygen adsorption properties of warped graphitic layers (obtained by oxidative heat treatment of fullerene extraction residues) demonstrated that these two parameters are well correlated [41].

The ORR activity was well correlated with the work function (Figure 6b), which represents the energy of the Fermi level with respect to that of the vacuum level that would be brought by the introduction of P2 and P3 species, showing good correlation as discussed above. Several reports on the relationship between the work function of cathode catalysts and their ORR activity demonstrated that the former parameter strongly influences the latter and affects electron transfer in elementary reaction steps. As the Fermi level is the highest-energy electronic level of a given solid, the ORR reaction proceeds spontaneously when this level exceeds the ORR standard potential of 5.6 eV [42-44].

As shown in Figure 6a, PH-series carbon materials had work functions of less than 5.6 eV and could therefore spontaneously promote the ORR. The two structural features of PN-doped carbon materials, i.e., the presences of particular P-containing species and the warped graphitic layers, should be the important factors determining ORR activity through facilitating O_2 adsorption and/or electron transfer at the catalyst surface.

Conclusion

Herein, we applied controlled phosphoric acid treatment (CPAT) of folic acid (FA) to prepare P-doped precursors, which were then carbonized to afford PN-doped carbon materials as oxygen reduction reaction (ORR) catalysts. Essentially, FA was heated in the presence of phosphoric acid at an optimal temperature of 700 °C to maximize the P content of precursors before the occurrence of chemical activation. The P/C ratio of precursors was found to be positively correlated with that of the corresponding carbon materials and carbon ORR activity. In contrast to previous studies, where ORR activity has been largely attributed to the presence of active sites based on pyridinic N, the enhanced ORR activity of our carbon materials was ascribed to the presence of $-C-PO_2$ and $C-PO_3$ moieties. Moreover, this activity increased with decreasing work function of the carbon materials. Given that an optimal treatment temperature is selected, we believe that the CPAT technique can be applied to all types of N-containing compounds, e.g., naturally occurring ones. However, fundamental studies on the kinetics and mechanisms of ORR activity enhancement induced by PN-doping are required to clarify the remaining questions and will be conducted in due course.

Experimental
CPAT

N- and P-containing precursors were prepared by heating FA in the presence of PA. Typically, FA (1 g; Wako, Wako Special Grade) was ground with ethanolic PA (85 wt %, 1 g; Wako, Wako Special Grade) using a mortar and pestle, and the obtained mixture was placed in a furnace, heated to 400–800 °C in a flow of N_2 at a rate of 50 °C·min^{-1}, and then held at this temperature for 1 h. The carbonized samples were then pulverized at 650 rpm for 50 min using a planetary ball mill (P-7, Fritsch), sieved to retrieve particles smaller than 106 μm in diameter, vigorously stirred in deionized water at 80 °C for 1 h, and dried to obtain P-T specimens (T = CPAT temperature). Controls were prepared in the same manner without the addition of PA and were referred to as H-T (T = pretreatment temperature).

Carbonization

The doped and control precursors were carbonized at 1000 °C for 1 h in a stream of N_2 to afford PH-T and HH-T specimens, respectively (T = treatment temperature). Moreover, carbon ma-

terials were also prepared by directly heating FA or PA-FA mixtures to 1000 °C (H-1000 and P-1000 samples, respectively). To study the influence of P-only doping, the above carbonization procedure was applied to poly(furfuryl alcohol) (PFA). Two types of PFA-based carbon materials were prepared by using hydrochloric acid or phosphoric acid as polymerization initiators (non-doped and P-doped PFA carbon materials, respectively).

Electrochemical methods

The ORR activity of carbon materials was probed by rotating disk electrode voltammetry. The working electrode was prepared by loading the catalyst (200 μg·cm^{-2}) on a glassy carbon disk electrode. The carbon ink was prepared in the following manner: 2.5 mg of the prepared sample was mixed with 25 μL of Nafion solution (5% solution of lower aliphatic alcohols, Aldrich), 75 μL of ethanol (99.5%, Wako Pure Chemicals, Co. Ltd.) and 75 μL of ultrapure water in a plastic conical vial (1.5 mL). The working electrode was a 4 mm diameter glass-like carbon electrode (BAS Inc.). The carbon ink (1.78 μL) was pasted onto the whole area of the glass-like carbon electrode (catalyst loading is 200 μg·cm^{-2}). A reversible hydrogen electrode (RHE) and a glassy carbon plate were employed as reference and counter electrodes, respectively. The electrolyte was a 0.5 M solution of H_2SO_4 in deionized water. Prior to the measurements, dissolved oxygen in the acid solution was purged by bubbling nitrogen gas. Cyclic voltammetry measurements were performed by sweeping the potential between 0.0 V and 1.0 V vs RHE at 50 mV/s for five cycles with a potentiostat (ALS 2323, BAS Inc.). Net ORR voltammograms were obtained as the difference between linear sweep voltammograms recorded at 1500 rpm in O_2-saturated and N_2-saturated electrolytes (RRDE-3A, BAS Inc.). Koutecky–Levich analysis was conducted for a selected sample by taking $D_{O2} = 1.40 \times 10^{-5}$ cm^2·s^{-1} and $v = 1.00 \times 10^{-2}$ cm^2·s^{-1} [45]. The oxygen concentration was determined using an optical oxygen meter (FireStingO$_2$, Pyro Science GmbH) as $C_{O2} = 1.20 \times 10^{-6}$ mol·cm^{-3}. Prior to the tests of the prepared samples, we evaluated Pt/C (IFPC40, ISHIFUKU Metal Industry Co., Ltd.), and the onset potential of Pt/C was 0.96 V.

The membrane–electrode assembly was fabricated as follows: The catalyst ink, i.e., the dispersion of the catalyst in Nafion solution ((5 wt % solution of lower aliphatic alcohols, Aldrich), ionomer/catalyst weight ratio ≈ 0.7:1) was sprayed onto a diffusion layer (29BC, SGL CARBON GmbH). A Pt/C catalyst was used as the anode (catalyst loading = 0.3 mg·cm^{-2}), and PH-700 was used as the cathode (catalyst loading = 3.5 mg·cm^{-2}). A 5 cm^2 cell was used for fuel-cell testing. Polarization curves were obtained at a cell temperature of 80 °C, a back pressure of 200 kPa, and a reactant gas relative humidity of 100% using H_2

(1 L·min^{-1}) and O$_2$ (1 L·min^{-1}) as anode and cathode gases, respectively.

Characterization techniques

The Brunauer–Emmett–Teller (BET) surface area was evaluated by N$_2$ adsorption measurements (BELSORP Max, Microtrac BEL). Samples were placed in a tube and degassed at 200 °C for 2 h under dynamic vacuum conditions. C 1s, N 1s, O 1s, and P 2p core-level X-ray photoelectron spectra were recorded using Mg Kα radiation (Kratos AXIS-NOVA, Shimadzu Corp.). Generally, the charge-up shift correction was performed by setting the C 1s peak binding energy to 284.5 eV. Charge-up corrections for PA-400, 500, and 600 were performed by bringing these samples into contact with In foil and setting the In 3d peak binding energy to 451.4 eV. Work functions were measured under N$_2$ by a vibration capacity electrometer (DCU series10, KP Technology).

Supporting Information

Supporting Information File 1

Additional experimental data.
[https://www.beilstein-journals.org/bjnano/content/supplementary/2190-4286-10-148-S1.pdf]

ORCID® iDs

Jun-ichi Ozaki - https://orcid.org/0000-0002-1369-9004

Preprint

A non-peer-reviewed version of this article has been previously published as a preprint doi:10.3762/bxiv.2019.2.v1

References

1. Banham, D.; Choi, J.-Y.; Kishimoto, T.; Ye, S. *Adv. Mater. (Weinheim, Ger.)* **2019,** 1804846. doi:10.1002/adma.201804846
2. Toda, T.; Igarashi, H.; Watanabe, M. *J. Electroanal. Chem.* **1999,** *460,* 258–262. doi:10.1016/s0022-0728(98)00361-1
3. Zhang, J.; Lima, F. H. B.; Shao, M. H.; Sasaki, K.; Wang, J. X.; Hanson, J.; Adzic, R. R. *J. Phys. Chem. B* **2005,** *109,* 22701–22704. doi:10.1021/jp055634c
4. Jasinski, R. *Nature* **1964,** *201,* 1212–1213. doi:10.1038/2011212a0
5. Jahnke, H.; Schönborn, M.; Zimmermann, G. Organic dyestuffs as catalysts for fuel cells. *Physical and Chemical Applications of Dyestuffs;* Topics in Current Chemistry; Springer-Verlag: Berlin, Germany, 1976; pp 133–181. doi:10.1007/bfb0046059
6. Lefèvre, M.; Dodelet, J. P.; Bertrand, P. *J. Phys. Chem. B* **2002,** *106,* 8705–8713. doi:10.1021/jp020267f
7. Lefèvre, M.; Proietti, E.; Jaouen, F.; Dodelet, J.-P. *Science* **2009,** *324,* 71–74. doi:10.1126/science.1170051
8. Ozaki, J.-i.; Imashiro, Y. *Electrochemistry* **2015,** *83,* 319–325. doi:10.5796/electrochemistry.83.319
9. Ozaki, J.-i.; Nozawa, K.; Yamada, K.; Uchiyama, Y.; Yoshimoto, Y.; Furuichi, A.; Yokoyama, T.; Oya, A.; Brown, L. J.; Cashion, J. D. *J. Appl. Electrochem.* **2006,** *36,* 239–247. doi:10.1007/s10800-005-9054-2
10. Ozaki, J.-i.; Tanifuji, S.-i.; Furuichi, A.; Yabutsuka, K. *Electrochim. Acta* **2010,** *55,* 1864–1871. doi:10.1016/j.electacta.2009.10.037
11. Ozaki, J.-i.; Anahara, T.; Kimura, N.; Ida, C.; Oya, A.; Bokhonov, B. B.; Korchagin, M. A.; Sakashita, M. *Tanso* **2007,** 153–157. doi:10.7209/tanso.2007.153
12. Banham, D.; Kishimoto, T.; Sato, T.; Kobayashi, Y.; Narizuka, K.; Ozaki, J.-i.; Zhou, Y.; Marquez, E.; Bai, K.; Ye, S. *J. Power Sources* **2017,** *344,* 39–45. doi:10.1016/j.jpowsour.2017.01.086
13. Banham, D.; Kishimoto, T.; Zhou, Y.; Sato, T.; Bai, K.; Ozaki, J.-i.; Imashiro, Y.; Ye, S. *Sci. Adv.* **2018,** *4,* eaar7180. doi:10.1126/sciadv.aar7180
14. Ballard to Offer World's First PEM Fuel Cell Product Using Non Precious Metal Catalyst. http://ballard.com/about-ballard/newsroom/news-releases/2017/09/13/ballard-to-offer-world-s-first-pem-fuel-cell-product-using-non-precious-metal-catalyst (accessed March 28, 2019). doi:10.1016/s1464-2859(17)30338-3
15. Nisshinbo Holdings Inc.. R&D Activities | Research and Development. https://www.nisshinbo.co.jp/english/r_d/activity.html (accessed March 28, 2019).
16. Maldonado, S.; Stevenson, K. J. *J. Phys. Chem. B* **2005,** *109,* 4707–4716. doi:10.1021/jp044442z
17. Shui, J.; Wang, M.; Du, F.; Dai, L. *Sci. Adv.* **2015,** *1,* e1400129. doi:10.1126/sciadv.1400129
18. Ozaki, J.-i.; Kimura, N.; Anahara, T.; Oya, A. *Carbon* **2007,** *45,* 1847–1853. doi:10.1016/j.carbon.2007.04.031
19. Zhang, J.; Dai, L. *Angew. Chem., Int. Ed.* **2016,** *55,* 13296–13300. doi:10.1002/anie.201607405
20. Choi, C. H.; Chung, M. W.; Park, S. H.; Woo, S. I. *Phys. Chem. Chem. Phys.* **2013,** *15,* 1802–1805. doi:10.1039/c2cp44147k
21. Strelko, V. V.; Kuts, V. S.; Thrower, P. A. *Carbon* **2000,** *38,* 1499–1503. doi:10.1016/s0008-6223(00)00121-4
22. Gao, J.; Ma, N.; Tian, J.; Shen, C.; Wang, L.; Yu, P.; Chu, Y.; Liu, W.; Tan, X.; Li, X.; Yin, Z. *J. Solid State Electrochem.* **2018,** *22,* 519–525. doi:10.1007/s10008-017-3785-y
23. Li, R.; Wei, Z.; Gou, X. *ACS Catal.* **2015,** *5,* 4133–4142. doi:10.1021/acscatal.5b00601
24. Razmjooei, F.; Singh, K. P.; Song, M. Y.; Yu, J.-S. *Carbon* **2014,** *78,* 257–267. doi:10.1016/j.carbon.2014.07.002
25. von Deak, D.; Biddinger, E. J.; Luthman, K. A.; Ozkan, U. S. *Carbon* **2010,** *48,* 3637–3639. doi:10.1016/j.carbon.2010.05.022
26. Li, J.-C.; Hou, P.-X.; Cheng, M.; Liu, C.; Cheng, H.-M.; Shao, M. *Carbon* **2018,** *139,* 156–163. doi:10.1016/j.carbon.2018.06.023
27. Puziy, A. M.; Poddubnaya, O. I.; Ziatdinov, A. M. *Appl. Surf. Sci.* **2006,** *252,* 8036–8038. doi:10.1016/j.apsusc.2005.10.044

28. Rosas, J. M.; Bedia, J.; Rodríguez-Mirasol, J.; Cordero, T. *Fuel* **2009,** *88,* 19–26. doi:10.1016/j.fuel.2008.08.004

29. Wu, J.; Yang, Z.; Li, X.; Sun, Q.; Jin, C.; Strasser, P.; Yang, R. *J. Mater. Chem. A* **2013,** *1,* 9889–9896. doi:10.1039/c3ta11849e

30. Borghei, M.; Laocharoen, N.; Kibena-Põldsepp, E.; Johansson, L.-S.; Campbell, J.; Kauppinen, E.; Tammeveski, K.; Rojas, O. J. *Appl. Catal., B* **2017,** *204,* 394–402. doi:10.1016/j.apcatb.2016.11.029

31. Zhao, S.; Liu, J.; Li, C.; Ji, W.; Yang, M.; Huang, H.; Liu, Y.; Kang, Z. *ACS Appl. Mater. Interfaces* **2014,** *6,* 22297–22304. doi:10.1021/am506284k

32. Zuo, S.; Yang, J.; Liu, J.; Cai, X. *Fuel Process. Technol.* **2009,** *90,* 994–1001. doi:10.1016/j.fuproc.2009.04.003

33. Fierro, V.; Torné-Fernández, V.; Montané, D.; Celzard, A. *Thermochim. Acta* **2005,** *433,* 142–148. doi:10.1016/j.tca.2005.02.026

34. Myglovets, M.; Poddubnaya, O. I.; Sevastyanova, O.; Lindström, M. E.; Gawdzik, B.; Sobiesiak, M.; Tsyba, M. M.; Sapsay, V. I.; Klymchuk, D. O.; Puziy, A. M. *Carbon* **2014,** *80,* 771–783. doi:10.1016/j.carbon.2014.09.032

35. Puziy, A. M.; Poddubnaya, O. I.; Socha, R. P.; Gurgul, J.; Wisniewski, M. *Carbon* **2008,** *46,* 2113–2123. doi:10.1016/j.carbon.2008.09.010

36. Gao, J.; Ma, N.; Tian, J.; Shen, C.; Wang, L.; Yu, P.; Chu, Y.; Liu, W.; Tan, X.; Li, X.; Yin, Z. *J. Solid State Electrochem.* **2018,** *22,* 519–525. doi:10.1007/s10008-017-3785-y

37. Perry, W. B.; Schaaf, T. F.; Jolly, W. L. *J. Am. Chem. Soc.* **1975,** *97,* 4899–4905. doi:10.1021/ja00850a019

38. Hulicova-Jurcakova, D.; Seredych, M.; Lu, G. Q.; Kodiweera, N. K. A. C.; Stallworth, P. E.; Greenbaum, S.; Bandosz, T. J. *Carbon* **2009,** *47,* 1576–1584. doi:10.1016/j.carbon.2009.02.006

39. Choi, C. H.; Park, S. H.; Woo, S. I. *ACS Nano* **2012,** *6,* 7084–7091. doi:10.1021/nn3021234

40. Yu, D.; Xue, Y.; Dai, L. *J. Phys. Chem. Lett.* **2012,** *3,* 2863–2870. doi:10.1021/jz3011833

41. Takigami, M.; Kobayashi, R.; Ishii, T.; Imashiro, Y.; Ozaki, J. *Beilstein J. Nanotechnol.* **2019,** *10,* 1391–1400. doi:10.3762/bjnano.10.137

42. Liu, M.; Liu, J.; Li, Z.; Wang, F. *ACS Appl. Mater. Interfaces* **2018,** *10,* 7052–7060. doi:10.1021/acsami.7b16549

43. Landoldt, D. *Corrosion and surface chemistry of metals;* EPFL Press, 2007; pp 57–58.

44. Winget, P.; Cramer, C. J.; Truhlar, D. G. *Theor. Chem. Acc.* **2004,** *112,* 217–227. doi:10.1007/s00214-004-0577-0

45. Wang, X.; Zhou, J.; Fu, H.; Li, W.; Fan, X.; Xin, G.; Zheng, J.; Li, X. *J. Mater. Chem. A* **2014,** *2,* 14064–14070. doi:10.1039/c4ta01506a

Upcycling of polyurethane waste by mechanochemistry: synthesis of N-doped porous carbon materials for supercapacitor applications

Christina Schneidermann[‡1], Pascal Otto[‡1], Desirée Leistenschneider[2], Sven Grätz[3], Claudia Eßbach[1] and Lars Borchardt[*1,3]

Full Research Paper

Address:
[1]Technische Universität Dresden, Department of Inorganic Chemistry, Bergstraße 66, 01069 Dresden, Germany, [2]University of Alberta, Department of Chemical and Materials Engineering, 12-340 Donadeo Innovation Centre for Engineering, 9211 - 116 Street, AB T6G 1H9 Edmonton, Canada and [3]Ruhr-Universität Bochum, Department of Inorganic Chemistry, Universitätsstrasse 150, 44801 Bochum, Germany

Email:
Desirée Leistenschneider - leistens@ualberta.ca; Lars Borchardt[*] - lars.borchardt@rub.de

* Corresponding author   ‡ Equal contributors

Keywords:
mechanochemistry; polyurethane; porous carbon; supercapacitor; waste

Abstract

We developed an upcycling process of polyurethane obtaining porous nitrogen-doped carbon materials that were applied in supercapacitor electrodes. In detail, a mechanochemical solvent-free one-pot synthesis is used and combined with a thermal treatment. Polyurethane is an ideal precursor already containing nitrogen in its backbone, yielding nitrogen-doped porous carbon materials with N content values of 1–8 wt %, high specific surface area values of up to 2150 $m^2 \cdot g^{-1}$ (at a N content of 1.6 wt %) and large pore volume values of up to 0.9 $cm^3 \cdot g^{-1}$. The materials were tested as electrodes for supercapacitors in aqueous 1 M Li_2SO_4 electrolyte (100 $F \cdot g^{-1}$), organic 1 M TEA-BF$_4$ (ACN, 83 $F \cdot g^{-1}$) and EMIM-BF$_4$ (70 $F \cdot g^{-1}$).

Introduction

Currently more than 275 million tons of plastics end up as waste every year, 12.7 million tons of which accumulate in the oceans [1,2]. This waste is mainly packaging materials such as polyethylene (PE), polypropylene (PP), polyurethane (PU), disposable bottles such as polyethylene terephthalate (PET) and

construction materials such as polyvinyl chloride (PVC) and PU. At the same time, more than 300 million tons of new plastic materials are produced every year, with an increasing tendency [3-5]. So far, different recycling techniques have been devised to counteract environmental pollution through accumu-

lation of plastic waste. Especially, the recovery of PE and PP, as well as depolymerization processes for PET and the reprocessing of PVC by crushing and melting in conversion systems are well developed [6-9]. Commonly, 10–30% of the plastic waste is recycled by manufacturing new plastic products. Another 10–25% is used for energy recovery as fuel for industrial processes. However, 55–80% still end up in landfills or even in the environment [3,4,10]. Some of the polymers that accumulate as plastic waste are poorly recyclable because of low recycling yields and insufficient properties of the recycled polymers in terms of elasticity, rheology, and thermal and mechanical stability [5]. Amongst them is PU, a thermosetting polymer with a cross-linked structure [5,11,12]. PU is mainly used for the production of disposable packaging materials and sponges, for long-term applications in upholstered furniture and car seats, and as spray foam for insulation [13-15]. Approximately 19 million tons of PU waste accumulate annually [13,15-18]. Therefore, it is essential to develop sustainable upcycling methods that reduce environmental pollution on the one hand and ensure a good material utilization on the other hand. One approach is the synthesis of porous carbon materials from PU waste. At the industrial scale, activated carbon materials are already obtained from coconut shells and other biomass waste [19-21]. However, the industrial use of plastics for this purpose has not been established yet.

The main properties of porous carbon materials [22,23] such as high specific surface area and high electrical conductivity allow for a variety of applications in catalysis [24-26], gas sorption/separation [27-29] and electrochemical energy storage/conversion. For the latter, porous carbon materials are established as electrode materials in fuel cells [30-33], Li–S cells [34-37], and supercapacitors [38]. In addition, these carbon materials can be functionalized with heteroatoms such as nitrogen, which was reported to affect the electrical conductivity [39-42], the energy storage capacity, and the wettability of the electrodes with electrolyte [43-45]. Commonly, nitrogen is inserted into the carbon framework either by solution-based impregnation with nitrogen-containing precursors, e.g., melamine or urea [19,46], or via post-treatment processes with gaseous, nitrogen-containing precursors, e.g., N_2 or NH_3, at high temperatures [31,47,48]. In PU nitrogen is already part of the urethane group rendering it a suitable nitrogenous carbon precursor. The conventional production of N-doped porous carbon materials from PU, however, requires many process steps and produces large quantities of solvent waste from crushing and dissolving steps, the addition of toxic chemicals, as well as the subsequent drying and carbonization [49]. The utilization of a solvent in general has to be critically examined, since it has to be separated from the product, which is time-consuming and costly, and later on accumulates as waste that has to be reprocessed in an energy-intensive procedure. Furthermore, solvents can be hazardous to the environment or toxic to humans. PU, for example, is hardly soluble and some PU materials only dissolve in organic solvents such as DMF, DMSO or THF. Consequently, it is necessary to implement sustainable and effective processes that use renewable raw materials or plastic waste and can be conducted in a solvent-free manner [50-52]. Mechanochemistry is an innovative synthesis concept that can be conducted without solvents. It is cost-efficient and sustainable at the same time [53]. Mechanochemistry is well established in the field of pharmaceutical [54,55], organic [56-58], and inorganic chemistry [59-62]. Mechanochemical reactions are initiated and controlled by mechanical energy, for example provided by the collisions of milling balls in high-energy ball mills. The advantages of mechanochemistry are obvious. Syntheses can be conducted without solvents [63,64], and within short reaction times [59,65]. Also, the potential of mechanochemistry for upscaling
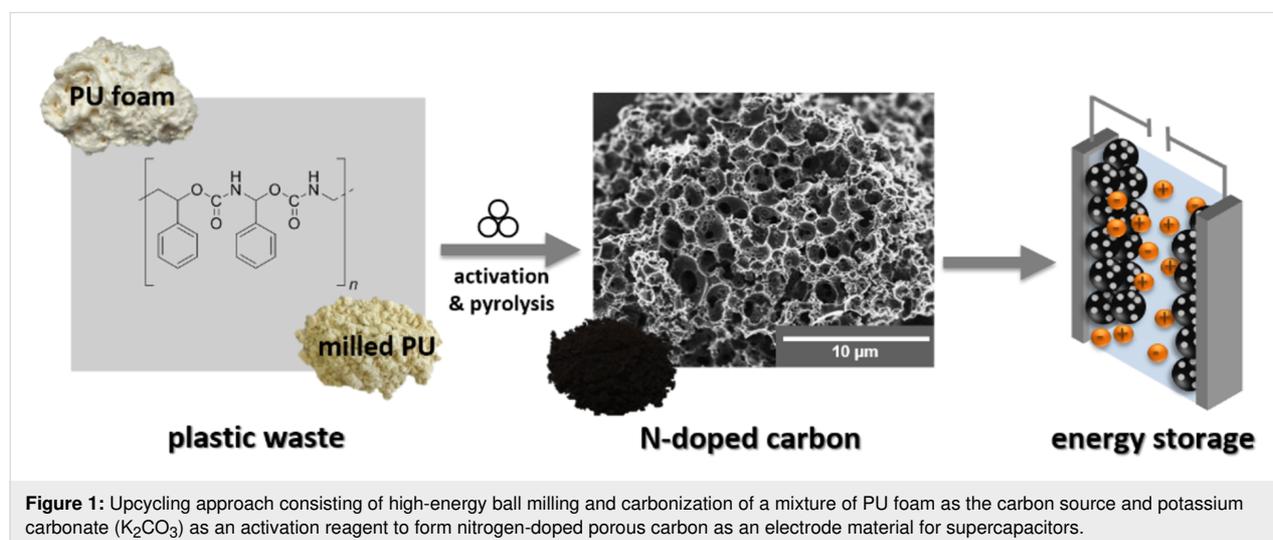

Figure 1: Upcycling approach consisting of high-energy ball milling and carbonization of a mixture of PU foam as the carbon source and potassium carbonate (K_2CO_3) as an activation reagent to form nitrogen-doped porous carbon as an electrode material for supercapacitors.

has recently been discussed by Stolle and co-workers. An upscaling from the milligram scale to the multiple-gram scale has been shown to be feasible [66,67]. For the kilogram scale other milling techniques such as impact mills or extruders may be applicable [68].

Here, we present a fast and scalable synthesis for the production of N-doped carbon materials (Figure 1). PU (spray foam) is used as a nitrogenous carbon source and potassium carbonate (K_2CO_3) is used as an activation agent. Urea (CH_4N_2O) can optionally be added to further increase the nitrogen content. Pre-milling of the PU foam and the mechanochemical reaction of all components are carried out in a planetary ball mill. The received polymer mixture is carbonized to form a nitrogen-doped carbon material with a surface area of up to 2150 $m^2 \cdot g^{-1}$ and a total pore volume of up to 0.9 $cm^3 \cdot g^{-1}$. In order to generate different nitrogen contents and to increase the porosity of the carbon material, we used different ratios of urea and K_2CO_3. Moreover, the N-doped carbon materials have been investigated as electrode material for supercapacitors in aqueous Li_2SO_4, organic TEA-BF_4 in acetonitrile, and an ionic liquid EMIM-BF_4 electrolyte.

Results and Discussion
Characterization and mechanochemical treatment of PU

Polyurethane is a polymer formed by polyaddition of diisocyanates $R^1(-NCO)_2$ with polyols $R^2(-OH)_n$. It is characterized by the resulting urethane group NH-(CO)-O. The special feature of these compounds is the large variety of monomers that can be used for the production of polyurethane materials, such as various aliphatic or aromatic isocyanate components (R^1) and dihydric or polyhydric alcohols as polyol components (R^2). This wide range of monomers allows for different functional groups to be integrated into the PU framework and the adjustment of certain reaction conditions or specific properties, such as ensuring fast reactions and stable polymer chains through aromatic isocyanates. The spray foam used here (PU-F) is a one-component foam and, according to the supplier (Soudal), consists of polyisocyanate with an aromatic residual group (polymethylene–polyphenyl isocyanate). Due to the delocalized charges in the aromatic residue of the monomers, they directly react with moisture and do not require an additional diol, as is the case with two-component foams. The spray of the one-component foam contains small amounts of a flame retardant (tris(2-chloro-1-methylethyl)phosphate) and propellants such as propane, isobutene and dimethyl ether, which cause the foaming. The foam has a low density of 25 $kg \cdot m^{-3}$, which is required for the application, but makes recycling difficult due to its poor processability, and low yields of energy and material. High-energy ball milling is initially used for comminution of

the foam (PU-F) to a powder (PU-BM). This does not lead to any changes in the chemical bonding according to infrared spectra (Figure S1A, Supporting Information File 1).

After addition of K_2CO_3 powder, the mechanochemical treatment also ensures a homogeneous distribution of the latter within the polymer. This ensures an optimal subsequent activation process. First investigations were made to understand the influence of the K_2CO_3 concentration on the activation process by varying the K_2CO_3 content, while keeping the PU content constant (Table 1). The samples are indexed as follows: polyurethane (PU), K_2CO_3 (PC), and "800" standing for the pyrolysis temperature and a sequence number at the end of the sample code. The obtained plastic-derived carbon materials were investigated by N_2 physisorption at −196 °C (Figure 2A), and the calculation of the pore size distributions was carried out under the assumption of slit and cylindrical pore geometry using quenched solid density functional theory (QSDFT; Figure 2B).

The sample PU-BM-800 (i.e., the reference with no K_2CO_3) does not show any porosity and a slightly decreased nitrogen content of 3.9 wt % compared to the pure PU-BM (5.7 wt %, Table 1). In contrast, a microporous material is obtained after adding only a small amount of K_2CO_3 (PUPC-800-1, Figure 2A) [69]. PUPC-800-1 exhibits a surface area of 950 $m^2 \cdot g^{-1}$, a total pore volume of 0.41 $cm^3 \cdot g^{-1}$ and a N content of 1.1 wt %. Please note, the nitrogen content decreased during the activation process and thus nitrogenous compounds must have been released from the polymer during carbonization. The further increase of the K_2CO_3 content results in even more porous carbon materials with increased surface area of 1420 $m^2 \cdot g^{-1}$ (PUPC-800-2) and 1670 $m^2 \cdot g^{-1}$ (PUPC-800-3) and pore volume of 0.62 $cm^3 \cdot g^{-1}$ and 0.71 $cm^3 \cdot g^{-1}$, while the N content does not further decrease and remains at 1.1 wt % and 1.2 wt %, respectively (Table 1). The proposed mechanism according to McKee et al. is given in section S3 of Supporting Information File 1 [70]. It can be concluded, that the activation of PU foam provides porous carbon materials, but the activation alone is not sufficient to ensure both, a high surface area and nitrogen content.

Increase of the N content through addition of urea

Since we observed a decreasing N content during the activation process of PU, we added urea as an additional nitrogenous precursor to the mechanochemical synthesis. Please note the modified sample code, with polyurethane–urea–K_2CO_3 as PUUPC and a new sequence number (Table 1). The IR spectra reveal that polymerization reactions occur during ball milling (Figure S1B, Supporting Information File 1). In particular, the conden-

Table 1: Characterization data of different N-doped carbon samples after milling and carbonization. Physisorption data derived from N_2 isotherms measured at −196 °C. Element concentrations derived from elemental analysis.

sample	mass ratio of PU/urea/K_2CO_3	SSA_{BET}^{a} / $m^2 \cdot g^{-1}$	SSA_{DFT}^{b} / $m^2 \cdot g^{-1}$	$V(N_2)_{total}^{c}$ / $cm^3 \cdot g^{-1}$	$V(N_2)_{micro}^{d}$ / $cm^3 \cdot g^{-1}$	$V(N_2)_{meso}^{e}$ / $cm^3 \cdot g^{-1}$	W_x^{f} / wt %			
							N	C	H	rest
PU-BM	—	0.2	0	—	—	—	5.7	61.0	6.3	27
PU-BM-800	—	0	0	—	—	—	3.9	81.7	0.8	13.6
PUPC-800-1	3:0:1	950	1383	0.41	0.39	0.02	1.1	86.2	0.3	12.4
PUPC-800-2	3:0:2	1421	1953	0.62	0.58	0.04	1.1	71	1.2	26.7
PUPC-800-3	3:0:3	1668	2094	0.71	0.67	0.04	1.2	61.8	0.9	36.1
PUUPC-800-1	3:1:3	2147	2029	0.89	0.76	0.13	1.6	62.0	1.0	35.4
PUUPC-800-2	3:2:3	2005	1390	0.84	0.61	0.23	2.8	60.0	1.2	36.0
PUUPC-800-3	3:3:3	668	823	0.27	0.27	—	6.3	64.4	1.9	27.4
PUUPC-800-4	3:3:2	1005	1368	0.40	0.40	—	7.4	62.0	2.7	27.9
PUUPC-800-5	3:3:1	174	221	0.07	0.07	—	8.4	63.3	1.8	26.5

[a]Multi-point BET-method for $0.05 \leq p/p_0 \leq 0.2$; [b]SSA of micropores determined by QSDFT below 2 nm; [c]total pore volume at $p/p_0 = 0.95$; [d]applying QSDFT method assuming slit and cylindrical shaped pores using the adsorption branch; [d]$V_{pore,meso} = V_{pore,total} - V_{pore,micro}$; [f]chemical composition (W_x) obtained from elemental analysis, rest refers to the residual mass supposed to be oxygen, which is undetectable with this methode.
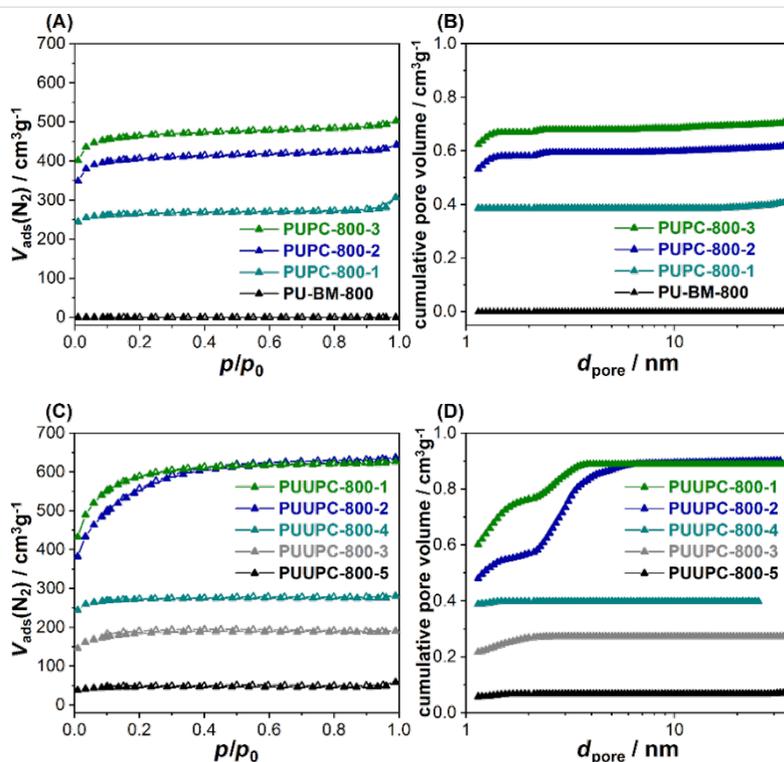

Figure 2: (A, C) Nitrogen adsorption/desorption (filled symbols/empty symbols) isotherms (measured at −196 °C) and (B, D) cumulative pore size distribution (PSD) using QSDFT with cylindrical/slit-shaped pores of the samples (A, B): PUPC-800-1 (cyan), PUPC-800-2 (blue), PUPC-800-3 (green), and PU-BM-800 (black) and the samples (C, D): PUUPC-1-800 (green), PUUPC-2-800 (blue), PUUPC-3-800 (grey), PUUPC-4-800 (cyan) and PUUPC-5-800 (black).

sation of urea with the urethane group is initiated during the milling process shown by the disappearing peaks of NH_2 (3335 cm^{-1}) and of C=O (1715 cm^{-1}). In addition, the morphological conversion of the PU powder (Figure S3, Supporting Information File 1) to an agglomerated polymer (Figure S4, Supporting Information File 1) as well as the optical observation that moisture is produced during milling, indicates that a condensation reaction must have taken place.

Since an equal ratio of PU and K_2CO_3 (PUPC-800-3) has yielded the highest porosity in the previous section, we kept the PU and K_2CO_3 ratio constant and added specific amounts of urea to investigate the influence of the nitrogen precursor on the nitrogen content and surface area. Already by adding small amounts of urea, the nitrogen content of the obtained N-doped carbon materials is slightly increased to 1.6 wt % (PUUPC-800-1) and 2.8 wt % (PUUPC-800-2, Table 1). Moreover, the addition of urea influences the activation process itself [64], resulting in an increased surface area of 2150 m$^2 \cdot$g^{-1} (PUUPC-800-1) and 2010 m$^2 \cdot$g^{-1} (PUUPC-800-2) and pore volume of 0.89 cm$^3 \cdot$g^{-1} and 0.84 cm$^3 \cdot$g^{-1} with a small fraction of mesopores (Figure 2C,D) [69]. However, when urea was added in the same ratio as PU and K_2CO_3 (PUUPC-800-3), the surface area and the pore volume significantly decreased to 670 m$^2 \cdot$g^{-1} and to 0.27 cm$^3 \cdot$g^{-1}, while the nitrogen content increases to 6.3 wt % (Table 1). This observation is related to an intensified chemical activation process due to the high amount of urea and the formation of ammonia during the high-temperature treatment, leading to a higher consumption of carbon and its partial textural destruction. In addition to the formation of ammonia and the activation of the carbon, urea can form $(NH_4)_2(CO_3)$, which further decomposes to gaseous H_2O, CO_2 and NH_3 and leads to additional porosity of the carbon.

In order to attenuate the activation process, while ensuring a high nitrogen content at the same time, we reduced the K_2CO_3 content, while keeping the content of PU and urea constant. Reducing the K_2CO_3 content results in a specific surface area of 1010 m$^2 \cdot$g^{-1}, a nitrogen content of 7.4 wt % and a pore volume of 0.40 cm$^3 \cdot$g^{-1} (PUUPC-800-4, Table 1). However, further reduction of the K_2CO_3 content leads to a decreased porosity (SSA = 170 m$^2 \cdot$g^{-1}), while the N content is further increased up to 8.4 wt % (PUUPC-800-5, Table 1). As a result, if the K_2CO_3 content is insufficient, the activation process is incomplete and a high porosity cannot be obtained.

Water vapor adsorption was performed exemplarily for the samples PUPC-800-3, PUUPC-800-1, and PUUPC-800-2 to demonstrate the effect of the porosity and the generated nitrogen functionalities on sorption, phase and wetting behavior. The water isotherms of all measured samples are assigned to a type V isotherm according to the IUPAC classification (Figure 3A) [69]. Up to a relative pressure of $p/p_0 < 0.4$ almost no adsorptive interactions take place. The step at a relative pressure of $p/p_0 = 0.4$ is assigned to the filling of micropores. PUUP-800-1 shows the highest uptake in this range because it has the highest micropore volume. At relative pressures of $p/p_0 > 0.8$, PUUP-800-1 shows a lower water adsorption uptake than sample PUUP-800-2. This can be attributed to the higher mesopore volume of PUUP-800-2 [71]. A direct correlation between the nitrogen content of the samples and the water adsorption behavior is not observed since the uptake is not significantly shifted to lower relative pressures. A reduction of the total amount of adsorbed water is observed for sample PUPC-800-3 and corresponds to a decreased total pore volume and nitrogen content (Table 1, Figure 2B,D). The hydrophilicity of the N-doped carbon materials has been confirmed by using the
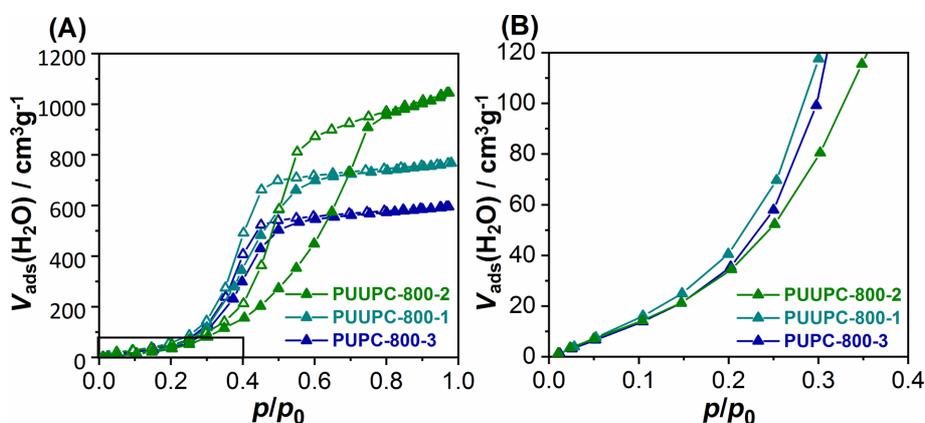

Figure 3: (A) Water vapor sorption isotherms (adsorption/desorption = filled symbols/empty symbols) measured at 25 °C and (B) magnification of the lower relative pressure range of the samples: PUUPC-800-1 (cyan), PUUPC-800-2 (green) and PUPC-800-3 (blue).

dynamic contact angle technique (Figure S7, Supporting Information File 1). As expected, the samples absorbed the water droplet almost immediately after its release. The sample PUUPC-800-2 absorbed the water droplet completely after only 8 s, whereas sample PUPC-800-3, exhibiting a lower nitrogen content, absorbed the water after 20 s. Thus, the higher nitrogen content benefits the wettability of the carbon surface.

Electrochemical characterization

The produced carbon materials differ in terms of specific surface area, pore sizes, and nitrogen content. Therefore, we selected three carbon materials that represent a wide range of structure characteristics for electrochemical characterization: PUPC-800-3, PUUPC-800-1, and PUUPC-800-2. First, we determined the powder resistance of the carbon materials. Two general trends are observable. Firstly, the resistance increases with a higher specific surface area (compare PUUPC-800-1 and PUPC-800-3, Table 2). This was previously observed by Casco et al. [39] for a different carbon system, too. Secondly, regarding PUUPC-800-1 and PUUPC-800-2, which mainly differ in their nitrogen content, the resistance increased with in-

creasing nitrogen content. Thus, nitrogen-doping has no beneficial influence on the conductivity of the electrodes in contrast to expectations.

The materials have been processed to free-standing electrodes and characterized as symmetrical supercapacitors in three different electrolytes: 1 M Li$_2$SO$_4$ (AQ), 1 M TEA-BF$_4$ (O) in acetonitrile (ACN) and EMIM-BF$_4$ (IL). The supercapacitors show a rectangular CV shape in all three electrolytes (Figure S8, Supporting Information File 1). The CVs of the three carbon materials are exemplarily shown for the organic electrolyte (O) in Figure 4A and give hint to a purely capacitive energy storage mechanism due to the absence of peaks. Further electrochemical characterization data can be found in Supporting Information File 1 (Figures S9–S12). The specific capacitances for the different carbon materials measured in different electrolytes are calculated by galvanostatic charge–discharge curves (Table 2). In general, all carbon materials show a higher specific capacitance ($C_{spec.}$) in aqueous electrolyte, which can be attributed to the higher ion conductivity of aqueous electrolytes [72]. The highest value of $C_{spec.}$ was calculated for PUUPC-800-2 with 99 F·g^{-1}, which is associated to the high specific

Table 2: Electrochemical characterization data of PUPC-800-3, PUUPC-800-1 and PUUPC-800-2 measured in aqueous (1 M Li$_2$SO$_4$), organic (1 M TEA-BF$_4$ in ACN) and ionic liquid (EMIM-BF$_4$) electrolytes calculated from galvanostatic charge–discharge measurements at different specific currents.

electrolyte	powder resistance[a] / Ω·cm	specific current / A·g^{-1}	specific capacitance[b] / F·g^{-1}		
			1 M Li$_2$SO$_4$	1 M TEA-BF$_4$(ACN)	EMIM-BF$_4$
PUPC-800-3	0.39	0.1	90	47	56
		1	73	62	71
PUUPC-800-1	0.47	0.1	90	73	69
		1	81	72	63
PUUPC-800-2	0.75	0.1	99	59	36
		1	82	57	42

[a]Powder pressed with 2 t, *d* = 1 cm; [b]obtained from the discharge branch.

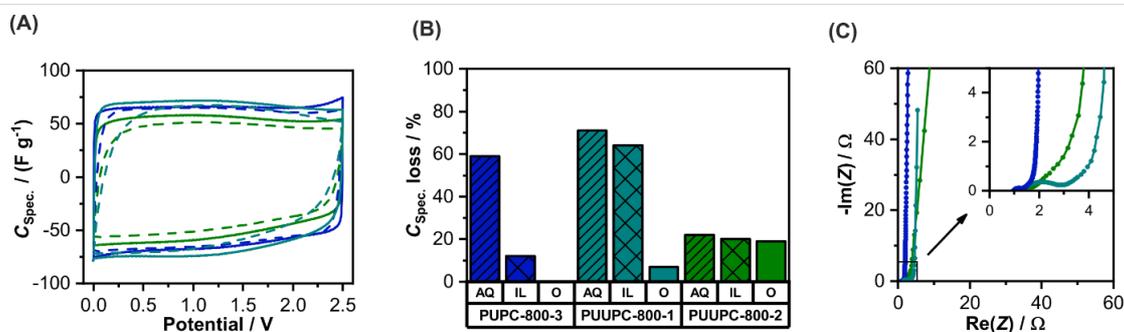**Figure 4:** (A) Cyclic voltammogram measured in 1 M TEABF$_4$ (ACN) with a scan rate of 10 mV·s^{-1} (solid lines) and 100 mV·s^{-1} (dashed lines), (B) loss of the specific capacitance in three different electrolytes, and (C) Nyquist plot for the three samples PUPC-800-3 (blue), PUUPC-800-1 (cyan), and PUUPC-800-2 (green).

surface area of this sample compared to PUPC-800-3 and PUUPC-800-1.

Regarding the loss of specific capacitance when increasing the specific current from 0.1 to 10 A·g^{-1}, PUUPC-800-2 shows the best rate capability in the aqueous electrolyte (Figure 4B). This can be associated with the higher volume ratio of mesopores to micropores, since mesopores are acting as transport pores enabling a fast electrolyte ion mobility [73,74]. Interestingly, the rate capability for this material in organic and ionic liquid electrolytes, however, is worse compared to the other two materials. This can be attributed to a low electric conductivity of the electrodes accompanied with the lower ionic conductivity of such electrolytes. This causes a higher resistance of the whole device and results in a lower rate capability. The difference of the electrode conductivities is also shown in the Nyquist plot (Figure 4C). A higher nitrogen content reduces the electric conductivity of the electrodes and thus, does not have a beneficial influence on the supercapacitor performance.

Conclusion

We introduced an upcycling process for plastic waste to produce N-doped carbon materials in a sustainable synthesis. Polyurethane waste serves as a carbon (and nitrogen) source and is converted via a mechanochemical pathway with K_2CO_3 and, optionally, urea. The mechanochemical approach does not require any solvent, has a short reaction and process time and is realized in a facile setup. By using different amounts of activation and doping reagents, we obtained optimized carbon materials offering excellent properties such as a high specific surface area of 2150 m^2·g^{-1}, and a total pore volume of 0.9 cm^3·g^{-1} (PUUPC-800-1). These N-doped carbon materials performed similarly well as supercapacitors from commercial carbon materials such as YP-50F, showing a specific capacitance up to 99 F·g^{-1} in Li_2SO_4, as well as a stable performance in TEA-BF_4 with 83 F·g^{-1}. By the mechanochemical upcycling with additional urea, the rate capability of the supercapacitor was enhanced and the obtained device exhibits 80% of its capacitance at a high specific current of 10 A·g^{-1} in aqueous electrolyte. The broader intention would be to transfer the process presented here to other difficult-to-process polymer waste and thus be able to further counteract the generation of waste. The application possibilities of these materials could also be extended to other energy storage systems such as Li-ion batteries or wastewater purification, wherever materials with a high surface area and improved wettability are required.

Experimental
Synthesis of N-doped carbon

In a similar manner to [36,64], nitrogen-doped porous carbon materials were produced from polyurethane (PU) foam as the carbon source, urea (U) added as a supplementary nitrogen source and potassium carbonate (PC) added as an activation reagent. The nitrogen source and the activation reagent were used in different molar ratios (Table 3). The synthesis was carried out in a 45 mL zirconium oxide milling vessel with twenty-two 10 mm diameter zirconium oxide milling balls (3.19 g each). First, the sprayed polyurethane was milled for 10 min in a Fritsch Pulverisette 7 premium line planetary ball mill operating at a rotation speed of 600 rpm. After addition of the activation and doping reagents, the mixture was then milled in the same ball mill and vessel for 30 min and at a rotation speed of 800 rpm. The resulting polymer was pyrolyzed for one hour in argon at 800 °C with a heating rate of 150 °C·h^{-1} and afterwards purified with diluted HCl and water.

Table 3: Sample code and amounts of PU, urea and K_2CO_3.

sample code	PU / g	urea / g	K_2CO_3 / g
PUPC-1	3	0	1
PUPC-2	3	0	2
PUPC-3	3	0	3
PUUPC-1	3	1	3
PUUPC-2	3	2	3
PUUPC-3	3	3	3
PUUPC-4	3	3	2
PUUPC-5	3	3	1

Characterization

Nitrogen physisorption measurements were performed with a Quadrasorb EVO/SI from Quantachrome Instruments at −196 °C. The samples were degassed before all measurements under vacuum at 150 °C for at least 24 h. The multi-point BET method was used to calculate the specific surface areas of the materials. For each sample, the relative pressure range is given at the corresponding location.

The calculation of the total pore volume was performed at a relative pressure of $p/p_0 = 0.95$. Assuming slit and cylindrical pore geometry, the pore size distributions were calculated from the adsorption branch using quenched solid density functional theory (QSDFT) method incorporated into the ASiQwin analysis software (Quantachrome). Micropore volumes were calculated from the cumulative pore volumes at a diameter of 2 nm.

Water vapor adsorption measurements were carried out at 25 °C on an Autosorb iQ from Quantachrome Instruments after vacuum activation at 150 °C for at least 24 h. The total pore volume was calculated at relative pressure of $p/p_0 = 0.96$ for each material.

Elemental analysis was carried out with a vario Micro cube from Elementar. The elemental composition of carbon, hydrogen, nitrogen and sulfur of all samples is the average of three measurements.

IR spectra were measured on a BRUKER Vertex 70 with a Specac Golden Gate ATR unit. A resolution of 2 cm^{-1} was utilized and the resulting spectra were treated with ATR correction by the OPUS 6.5 software. The spectra were recorded in the range of 4000–400 cm^{-1}.

Electric powder conductivities were measured with an Agilent 34420A combined with a custom-built cell with a diameter of 1 cm. The powders were pressed with 2 t.

For the preparation of the electrodes, we added 5 wt % of polytetrafluoroethylene (PTFE granular, 98 wt % from Sigma-Aldrich) as binder to the N-doped carbon material, which was ground under heat treatment in a mortar. The resulting dough-like material was rolled out to a thickness of 100–200 μm and then cut out to a round electrode with a diameter of 10 mm. The electrodes were dried in a vacuum oven at 120 °C for 24 h.

For electrochemical testing, a specially manufactured polyether ether ketone (PEEK) cell with spring-loaded titanium pistons was used as symmetrical full cell, as described in detail elsewhere [75]. Electrode discs with a thickness of 100–200 μm and a diameter of 10 mm were punched out of the free-standing film electrode. Electrodes with the same mass were selected as the working and the counter electrode, which were placed on the current collector and separated by a glass-fiber separator (GF/A, Whatman). The prepared cells were filled with the electrolyte. We used a potentiostat/galvanostat VMP-3 from BioLogic for cyclic voltammetry (CV) and galvanostatic cycling with potential limitation (GCPL). CVs were recorded in full-cell mode at a scan rate 5 mV·s^{-1}. In GCPL mode the specific current was increased from 0.1 to 10 A·g^{-1}. In order to obtain information about the IR drop, a rest period of 10 s was introduced between charging and discharging.

The gravimetric capacitance was calculated from the discharge curve via the following equation:

$$C_\mathrm{spec} = \frac{4I}{\dfrac{\Delta U}{\Delta t} \cdot m}, \tag{1}$$

with specific capacitance C_spec, cell voltage U corrected by IR drop, and carbon mass of both electrodes m (without binder).

ORCID® iDs
Sven Grätz - https://orcid.org/0000-0001-6026-097X
Lars Borchardt - https://orcid.org/0000-0002-8778-7816

References

1. Jambeck, J. R.; Geyer, R.; Wilcox, C.; Siegler, T. R.; Perryman, M.; Andrady, A.; Narayan, R.; Law, K. L. *Science* **2015,** *347,* 768–771. doi:10.1126/science.1260352
2. Ocean plastic, Greenpeace UK. https://www.greenpeace.org.uk/what-we-do/oceans/plastics/ (accessed June 19, 2019).
3. Geyer, R.; Jambeck, J. R.; Law, K. L. *Sci. Adv.* **2017,** *3,* e1700782. doi:10.1126/sciadv.1700782
4. Plastic Pollution. https://ourworldindata.org/plastic-pollution (accessed June 19, 2019).
5. Ignatyev, I. A.; Thielemans, W.; Vander Beke, B. *ChemSusChem* **2014,** *7,* 1579–1593. doi:10.1002/cssc.201300898
6. Achilias, D. S.; Roupakias, C.; Megalokonomos, P.; Lappas, A. A.; Antonakou, E. V. *J. Hazard. Mater.* **2007,** *149,* 536–542. doi:10.1016/j.jhazmat.2007.06.076
7. Goto, M. *J. Supercrit. Fluids* **2009,** *47,* 500–507. doi:10.1016/j.supflu.2008.10.011
8. Paszun, D.; Spychaj, T. *Ind. Eng. Chem. Res.* **1997,** *36,* 1373–1383. doi:10.1021/ie960563c
9. Sadat-Shojai, M.; Bakhshandeh, G.-R. *Polym. Degrad. Stab.* **2011,** *96,* 404–415. doi:10.1016/j.polymdegradstab.2010.12.001
10. Market data, PlasticsEurope. https://www.plasticseurope.org/en/resources/market-data (accessed June 19, 2019).
11. Yu, K.; Taynton, P.; Zhang, W.; Dunn, M. L.; Qi, H. J. *RSC Adv.* **2014,** *4,* 10108–10117. doi:10.1039/c3ra47438k
12. Behrendt, G.; Naber, B. W. *J. Univ. Chem. Technol. Metall.* **2009,** *44,* 3–23.
13. Polyurethanes. http://www.essentialchemicalindustry.org/polymers/polyurethane.html (accessed June 19, 2019).
14. Polyurethanes Applications. https://polyurethane.americanchemistry.com/Applications/ (accessed June 19, 2019).

15. Polyurethane Production, Pricing and Market Demand. https://www.plasticsinsight.com/resin-intelligence/resin-prices/polyurethane/ (accessed June 19, 2019).

16. Yang, W.; Dong, Q.; Liu, S.; Xie, H.; Liu, L.; Li, J. *Procedia Environ. Sci.* **2012,** *16,* 167–175. doi:10.1016/j.proenv.2012.10.023

17. Nikje, M. M. A.; Garmarudi, A. B.; Idris, A. B. *Des. Monomers Polym.* **2011,** *14,* 395–421. doi:10.1163/138577211x587618

18. Zevenhoven, R. *Treatment and Disposal of Polyurethane Wastes: Options for Recovery and Recycling;* Helsinki University of Technology: Espoo, Finland, 2004. http://users.abo.fi/rzevenho/tkk-eny-19.pdf (accessed June 19, 2019).

19. Hulicova-Jurcakova, D.; Seredych, M.; Lu, G. Q.; Bandosz, T. J. *Adv. Funct. Mater.* **2009,** *19,* 438–447. doi:10.1002/adfm.200801236

20. Gratuito, M. K. B.; Panyathanmaporn, T.; Chumnanklang, R.-A.; Sirinuntawittaya, N.; Dutta, A. *Bioresour. Technol.* **2008,** *99,* 4887–4895. doi:10.1016/j.biortech.2007.09.042

21. Thomas, B. N.; George, S. C. *Trends Green Chem.* **2015,** *1,* No. 7. doi:10.21767/2471-9889.100007

22. Wang, G.; Zhang, L.; Zhang, J. *Chem. Soc. Rev.* **2012,** *41,* 797–828. doi:10.1039/c1cs15060j

23. Frąckowiak, E. *Phys. Chem. Chem. Phys.* **2007,** *9,* 1774–1785. doi:10.1039/b618139m

24. Rodríguez-reinoso, F. *Carbon* **1998,** *36,* 159–175. doi:10.1016/s0008-6223(97)00173-5

25. Serp, P.; Figueiredo, J. L. *Carbon Materials for Catalysis;* John Wiley & Sons: Hoboken, NJ, USA, 2009. doi:10.1002/9780470403709

26. Serp, P. *Appl. Catal., A* **2003,** *253,* 337–358. doi:10.1016/s0926-860x(03)00549-0

27. Ismail, A.; David, L. *J. Membr. Sci.* **2001,** *193,* 1–18. doi:10.1016/s0376-7388(01)00510-5

28. Kockrick, E.; Schrage, C.; Borchardt, L.; Klein, N.; Rose, M.; Senkovska, I.; Kaskel, S. *Carbon* **2010,** *48,* 1707–1717. doi:10.1016/j.carbon.2010.01.004

29. Presser, V.; McDonough, J.; Yeon, S.-H.; Gogotsi, Y. *Energy Environ. Sci.* **2011,** *4,* 3059–3066. doi:10.1039/c1ee01176f

30. Steele, B. C. H.; Heinzel, A. Materials for fuel-cell technologies. *Materials for Sustainable Energy;* World Scientific, 2010; pp 224–231. doi:10.1142/9789814317665_0031

31. Shao, Y.; Sui, J.; Yin, G.; Gao, Y. *Appl. Catal., B* **2008,** *79,* 89–99. doi:10.1016/j.apcatb.2007.09.047

32. Antolini, E. *Appl. Catal., B* **2009,** *88,* 1–24. doi:10.1016/j.apcatb.2008.09.030

33. Guo, D.; Shibuya, R.; Akiba, C.; Saji, S.; Kondo, T.; Nakamura, J. *Science* **2016,** *351,* 361–365. doi:10.1126/science.aad0832

34. Bruce, P. G.; Freunberger, S. A.; Hardwick, L. J.; Tarascon, J.-M. *Nat. Mater.* **2012,** *11,* 19–29. doi:10.1038/nmat3191

35. Wang, D.-W.; Zeng, Q.; Zhou, G.; Yin, L.; Li, F.; Cheng, H.-M.; Gentle, I. R.; Lu, G. Q. M. *J. Mater. Chem. A* **2013,** *1,* 9382–9394. doi:10.1039/c3ta11045a

36. Schneidermann, C.; Kensy, C.; Otto, P.; Oswald, S.; Giebeler, L.; Leistenschneider, D.; Grätz, S.; Dörfler, S.; Kaskel, S.; Borchardt, L. *ChemSusChem* **2019,** *12,* 310–319. doi:10.1002/cssc.201801997

37. Song, J.; Gordin, M. L.; Xu, T.; Chen, S.; Yu, Z.; Sohn, H.; Lu, J.; Ren, Y.; Duan, Y.; Wang, D. *Angew. Chem.* **2015,** *127,* 4399–4403. doi:10.1002/ange.201411109

38. Zhang, L. L.; Zhao, X. S. *Chem. Soc. Rev.* **2009,** *38,* 2520. doi:10.1039/b813846j

39. Casco, M. E.; Kirchhoff, S.; Leistenschneider, D.; Rauche, M.; Brunner, E.; Borchardt, L. *Nanoscale* **2019,** *11,* 4712–4718. doi:10.1039/c9nr01019j

40. Lota, G.; Grzyb, B.; Machnikowska, H.; Machnikowski, J.; Frackowiak, E. *Chem. Phys. Lett.* **2005,** *404,* 53–58. doi:10.1016/j.cplett.2005.01.074

41. Krüner, B.; Odenwald, C.; Quade, A.; Kickelbick, G.; Presser, V. *Batteries Supercaps* **2018,** *1,* 135–148. doi:10.1002/batt.201800051

42. Borenstein, A.; Hanna, O.; Attias, R.; Luski, S.; Brousse, T.; Aurbach, D. *J. Mater. Chem. A* **2017,** *5,* 12653–12672. doi:10.1039/c7ta00863e

43. Zhai, Y.; Dou, Y.; Zhao, D.; Fulvio, P. F.; Mayes, R. T.; Dai, S. *Adv. Mater. (Weinheim, Ger.)* **2011,** *23,* 4828–4850. doi:10.1002/adma.201100984

44. Ewert, J.-K.; Weingarth, D.; Denner, C.; Friedrich, M.; Zeiger, M.; Schreiber, A.; Jäckel, N.; Presser, V.; Kempe, R. *J. Mater. Chem. A* **2015,** *3,* 18906–18912. doi:10.1039/c5ta04773k

45. Wood, K. N.; O'Hayre, R.; Pylypenko, S. *Energy Environ. Sci.* **2014,** *7,* 1212–1249. doi:10.1039/c3ee44078h

46. Seredych, M.; Hulicova-Jurcakova, D.; Lu, G. Q.; Bandosz, T. J. *Carbon* **2008,** *46,* 1475–1488. doi:10.1016/j.carbon.2008.06.027

47. Mangun, C. L.; Benak, K. R.; Economy, J.; Foster, K. L. *Carbon* **2001,** *39,* 1809–1820. doi:10.1016/s0008-6223(00)00319-5

48. Przepiórski, J.; Skrodzewicz, M.; Morawski, A. W. *Appl. Surf. Sci.* **2004,** *225,* 235–242. doi:10.1016/j.apsusc.2003.10.006

49. Xue, C.; Tu, B.; Zhao, D. *Adv. Funct. Mater.* **2008,** *18,* 3914–3921. doi:10.1002/adfm.200800708

50. Poliakoff, M. *Science* **2002,** *297,* 807–810. doi:10.1126/science.297.5582.807

51. Anastas, P.; Eghbali, N. *Chem. Soc. Rev.* **2010,** *39,* 301–312. doi:10.1039/b918763b

52. Sheldon, R. A. *Green Chem.* **2014,** *16,* 950–963. doi:10.1039/c3gc41935e

53. James, S. L.; Adams, C. J.; Bolm, C.; Braga, D.; Collier, P.; Friščić, T.; Grepioni, F.; Harris, K. D. M.; Hyett, G.; Jones, W.; Krebs, A.; Mack, J.; Maini, L.; Orpen, A. G.; Parkin, I. P.; Shearouse, W. C.; Steed, J. W.; Waddell, D. C. *Chem. Soc. Rev.* **2012,** *41,* 413–447. doi:10.1039/c1cs15171a

54. Weyna, D. R.; Shattock, T.; Vishweshwar, P.; Zaworotko, M. J. *Cryst. Growth Des.* **2009,** *9,* 1106–1123. doi:10.1021/cg800936d

55. Delori, A.; Friščić, T.; Jones, W. *CrystEngComm* **2012,** *14,* 2350–2362. doi:10.1039/c2ce06582g

56. Todres, Z. V. *Organic Mechanochemistry and Its Practical Applications;* CRC/Taylor & Francis: Boca Raton, FL, USA, 2006. doi:10.1201/9781420005882

57. Wang, G.-W. *Chem. Soc. Rev.* **2013,** *42,* 7668–7700. doi:10.1039/c3cs35526h

58. Hernández, J. G.; Bolm, C. *J. Org. Chem.* **2017,** *82,* 4007–4019. doi:10.1021/acs.joc.6b02887

59. Klimakow, M.; Klobes, P.; Thünemann, A. F.; Rademann, K.; Emmerling, F. *Chem. Mater.* **2010,** *22,* 5216–5221. doi:10.1021/cm1012119

60. Friščić, T. *Chem. Soc. Rev.* **2012,** *41,* 3493–3510. doi:10.1039/c2cs15332g

61. Katsenis, A. D.; Puškarić, A.; Štrukil, V.; Mottillo, C.; Julien, P. A.; Užarević, K.; Pham, M.-H.; Do, T.-O.; Kimber, S. A. J.; Lazić, P.; Magdysyuk, O.; Dinnebier, R. E.; Halasz, I.; Friščić, T. *Nat. Commun.* **2015,** *6,* 6662. doi:10.1038/ncomms7662

62. Troschke, E.; Grätz, S.; Lübken, T.; Borchardt, L.
    Angew. Chem., Int. Ed. **2017,** *56,* 6859–6863.
    doi:10.1002/anie.201702303
63. Do, J.-L.; Friščić, T. *Synlett* **2017,** *28,* 2066–2092.
    doi:10.1055/s-0036-1590854
64. Schneidermann, C.; Jäckel, N.; Oswald, S.; Giebeler, L.; Presser, V.;
    Borchardt, L. *ChemSusChem* **2017,** *10,* 2416–2424.
    doi:10.1002/cssc.201700459
65. Leistenschneider, D.; Jäckel, N.; Hippauf, F.; Presser, V.; Borchardt, L.
    Beilstein J. Org. Chem. **2017,** *13,* 1332–1341. doi:10.3762/bjoc.13.130
66. Mio, H.; Kano, J.; Saito, F. *Chem. Eng. Sci.* **2004,** *59,* 5909–5916.
    doi:10.1016/j.ces.2004.07.020
67. Stolle, A.; Schmidt, R.; Jacob, K. *Faraday Discuss.* **2014,** *170,*
    267–286. doi:10.1039/c3fd00144j
68. Borchardt, L.; Grätz, S. Reaktoren für spezielle technisch-chemische
    Prozesse: Tribochemische Reaktoren. In *Handbuch Chemische
    Reaktoren;* Reschetilowski, W., Ed.; Springer: Berlin, Heidelberg,
    Germany, 2018; pp 1–28. doi:10.1007/978-3-662-56444-8_40-1
69. Thommes, M.; Kaneko, K.; Neimark, A. V.; Olivier, J. P.;
    Rodriguez-Reinoso, F.; Rouquerol, J.; Sing, K. S. W. *Pure Appl. Chem.*
    2015, *87,* 1051–1069. doi:10.1515/pac-2014-1117
70. McKee, D. W. *Fuel* **1983,** *62,* 170–175.
    doi:10.1016/0016-2361(83)90192-8
71. Thommes, M.; Morell, J.; Cychosz, K. A.; Fröba, M. *Langmuir* **2013,** *29,*
    14893–14902. doi:10.1021/la402832b
72. Zhong, C.; Deng, Y.; Hu, W.; Qiao, J.; Zhang, L.; Zhang, J.
    Chem. Soc. Rev. **2015,** *44,* 7484–7539. doi:10.1039/c5cs00303b
73. Yan, R.; Antonietti, M.; Oschatz, M. *Adv. Energy Mater.* **2018,** *8,*
    1800026. doi:10.1002/aenm.201800026
74. Borchardt, L.; Leistenschneider, D.; Haase, J.; Dvoyashkin, M.
    Adv. Energy Mater. **2018,** *8,* 1870108. doi:10.1002/aenm.201870108
75. Weingarth, D.; Zeiger, M.; Jäckel, N.; Aslan, M.; Feng, G.; Presser, V.
    Adv. Energy Mater. **2014,** *4,* 1400316. doi:10.1002/aenm.201400316

BEILSTEIN JOURNAL OF NANOTECHNOLOGY

Tuning the performance of vanadium redox flow batteries by modifying the structural defects of the carbon felt electrode

Ditty Dixon[*1], Deepu Joseph Babu[2], Aiswarya Bhaskar[1], Hans-Michael Bruns[3], Joerg J. Schneider[2], Frieder Scheiba[3] and Helmut Ehrenberg[3]

Full Research Paper

Open Access

Address:
[1]Central Electrochemical Research Institute (CSIR-CECRI), Karaikudi, 630003, India, [2]Fachbereich Chemie, Eduard-Zintl Institut für Anorganische und Physikalische Chemie, Technische Universität Darmstadt, Alarich-Weiss-Straße 12, 64287 Darmstadt, Germany and [3]Institute for Applied Materials - Energy Storage Systems (IAM-ESS), Karlsruhe Institute of Technology (KIT), Hermann-von-Helmholtz-Platz 1, 76344 Eggenstein-Leopoldshafen, Germany

Email:
Ditty Dixon[*] - ditty@cecri.res.in

* Corresponding author

Abstract

Polyacrylonitrile (PAN)-based carbon felt was subjected to N_2-plasma treatment to increase the heteroatom defects and reactive edge sites as a method to increase the performance in vanadium redox flow batteries (VRFBs). N-doping in the felt was mainly in the form of pyrrolic and pyridinic nitrogen. Even though the amount of oxygen functional groups on the N_2-plasma-treated sample was very low, the felt showed enhanced electrochemical performance for both V^{3+}/V^{2+} as well as V^{5+}/V^{4+} redox reactions. The result is highly significant as the pristine electrode with the same amount of oxygen functional groups showed significantly less activity for the V^{3+}/V^{2+} redox reaction. Overall, the single-flow cell experiments with N_2-plasma-treated felt showed superior performance compared to the pristine sample. Therefore, the enhanced performance observed for the N_2-plasma-treated sample should be attributed to the increase in defects and edge sites. Thus, from the present study, it can be concluded that an alternate way to increase the performance of the VRFBs is to introduce specific defects such as N-doping/substitution or to increase the edge sites. In other words, defects induced in the carbon felt such as heteroatom doping are as beneficial as the presence of oxygen functional groups for the improved performance of VRFBs. Therefore, for an optimum performance of VRFBs, defects such as N-substitution as well as oxygen functionality should be tuned.

Introduction

In every part of the world, the contribution of electrical energy harvested from a renewable source, such as wind, photovoltaics, etc., to the electrical grid system is increasing. In contrast to electric energy production from fossil or nuclear fuels, the generation of energy from renewable sources is intermittent by nature. The intermittent nature of such energy production can lead to the destabilization of the grid. This issue demands the development of durable and efficient electrical energy storage systems which can store the excess electrical energy from renewable energy sources during peak production and supply the stored energy to the grid during a depletion in the production. In this context, the all-vanadium redox flow battery (VRFB) is one of the most promising and flexible stationary electrical energy storage systems. Unlike Pb acid, Li-ion batteries or even flow batteries like zinc/bromine, the electrical energy in VRFBs is completely stored by the electrolyte in an external tank. Thus, in VRFB systems, the power and energy can be decoupled, that is, to store more energy, only the tank size needs to be increased. Moreover, since the system uses only a single redox species, element cross-contamination issues, which are common in other redox flow batteries such as Cr/Fe, are obviously nonexistent [1]. Nevertheless, the system suffers from irreversible capacity fade due to parasitic reactions such as air oxidation of V^{2+} species and hydrogen evolution reaction (HER) at the negative electrode [2-4]. The air oxidation of V^{2+} species can be completely prevented by keeping the negative tank under inert gas atmosphere. However, the HER at the negative electrode is almost unavoidable as the redox potential of V^{3+}/V^{2+} (−0.26 V vs normal hydrogen electrode (NHE)) reaction is very close to HER (0 V vs NHE). To minimize the HER, the negative electrode surface structure should be tuned in such a way that it tends to preferably bind V^{3+}/V^{2+} ions over H^+ ions. Creating oxygen functional groups on the surface of the anode is one way to achieve this [5,6]. Langner et al. have shown that on a functionalized electrode, in the presence of V^{3+}, the HER is suppressed as the V^{3+} ions get preferentially bonded to the oxygen functional groups [6]. Furthermore, they proposed that it is essential to have at least 5% oxygen functionality on the surface of the carbon felt for the unhindered reduction of V^{3+} ions. In fact, carbon felt with a surface coverage as high as 23% oxygen functionality showed relatively enhanced VRFB performance [7]. Nevertheless, the above-mentioned electrode with a higher amount of oxygen functional groups, when used in a three-electrode configuration, showed poor electrochemical performance for the positive (V^{5+}/V^{4+}) redox reaction. Taking into account that the negative redox reaction is the limiting reaction in VRFB, the overall enhancement in the full cell performance was purely attributed to enhancement in the V^{3+}/V^{2+} redox kinetics due to the presence of functional groups [8]. Thus, it is extremely important to optimize and maintain the

amount of functional groups on the surface of the carbon felt especially when used as a negative electrode in VRFB. However, it has been found that due to electrochemical as well as chemical ageing, both electrode surfaces tend to oxidize with the additional formation of oxygen functional groups [9,10]. Excess oxidation of the carbon felt can also introduce nonselective functional groups such as –C–O and –C=O and reduces the sp^2 carbon content or the graphite content of the felt. The formation of nonselective functional groups can impede the redox reaction. For example, Estevez et al. showed that the presence of –O–C=O groups increases the performance of the VRFB whereas the presence of –C–O and –C=O degrades it [11]. In the long run, reduction in the graphite or sp^2 carbon content of the felt reduces the electrical conductivity, leading to performance loss. Furthermore, it has been proposed by Schweiss et al. that an increase in the amorphous content in the felt can increase the hydrogen evolution reaction [12]. In one way or the other, functionalization with heteroatoms will always reduce the graphitic nature as functionalization proceeds by breaking of the C_6 rings, and in many cases, with the formation of a sp^3 hybridized carbon atoms (out of plane with the graphene layer). Moreover, most of these functional groups will be predominantly formed at graphite edge sites which are much more active than a basal carbon [13]. Therefore, to obtain reasonable VRFB performance, the carbon edge sites of the carbon felt electrode should be preserved or the functional group formed on this site by chemical or electrochemical ageing should promote the redox reaction. Another possible way to create a reaction site or catalytic center in graphite is by doping it with heteroatoms such as B, N, or P. The heteroatom perturbs the electronic structure of the graphite layer subjected to doping, leading to enhanced polarization [14]. N-doped carbon-based electrodes have been successfully tested in VRFBs. For example, Wang et al. developed carbon felt deposited with N-doped carbon nanotubes which showed enhanced VRFB performance [15]. He et al. produced N-doped carbon felt by heating the commercial felt at 600 and 900 °C in the presence of NH_3 gas. This felt showed enhanced VRFB performance, owing to the increase in electrical conductivity as well as active sites [16]. In this work, a carbon felt electrode with minimum oxygen functional groups and a larger amount of defects in the form of N-doping and edge sites was prepared by employing the N_2 plasma technique. The N_2-plasma-treated sample showed enhanced electrochemical performance in a VRFB compared to the untreated sample with fewer defects. The commercial carbon felts (GFD-type) used as electrode materials in the present study are made out of a polyacrylonitrile (PAN) precursor. In contrast to the commonly employed thermal activation process, the plasma treatment process is quick, and subsequent physical or chemical changes incurred will be uniform across the felt.

Apart from that, it is observed that the surface area of the material is not affected by the plasma treatment process.

Results and Discussion

In this work, the N_2 plasma treatment process is applied to PAN-based felts to increase the amount of defects. The normalized spectra obtained for the Raman measurements are shown in Figure 1. In order to investigate the degree of graphitization and defects formed during the plasma treatment process, the intensity of the G- and D-band centered at 1590 cm^{-1} and 1356 cm^{-1} are compared. The G-band in graphitic material arises from the in-plane vibration of sp^2 carbon atoms. Whereas the D-band arises from out-of-plane vibrations from carbon associated with defects. Therefore, the ratio of the intensity of the D- and G-bands (I_D/I_G) gives direct information about the extent of defects in a graphite material [17,18]. From the Raman spectral analysis, it was found that the pristine sample had a lower I_D/I_G ratio of 1.2 compared to the N_2-plasma-treated sample of 1.7. This indicates that the N_2 plasma treatment process served to increase the defects in the carbon felt. Moreover, the D-band of the plasma-treated sample was shifted to a higher frequency, indicating an increase in the defect density. Mostly, this increase in defects can be correlated to heteroatom substitution/doping (N-doping) and the simultaneous creation of new edge sites [17]. At 2690 cm^{-1} a symmetric second order D-band (2D) is visible for both samples. Careful analysis reveals that the 2D peak intensity is lower for the plasma-treated sample, indicating possible doping [17].

In order to investigate the N-doping in a plasma-treated felt, X-ray photoelectron spectroscopy (XPS) analysis of the samples was carried out. The N_2-plasma-treated sample was characterized by a N 1s peak with maxima around 399 eV. The N 1s peak could be deconvoluted into pyridinic and pyrrolic N

contributions, with maxima at 398.3 and 399.8 eV, respectively. The XPS results, as well as the quantification of various groups on the surface of the felt are shown in Figure 2. Thus, from these results, it can be concluded that N_2 plasma treatment can be applied to induce N-doping defects. Both pyrrolic as well as pyridinic N observed in the XPS spectra are incorporated into the graphene layer [19,20]. The doping of N as observed here differs from the functionalization by the fact that during the doping process, the N atom is directly bonded with other carbon atoms inside the graphene framework, whereas during the functionalization process, the nitrogen groups are bonded on one of the edge sites of the carbon atoms. Since XPS shows only the presence of pyrrolic and pyridinic contributions, any N-functionalization can be ruled out [20,21]. In contrast to oxygen, nitrogen is less reactive, and its atomic size is close to carbon. Therefore, with N_2 plasma treatment, doping prevails over functionalization. The elementary composition from the XPS analysis revealed the presence of approximately 2% of nitrogen on the surface of the felt, which translates into a substantial amount of N doping, given that a N-doping level as low as 1 atom % can have a significant effect on the electronic structure of carbon materials [22].

Additionally, from the XPS analysis, approximately 2% and 3% of oxygen functional groups (C=O and C–O) was found to be present on both pristine as well as plasma-treated samples, respectively. Furthermore, it can also be seen from the XPS results that, compared to the pristine sample, the N_2-plasma-treated sample has the highest graphitic content on the surface. This result contradicts the Raman spectroscopy result where the plasma-treated sample in fact showed more defects. It must be emphasized that in the present work no peak fitting was carried out on the C 1s peak to quantify the defects. It may be stressed that the graphite content obtained from XPS also has a contribu-
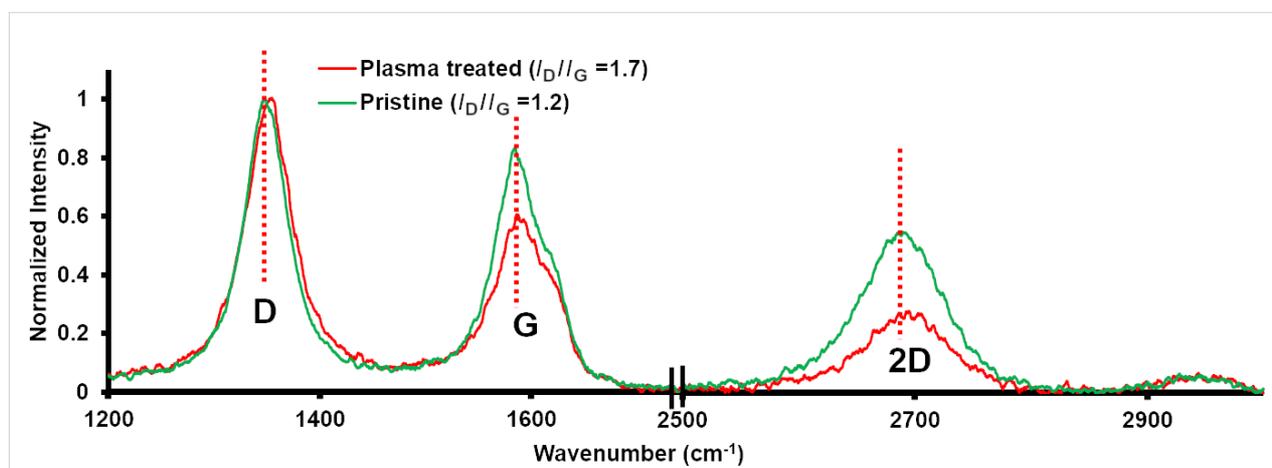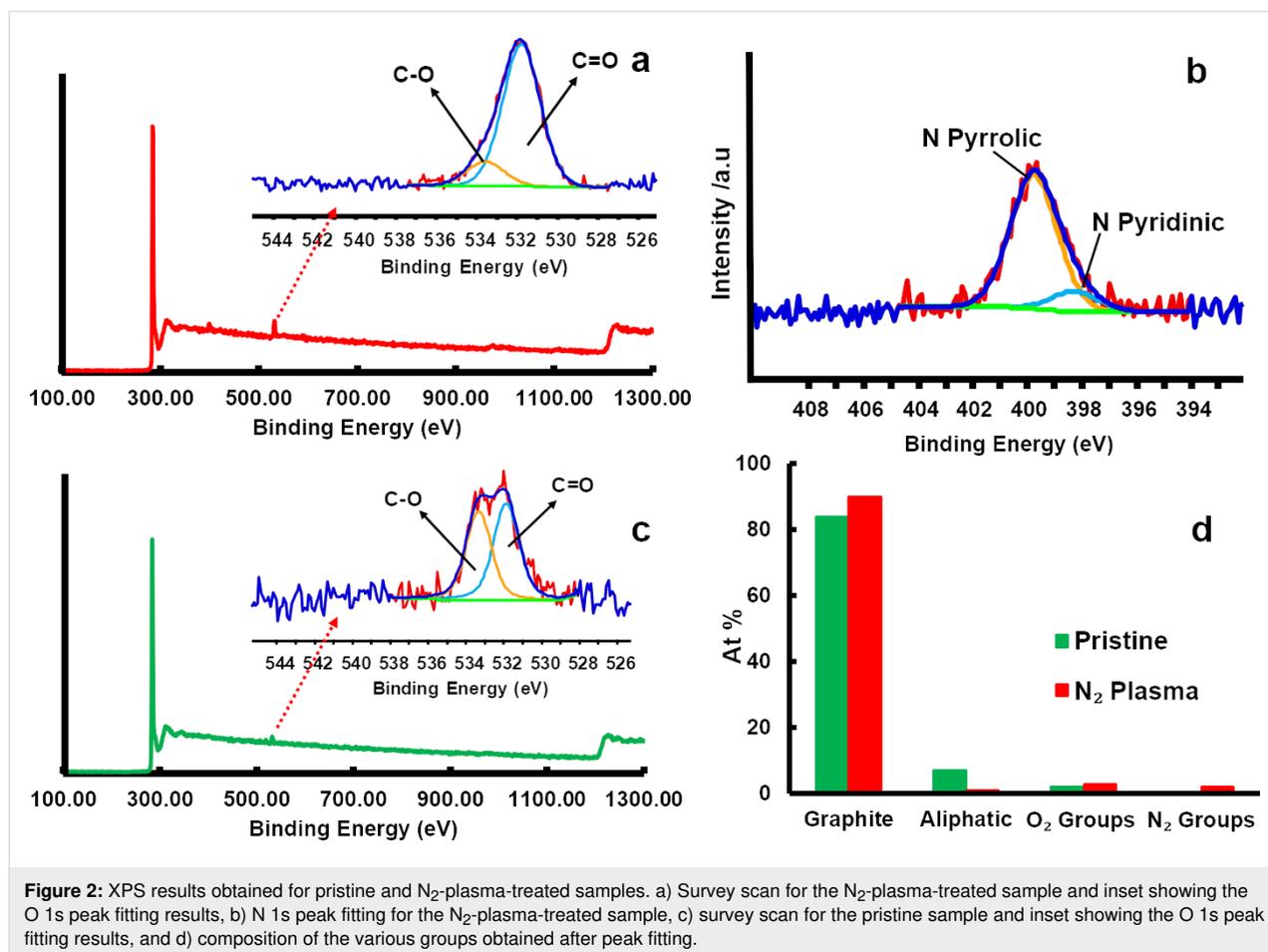

Figure 1: Raman spectra obtained for pristine as well as N_2-plasma-treated sample.

Figure 2: XPS results obtained for pristine and N_2-plasma-treated samples. a) Survey scan for the N_2-plasma-treated sample and inset showing the O 1s peak fitting results, b) N 1s peak fitting for the N_2-plasma-treated sample, c) survey scan for the pristine sample and inset showing the O 1s peak fitting results, and d) composition of the various groups obtained after peak fitting.

tion from the defects. The increase in the graphitic amount could be correlated to the corresponding decrease in the amount of aliphatic carbon. The source of this aliphatic carbon is either from the graphitization process of the PAN fibers or simply the atmospheric ageing of the felt. It is already known from the literature that graphitization or atmospheric ageing can leave some aliphatic or polyaromatic tar-like residues on the surface of the felt [6,23]. Thus, it can be concluded that apart from inducing N-doping, the N_2 plasma treatment also increased the apparent graphite amount on the surface by removing the aliphatic groups (C–H and C–C) from the surface of the fibers. The schematic representation of N-doping induced by the N_2 plasma treatment in a graphite lattice is shown in Figure 3.

From the scanning electron microscopy (SEM) analysis, it can be seen that the surface morphology of the fibers of both samples looked identical and thus any kind of surface roughening leading to an increase of the surface area can be ignored. This is further supported by our previous study were the BET measurements did not show any increase in surface area for oxygen-plasma-treated samples [7]. The SEM images of the pristine as well as the N_2-plasma-treated samples are shown in Figure 4.

In order to evaluate the electrochemical performance of the N_2-plasma-treated sample, cyclic voltammetry (CV) measurements were carried out. In contrast to the pristine sample, a prominent V^{3+}/V^{2+} redox peak is observed for the N_2-plasma-treated sample. The CV of the pristine sample is mainly characterized by a hydrogen evolution peak. The CV curves for both negative and positive redox reactions are shown in Figure 5.

Given that the pristine and N_2-plasma-treated samples have almost the same amount of oxygen functional groups, the enhanced activity shown by N_2-plasma-treated samples towards the V^{3+}/V^{2+} redox reaction should be attributed to the specific defects such as N-doping and the increase of the edge sites. More recently, Xu et al. showed, using first-principle calculations, that N-doping (especially the pyridinic and pyrrolic forms) enhances the water adsorption or hydrophilicity of the graphite electrode [24]. Thus, it may be concluded that the pyridinic and pyrrolic nitrogen formed during the N_2-plasma process enhanced the wettability of the felt, which in turn facilitates the adsorption of the V^{2+}/V^{3+} ions. Apart from defects in the form of N-doping, a higher amount of edge sites formed
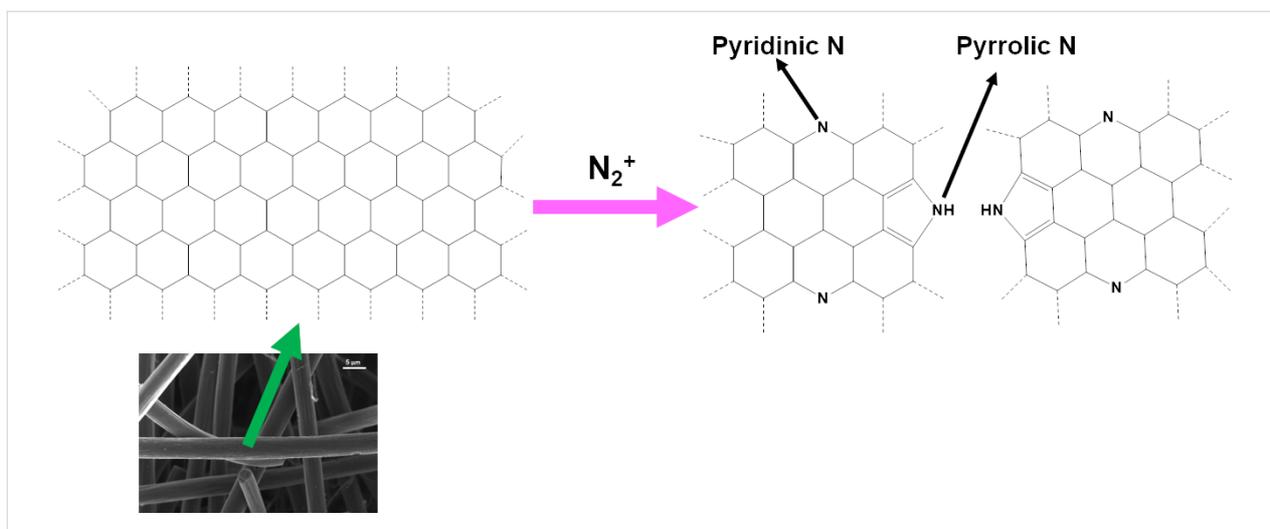
Figure 3: Schematic representation of N-doping induced by N_2 plasma treatment in a graphite lattice.
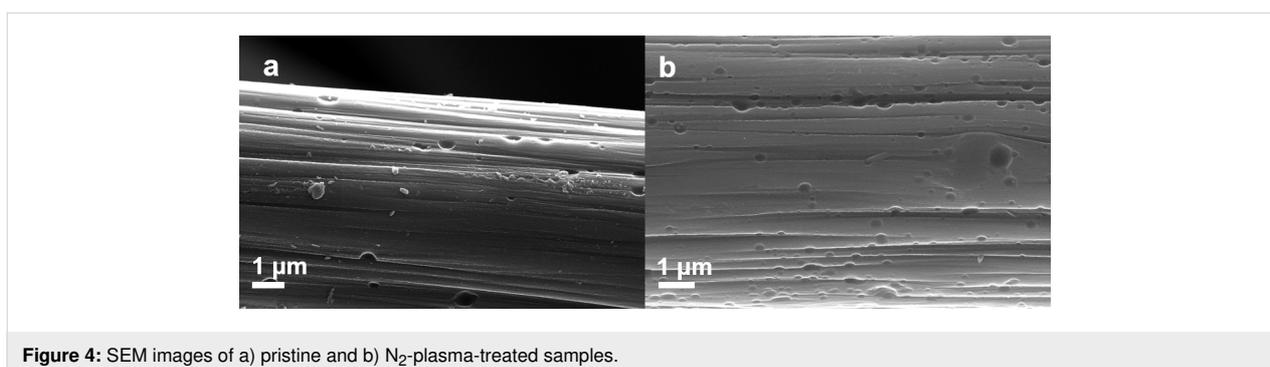

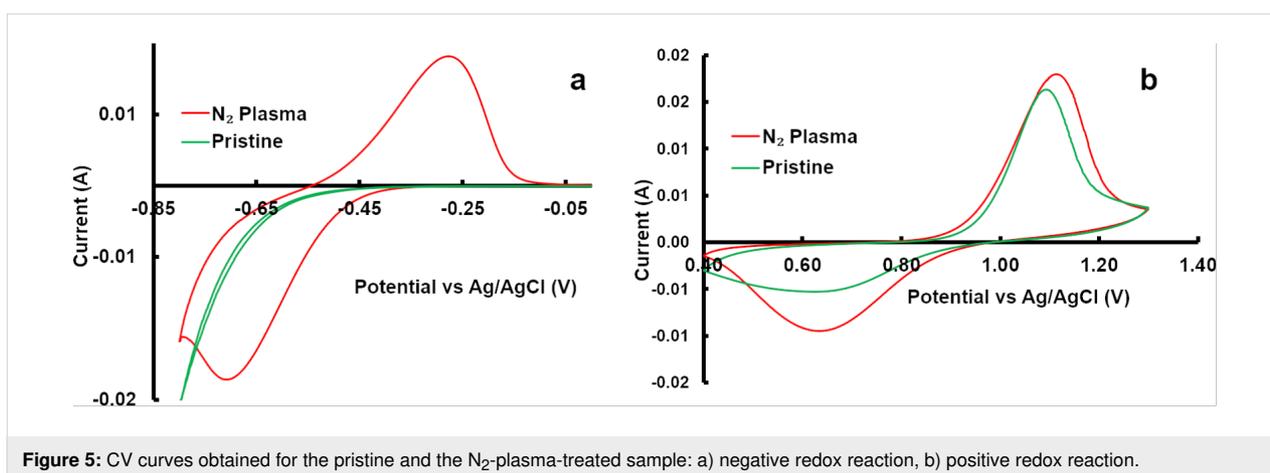**Figure 4:** SEM images of a) pristine and b) N_2-plasma-treated samples.

Figure 5: CV curves obtained for the pristine and the N_2-plasma-treated sample: a) negative redox reaction, b) positive redox reaction.

during the N_2-plasma process also influences the V^{3+}/V^{2+} redox reaction. This is because the half-cell reaction is known to depend greatly on the carbon edge sites [25]. Another reason for the enhanced activity of the N_2-plasma-treated samples towards the V^{3+}/V^{2+} reaction is that the aliphatic carbonaceous materials on th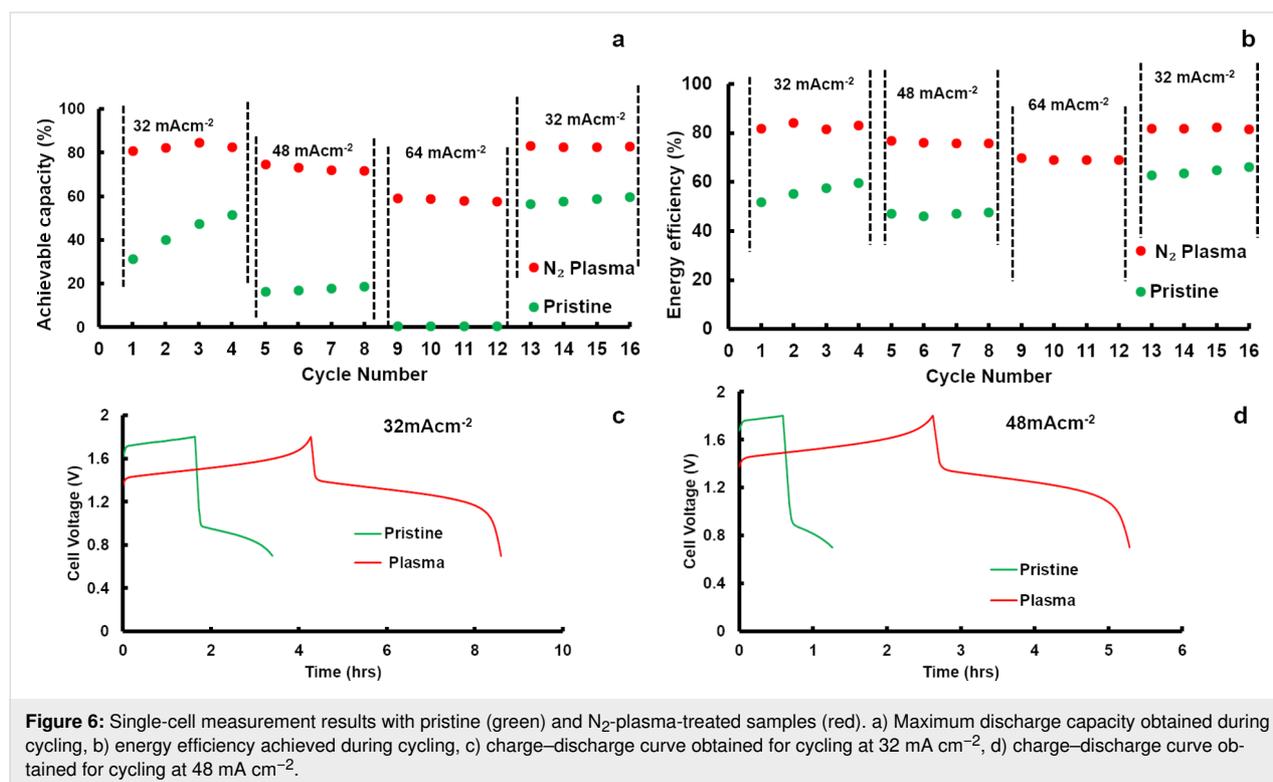e surface of the felts are removed during the N_2-plasma process. As a result of this process, more electrochemically active sites (edge sites) are available for the V^{3+}/V^{2+} redox reaction. As far as the V^{5+}/V^{4+} redox reaction (i.e., the positive redox reaction) is concerned, both pristine, as well as N_2-plasma-treated carbon felts showed electrochemical activity. Compared to pristine carbon felt the N_2-plasma-treated sample

showed an earlier onset potential for the V^{5+}/V^{4+} redox reaction. Thermodynamically, the V^{4+} to V^{5+} redox reaction takes place at 1.0 V vs a normal hydrogen electrode (NHE). Taking into account that carbon oxidation is feasible at potentials as low as 207 mV vs NHE [26], the higher potential of positive electrode of the VRFB can accelerate the carbon oxidation. During the carbon oxidation process, oxygen functional groups can be formed as an intermediate on the carbon electrode [27,28]. Therefore, oxygen functional groups can be formed on the surface of the felt, and especially on the positive electrode as it experiences a relatively higher potential. In fact, Derr et al. have observed an increase in the amount of functional groups on the surface of both negative and positive carbon felt electrodes after prolonged cycling [9]. Given that a higher potential is favorable for carbon oxidation, it can be concluded that the presence of functional groups on the carbon felt is not a prerequisite for the onset of the V^{5+}/V^{4+} redox reaction. CV studies were further supported by full cell studies, where the electrochemical performance of the N_2-plasma-treated sample was superior to the pristine sample. The cell with the N_2-plasma-treated sample showed a higher energy efficiency and delivered higher capacities at all investigated current densities. The single-cell measurement results are shown in Figure 6. With the pristine sample at higher current densities ($\geq$64 mA cm^{-2}), the cell ran into HER. Since the negative electrode reaction is the performance-limiting reaction, the superior performance observed for the single-cell measurement could be attributed to the

enhancement in the V^{2+}/V^{3+} redox reaction. However, it could also be seen that the performance of the pristine and the N_2-plasma-treated sample improves with further cycling, and during the final cycle (13–16) the cells delivered higher capacities compared to the initial cycles (1–4).

This increase in performance can be attributed to oxygen functional groups (both hydroxyl and carboxyl) formed on the surface of the felt due to the chemical and the electrochemical ageing process as elucidated by Derr et al. [9]. Nevertheless, a capacity fade was observed on the N_2-plasma-treated sample after long-term cycling at a current density of 80 mA cm^{-2} (see Figure 7). Capacity fade can be partially attributed to the HER taking place at the negative electrode due to the very low amount of oxygen functional groups. Moreover, the Nafion 117 membrane used for higher current density cycling leads to an electrolyte imbalance. A detailed investigation is still required to understand the overall mechanism of the capacity fade.

In a previous study [7], a similar extent of capacity fade was observed for heat-treated GFD (graphite-based) carbon felt samples with a higher amount of oxygen functional groups and a larger surface area than in this study. Nevertheless, the energy efficiency of the cell with the N_2-plasma-treated electrode is higher than that with the heat-treated electrode. Therefore, for achieving the optimum VRFB performance, the electrodes, especially the anode, must be tuned for defects such as N-sub-
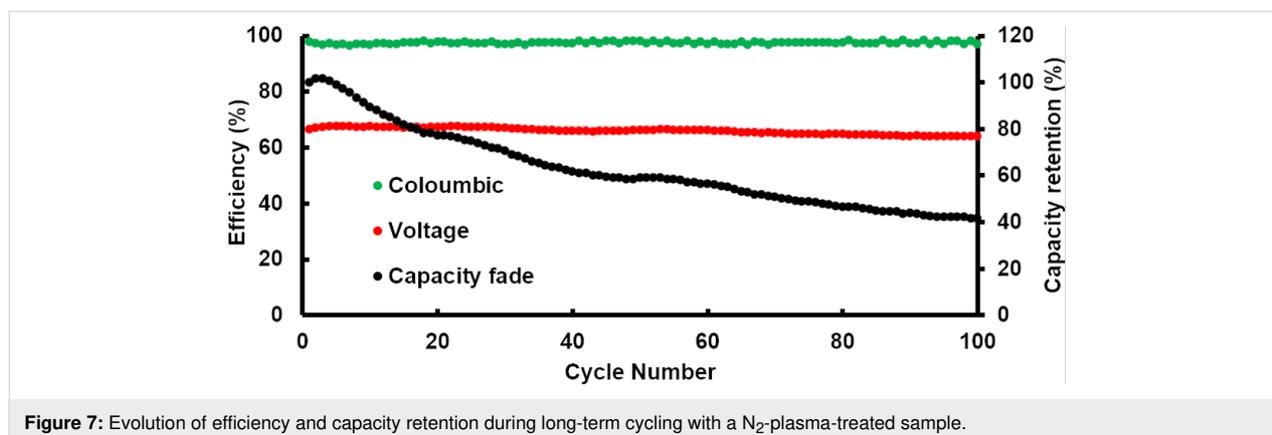

Figure 6: Single-cell measurement results with pristine (green) and N_2-plasma-treated samples (red). a) Maximum discharge capacity obtained during cycling, b) energy efficiency achieved during cycling, c) charge–discharge curve obtained for cycling at 32 mA cm^{-2}, d) charge–discharge curve obtained for cycling at 48 mA cm^{-2}.

Figure 7: Evolution of efficiency and capacity retention during long-term cycling with a N_2-plasma-treated sample.

stitution as well as oxygen functionality (specifically –O–C=O groups). The present study predicts that the combination of various plasma techniques (O_2/N_2) and thermal activation could produce an ideal electrode for the anode in VRFB.

Conclusion

When PAN-based GFD-type felts are subjected to N_2 plasma treatment, defects are formed on the carbon felt. In addition to the increase in the amount of reactive edge sites, also heteroatom defects involving N-doping are created by the N_2 plasma treatment. The surface of the plasma-treated samples was characterized by the presence of pyrrolic and pyridinic nitrogen. The N_2-plasma-treated felt showed enhanced electrochemical performance compared to the pristine felt. Since both the pristine as well as the N_2-plasma-treated sample had almost the same amount of oxygen functional groups, the superior performance observed for the former one is attributed to the additional defects formed during the plasma treatment. Nevertheless, the cell operated with the N_2-plasma-treated sample suffered from capacity fade, which can most likely be attributed to hydrogen evolution at the negative electrode. Therefore, it may be concluded that for the optimum performance of the VRFB, a balance should be found between the amount of various defects such as heteroatom doping, edge sites and functional groups.

Experimental
Plasma treatment process

The plasma treatment was carried out on a pristine GFD-type carbon felt, obtained from SGL Carbon (SIGRACELL GFD3 EA), having a thickness of 3 mm, in a radiofrequency (rf) 13.56 MHz plasma setup (Femto, Diener electronic GmbH, Germany) [28]. The power rating of the rf generator is 300 W (max. rf power limited to 200 W). 5 × 5 cm felts were loaded into the plasma chamber which was subsequently evacuated to a pressure below 0.2 mbar before the chamber was filled with about 0.8 mbar of nitrogen. All plasma treatments were carried out for 40 min at 20% of the maximum power. In the present

work a capacitively coupled parallel plate rf plasma was used. The separation between the plate was 10 cm and the samples were always placed on the bottom plate without any further connections.

Raman spectroscopy

Raman measurements were carried out using a HORIBA (model: LabRAM HR Evolution) Raman spectrometer and microscope. An Oxxius 532 nm laser (100 mW) and a 50× optical lens were used to obtain the spectra. The spectra were recorded between 500 cm^{-1} to 3000 cm^{-1}. The spectra were recorded with an acquisition time of 3 s. To prevent sample damage, the laser power was reduced to 10%.

X-ray photoelectron spectroscopy (XPS)

XPS measurements were performed using a K-Alpha XPS instrument (Thermo Fisher Scientific, East Grinstead, UK). The data acquisition and processing using the Thermo Advantage software is described elsewhere [29]. All samples were analyzed using a focused (30–400 µm spot size), monochromatic Al Kα X-ray source. The Kα charge compensation system was employed during the experiment, using electrons of 8 eV energy and low-energy argon ions to prevent any localized charge build-up. The spectra were fitted with one or more Voigt profiles (binding energy (BE) uncertainty: ±0.2 eV). The analyzer transmission function, Scofield sensitivity factors [29], and effective attenuation lengths (EALs) for photoelectrons were applied for quantification. The EALs were calculated using the standard TPP-2M formalism [30]. All spectra were referenced to the C 1s peak of hydrocarbon at 285.0 eV binding energy, controlled by means of the well-known photoelectron peaks of metallic Cu, Ag, and Au.

Scanning electron microscopy (SEM)

The carbon surface fiber morphology was investigated in a Zeiss Supra 55 SEM with primary electron energies of 5 keV and 15 keV and an in-lens detector.

Electrochemical measurements

In this work, commercial carbon felts obtained from SGL Carbon in pristine form and after N_2 plasma treatment were used as electrode materials. Cyclic voltammetry (CV) was performed in a three-electrode setup using a Reference 3000 instrument from Gamry with a Ag/AgCl reference electrode and a platinum mesh as a counter electrode. A modified configuration developed by Fink et al. was used as the setup for the working electrode (WE) [31]. The configuration was modified so that punched-out disks (Ø = 6 mm) of the felts attached to a glassy carbon rod were used as the WE. To achieve a better electrical contact, the punched-out felt was pierced through the middle by 5 cm long glassy carbon rod with a diameter of 1 mm. The positive half-cell reaction was measured in 0.1 molar vanadyl sulphate (Alfa Aeser) dissolved in 2 molar sulfuric acid (Sigma Aldrich). In order to obtain the V^{3+} electrolyte for the negative half-cell reaction, both tanks were filled with the same volume of the V^{4+} electrolyte and then potentiostatically charged at 1.7 V in a 10 cm^{-2} flow cell. The reduction to V^{3+} was determined as complete when the charging current reached less than 10 mA cm^{-2}. All the cyclic voltammetry measurements were carried out at a scan rate of 5 mV s^{-1}.

Single-cell measurements were performed using a modified direct methanol fuel cell from ElectroChem, having a pin-type flow field with an active area of 25 cm^2. Additionally, a 2 mm Viton gasket was used as a spacer around the flow fields to achieve uniform compression. A commercial electrolyte from GFE GmbH Germany with 1.6 M vanadium salt (50/50 mol/mol V^{4+}/V^{3+}) and an anion exchange membrane, VX 20 from Fumatech was used for most of the single-cell experiments. Galvanostatic cycling was carried out using a single-cell test bench from Scribner (875 Redox Flow Cell Test System) at current densities of 32, 48, and 64 mA cm^{-2}. Both electrolyte tanks were filled with 100 mL of electrolyte and the negative tank was always kept under nitrogen gas flow. Cut-off voltages of 1.8 V and 0.7 V were used for the charging and discharging steps, respectively. Between the charging and discharging, the cell was kept at an open-circuit voltage condition for 5 min. Long-term cycling measurements were carried out at a current density of 80 mA cm^{-2} with fresh electrolyte and fresh electrode and activated Nafion 117 membrane. In all the experiments, the electrolyte flow rate was kept at 100 mL min^{-1}. The temperature of the cell and electrolyte was maintained at 22 °C throughout the electrochemical investigations.

Acknowledgements

ORCID® iDs

Ditty Dixon - https://orcid.org/0000-0002-6529-6936
Hans-Michael Bruns - https://orcid.org/0000-0002-0462-3948
Helmut Ehrenberg - https://orcid.org/0000-0002-5134-7130

References

1. SkyllasKazacos, M.; Rychcik, M.; Robins, R. G.; Fane, A. G.; Green, M. A. *J. Electrochem. Soc.* **1986,** *133,* 1057–1058. doi:10.1149/1.2108706
2. Tang, A.; Bao, J.; Skyllas-Kazacos, M. *J. Power Sources* **2011,** *196,* 10737–10747. doi:10.1016/j.jpowsour.2011.09.003
3. Shah, A. A.; Al-Fetlawi, H.; Walsh, F. C. *Electrochim. Acta* **2010,** *55,* 1125–1139. doi:10.1016/j.electacta.2009.10.022
4. Whitehead, A. H.; Harrer, M. *J. Power Sources* **2013,** *230,* 271–276. doi:10.1016/j.jpowsour.2012.11.148
5. Wang, L.; Zhang, H.; Cao, G.; Zhang, W.; Zhao, H.; Yang, Y. *Electrochim. Acta* **2015,** *186,* 654–663. doi:10.1016/j.electacta.2015.11.007
6. Langner, J.; Bruns, M.; Dixon, D.; Nefedov, A.; Wöll, C.; Scheiba, F.; Ehrenberg, H.; Roth, C.; Melke, J. *J. Power Sources* **2016,** *321,* 210–218. doi:10.1016/j.jpowsour.2016.04.128
7. Dixon, D.; Babu, D. J.; Langner, J.; Bruns, M.; Pfaffmann, L.; Bhaskar, A.; Schneider, J. J.; Scheiba, F.; Ehrenberg, H. *J. Power Sources* **2016,** *332,* 240–248. doi:10.1016/j.jpowsour.2016.09.070
8. Agar, E.; Dennison, C. R.; Knehr, K. W.; Kumbur, E. C. *J. Power Sources* **2013,** *225,* 89–94. doi:10.1016/j.jpowsour.2012.10.016
9. Derr, I.; Bruns, M.; Langner, J.; Fetyan, A.; Melke, J.; Roth, C. *J. Power Sources* **2016,** *325,* 351–359. doi:10.1016/j.jpowsour.2016.06.040
10. Derr, I.; Przyrembel, D.; Schweer, J.; Fetyan, A.; Langner, J.; Melke, J.; Weinelt, M.; Roth, C. *Electrochim. Acta* **2017,** *246,* 783–793. doi:10.1016/j.electacta.2017.06.050
11. Estevez, L.; Reed, D.; Nie, Z.; Schwarz, A. M.; Nandasiri, M. I.; Kizewski, J. P.; Wang, W.; Thomsen, E.; Liu, J.; Zhang, J.-G.; Sprenkle, V.; Li, B. *ChemSusChem* **2016,** *9,* 1455–1461. doi:10.1002/cssc.201600198
12. Schweiss, R.; Pritzl, A.; Meiser, C. *J. Electrochem. Soc.* **2016,** *163,* A2089–A2094. doi:10.1149/2.1281609jes
13. Boukhvalov, D. W.; Katsnelson, M. I. *Nano Lett.* **2008,** *8,* 4373–4379. doi:10.1021/nl802234n
14. Banhart, F.; Kotakoski, J.; Krasheninnikov, A. V. *ACS Nano* **2011,** *5,* 26–41. doi:10.1021/nn102598m
15. Wang, S.; Zhao, X.; Cochell, T.; Manthiram, A. *J. Phys. Chem. Lett.* **2012,** *3,* 2164–2167. doi:10.1021/jz3008744
16. He, Z.; Shi, L.; Shen, J.; He, Z.; Liu, S. *Int. J. Energy Res.* **2015,** *39,* 709–716. doi:10.1002/er.3291
17. Ferrari, A. C. *Solid State Commun.* **2007,** *143,* 47–57. doi:10.1016/j.ssc.2007.03.052
18. Pimenta, M. A.; Dresselhaus, G.; Dresselhaus, M. S.; Cançado, L. G.; Jorio, A.; Saito, R. *Phys. Chem. Chem. Phys.* **2007,** *9,* 1276–1290. doi:10.1039/b613962k

19. Ouyang, B.; Zhang, Y.; Wang, Y.; Zhang, Z.; Fan, H. J.; Rawat, R. S. *J. Mater. Chem. A* **2016,** *4,* 17801–17808. doi:10.1039/c6ta08155j

20. Babu, D. J.; Bruns, M.; Schneider, R.; Gerthsen, D.; Schneider, J. J. *J. Phys. Chem. C* **2017,** *121,* 616–626. doi:10.1021/acs.jpcc.6b11686

21. Kiuchi, H.; Shibuya, R.; Kondo, T.; Nakamura, J.; Niwa, H.; Miyawaki, J.; Kawai, M.; Oshima, M.; Harada, Y. *Nanoscale Res. Lett.* **2016,** *11,* 127. doi:10.1186/s11671-016-1344-6

22. Nevidomskyy, A. H.; Csányi, G.; Payne, M. C. *Phys. Rev. Lett.* **2003,** *91,* 105502. doi:10.1103/physrevlett.91.105502

23. Rabbow, T. J.; Trampert, M.; Pokorny, P.; Binder, P.; Whitehead, A. H. *Electrochim. Acta* **2015,** *173,* 24–30. doi:10.1016/j.electacta.2015.05.058

24. Xu, A.; Shi, L.; Zeng, L.; Zhao, T. S. *Electrochim. Acta* **2019,** *300,* 389–395. doi:10.1016/j.electacta.2019.01.109

25. Chen, P.; Fryling, M. A.; McCreery, R. L. *Anal. Chem. (Washington, DC, U. S.)* **1995,** *67,* 3115–3122. doi:10.1021/ac00114a004

26. Pourbaix, M. *Electrochemical Equilibria in Aqueous Solutions;* Pergamon Press: Oxford, United Kingdom, 1966.

27. Nose, M.; Kinumoto, T.; Choo, H.-S.; Miyazaki, K.; Abe, T.; Ogumi, Z. *Fuel Cells* **2009,** *9,* 284–290. doi:10.1002/fuce.200800077

28. Babu, D. J.; Yadav, S.; Heinlein, T.; Cherkashinin, G.; Schneider, J. J. *J. Phys. Chem. C* **2014,** *118,* 12028–12034. doi:10.1021/jp5027515

29. Parry, K. L.; Shard, A. G.; Short, R. D.; White, R. G.; Whittle, J. D.; Wright, A. *Surf. Interface Anal.* **2006,** *38,* 1497–1504. doi:10.1002/sia.2400

30. Tanuma, S.; Powell, C. J.; Penn, D. R. *Surf. Interface Anal.* **2011,** *43,* 689–713. doi:10.1002/sia.3522

31. Fink, H.; Friedl, J.; Stimming, U. *J. Phys. Chem. C* **2016,** *120,* 15893–15901. doi:10.1021/acs.jpcc.5b12098

Synthesis of amorphous and graphitized porous nitrogen-doped carbon spheres as oxygen reduction reaction catalysts

Maximilian Wassner[‡1], Markus Eckardt[‡2], Andreas Reyer[1], Thomas Diemant[2], Michael S. Elsaesser[1], R. Jürgen Behm[*2] and Nicola Hüsing[*1]

Abstract

Amorphous and graphitized nitrogen-doped (N-doped) carbon spheres are investigated as structurally well-defined model systems to gain a deeper understanding of the relationship between synthesis, structure, and their activity in the oxygen reduction reaction (ORR). N-doped carbon spheres were synthesized by hydrothermal treatment of a glucose solution yielding carbon spheres with sizes of 330 ± 50 nm, followed by nitrogen doping via heat treatment in ammonia atmosphere. The influence of a) varying the nitrogen doping temperature (550–1000 °C) and b) of a catalytic graphitization prior to nitrogen doping on the carbon sphere morphology, structure, elemental composition, N bonding configuration as well as porosity is investigated in detail. For the N-doped carbon spheres, the maximum nitrogen content was found at a doping temperature of 700 °C, with a decrease of the N content for higher temperatures. The overall nitrogen content of the graphitized N-doped carbon spheres is lower than that of the amorphous carbon spheres, however, also the microporosity decreases strongly with graphitization. Comparison with the electrocatalytic behavior in the ORR shows that in addition to the N-doping, the microporosity of the materials is critical for an efficient ORR.

Introduction

Fuel cells and metal–air batteries are important renewable energy technologies. Both rely on the oxygen reduction reaction (ORR). The best established ORR catalysts are so far based on Pt nanoparticles or Pt alloys. However, Pt is expensive and its stability under fuel-cell working conditions is limited. Therefore, alternative catalysts based on noble-metal-free, less expen- sive and stable materials are highly needed. Metal-free carbon materials, single- or multi-doped with N, B, P, S, halogens, Si or Se, have turned out to be promising ORR catalysts [1-6]. N-doped carbon materials show promising ORR activities along with high electric conductivity, in addition they can result in further advantages such as an improved tolerance towards

impurities compared to Pt-based catalysts [1]. A wide variety of N-doped carbon materials is known from the literature, reaching from N-doped graphene and graphite, N-doped carbon nanotubes, carbon cages, carbon cups and carbon fibers [7-10], N-doped 3D ordered (meso)porous carbon materials [11], N-doped carbon composites (e.g., carbon nanotubes/graphene) [12], and N-doped carbon spheres [13,14] to graphitic-C_3N_4 carbon nitride composites [15].

In the present work we report results of a systematic study on the synthesis and characterization of N-doped carbon spheres as possible ORR catalysts. Before presenting our results, we will briefly summarize relevant previous findings. There are two main strategies for the synthesis of N-doped carbons: first, in situ doping with nitrogen, employing C- and N-containing precursors directly in the synthesis of the material, which leads to the direct formation of C–N bonds; and second, post-synthesis N-doping via substitutional incorporation of N into the carbon lattice of as-synthesized carbon materials with a reactive nitrogen-containing agent. Established in situ syntheses are chemical vapor deposition (CVD) and arc discharge methods for N-doped graphene, graphite, and carbon nanotubes [9]. Most commonly, the post-synthetic approach is carried out by thermal treatment of carbon in ammonia atmosphere, typically leading to surface N-doping. A variety of N bonding configurations can be formed within the carbon lattice [8], among them the pyridinic and quarternary (also: graphitic) nitrogen bonding configurations were assumed as origin of the ORR activity of these N-doped carbon materials [16]. The exact nature of the active site is controversially discussed; some researchers ascribe the ORR activity to graphitic nitrogen sites [17-21], while others propose pyridinic nitrogen as more important [16,22-26]. Previous results of our groups indicate that the ORR activity of nitrided carbon is dominated by the carbon edge atoms of micropores in graphenic structures and the electronic structure of those atoms which is additionally modified by low-level N-doping [26,27]. This may include both graphitic and pyridinic N-doping. Kim et al. [28] suggested that both bonding situations interconvert during the ORR and that both might be equally important. A directed tailoring of the active sites in the carbon material is a prerequisite for a knowledge-based optimization of the ORR activity. As reported by Lai et al. [18], this can be achieved to a certain extent by varying the reaction temperature and the utilization of different N(C) precursors. Annealing graphene oxide (GO) in an ammonia atmosphere at 550 °C led to pyridinic N-doped graphene, while at a temperature of 850 °C graphitic nitrogen coexisted with pyridinic nitrogen, and for higher temperatures the amount of graphitic N increased. Annealing GO at 850 °C in the presence of polyaniline or polypyrrole instead of ammonia resulted in pyridinic or pyrrolic N moieties, respectively [18].

Beside the N bonding configuration, the ORR activity is affected by the N content, the surface area (porosity) and possibly the degree of graphitization [27]. The nitrogen content defines, among others, the density of N sites, which influence the ORR activity even if they are not the active ORR sites themselves [27]. The N content depends on the amount of nitrogen in the precursor, the N(C) precursor concentration, the reaction temperature as well as the duration of the doping treatment. During ammonia nitriding of carbon a significant increase of the N content occurs at reaction temperatures higher than 550 °C (formation of nitriding-active species based on ammonia decomposition), and at ca. 650 °C the maximum N content is reached. For higher temperatures, the N content decreases again, here the formation of C–C bonds is favored over the formation of C–N bonds. At a given reaction temperature, the N content increases with higher ammonia concentrations up to a certain maximum, however, only a limited amount of N can be incorporated. Exceeding this point leads to the formation of defects causing decomposition of the carbon framework and a decrease of the N content [29,30]. The availability of active sites (for a certain electrochemical reaction) correlates with the electrochemically active surface area for this reaction. For most conventional porous carbon materials micropores contribute significantly to the surface area, but their small pore size is considered to only allow a limited mass transport, which might result in a low accessibility of the active sites therein for electrochemical processes. Investigations of N-doped 3D ordered porous carbon materials showed, e.g., that a high content of meso- and macropores is beneficial for the ORR activity [11]. Finally, a higher degree of graphitization generally leads to an improved electrical conductivity, which should improve the overall ORR activity. On the other hand, it may alter also the properties of the active sites, which may be either beneficial or disadvantageous. The degree of graphitization can be increased, e.g., by higher reaction temperatures or catalytic graphitization [31-33].

Previously, we had reported on core–shell titanium (oxy)nitride and tantalum (oxy)nitride@N-doped carbon composite spheres, which were based on a similar conducting carbon core as investigated in the present study, and their performance as ORR catalysts [34,35]. For these systems, which turned out to be promising ORR catalysts, we found that nitriding the metal-oxide shell concomitantly results in drastic structural changes and nitriding of the carbon core. In this study we aim at gaining deeper insights in the role of the N-doped spherical carbon core in the ORR. We are well aware of the fact that many groups reported the synthesis of N-doped carbon spheres and some even their application in electrocatalysis, however, a fundamental and detailed discussion of the changes during nitridation regarding chemistry, structure and morphology combined with a correla-

tion of the ORR activity for these materials has been, to our knowledge, not provided. In this study we also added a discussion on the influence of a higher degree of graphitization on the ORR by comparison of as-synthesized and pre-graphitized N-doped carbon spheres. We believe that the use of structurally and chemically well-defined model systems, which necessarily might not be as sophisticated as other reported materials, is the proper way to gain a fundamental understanding of correlations between structural properties and electrochemical performance.

In the following we will first give a detailed structural and chemical analysis of the resulting materials (section 1 in "Results and Discussion"), followed by a discussion of their performance as ORR catalyst in electrocatalytic measurements under controlled electrolyte transport, employing a rotating ring disk electrode (RRDE) setup (section 2 in "Results and Discussion"). We will compare the ORR performance with those of the previously reported TiON@NCS and TaON@NCS composite materials. A more detailed account of the electrochemical properties and of the ORR activity and mechanism is given elsewhere [27].

Results and Discussion
1 Synthesis and structural/chemical analysis of (graphitized) N-doped carbon spheres

Carbon spheres were synthesized by hydrothermal treatment of a glucose solution (Figure 1), following a previously reported approach [36]. They were either directly nitrided (nitrided carbon spheres, NCSs) or graphitized and then nitrided (graphitized nitrided carbon spheres, g-NCSs). Heat treatments, which are necessary for the nitridation but also for the graphitization, were performed between 550 and 1000 °C (with steps of 150 °C).

The as-synthesized carbon particles show a well-defined spherical shape with diameters of 330 ± 50 nm and a smooth surface (see also the scanning electron microscopy (SEM) image in Figure 2a). Fe_2O_3 particles, as graphitization catalyst, are loaded successfully on pre-carbonized carbon spheres; yet there are domains of higher or lower loadings. After nitriding with ammonia, g-NCS-550, g-NCS-700 and all samples of the NCS series still show a spherical shape with a smooth surface (Figure 2b and Figure 2c show, respectively, NCS-550 and NCS-1000 as examples). No remaining catalyst particles are observed for the graphitized samples via energy dispersive X-ray spectroscopy (EDX) and X-ray photoelectron spectroscopy (XPS). However, we cannot fully exclude small amounts of residual iron in the graphitized catalysts below the detection limit of XPS (about 0.2 atom %) and EDX (about 0.1 wt %).

TEM images (Figure 3a–d) reveal no highly ordered domains (e.g., graphene layers) of the said N-doped carbon spheres, which is in good agreement with the results of the X-ray diffraction measurements (XRD, Figure 4), confirming an amorphous carbon structure for all particles mentioned so far. Upon catalytic graphitization of g-NCS-850 and g-NCS-1000, the smooth surface becomes texturized or perforated as seen in the SEM images (cf. Figure 2d,e), and the spheres partially erode. This can be explained as a result of catalytic graphitization, for which the following mechanism was proposed by Nettelroth et al. [32]: The catalyst particles carve themselves into the underlying carbon atom structure by a redox reaction, leading to a partial gasification and rearrangement of the carbon atoms. Due to the inhomogeneous distribution of the Fe_2O_3 catalyst particles (Figure 2a), g-NCS-850 and g-NCS-1000 (Figure 3g,h) show a varying degree of perforation and erosion. Within these spheres, fibrous structures probably consisting of
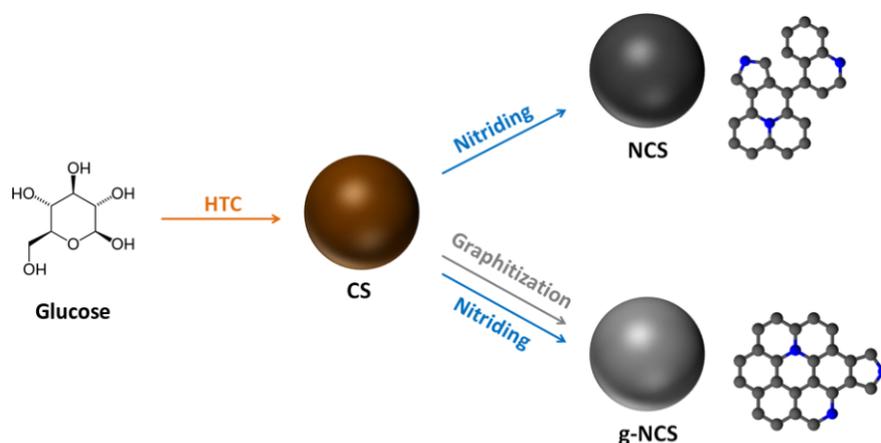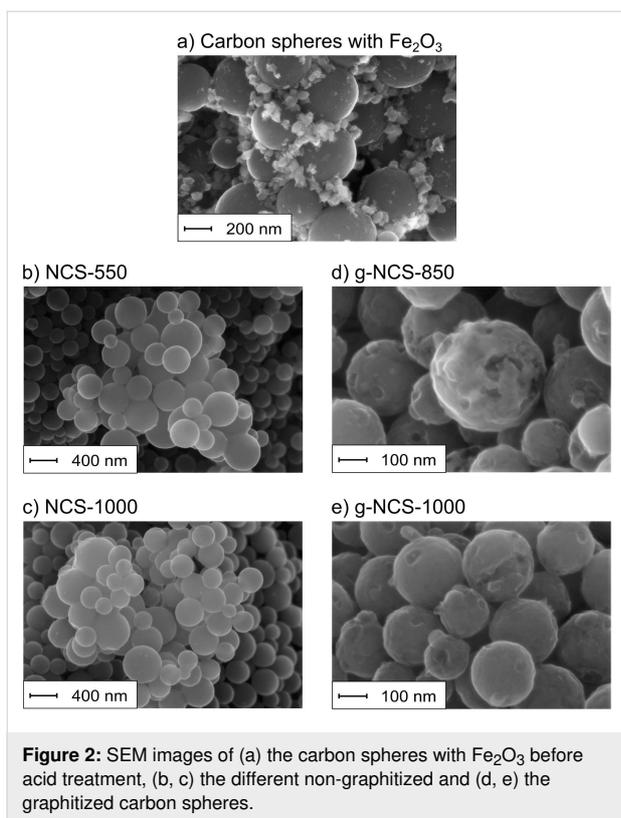

Figure 1: Schematic synthesis overview of amorphous N-doped carbon spheres (NCSs) and graphitized N-doped carbon spheres (g-NCSs) by hydrothermal carbonization (HTC) of a glucose solution yielding carbon spheres that are either directly nitrided with ammonia or graphitized and then nitrided (nitrogen atoms in the graphitic lattice are given in blue).

Figure 2: SEM images of (a) the carbon spheres with Fe_2O_3 before acid treatment, (b, c) the different non-graphitized and (d, e) the graphitized carbon spheres.

Figure 3: TEM images of (a–d) the NCS catalysts and (e–h) the g-NCS catalysts. The TEM images in (a–d) are reprinted with permission from [27], copyright 2019 Elsevier.

graphitic carbon are formed with a thickness of 7–9 nm, as detected by transmission electron microscopy (TEM). The observed thickness matches very well with the average stacking thickness of the graphite layers L_c determined by X-ray diffraction measurements. Similar observation was made by Liu et al. for carbon spheres that were synthesized by hydrothermal treatment of a sucrose solution and subsequently graphitized in the presence of nickel-oxide particles. High-resolution TEM (HRTEM) images of the resulting particles showed that the graphite layers are arranged along the longitudinal axis of the fibers [37]. After the acidic washing process, neither XPS nor EDX showed, for g-NCS-850 and g-NCS-1000, Fe or Fe_3C particles within the spheres, which are commonly found for the Fe-based catalytic graphitization of carbon [38]. Hence, under these conditions acid leaching is sufficient to fully remove the metal catalyst. For both sample series, NCS and g-NCS, the particle diameter decreases compared to the initial diameter of the as-synthesized carbon spheres (NCS-550 = 260 ± 35 nm, NCS-1000 = 240 ± 30 nm; g-NCS-550 = 255 ± 35 nm, g-NCS-1000 = 220 ± 30 nm). This is due to the carbonization and decomposition processes taking place at higher reaction temperatures, together with H_2 etching as side reaction of the ammonia nitriding [34].

The elemental bulk composition of the NCSs and g-NCSs, determined by CHN analyses (supported by EDX measurements,
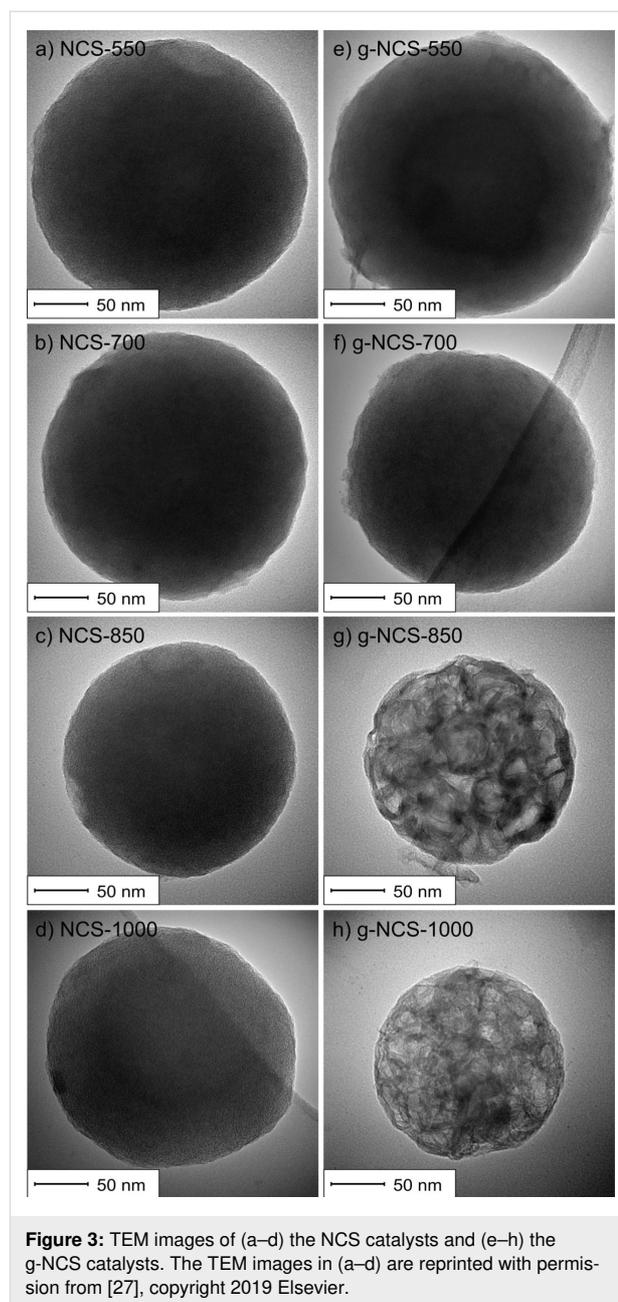
e.g., absence of Fe), as well as the elemental surface composition and N bonding configurations, determined by XPS measurements, are given in Table 1 and Table 2. As expected the samples are made up of a carbon matrix including O- and H-based functional groups [39]. Subsequent N-doping of the carbon lattice results in multiple nitrogen bonding configurations (Table 2). Possible Fe contaminations of the g-NCS samples originating from the Fe_2O_3 graphitization catalyst are below the detection limit of the EDX and XPS measurements. The carbonization process of the carbon spheres involves the decomposition of the functional groups to gases such as CO_2, H_2O and CH_4 [39]. Therefore, the carbon weight fraction of the
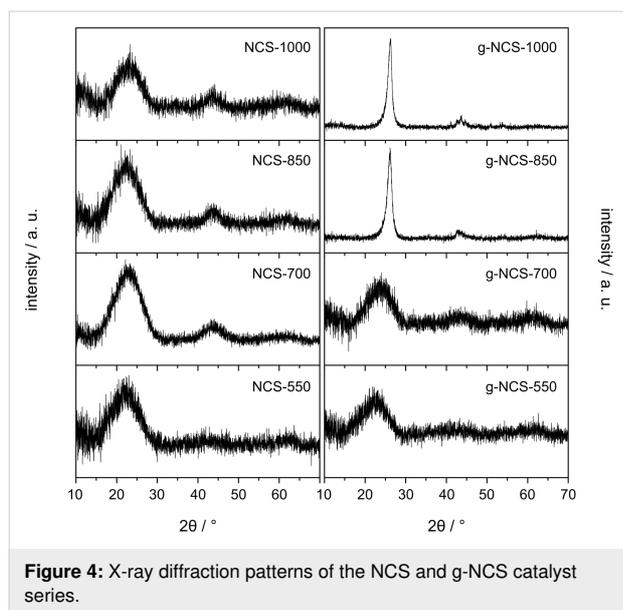
Figure 4: X-ray diffraction patterns of the NCS and g-NCS catalyst series.

elemental bulk composition increases constantly with higher reaction temperatures, whereas the hydrogen and oxygen contents decrease. The gasification process leads to a lower residual mass, and explains in part the shrinkage of the carbon spheres, as investigated in more depth in our former work [34]. NCS-550 and g-NCS-550 show a bulk N-content of 1.3 wt % and 1.8 wt %, respectively, and the maximum N content is reached for NCS-700 (4.3 wt %) and g-NCS-700 (3.5 wt %). With higher reaction temperatures, the N content of the NCS samples decreases to ca. 1.0 wt %, and even more for the g-NCS samples with a value of only 0.3 wt %. This development is typical for substitutional N-doping of carbon materials by a post-synthetic heat treatment in ammonia atmosphere (see the review by Daems and co-workers [7]). The direct comparison of the N content of NCS-850 and NCS-1000 with the g-NCS-850 and g-NCS-1000 spheres reveals that substitutional N-doping of the amorphous carbon matrix is easier than that of the graphitic one.

Table 1: Elemental bulk composition determined by CHN analyses (supported by SEM/EDX measurements).

sample	elemental bulk composition			
	C / wt %	H / wt %	N / wt %	O / wt %
NCS-550	88.3	2.1	1.3	8.3
NCS-700	89.8	1.0	4.3	4.9
NCS-850	95.1	0.7	1.1	3.1
NCS-1000	94.9	0.4	0.9	3.8
g-NCS-550	89.6	1.9	1.8	6.7
g-NCS-700	91.0	1.0	3.5	4.5
g-NCS-850	96.9	0.2	0.3	2.6
g-NCS-1000	97.0	0.2	0.3	2.5

The elemental surface composition measured by XPS is similar to the overall elemental composition (CHN analysis), which indicates a homogeneous N-doping of the carbon material. In agreement with the data from elemental analysis, XPS shows the largest amount of N for NCS-700 and g-NCS-700, followed by a strong decrease of the N surface content for (g-)NCS-850 and (g-)NCS-1000. The most plausible bonding configuration of N on the surface is shown in Figure 5. The XPS measurements detect pyridinic N at ca. 398.6 eV, pyrrolic N at ca. 400.1 eV and graphitic N at ca. 401.6 eV on the catalyst surface, whereas no oxidic N could be found at 403–404 eV [15,39,40].
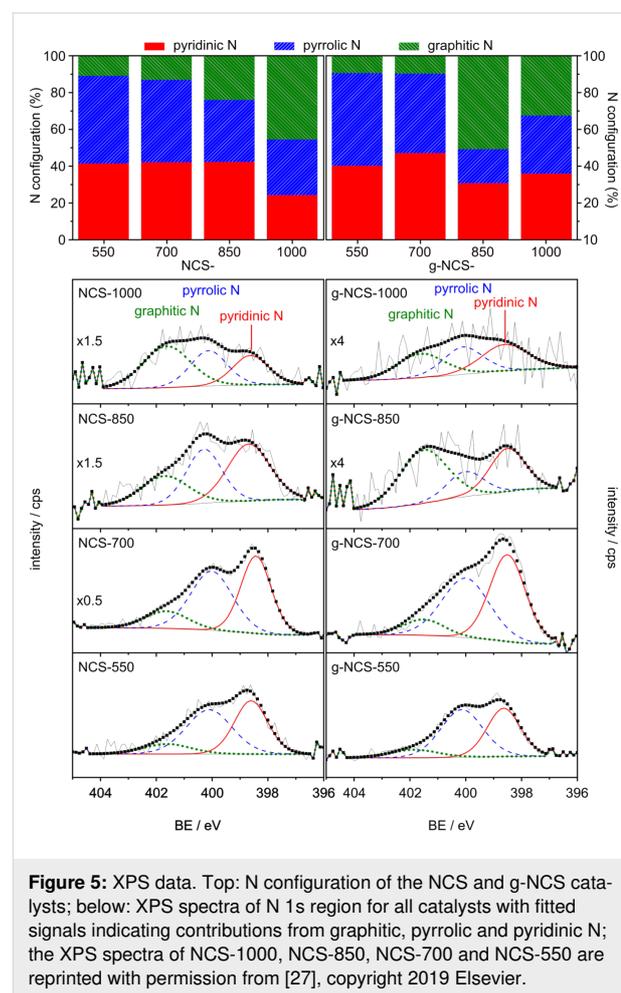

Figure 5: XPS data. Top: N configuration of the NCS and g-NCS catalysts; below: XPS spectra of N 1s region for all catalysts with fitted signals indicating contributions from graphitic, pyrrolic and pyridinic N; the XPS spectra of NCS-1000, NCS-850, NCS-700 and NCS-550 are reprinted with permission from [27], copyright 2019 Elsevier.

NCS spheres that were nitrided at 550 and 700 °C show high fractions of pyridinic and pyrrolic nitrogen atoms. These contents decrease at higher temperatures in favor of an increase of the graphitic N share, reaching around 50% for NCS-1000. A similar trend is found for the N-doped/nitrided graphitized carbon spheres, which show a higher content of graphitic N for the samples treated at 850 °C and 1000 °C, while mainly the amount of pyrrolic N decreases slightly. Here we want to

Table 2: Elemental surface composition and share of different N bonding configurations determined by XPS measurements.

sample	elemental surface composition			N bonding configuration		
	C / wt %	N / wt %	O / wt %	pyridinic N / wt %	pyrrolic N / wt %	graphitic N / wt %
NCS-550	90.27	0.99	8.74	0.41	0.47	0.11
NCS-700	90.25	2.90	6.85	1.22	1.29	0.38
NCS-850	91.66	0.87	7.47	0.37[a]	0.29[a]	0.21[a]
NCS-1000	92.09	0.59	7.32	0.14[a]	0.18[a]	0.27[a]
g-NCS-550	89.43	1.72	8.85	0.69	0.86	0.16
g-NCS-700	90.57	2.52	6.91	1.18	1.08	0.25
g-NCS-850	95.52	0.34	4.14	0.10[a]	0.06[a]	0.17[a]
g-NCS-1000	95.82	0.29	3.89	0.10[a]	0.09[a]	0.09[a]

[a]Quite large relative deviations are possible for the catalysts nitrided at 850 and 1000 °C due to the low N content yielding a noisy N 1s signal.

mention that the N 1s signal of the catalysts nitrided at high temperatures is rather noisy, which results in a larger error when evaluating the quantitative amounts of each N configuration. This does not change, however, the trends resulting from the XPS data discussed later.

Focusing on structural aspects, the NCS series, g-NCS-550 and g-NCS-700 samples exhibit XRD patterns characterized by very broad reflections at 2θ values of around 22.5° and 43°, which is typical for amorphous carbon (Figure 4). Obviously, the minimum temperature required for the catalytic graphitization has not been reached for g-NCS-550 and g-NCS-700. This is different for g-NCS-850 and g-NCS-1000, where successful catalytic graphitization is proven by reflections at 26.16° (interplanar distance: $d_{002} = 0.340$ nm) and 26.27° ($d_{002} = 0.339$ nm), respectively, corresponding to the (002) crystal planes of graphite. Applying the Scherrer equation gives an average stacking thickness of the graphite layers L_c of 7.6 and 8.6 nm, respectively, which matches very well to the thickness of the carbon fibers as detected in the TEM images. The degree of graphitization, g, is calculated using the interplanar distance d_{002}: $g = (0.344 \text{ nm} - d_{002})/(0.344 \text{ nm} - 0.3354 \text{ nm})$, with 0.344 nm for the interplanar distance in carbon with a turbostratic structure, and 0.3354 nm for the interplanar distance in a defect-free single crystal of graphite [41,42]. For g-NCS-850 and g-NCS-1000, g values of 0.43 and 0.59 were calculated, respectively. The reflections at 41.2° and 43.6° are associated to the (100) and (101) crystal planes of the graphite lattice.

All Raman spectra (Figure 6 and Table 3) of the N-doped carbon spheres show two bands at ca. 1350 cm^{-1} (D band) and ca. 1600 cm^{-1} (G band). The G band is due to the E_{2g} in-plane vibration mode of the graphite lattice and hence assigned to the sp^2-hybridized carbon atoms inside the graphite layers; the D band is associated to the A_{1g} in-plane breathing vibration mode occurring at the edges of sp^2-hybridized carbon domains, which appear for structural defects and disordered structures. A

relative degree of graphitization can be evaluated by the ratio between the band areas, A_D/A_G; the higher the ratio, the more disordered the carbon material [43-45]. We assume that with higher reaction temperatures the amorphous NCS samples become more ordered through rearrangement to turbostratic-type carbon, indicated by a declining A_D/A_G ratio (2.7 to 1.9) and a simultaneously decreasing full width at half maximum (FWHM) of the D band. As a result of the structural change from amorphous (disordered) to more graphitic carbon, the A_D/A_G ratio of g-NCS-850 (1.2) and g-NCS-1000 (1.0) as well as the FWHM of the D band drop significantly. In addition, the D* band (also named 2D or G′ band) at ca. 2700 cm^{-1} is observed as an overtone of the D band, which has the shape we observe for g-NCS-850 and g-NCS-1000, with a shoulder at around 2680 cm^{-1}, typically obtained for ordered and disordered graphite [46,47]. The assignment of the low-intensity
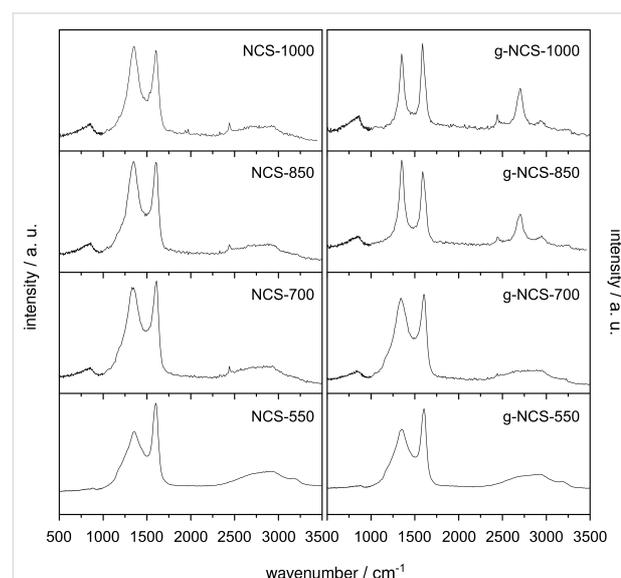

Figure 6: Raman spectra of the NCS and g-NCS catalysts (the *x*-axis represents the Raman shift relative to the excitation laser wavelength given in cm^{-1}).

Table 3: Position and ratio of the band areas A_D/A_G and full width at half maximum of the carbon D- and G-bands in the Raman spectra.

sample	position (D) / cm^{-1}	position (G) / cm^{-1}	A_D/A_G	FWHM (D) / cm^{-1}	FWHM (G) / cm^{-1}
NCS-550	1348	1598	2.67	303	78
NCS-700	1338	1602	2.75	267	92
NCS-850	1347	1601	2.54	235	90
NCS-1000	1349	1601	1.87	188	102
g-NCS-550	1345	1600	2.63	285	80
g-NCS-700	1339	1601	2.76	266	92
g-NCS-850	1345	1586	1.24	104	85
g-NCS-1000	1347	1581	1.04	89	71

bands at, e.g., ca. 860 cm^{-1} and ca. 2440 cm^{-1} is described in detail by Kawashima and Dresselhaus and co-workers [46,48]. Higher N contents result in more defects of the carbon lattice and lead to an increase of the A_D/A_G ratio. Accordingly, NCS-700 and g-NCS-700, which exhibit the highest N content, show the highest A_D/A_G ratios. For (amorphous) non-doped carbon the G band is located at ca. 1575 cm^{-1}. N-doping shifts the G band to higher wavenumbers [49]. This is seen, e.g., for the NCS samples as well for g-NCS-550 and g-NCS-700 with a position of the G band at ca. 1600 cm^{-1}. As the N content lowers for g-NCS-850 and g-NCS-1000 the G band shifts back to 1586 cm^{-1} and 1581 cm^{-1}, respectively.

The NCS samples are highly microporous, which is indicated by the measured type-I N$_2$ sorption isotherms (Figure 7), combined with a low external surface area compared to the specific surface area (Table 4). The micropore surface area increases with higher reaction temperatures from 485 to 742 m$^2 \cdot$g^{-1}, whereas the external surface area is relatively constant (34–42 m$^2 \cdot$g^{-1}), leading to specific surface areas of

527 m$^2 \cdot$g^{-1} for NCS-550 to 776 m$^2 \cdot$g^{-1} for NCS-1000. The formation of micropores is mainly caused by the loss of oxygen, hydrogen and carbon atoms due to gasification and the arrangement to turbostratic-type carbon after heat treatment, as described in more detail in our former publication [36]. The g-NCS samples of lower reaction temperatures (g-NCS-550 and g-NCS-700) are very similar to their NCS counterparts regarding porosity and surface areas. With the onset of graphitization, however, the g-NCS-850 and g-NCS-1000 samples develop a distinct mesoporosity (type-IV isotherms and a H2 hysteresis loop, Figure 7), concomitant with a loss of microporosity of about 66%. The formation of mesopores can be explained by the perforation and erosion of the graphitized N-doped carbon spheres (Figure 2). The micropore system, located within the amorphous carbon, is partially lost with the rearrangement to a more ordered graphitic structure of the carbon lattice. The drastic decrease of the micropore surface area leads to lower specific surface areas of 206 m$^2 \cdot$g^{-1} for g-NCS-850 and 182 m$^2 \cdot$g^{-1} for g-NCS-1000 compared to the non-graphitized analogues, NCS-850 (682 m$^2 \cdot$g^{-1}) and NCS-1000
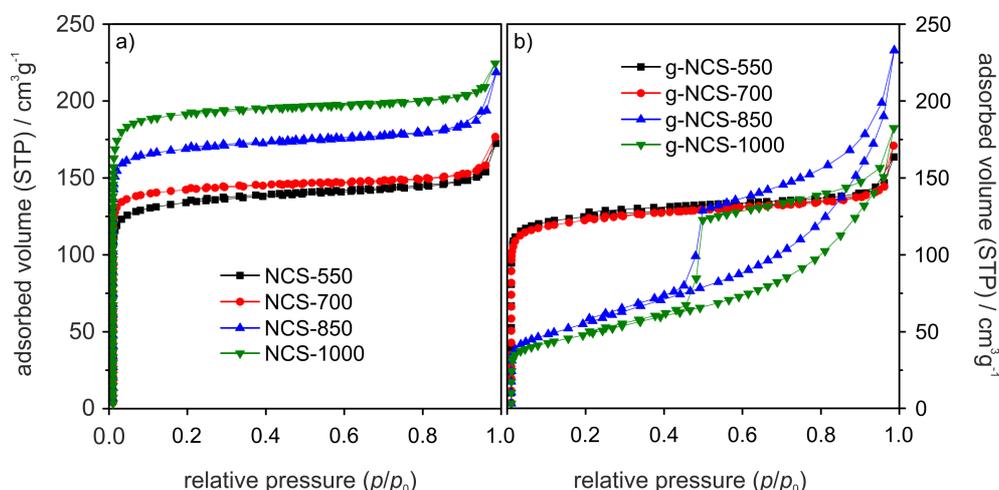

Figure 7: N$_2$ sorption isotherms of the (a) NCS and (b) g-NCS catalyst series.

Table 4: Specific surface area (SSA), external surface area (ESA), micropore surface area (MPSA) and micropore volume (MPV) measured via N_2 sorption [SSA = ESA + MPSA].

sample	N₂ sorption			
	SSA / $m^2 \cdot g^{-1}$	ESA / $m^2 \cdot g^{-1}$	MPSA / $m^2 \cdot g^{-1}$	MPV / $cm^3 \cdot g^{-1}$
NCS-550	527	42	485	0.19
NCS-700	575	39	536	0.21
NCS-850	682	38	644	0.25
NCS-1000	776	34	742	0.28
g-NCS-550	503	39	464	0.18
g-NCS-700	493	50	443	0.17
g-NCS-850	206	168	38	0.02
g-NCS-1000	182	129	53	0.02

($776 \ m^2 \cdot g^{-1}$) (Table 4). For both sample series, NCS and g-NCS, an increase of the adsorbed volume is observed for higher p/p_0 values, which can be correlated to the presence of interstitial macropores between agglomerated spheres.

In summary, all N-doped carbon spheres of the NCS series, g-NCS-550, and g-NCS-700 are amorphous presumably with only local graphenic structures. A structural change to graphitic carbon is observed for g-NCS-850 and g-NCS-1000. Amorphous carbon spheres show a smooth surface and distinct microporosity; upon graphitization the surface becomes partially perforated or eroded creating a mesoporous system. For both sample series, NCS and g-NCS, the C content increases while the amount of O and H decreases with higher reaction temperatures. The N content has its maximum for (g)-NCS-700; graphitic carbon spheres reveal a lower N content than their amorphous equivalents. Pyridinic, pyrrolic and graphitic N bonding configurations are observed for all samples; here the percentage of the latter increases with higher reaction temperatures.

2 Electrochemical and electrocatalytic results

The electrocatalytic ORR activities of the amorphous and graphitized N-doped carbon materials in acidic electrolyte (0.5 M H_2SO_4) are compiled in Figure 8, showing (Figure 8a,d) the ORR current densities, (Figure 8b,e) the ring current densities and (Figure 8c,f) the hydrogen peroxide yield. First of all, the data indicate that the carbon NCS-550 spheres are essentially inactive, while with higher nitriding temperatures the NCS samples are significantly more active. For the NCS-550 sample, this inactivity is at least partly due to its high electric resistance determined in resistance measurements (Table 5). For all catalysts nitrided at temperatures above 550 °C, which show a rather low electric resistance (Table 5), conductivity effects can be neglected. We had seen earlier that the trends with increasing nitridation temperature for the ORR in acidic and alkaline media are identical and only the overpotentials are lower in

the latter case. Therefore, we focussed in this study on acidic electrolytes.

Going to higher nitriding temperatures the onset potential (the potential at 0.1 $mA \cdot cm^{-2}$; Table 6) increases with temperature. The most active sample, the NCS-1000 sample, shows an onset potential of about 0.75 V, which is, however, still more than 200 mV below that of the commercial Pt/C catalyst. Another important aspect of the N-doped carbon spheres is that the current increase with overpotential is much slower than for the Pt/C catalyst. These catalysts do not reach the transport-limited current indicated by the Pt/C catalyst; in fact, they do not seem to reach a constant current at all, indicating that kinetic limitations are active up to very high overpotentials.

Correlating the trend in the ORR activity, as indicated by the ORR onset potential (Table 6) and the current density, with the N content of the surfaces (Table 2) for the non-graphitized catalysts, we would expect the highest ORR activity for NCS-700, since here the amount of surface N is largest for each bonding configuration. The data in Figure 8a show, however, a different trend, with the ORR activities of the NCS catalysts growing with increasing nitriding temperature. Hence, there is no direct correlation between the N surface content and the ORR activity of the catalysts, as shown in Figure 9. However, with increasing nitriding temperature, the microporosity increases strongly (Figure 9) and additionally we found a slight increase of the amount of graphenic structures in the catalysts, as indicated by the peak narrowing in the XRD patterns and the decreasing A_D/A_G ratio in the Raman signals. These structural changes may explain the increase of the ORR activity with higher nitriding temperatures, since previous calculations indicated that the ORR activity of the nitrided carbon catalysts results from the carbon edge atoms of micropores in low-level N-doped (graphitic and pyridinic N) graphene structures [24,26]. Thus, higher nitriding temperatures result in an increase of the proposed ORR active structures for the NCS catalysts. The amount
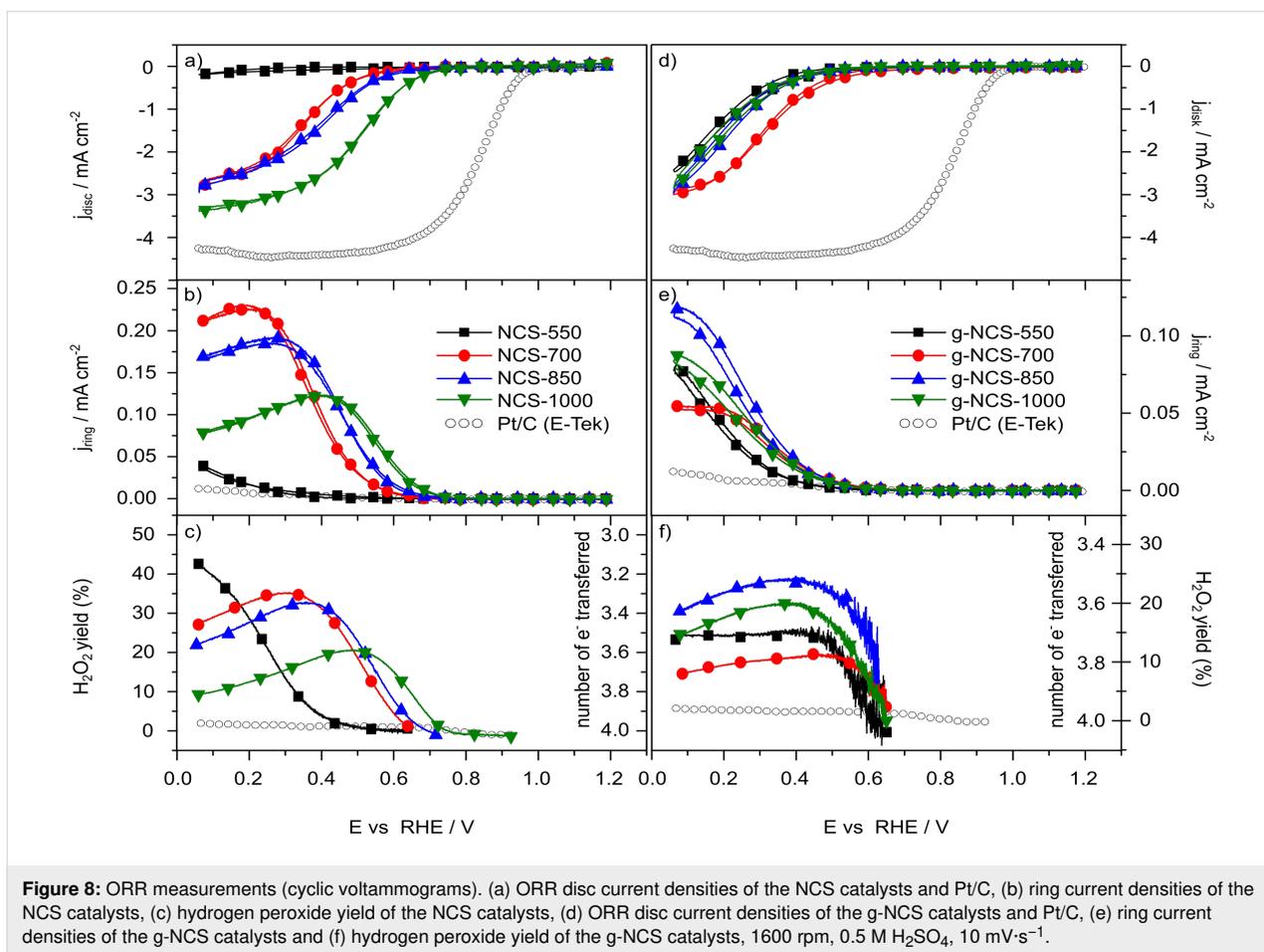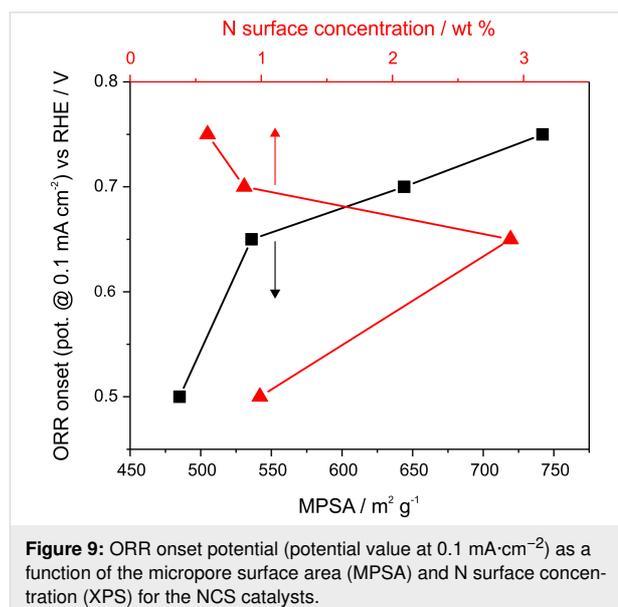
Figure 8: ORR measurements (cyclic voltammograms). (a) ORR disc current densities of the NCS catalysts and Pt/C, (b) ring current densities of the NCS catalysts, (c) hydrogen peroxide yield of the NCS catalysts, (d) ORR disc current densities of the g-NCS catalysts and Pt/C, (e) ring current densities of the g-NCS catalysts and (f) hydrogen peroxide yield of the g-NCS catalysts, 1600 rpm, 0.5 M H_2SO_4, 10 mV·s^{-1}.

Table 5: Resistance of the catalyst films of NCS and g-NCS (without catalyst film: 2 Ω).

sample	550	700	850	1000
NCS	$3 \cdot 10^6 \pm 1 \cdot 10^4$ Ω	12 ± 4 Ω	5 ± 2 Ω	3 ± 2 Ω
g-NCS	$3 \cdot 10^4 \pm 4 \cdot 10^3$ Ω	22 ± 5 Ω	7 ± 4 Ω	5 ± 2 Ω

Table 6: ORR onset potentials (potential value at 0.1 mA·cm^{-2}) of the NCS and g-NCS catalysts in the ORR measurements in Figure 8.

sample	ORR onset potential / V
NCS-550	0.50
NCS-700	0.65
NCS-850	0.70
NCS-1000	0.75
g-NCS-550	0.55
g-NCS-700	0.65
g-NCS-850	0.50
g-NCS-1000	0.50

Figure 9: ORR onset potential (potential value at 0.1 mA·cm^{-2}) as a function of the micropore surface area (MPSA) and N surface concentration (XPS) for the NCS catalysts.

of pyridinic sites, which is often correlated with the ORR activity of nitrided carbon materials [16,22-25], is highest for the NCS-700 catalyst and decreases with higher nitriding tempera-

tures. This is opposite to the trend of the ORR activity, which increases with nitriding temperature (Table 2). Similar, also the concentration of pyrrolic nitrogen sites decreases with increasing nitridation temperature, while the amount of graphitic N, which is sometimes also reported to be correlated with the ORR activity [17-21], is only slightly lower for nitriding at 1000 °C compared to nitriding at 700 °C. Hence, none of these different nitrogen configurations can simply explain the trend in the ORR activity. This agrees with the results of DFT-based calculations of a comparable model system, which showed that the active sites are not the N-sites themselves but rather carbon atoms at edge sites of pores in N-doped graphenic layers [26]. These calculations showed that too high amounts of N-doping and thus of graphitic N-sites can impair the ORR activity, in agreement with our observation that there is no simple correlation between the concentration of graphenic sites and the ORR activity. Instead, we suggest that for the catalysts presented here the changes in the ORR activity are mainly caused by the structural changes, in particular by the microporosity, which increases drastically with increasing nitriding temperature, rather than by the changes in the content of specific nitrogen configurations.

Moving on to the graphitized g-NCS catalysts, the trend for the ORR activities is different (Figure 8, Table 6). For the graphitized samples, the differences between the ORR activities at different nitriding temperatures are significantly smaller. The g-NCS-550 catalyst also suffers from a high ohmic resistance of the catalyst film, which, however, is two decades lower than that of NCS-550. Accordingly, the g-NCS-550 sample is significantly more active than the NCS-550 catalyst. The g-NCS-700 and NCS-700 samples show about the same ORR activity, and for nitriding temperatures above 700 °C, the ORR activities are lower again and clearly below those of the corresponding NCS samples.

The higher ORR current for the g-NCS-550 catalyst compared to NCS-550 can be caused by the higher N content of the g-NCS-550 catalyst, but also by the lower ohmic resistance of the catalyst film (Table 5). Since the g-NCS-700 catalyst shows no graphitization of the carbon (see section 1 in "Results and Discussion") and also otherwise closely resembles the NCS-700 material (similar N-configuration, N content, SSA/ESA, and microporosity), it is not astonishing that these two materials show comparable ORR activities (Figure 8a,d). Additionally, this result also strongly supports our claim that the acidic washing of the graphitized catalysts is able to largely remove the iron, since otherwise one would expect an increased ORR activity of the g-NCS-700 material. Similar to the NCS-850 and NCS-1000 samples, also for the g-NCS-850 and g-NCS-1000 catalysts the N content decreases significantly for every N configuration with higher nitriding temperatures. The decrease is,

however, more pronounced for the graphitized samples. Our previous suggestion that the ORR activity is related to carbon edge atoms at micropore structures in low-level N-doped graphene structures [24] can explain the decrease of the ORR activity of the g-NCS-850 and g-NCS-1000 samples compared with the non-graphitized counterparts, since the amount of micropores is drastically lower after graphitization (g-NCS-850 and g-NCS-1000). Overall, it seems that at higher temperatures (850 °C and above) the graphitization process has a negative impact on the ORR activity of the carbon spheres because of the decrease of the number of micropores, and thus of ORR active defect sites.

Finally, considering the selectivity for the 4-electron reaction pathway to H_2O, which is highly important for technical applications (Figure 8), we find that at potentials below 0.6 V the NCS-1000 catalyst, the best ORR catalyst in this series, has H_2O_2 yields between 10% and 20%, whereas the other catalysts show values between 20% and 40%. Regardless of that difference, the values are several times higher than the H_2O_2 yields obtained for commercial Pt-based catalysts (Figure 8). Hence, for technical applications in conventional PEMFCs, it is not only necessary to further improve the activity of nitrided carbon catalysts, but in particular also the selectivity for H_2O formation. The trend of higher H_2O_2 yields at higher overpotentials furthermore clearly demonstrates that the slow increase of the measured current densities towards the transport limited current cannot result from a transition from a 2-electron pathway to a 4-electron pathway with increasing overpotential.

The N-doped carbon spheres investigated in the present study were previously used as conducting carbon cores for composite catalysts (summary of the results in Figure 10), where they were covered by a layer of N-doped TiO_2 (TiON@NCS) [34] or
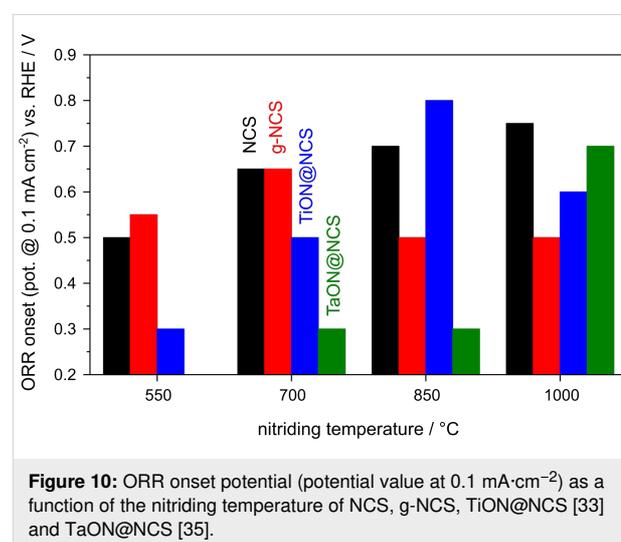

Figure 10: ORR onset potential (potential value at 0.1 mA·cm⁻²) as a function of the nitriding temperature of NCS, g-NCS, TiON@NCS [33] and TaON@NCS [35].

N-doped Ta$_x$O$_y$ (TaON@NCS) [33]. The covering was supposed to serve two purposes, first, to yield ORR activity and, second, to protect the (nitrided) carbon core against corrosion. In this study we used the same procedure for N-doping as applied in the present work, which resulted not only in doping of the oxide shell, but also of the carbon core. It was not clear, whether the significant ORR activity of these composite materials is due to the oxynitride shell or perhaps predominantly caused by the nitrided carbon cores. Further insight shall be given by the present study. However, one has to keep in mind, that a quantitative comparison will not be possible. We do not expect nitridation to give the exact same results with and without the presence of an oxide shell due to accessibility and diffusion limitations.

For TiON@NCS [34] we found, in general, similar ORR characteristics as in the present study, with a significantly lower slope of the kinetic ORR current densities in the onset potential range than for Pt/C. In addition, a purely transport-limited region was not reached. In this case the most active sample was that obtained upon nitriding at 850 °C, with an ORR onset at about 0.8 V, in contrast to the best NCS-1000 catalyst, for which an only slighly lower ORR activity was found after nitriding at 1000 °C (Figure 10). Nitriding at 1000 °C led to lower activities for the composite materials, with an ORR onset at about 0.6 V. For the TiON@NCS samples this can be explained by the structural development of the oxynitride shell upon nitridation. For TiON@NCS-1000 the SSA and MPSA values were lower than for TiON@NCS-850; for the latter one a pronounced mesopore formation of the TiON shell resulted in a better accessibility of the N-doped carbon core in the electrochemical studies, which also resulted in a better performance. For the NCS samples only the microporous character becomes more pronounced with increasing nitriding temperature. Hence, the ORR performance cannot be assumed to be identical in both cases, even if it were dominated only by the carbon core. Therefore, a simple quantification of the effect of the shell on the ORR performance is not possible. Nevertheless, it is clear from this comparison that the oxynitride shell does not lead to a general improvement of the ORR performance of the nitrided carbon spheres. This is true also for the H$_2$O$_2$ yields, which tend to be similar if not higher on the TiON@NCS composite catalysts (20–40%) than on the nitrided carbon spheres.

A similar comparison with the TaON@NCS catalyst [33] shows even more distinct differences (Figure 10). For these composite materials we found a clear ORR activity only after nitriding at 1000 °C. Only the sample TaON@NCS-1000 exhibited a mesoporous shell, thus improving access to the N-doped carbon core. The resulting TaON@NCS-1000 catalyst features a rather similar onset (0.7 V) as the NCS-1000 sample, and similar *j–E* char-

acteristics, but somewhat lower current densities. However, for these composites the differences in porosity/surface area between the oxynitride covered spheres and the pure nitrided carbon spheres are even more pronounced, with substantially lower surface areas for the TaON@NCS catalysts. Hence, in these cases direct comparison of the ORR performance after similar nitriding temperatures is even less possible. Nevertheless, for nitriding temperatures above and below 1000 °C, the TaON layer seems to block the ORR activity of the nitrided carbon cores very likely due to the lack of the permeable mesoporous shell. Also when comparing the H$_2$O$_2$ yields of the TaON@NCS composites [33], we find no advantage of the composite catalysts since the hydrogen peroxide yields are around 40% for all catalysts, which is higher than the values obtained for the pure nitrided carbon spheres (mostly around 20%).

Overall, the present findings underline that the metal (oxy)nitride shell of the composite catalysts does not lead to a general improvement of their ORR performance. Within the present series of catalysts, the non-graphitized carbon spheres nitrided at 1000 °C are the most suitable Pt-free ORR catalysts. Further work is needed, however, to improve the relative high peroxide yields obtained so far.

Conclusion

The N-doped carbon spheres (NCS) synthesized in the present work are characterized by a well-defined spherical shape and smooth surface. Originating from glucose, the carbon matrix of the spheres initially contains oxygen- and hydrogen-based functional groups. The N content (pyridinic, pyrrolic and graphitic bonding configurations) has its maximum after nitriding at 700 °C. The carbon structure is amorphous as proven by XRD and TEM measurements, with an increasing tendency to turbostratic-type carbon with higher reaction temperatures.

Graphitized carbon spheres were synthesized with the aid of an iron oxide catalyst at the respective nitriding temperature. For g-NCS-550 and g-NCS-700 materials, the minimum temperature required for the catalytic graphitization is not reached yet, therefore their properties are almost equal to those of the amorphous NCS counterparts. Graphitization at higher temperatures leads to the formation of mesopores, combined with the loss of the micropore system. Within the spheres clew-like strings are observed, their thickness matches the average stacking thickness of the graphite layers L_c leading to the conclusion, that the graphite layers are arranged along the longitudinal axis of the strings. The N content of the g-NCS catalysts is lower compared to the NCS samples. This ultimately results in a less efficient substitutional N-doping for graphitized carbon spheres.

The nitrided amorphous carbon spheres show a high ORR activity when nitrided at high temperatures (1000 °C), which, however, resulted in the lowest N content for all three N configurations of all NCS catalysts. We attribute the high ORR activity of this catalyst to the large amount of micropores (ORR-active C edge atoms) in low-level N-doped graphenic structures. The graphitization (g-NCS) seems to hinder the ORR activity even after high nitriding temperatures, because of the strong decrease of the micropores compared to the non-graphitized catalysts. In that picture the ORR activity is not associated directly to one of the N sites, but strongly depends on the amount of defect sites and thus on the microporosity/graphitization of the carbon surface, in combination with a low N-doping. These correlations between structure and ORR activity can be used to further improve the catalytic activity of N-doped carbon catalysts towards the ORR.

Experimental
Chemicals

All chemicals were purchased from commercial suppliers and were used without further purification unless stated otherwise: Glucose (Amresco, 98%), ethanol (VWR, 99.5%), iron(III) nitrate anhydrous (Sigma-Aldrich, 99.9%), hydrochloric acid (Merck Emsure, 37%), argon (Air Liquide, 99.99%), and ammonia (Air Liquide, 99.9%).

Synthesis of (graphitized) N-doped carbon spheres

The synthesis of the nitrided carbon spheres (NCS) was analogous to the procedure in our previous publications [27,34]. Carbon spheres were synthesized by hydrothermal treatment of a 0.75 M glucose solution in aqua dest. (165 mL) at 165 °C for 10.5 h. The resulting spherical carbon particles were washed three times with 200 mL aqua dest. and ethanol each, centrifuged and dried [36].

Synthesis of N-doped carbon spheres (NCS): The as-synthesized carbon spheres were carbonized under argon atmosphere in a tube furnace (V = 12 L) for 4 h (heating rate 5 °C·min^{-1}) at different temperatures, between 550 and 1000 °C with steps of 150 °C, followed by N-doping in an ammonia atmosphere (3 NL·h^{-1}), holding the individual carbonization temperature of each sample for 1 h. Cooling to room temperature was performed in an argon flow.

Synthesis of graphitized N-doped carbon spheres (g-NCS): As-synthesized carbon spheres were pre-carbonized in argon atmosphere for 1 h (heating rate 5 °C·min^{-1}) at 550 °C. A solution of 5.05 g iron(III) nitrate in 50 mL aqua dest. was added to 2.5 g pre-carbonized carbon spheres and stirred for 24 h, followed by refluxing for 5 h at 100 °C and subsequent filtration

and drying. Catalytic graphitization was carried out by annealing at different temperatures, between 550 and 1000 °C with steps of 150 °C, in argon atmosphere for 4 h (heating rate 5 °C·min^{-1}). Iron catalyst particles were removed by acid leaching with 2 M hydrochloric acid, followed by filtration, washing with aqua dest. to a neutral pH value and drying [32]. N-doping was realized in the same way as described for the NCS sample series; thereby the N-doping temperature is set to the same temperature as used for the catalytic graphitization of the given sample.

In the following, N-doped carbon spheres are labeled as NCS and graphitized N-doped carbon spheres as g-NCS. The number added to those labels represents the reaction temperature.

Characterization of (graphitized) N-doped carbon spheres

Scanning electron microscopy (SEM) images were recorded with a field-emission scanning electron microscope (FE-SEM, Zeiss Ultra Plus) at 10 to 12 keV beam energy. For imaging, the samples were deposited on a conducting carbon film. Energy-dispersive X-ray spectroscopy (EDX) measurements were performed on the same FE-SEM with an EDX large-area silicon-drift detector (Oxford X-Max 50), using an accelerating voltage of 15 kV with a counting time of 5 min per spot. Bright-field transmission electron microscopy (BF-TEM) images were taken with a JEOL1400 instrument equipped with a CCD camera. For sample preparation, a droplet of ethanol containing the dispersed sample powder (ca. 1 mg·mL^{-1}) was deposited on a carbonized Cu grid (Plano, Mesh 300), followed by evaporation of ethanol. For CHN elemental analysis, a Vario MICRO cube instrument (Elementar Analysensysteme GmbH) was used, the thermal decomposition temperature was 1000 °C in air. XPS measurements were performed in a Physical Electronics PHI 5800 Multi ESCA system at an emission angle of 45° and a pass energy of 29.35 eV (detail spectra), applying monochromatic Al Kα radiation (250 W, 13 kV). The thin-layer samples used for these measurements were prepared by depositing and drying 20 μL of an aqueous catalyst suspension on a silicon wafer, which was pre-cleaned by sequential rinsing in ultrapure water (MilliQ), 1 M KOH solution, and conc. H$_2$SO$_4$. By using silicon wafers instead of a carbon-containing support, we minimized contributions from the support to the C 1s signal of the carbon-containing catalyst film. The spectra showed minor charging effects, which were compensated by a neutralizer (low-energy electron flood gun). The C 1s peak was set to 284.8 eV for binding energy calibration [50]. Evaluation and deconvolution of the measured signals (Shirley background; peak shape: 70% Gaussian/30% Lorentzian) was carried out using the CasaXPS software package. X-ray diffraction (XRD) measurements were performed using a Bruker D8

Advance instrument (Bruker Karlsruhe), employing Cu Kα radiation (λ = 0.154 nm) in a 2θ range of 5° to 80° (0.02° continuous mode, 0.5 s per step). Porosity and specific surface area were determined by N_2 sorption measurements on a Micromeritics ASAP 2420 instrument (Micromeritics) in a relative pressure range of p/p_0 between 4×10^{-6} and 0.99 and a temperature of −196 °C. The specific surface area was calculated by the method of Brunauer, Emmett, and Teller in a relative pressure range of p/p_0 0.01 to 0.3. The ratio of micropore surface area to external surface area was calculated by the t-plot method (thickness curve: carbon black STSA, fitted thickness range: 0.4–0.6 nm). Raman spectroscopy measurements were performed by a Thermo DXR Raman microscope (Thermo, Madison) with a confocal microscope BX41 (Olympus Corp.). The diameter of the laser spot was approximately 2.5 μm (10× microscope objective, NA = 0.25), the laser power was 1 mW at 532 nm, the spectra were collected from 100 to 3700 cm^{-1} with a spectral resolution of 5 cm^{-1} (50 μm slit-like pinhole) with an exposure time of 5 s (10 accumulations).

Electrode preparation and electrochemical measurements

The catalyst thin-film electrode (catalyst loading of 0.285 $mg \cdot cm^{-2}$ for Pt-free catalyst, 140 $μg \cdot cm^{-2}$ loading (Pt loading: 28 $μg \cdot cm^{-2}$) for the 20 wt % Pt/C E-Tek reference catalyst) was prepared by pipetting an aqueous suspension of the synthesized materials (20 μL of a 4 $mg \cdot mL^{-1}$ suspension; Millipore MilliQ, 18.2 MΩ·cm) onto a mirror-polished glassy carbon (GC) disc (Sigradur G from Hochtemperatur Werkstoffe, d = 6 mm), followed by subsequent drying under a N_2 stream. With these loadings we could form homogeneous, thin and stable catalyst layers on the electrode. The resulting film was covered with the same volume of a 1 wt % aqueous Nafion solution and dried again to ensure the mechanical stability of the catalyst layer on the glassy carbon without creating additional diffusion limitations [51]. The geometric area of the electrochemically accessible part of the electrode is 0.28 cm^2. For the electrochemical experiments, we used a rotating ring disk electrode (RRDE) setup (Pine Instruments Analytical Rotator, AFASRE), with the thin-film electrode on the GC disc functioning as working electrode. The working electrode is surrounded by a Pt ring biased at 1.2 V, which allows one to measure the peroxide yield in the ORR. A reversible hydrogen electrode (RHE) served as reference electrode and a Pt wire as counter electrode, both separated by glass frits from the main cell. The RHE itself consists of a Pt plate in a glass tube containing the respective electrolyte used for the measurement and a H_2 bubbler. In the following, all potentials will be quoted versus that of the RHE. The potential was controlled by a bi-potentiostat (Pine Instruments AFRDE5). The potentiodynamic ORR measurements were performed in acidic electrolyte (0.5 M H_2SO_4, Merck Suprapur, Millipore MilliQ, 18.2 MΩ·cm) in O_2 saturated supporting electrolyte at a scan rate of 10 $mV \cdot s^{-1}$ and a rotation rate of 1600 rpm. For all ORR measurements, the currents in N_2-saturated electrolyte were subtracted from the measured ORR currents in order to remove double-layer charging currents. For each catalyst the cyclic voltammograms are presented, thus the ORR measurements of each catalyst consist of a cathodic (down-going scan, lower trace) and an anodic (up-going scan, upper trace) scan. For the calculation of the hydrogen peroxide yield we used Equation 1, where I_r is the measured ring current, I_d the disc current and N the collection efficiency of the setup (here the measured value specific for the current setup of N is 0.2):

$$ H_2O_2 \, (\%) = \frac{2|I_r|}{N|I_d| + |I_r|} \cdot 100. \qquad (1) $$

The resistance measurements of the catalyst film were performed by pipetting and drying 80 μL of the catalysts suspension on a glassy carbon disk, similar to preparation of the catalyst film for the electrochemical measurements. The dried catalyst film is than covered by another glassy carbon disk, and the two disks were tightly pressed together. The resistance between both glassy carbon units with the catalyst film in between was measured with a Keithley 197A multimeter. The onset potentials in Table 6 and Figure 9 and Figure 10 are defined as the potential at which the current geometric densities exceed 0.1 $mA \cdot cm^{-2}$.

ORCID® iDs

Andreas Reyer - https://orcid.org/0000-0001-7578-5066
Thomas Diemant - https://orcid.org/0000-0001-9701-9995
Michael S. Elsaesser - https://orcid.org/0000-0002-4675-9819
R. Jürgen Behm - https://orcid.org/0000-0002-7565-0628
Nicola Hüsing - https://orcid.org/0000-0003-2274-9779

References

1. Gong, K.; Du, F.; Xia, Z.; Durstock, M.; Dai, L. *Science* **2009,** *323,* 760–764. doi:10.1126/science.1168049

2. Liu, Z.-W.; Peng, F.; Wang, H.-J.; Yu, H.; Zheng, W.-X.; Yang, J. *Angew. Chem., Int. Ed.* **2011,** *50,* 3257–3261. doi:10.1002/anie.201006768

3. Liu, J.; Song, P.; Ning, Z.; Xu, W. *Electrocatalysis* **2015,** *6,* 132–147. doi:10.1007/s12678-014-0243-9

4. Wang, D.-W.; Su, D. *Energy Environ. Sci.* **2014,** *7,* 576–591. doi:10.1039/c3ee43463j

5. Yang, L.; Jiang, S.; Zhao, Y.; Zhu, L.; Chen, S.; Wang, X.; Wu, Q.; Ma, J.; Ma, Y.; Hu, Z. *Angew. Chem., Int. Ed.* **2011,** *50,* 7132–7135. doi:10.1002/anie.201101287

6. Yang, Z.; Nie, H.; Chen, X.; Chen, X.; Huang, S. *J. Power Sources* **2013,** *236,* 238–249. doi:10.1016/j.jpowsour.2013.02.057

7. Daems, N.; Sheng, X.; Vankelecom, I. F. J.; Pescarmona, P. P. *J. Mater. Chem. A* **2014,** *2,* 4085–4110. doi:10.1039/c3ta14043a

8. Lee, W. J.; Maiti, U. N.; Lee, J. M.; Lim, J.; Han, T. H.; Kim, S. O. *Chem. Commun.* **2014,** *50,* 6818–6830. doi:10.1039/c4cc00146j

9. Wei, Q.; Tong, X.; Zhang, G.; Qiao, J.; Gong, Q.; Sun, S. *Catalysts* **2015,** *5,* 1574–1602. doi:10.3390/catal5031574

10. Inagaki, M.; Toyoda, M.; Soneda, Y.; Morishita, T. *Carbon* **2018,** *132,* 104–140. doi:10.1016/j.carbon.2018.02.024

11. Zhu, C.; Li, H.; Fu, S.; Du, D.; Lin, Y. *Chem. Soc. Rev.* **2016,** *45,* 517–531. doi:10.1039/c5cs00670h

12. Li, Y.; Zhou, W.; Wang, H.; Xie, L.; Liang, Y.; Wei, F.; Idrobo, J.-C.; Pennycook, S. J.; Dai, H. *Nat. Nanotechnol.* **2012,** *7,* 394–400. doi:10.1038/nnano.2012.72

13. Ai, K.; Liu, Y.; Ruan, C.; Lu, L.; Lu, G. M. *Adv. Mater. (Weinheim, Ger.)* **2013,** *25,* 998–1003. doi:10.1002/adma.201203923

14. Yang, T.; Liu, J.; Zhou, R.; Chen, Z.; Xu, H.; Qiao, S. Z.; Monteiro, M. J. *J. Mater. Chem. A* **2014,** *2,* 18139–18146. doi:10.1039/c4ta04301d

15. Zheng, Y.; Jiao, Y.; Chen, J.; Liu, J.; Liang, J.; Du, A.; Zhang, W.; Zhu, Z.; Smith, S. C.; Jaronic, M.; Lu, G. Q.; Qiao, S. Z. *J. Am. Chem. Soc.* **2011,** *133,* 20116–20119. doi:10.1021/ja209206c

16. Guo, D.; Shibuya, R.; Akiba, C.; Saji, S.; Kondo, T.; Nakamura, J. *Science* **2016,** *351,* 361–365. doi:10.1126/science.aad0832

17. Geng, D.; Chen, Y.; Chen, Y.; Li, Y.; Li, R.; Sun, X.; Ye, S.; Knights, S. *Energy Environ. Sci.* **2011,** *4,* 760–764. doi:10.1039/c0ee00326c

18. Lai, L.; Potts, J. R.; Zhan, D.; Wang, L.; Poh, C. K.; Tang, C.; Gong, H.; Shen, Z.; Lin, J.; Ruoff, R. S. *Energy Environ. Sci.* **2012,** *5,* 7936–7942. doi:10.1039/c2ee21802j

19. Liu, R.; Wu, D.; Feng, X.; Müllen, K. *Angew. Chem., Int. Ed.* **2010,** *49,* 2565–2569. doi:10.1002/anie.200907289

20. Sharifi, T.; Hu, G.; Jia, X.; Wågberg, T. *ACS Nano* **2012,** *6,* 8904–8912. doi:10.1021/nn302906r

21. Wu, K.-H.; Wang, D.-W.; Su, D.-S.; Gentle, I. R. *ChemSusChem* **2015,** *8,* 2772–2788. doi:10.1002/cssc.201500373

22. Ding, W.; Wei, Z.; Chen, S.; Qi, X.; Yang, T.; Hu, J.; Wang, D.; Wan, L.-J.; Alvi, S. F.; Li, L. *Angew. Chem., Int. Ed.* **2013,** *52,* 11755–11759. doi:10.1002/anie.201303924

23. Rao, C. V.; Cabrera, C. R.; Ishikawa, Y. *J. Phys. Chem. Lett.* **2010,** *1,* 2622–2627. doi:10.1021/jz100971v

24. Xing, T.; Zheng, Y.; Li, L. H.; Cowie, B. C. C.; Gunzelmann, D.; Qiao, S. Z.; Huang, S.; Chen, Y. *ACS Nano* **2014,** *8,* 6856–6862. doi:10.1021/nn501506p

25. Morais, R. G.; Rey-Raap, N.; Figueiredo, J. L.; Pereira, M. F. R. *Beilstein J. Nanotechnol.* **2019,** *10,* 1089–1102. doi:10.3762/bjnano.10.109

26. Sakaushi, K.; Eckardt, M.; Lyalin, A.; Taketsugu, T.; Behm, R. J.; Uosaki, K. *ACS Catal.* **2018,** *8,* 8162–8176. doi:10.1021/acscatal.8b01953

27. Eckardt, M.; Sakaushi, K.; Lyalin, A.; Wassner, M.; Hüsing, N.; Taketsugu, T.; Behm, R. J. *Electrochim. Acta* **2019,** *299,* 736–748. doi:10.1016/j.electacta.2019.01.046

28. Kim, H.; Lee, K.; Woo, S. I.; Jung, Y. *Phys. Chem. Chem. Phys.* **2011,** *13,* 17505–17510. doi:10.1039/c1cp21665a

29. Roldán, L.; Armenise, S.; Marco, Y.; García-Bordejé, E. *Phys. Chem. Chem. Phys.* **2012,** *14,* 3568–3575. doi:10.1039/c2cp23609e

30. Xue, Y.; Wu, B.; Jiang, L.; Guo, Y.; Huang, L.; Chen, J.; Tan, J.; Geng, D.; Luo, B.; Hu, W.; Yu, G.; Liu, Y. *J. Am. Chem. Soc.* **2012,** *134,* 11060–11063. doi:10.1021/ja302483t

31. Gutiérrez-Pardo, A.; Ramírez-Rico, J.; Cabezas-Rodríguez, R.; Martínez-Fernández, J. *J. Power Sources* **2015,** *278,* 18–26. doi:10.1016/j.jpowsour.2014.12.030

32. Nettelroth, D.; Schwarz, H.-C.; Burblies, N.; Guschanski, N.; Behrens, P. *Phys. Status Solidi A* **2016,** *213,* 1395–1402. doi:10.1002/pssa.201532796

33. Tang, J.; Liu, J.; Torad, N. L.; Kimura, T.; Yamauchi, Y. *Nano Today* **2014,** *9,* 305–323. doi:10.1016/j.nantod.2014.05.003

34. Wassner, M.; Eckardt, M.; Gebauer, C.; Bourret, G. R.; Hüsing, N.; Behm, R. J. *Electrochim. Acta* **2017,** *227,* 367–381. doi:10.1016/j.electacta.2016.12.145

35. Wassner, M.; Eckardt, M.; Gebauer, C.; Hüsing, N.; Behm, R. J. *ChemElectroChem* **2016,** *3,* 1641–1654. doi:10.1002/celc.201600246

36. Romero-Anaya, A. J.; Ouzzine, M.; Lillo-Ródenas, M. A.; Linares-Solano, A. *Carbon* **2014,** *68,* 296–307. doi:10.1016/j.carbon.2013.11.006

37. Liu, T.; Liu, E.; Ding, R.; Luo, Z.; Hu, T.; Li, Z. *Electrochim. Acta* **2015,** *173,* 50–58. doi:10.1016/j.electacta.2015.05.042

38. Anton, R. *Carbon* **2009,** *47,* 856–865. doi:10.1016/j.carbon.2008.11.038

39. Sevilla, M.; Fuertes, A. B. *Chem. – Eur. J.* **2009,** *15,* 4195–4203. doi:10.1002/chem.200802097

40. Nagaiah, T. C.; Kundu, S.; Bron, M.; Muhler, M.; Schuhmann, W. *Electrochem. Commun.* **2010,** *12,* 338–341. doi:10.1016/j.elecom.2009.12.021

41. Barnakov, C. N.; Khokhlova, G. P.; Malysheva, V. Y.; Popova, A. N.; Ismagilov, Z. R. *Solid Fuel Chem.* **2015,** *49,* 25–29. doi:10.3103/s0361521915010036

42. Chi, S.-H.; Kim, G.-C. *J. Nucl. Mater.* **2008,** *381,* 9–14. doi:10.1016/j.jnucmat.2008.07.027

43. Barbera, K.; Frusteri, L.; Italiano, G.; Spadaro, L.; Frusteri, F.; Perathoner, S.; Centi, G. *Chin. J. Catal.* **2014,** *35,* 869–876. doi:10.1016/s1872-2067(14)60098-x

44. Wollbrink, A.; Volgmann, K.; Koch, J.; Kanthasamy, K.; Tegenkamp, C.; Li, Y.; Richter, H.; Kämnitz, S.; Steinbach, F.; Feldhoff, A.; Caro, J. *Carbon* **2016,** *106,* 93–105. doi:10.1016/j.carbon.2016.04.062

45. Malard, L. M.; Pimenta, M. A.; Dresselhaus, G.; Dresselhaus, M. S. *Phys. Rep.* **2009,** *473,* 51–88. doi:10.1016/j.physrep.2009.02.003

46. Dresselhaus, M. S.; Dresselhaus, G.; Saito, R.; Jorio, A. *Phys. Rep.* **2005,** *409,* 47–99. doi:10.1016/j.physrep.2004.10.006

47. Reich, S.; Thomsen, C. *Philos. Trans. R. Soc., A* **2004,** *362,* 2271–2288. doi:10.1098/rsta.2004.1454

48. Kawashima, Y.; Katagiri, G. *Phys. Rev. B* **1995,** *52,* 10053–10059. doi:10.1103/physrevb.52.10053

49. Kaufman, J. H.; Metin, S.; Saperstein, D. D. *Phys. Rev. B* **1989,** *39,* 13053–13060. doi:10.1103/physrevb.39.13053

50. Moulder, J. F.; Stickle, W. F.; Sobol, P. E.; Bomben, K. D. *Handbook of X-ray Photoelectron Spectroscopy;* Perkin Elmer Corp.: Eden Prairie, MN, U.S.A., 1992.

51. Schmidt, T. J.; Gasteiger, H. A.; Stäb, G. D.; Urban, P. M.; Kolb, D. M.;
    Behm, R. J. *J. Electrochem. Soc.* **1998,** *145,* 2354–2358.
    doi:10.1149/1.1838642